Nonlinear Modeling of Radial Stellar Pulsations

Radosław Smolec

Ph.D. Thesis under supervision of Dr hab. Paweł Moskalik

Acknowledgements

Contents

Preface

In this thesis, I present the results of my work concerning the nonlinear modeling of radial stellar pulsations. I will focus on classical Cepheids, particularly on the double-mode phenomenon.

History of nonlinear modeling of radial stellar pulsations begins in the sixties of the previous century. It is summarized in the Introduction (Chapter 1). At the beginning convection was disregarded in model equations. Qualitatively, almost all features of the radial pulsators were successfully modeled with purely radiative hydrocodes. Among problems that remained, the most disturbing was modeling of the double-mode phenomenon. This long-standing problem seemed to be finally solved with the inclusion of turbulent convection into the model equations. Turbulent convection recipes are described in more detail in Chapter 2, which can be regarded as second part of the Introduction. This detailed description provides necessary theoretical background for the further considerations presented in this thesis.

Although dynamical aspects of the double-mode behaviour were extensively studied, its origin, particularly the specific role played by convection, remained obscure. To study this and other problems of radial stellar pulsations, I implemented the convection into pulsation hydrocodes. These codes are partly based on old radiative Stellingwerf's codes. Implementation of turbulent convection into the model equations is not an easy task. Construction of the static model builder, as well as linear stability analysis, require substantially different methods than used in radiative codes. Hence, model builder and linear nonadiabatic codes were written anew. Nonlinear code was largely rewritten. All the codes, their physical and numerical ingredients, are described in detail in Chapter 3. Some test results presented in Chapter 4, concerning the modeling of single-mode Cepheids confirm, that the codes are robust and reproduce basic properties of the observed Cepheids.

Described codes adopt the Kuhfuß convection model. In other codes, particularly in the Florida-Budapest hydrocode, used in computation of most of the published double-mode models, different approximations concerning *e.g.*, eddy-viscous terms or treatment of convectively stable regions are adopted. Particularly the neglect of negative buoyancy effects in the Florida-Budapest code and its consequences, were never discussed in the literature. These consequences are severe, as I describe in Chapters 5 and 6. Concerning the single-mode pulsators, neglect of negative buoyancy leads to smaller pulsation amplitudes, in comparison to amplitudes computed with code including these effects (Chapter 5). In Chapter 6, I show that this effect reduces the amplitude of the fundamental mode very strong. This property of the Florida-Budapest models is crucial in bringing up the stable double-mode Cepheid pulsation involving fundamental and first overtone modes (F/1O). Such behaviour is not observed in models computed including negative buoyancy. As the neglect of

negative buoyancy is physically not correct, so are the double-mode Cepheid models computed with the Florida-Budapest hydrocode.

Extensive search for F/1O double-mode Cepheid pulsation with the codes including negative buoyancy effects yielded null result. Some resonant double-mode F/1O Cepheid models were found (Chapter 7), but their occurrence was restricted to a very narrow domain in the Hertzsprung-Russel diagram. Resonant excitation of the doubly-periodic pulsation is discussed in Chapter 7, based on very interesting radiative models. These considerations provide the background for the double-overtone Cepheid models, involving first and second overtones, discussed in Chapter 8. Model computations intended to model the double-overtone Cepheids in the Large Magellanic Cloud, revealed some stable double-mode pulsations, however, restricted to a narrow period range. Resonances are most likely conductive in bringing up the double-mode behaviour observed in these models. However, majority of the double-overtone LMC Cepheids cannot be reproduced with our codes. Hence, the modeling of double-overtone Cepheids with convective hydrocodes is not satisfactory, either.

As I summarize in Chapter 9, double-mode pulsation still lacks satisfactory explanation, and problem of its modeling remains open.

This thesis presents and extends the results included first of all in the two refereed papers:

    Smolec & Moskalik (2008a) *– Chapters 3, 4 and 5*
    Smolec & Moskalik (2008b) *– Chapter 6*

Also some results from the following publications are presented,

    Baranowski, Smolec, Dimitrov *et al.* (2009) *– Chapter 4*
    Smolec & Moskalik (2007) *– Chapter 7*
    Smolec (2009) *– Chapter 7*
    Dziembowski & Smolec (2009) *– Chapter 8*

Unpublished material is included in Chapter 7 (Section 7.3) and in Chapter 8 (Section 8.3).

Chapter 1

Introduction

1.1 Stellar pulsation in the pre-computer era

One of the most important classes of variable stars in astronomy are Cepheids. Variability of the prototype of the class, δ Cephei, was discovered by JOHN GOODRICKE (1786). However, the first Cepheid variable, η Aquilae, was discovered one month before by Edward Pigott (PIGOTT 1785). Light curves of these periodic variables have very characteristic non-symmetric shape, with shorter rising branch, and about twice as long descending branch. Few years earlier, Goodricke discovered other variable star, Algol (GOODRICKE 1783). Symmetric light curve led him to interpretation of Algol's variability in terms of eclipses[1]. In case of δ Cephei, Goodricke didn't make any statements regarding the nature of its variability. Due to the absence of any other ideas on causing the light variation in stars, also δ Cephei and other variables with similar light curves were interpreted as binaries. Better telescopes and systematic observations led to the discovery of plenty of Cepheid-like stars at the onset of the twentieth century. So-called cluster variables with periods below one day, found mostly in globular clusters, are prototypes of other very important class of variables, RR Lyrae stars. At that time however, distinction between RR Lyrae stars and Cepheids was not clear, and many authors regarded it as artificial, treating cluster variables as short period Cepheids. Extensive observations of the Magellanic Clouds with the 24-inch Bruce Telescope at Harvard Observatory, led to the discovery of 1777 variables, reported by LEAVITT (1908). Light curves of many of these stars resembled those of cluster variables. For sixteen of them, period was determined, and already in 1908 Mrs Leavitt stated, *It is also worthy of notice that (in Table VI) the brighter variables have the longer periods.* This was the first statement of the period-luminosity relation, fully established by PICKERING (1912). Two years later, HERTZSPRUNG (1914) calibrated the period-luminosity relation and used it to derive the distance to the Small Magellanic Cloud. The career of Cepheids as one of the most important distance indicators in astrophysics began.

At the beginning of the twentieth century the binary hypothesis was in serious trouble. SCHWARZSCHILD (1900) discovered that η Aquilae not only changes its brightness, but also colour, and hence, a spectral type. Even complicated models, assuming multiple star systems, couldn't account for the bumps, clearly present on

---

[1] original suggestion was by Pigott; *see* HOSKIN (1979) for the exciting history of the cooperation of these two astronomers, living in York, next to each other

the light curves of Cepheid-type variables. In no case the second component was visible in the spectrum. In a seminal paper, *On the Nature and Cause of Cepheid Variation*, SHAPLEY (1914) collected all the arguments against binary hypothesis. He pointed out that the only thing Cepheids have in common with ordinary spectroscopic binaries is periodic oscillation of spectral lines, in all other respects *Cepheids stand out as unexplainable anomalies.* The strongest argument of Shapley was based on the size of the orbits. Shapley convincingly showed that in many cases of short-period variables, postulated orbits are smaller than the size of the visible component of the system. At that time, the basics of the today's Hertzsprung-Russell diagram were just established (HERTZSPRUNG 1905, 1907, RUSSELL 1913, 1914) and it became clear that Cepheid are much more luminous than the Sun, and also remarkably larger. Shapley concluded that the radial pulsation of the star's atmosphere is the simplest explanation, void of difficulties inherent in binary hypothesis.

Probably the last paper attempting to interpret the Cepheid variability in terms of binary motion was published by HOYLE & LYTTLETON (1943). However, much earlier BAADE (1926) proposed a test for pulsation hypothesis, that proved beyond doubt, that intrinsic pulsation is responsible for the observed variability. Periodic variation of stellar surface induces temperature and luminosity changes. These two effects can be separated to yield the radius variation, that can be checked independently through the integration of the radial velocity curve.

The idea of pulsation was not entirely new. Already in 1879, August Ritter (RITTER 1789) studied the properties of pulsating spheres of constant density. Particularly, he established the famous period-density relation, stating that the pulsation period is proportional to the inverse square-root of the density. Although Ritter suggested that variable stars can be pulsating gas spheres, his work was not noticed by the astronomers of that time. It was sir Arthur Eddington who played a key role in establishing the theory of stellar pulsation. At that time stellar astrophysics was in infancy. However, EDDINGTON (1918, 1919) was able to describe the basic physical ideas behind the stellar pulsation. He considered the pulsating stars as thermodynamical engines for which energy gains should compensate the dissipation. He realized that without a driving mechanism, pulsations would die out. In his famous monograph, *Internal Constitution of the Stars*, EDDINGTON (1926) concluded that under appropriate conditions stars can pulsate self-excitedly. He proposed two different mechanisms to maintain the pulsations. In the first one (today called the ϵ-mechanism), energy input is modulated during the pulsation cycle, just as in ordinary engine. The mechanism assumes increased energy release from internal atomic sources during the compression phase. At that time the nuclear source of star's energy was just being established. In the second mechanism, so-called valve mechanism (or κ-mechanism, as we call it today), pulsations can be excited even in case of constant heat input. Mechanism requires the valve which could temporarily modulate the heat flow, leading to minimum heat leakage during the compression phase. This can be assured by increased opacity of stellar material during the compression.

Due to poor understanding of the composition and structure of giant stars, the first mechanism, the modulation of energy generation, was regarded as main cause of stellar pulsation. Particularly, it was not known that in giant stars the density contrast is very high, the ratio of the central density, ρ_c, to the mean density, $\bar{\rho}$

exceeding 10^5. Therefore, the central displacement amplitude was overestimated by many orders of magnitude. Around 1950 attempts were made to construct more reliable models of giant stars. To this purpose ENIAC was used in Princeton by the group led by Martin Schwarzschild (RICHARDSON & SCHWARZSCHILD 1948, HEN & SCHWARZSCHILD 1949). One of the main findings was the extremely high central mass concentration in giant stars. EPSTEIN (1950) analysed these results in the context of pulsation theory. He found that the displacement in nuclear active regions was $\approx 10^{-6}$ of that at the surface, and hence, the properties of pulsation were not determined in the central regions of stars, but in their envelopes. It became clear that the appropriate valve has to be found.

Solution was found already in 1953 by soviet astrophysicist Sergei Zhevakin (ZHEVAKIN 1953). He analysed stellar envelopes including second helium ionization zone. Zhevakin found significant driving associated with that zone, and postulated that it can overcome the dissipation present in other parts of the envelope. Works of Zhevakin were published in Russian and at the time of cold war, and therefore, were not widely known outside the Soviet Union, until he was invited to contribute to the *Annual Review of Astronomy and Astrophysics* in 1963 (ZHEVAKIN, 1963). The crucial role of He$^+$ ionization was also found by COX (1958) and COX & WHITNEY (1958), however, in indirect way. COX (1958) attempted to explain the observed phase-lag between light and velocity variation of Cepheid variables. He concluded that the energy flux must be modulated in the regions of partial ionization of abundant chemical elements. COX & WHITNEY (1958) used semi-theoretical arguments to derive the period-luminosity relation, and concluded that only second ionization of helium provides quantitative agreement with observed relation. Numerical computation of reliable giant models and analysis of their stability by BAKER & KIPPENHAHN (1962), confirmed the role of partial ionization regions in exciting the stellar pulsation. Since that time computers became wide-spread and numerical computations started to play a key role in our understanding of stellar pulsation. Short review of these computations will be presented in Section 1.4. For more detailed review on the historical, pre-computer works, I refer the reader to the article by GAUTSCHY (2003).

In the last decades thousands of pulsating variable stars were discovered. They can be separated into several groups populating almost all regions of the Hertzsprung-Russel diagram, from compact and faint white dwarfs, through the many type of pulsators located close to the main sequence, up to luminous giant variables. Many of these objects are non-radial pulsators, with very small amplitudes, close to detection limits of ground-based observations (milimagnitudes). However, large amplitude, radially pulsating Cepheids are still in the center of astrophysical interest, being not only one of the most important distance indicators, but also extremely interesting objects, still providing challenges for stellar pulsation and evolution theories. They are the main subject of this thesis.

1.2 Challenges for radial stellar pulsation theory

Before describing the results obtained with the pulsation hydrocodes, it is worthwhile to review the observational status of Cepheids, and challenges it presented and still presents for stellar pulsation theory. Also, stellar evolution theory provides specific

constraints and will be briefly reviewed here.

Problems to be solved and phenomena to be modeled and understood have remained nearly the same for the last few decades. However, in recent years the number of known pulsating variable stars has grown explosively. Massive surveys, such as OGLE[2], MACHO[3], EROS[4] or ASAS[5], have provided long-term homogeneous photometric data for millions of stars in our Galaxy and in the Magellanic Clouds. Thousands of them appeared to be Cepheids.

Cepheids are periodic variable stars, pulsating radially with periods ranging from one day up to over hundred days for the most luminous variables. They obey an empirical period-luminosity ($P - L$) relation, discovered 100 years ago by LEAVITT (1908). It was early realized (*e.g.*, RUSSELL 1927) that they populate a rather narrow strip in the HR diagram, being relatively cool, giant stars. This is illustrated in Figure 1.1, in which theoretical H-R diagram is presented. Cepheids cluster around red dotted line, location of which was computed from the formulae given in SANDAGE, TAMMANN & REINDL (2004). This ridge line represents the fit to the observed distribution of the LMC Cepheids transformed from the colour-magnitude plane to the theoretical plane. Estimated values of the width of the instability strip do not exceed 1000 Kelvins. Pulsation calculations should reproduce the location and width of the instability region, as well as should explain the observed period-luminosity relation.

Solid black lines in Figure 1.1 are evolutionary tracks computed by GIRARDI *et al.* (2000) for the stellar masses indicated in the Figure and chemical composition corresponding to LMC. Depending on the mass, star can cross the instability region up to three times. The first crossing occurs in the post-main sequence evolution, before helium ignites, while the star evolves very quickly toward the red giant branch. After helium ignition, more massive stars enter the horizontal blue loop, crossing the instability strip twice, during blue-ward and then, red-ward evolution. Corresponding second and third crossings last roughly two orders of magnitude longer than the first crossing. Hence, most of the observed Cepheids are expected to be the helium burning objects. In the presented computations, the minimum mass for the blue loop to enter the instability strip (schematically drawn with dotted blue lines in Figure 1.1), M_{BL}, is around $4\mathrm{M}_\odot$. Evolutionary tracks of the same authors for Galactic chemical composition indicate $M_{\mathrm{BL}} > 5\mathrm{M}_\odot$. For less massive stars only first crossing is possible. Thus, evolutionary computations put constraints on the Cepheid masses. Most of the observed variables, should have $M > M_{\mathrm{BL}}$, being helium burning objects. It is also clear from the Figure 1.1, that Cepheids should obey an evolutionary mass-luminosity ($M - L$) relation, depending on their evolutionary state, different for post-main sequence and helium burning objects. Most of the Cepheids should obey the latter one. Evolutionary computations at the helium burning phase are difficult. Results depend not only on metallicity used, but also on the description of macroscopic element mixing. Assumed amount of overshooting from the convective core affects not only M_{BL} but also the $M - L$ relation, models computed with overshooting being brighter, than those computed without overshooting. However,

---

[2]Optical Gravitational Lensing Experiment, *see e.g.*, SOSZYŃSKI *et al.* (2008b)

[3]MAssive Compact Halo Objects, *see e.g.*, ALCOCK *et al.* (1999)

[4]Expérience de Recherche d'Objets Sombres, *see e.g.*, BEAULIEU *et al.* (1995)

[5]All Sky Automated Survey, *see e.g.*, POJMAŃSKI (1997)
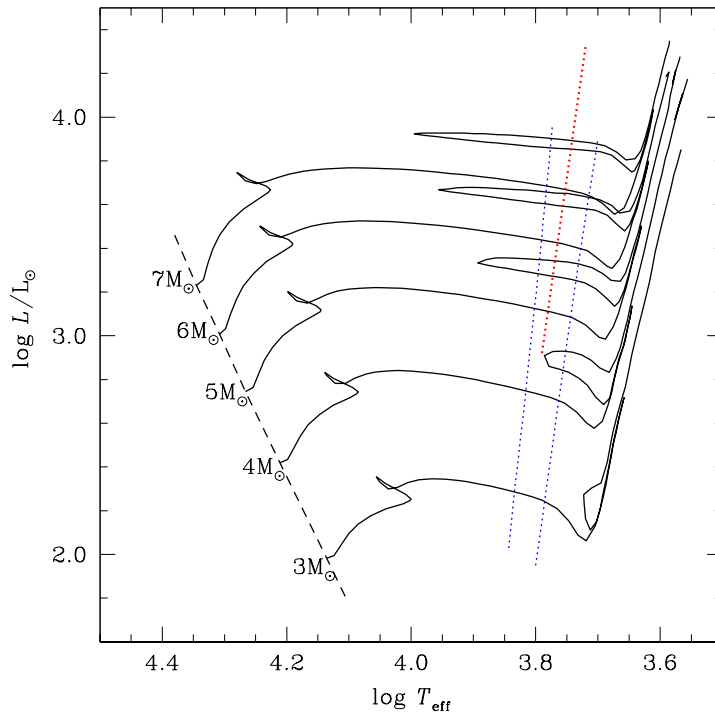
Figure 1.1: Theoretical HR diagram showing the ridge line for the LMC Cepheids, computed from the formulae given by SANDAGE, TAMMANN & REINDL (2004) (red dotted line). Edges of the instability region are schematically marked with dotted blue lines. Solid black lines show the evolutionary tracks from GIRARDI *et al.* (2000), computed for models with metallicity corresponding to LMC ($Z = 0.008$) and including overshooting from the convective core. Dashed line shows the location of the zero-age main sequence (ZAMS).

described scenario of Cepheid evolution remains qualitatively the same since the early stellar evolution computations (*see e.g.*, review article by IBEN 1967).

In constructing envelope pulsation models we are not bound by evolutionary tracks, and model masses and luminosities can be chosen independently to satisfy various observational constraints. Emerging *pulsational* mass-luminosity relation should agree reasonably with the evolutionary counterpart, significant differences indicating possible problems of the underlying pulsation and/or evolution theories.

Singly periodic Cepheids pulsate either in the fundamental (F) mode, or in the first overtone (1O). Few examples of second overtone (2O) pulsators are also known. The most interesting objects however, are double-mode Cepheids. These pulsate simultaneously in two modes, either in the fundamental mode and in the first overtone (F/1O), or in the first and second overtones (1O/2O). Two 1O/3O double-mode Cepheids are known (SOSZYŃSKI *et al.* 2008a). Some triple-mode F/1O/2O and 1O/2O/3O Cepheids are also observed in the LMC (MOSKALIK, KOŁACZKOWSKI & MIZERSKI 2004, SOSZYŃSKI *et al.* 2008a). Pulsation periods can be measured with very high precision and are independent of interstellar absorption and photometric system used. Hence, two or three observed periods provide excellent opportunity

to constrain the physical parameters of the pulsator, such as mass or metallicity. To this purpose a PETERSEN (1973) diagram is often used, in which the shorter (P_S) to longer (P_L) period ratio is plotted against the longer period. In Figure 1.2, Petersen diagram for the LMC double-mode pulsators from the OGLE-III database is plotted. Both F/1O and 1O/2O pulsators are not distributed randomly, but form a well defined sequences on the Petersen diagram. Modeling of this data represents a challenging task for both pulsation and evolution theories (*see* Chapter 8). Specially hard and longstanding problem is the dynamical modeling of the double-mode behaviour, which is also one of the main subjects of this thesis.
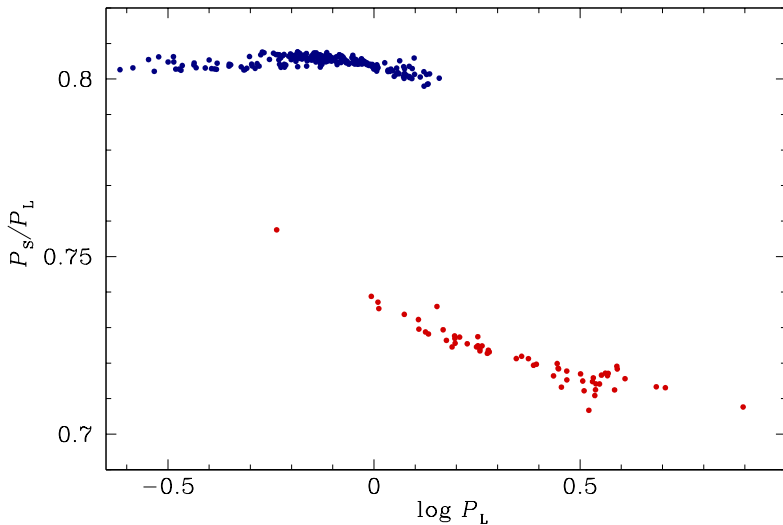
Figure 1.2: Petersen diagram for the LMC F/1O (red dots) and 1O/2O (blue dots) double-mode Cepheids. Shorter to longer period ratio, P_S/P_L, is plotted *versus* the logarithm of the longer period, P_L. Data from SOSZYŃSKI *et al.* (2008b).

Pulsation computations should also explain the observed light and radial velocity curves, their shape and its variation with pulsation period. The shape of the light/radial velocity curves can be quantitatively described by their Fourier decomposition parameters, as originally suggested by SIMON & LEE (1981). The light/radial velocity curve is fitted with the Fourier series,

$$m(t) = A_0 + \sum_{k=1}^{N} A_k \sin(2\pi k f t + \varphi_k), \tag{1.1}$$

where f denotes the pulsation frequency. Fourier decomposition parameters are defined as,

$$R_{k1} = \frac{A_k}{A_1}, \quad \varphi_{k1} = \varphi_k - k\varphi_1. \tag{1.2}$$

Fourier parameters allow for objective comparison of model light/radial velocity curves with observations. In Figures 1.3 and 1.4 low order Fourier decomposition parameters of light and radial velocity curves for a sample of Galactic Cepheids are presented. Blue and red circles correspond to fundamental and first overtone pulsators, respectively.
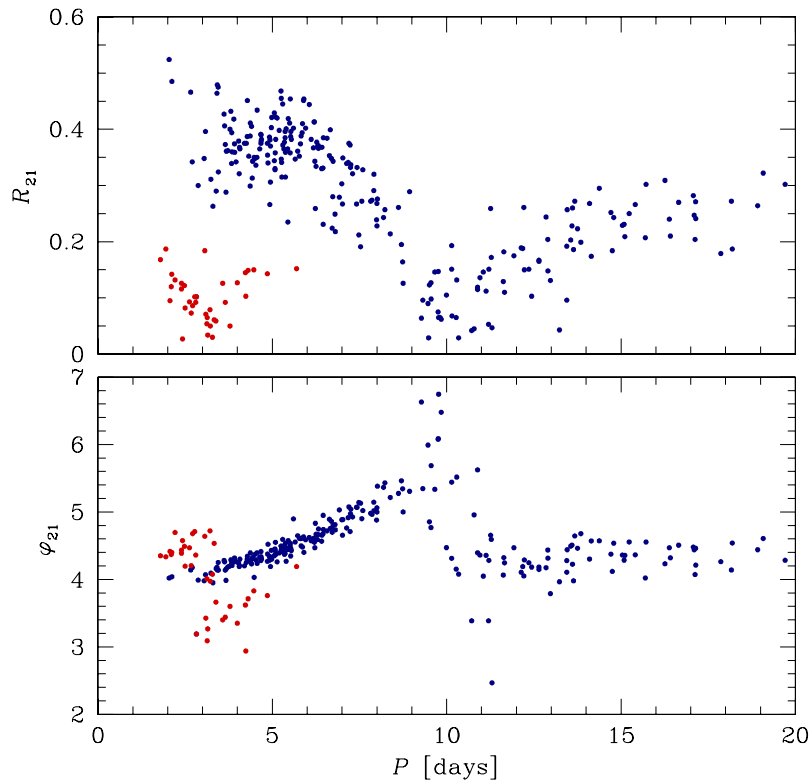
Figure 1.3: Fourier decomposition parameters of V-band light curves for Galactic Cepheids. Blue and red dots correspond to fundamental mode and first overtone Cepheids, respectively. Data from various sources; Antonello & Morelli (1996), Antonello & Poretti (1986), Antonello, Poretti & Reduzzi (1990), Mantegazza & Poretti (1992), Moffett & Barnes (1985), Poretti (1994), Simon & Kanbur (1995) and Simon & Lee (1981).

Light and radial velocity curves change with pulsation period, which is reflected in non-monotonic behaviour of Fourier decomposition parameters in the Figures. On the light/radial velocity curves of fundamental mode Cepheids with pulsation periods around ten days, a prominent bump is visible. Hertzsprung (1926) described the relation between pulsation period and location of the bump on the light curve. For short periods (around 5–6 days) bump appears first on the descending branch and, as pulsation period gets longer, it moves toward ascending branch of the light curve. Described behaviour manifests in the bell-shape of the φ_{21} progression and in the drop of R_{21} values around 10 days. Similar structures are visible for first overtone pulsators at periods around 3–4 days. The goal of pulsation computations is not only to reproduce the observed run of the Fourier decomposition parameters, but first of all, to explain the underlying physical processes shaping these progressions.
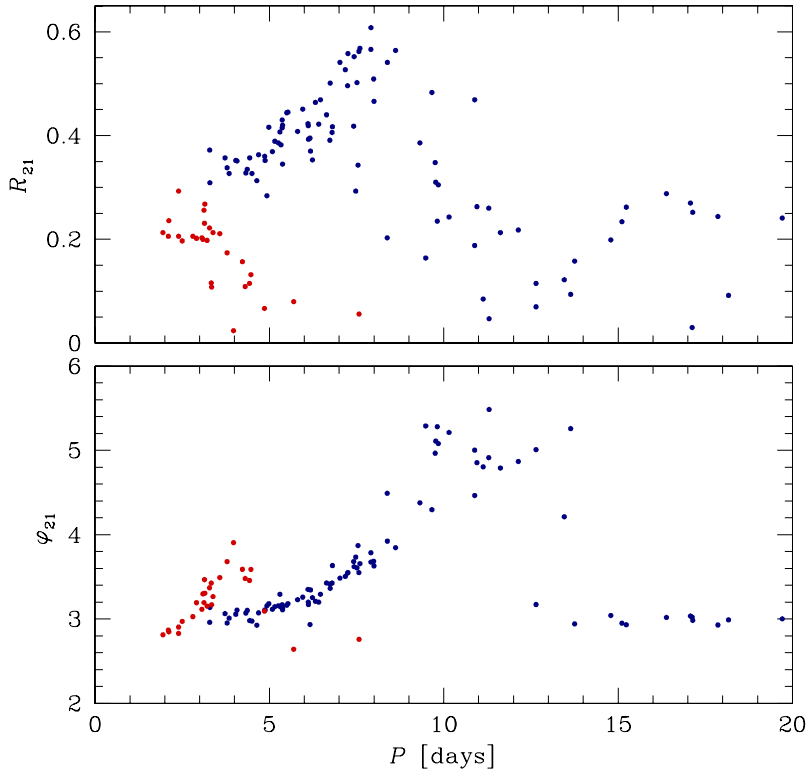
Figure 1.4: Fourier decomposition parameters of radial velocity curves for Galactic Cepheids. Blue and red dots correspond to fundamental mode and first overtone Cepheids, respectively. Data from MOSKALIK, GORYNYA & SAMUS, in prep. and from BARANOWSKI *et al.* (2009) (for V440 Persei).

1.3 Basic equations

In this Section, I describe the basic equations and concepts of radial pulsation theory. Just as in almost all early hydrodynamical computations, convective energy transfer is neglected in the following. Detailed derivations are not presented, as these may be found in any textbook on stellar pulsation theory (*e.g.*, COX 1980, UNNO *et al.* 1989) and in references cited. The purpose of this Section is to provide a background, for the discussion of convective pulsation models in the next Chapters, where more extensive description of numerical techniques will be given.

Since the work of EPSTEIN (1950), it is clear that for giant stars, such as Cepheids, pulsation amplitude is very small in the interior, and these are the external layers that determine the properties of the pulsation. Therefore, it is not necessary to consider a complete stellar model, but only its external layers, the envelope. Energy generation can be neglected and constant luminosity flux passing through the lower boundary of the envelope can be assumed.

Time-dependent equations describing the radial pulsation of spherically symmetric star are momentum equation,

$$\frac{\mathrm{d}u}{\mathrm{d}t} = -\frac{1}{\rho}\frac{\partial p}{\partial r} - \frac{GM_r}{r^2}, \qquad (1.3)$$

and the heat flow equation,

$$\frac{\mathrm{d}q}{\mathrm{d}t} = T\frac{\mathrm{d}s}{\mathrm{d}t} = \frac{\mathrm{d}E}{\mathrm{d}t} + p\frac{\mathrm{d}V}{\mathrm{d}t} = -\frac{1}{\rho}\frac{\partial(r^2 F_{\mathrm{r}})}{r^2\partial r}. \tag{1.4}$$

In the above equations, t is time, u is fluid velocity, which is time derivative of radius,

$$\frac{\mathrm{d}r}{\mathrm{d}t} = u, \tag{1.5}$$

M_r is mass enclosed by the sphere of radius r, G is gravitational constant, p is pressure, T is temperature, q is specific heat, s is specific entropy per gram, E is internal energy per gram and V is specific volume, that is inverse of density, ρ. In the radiative models, heat flow is usually assumed to be entirely through the radiation diffusion, which yields the radiative flux at a given level (diffusion approximation),

$$F_{\mathrm{r}} = -k_{\mathrm{r}}\frac{\partial T}{\partial r}, \tag{1.6}$$

where k_{r} is radiation diffusion coefficient,

$$k_{\mathrm{r}} = \frac{4acT^3}{3\kappa\rho}, \tag{1.7}$$

and radiation constant is denoted by a, speed of light by c and opacity (per gram) by κ. The remaining equation is continuity equation,

$$V = \frac{1}{\rho} = 4\pi r^2\frac{\partial r}{\partial M_r}. \tag{1.8}$$

Pressure, internal energy and opacity are usually computed as functions of temperature and volume, through the equation of state (EOS) and opacity tables.

To complete the problem, two boundary conditions are required for each of equations (1.3) and (1.4), at the top and at the bottom of the envelope. Different choices were adopted for boundary conditions by different authors. Here, I adopt the simplest choice, used in the earliest hydrocodes, as well as in the convective hydrocodes to be described in Chapter 3. At the inner boundary, rigid core, with constant luminosity passing through its boundary is assumed,

$$\left(\frac{\partial r}{\partial t}\right)_{\mathrm{i}} = 0, \tag{1.9}$$

$$L_{\mathrm{i}} = L_0, \tag{1.10}$$

while at the surface, the pressure is assumed to vanish, and temperature of the surface is assumed to satisfy the Eddington's gray atmosphere approximation,

$$p_{\mathrm{s}} = 0, \tag{1.11}$$

$$T_{\mathrm{s}}^4 = \frac{1}{2}T_{\mathrm{eff}}^4. \tag{1.12}$$

Direct solution of the above pulsation equations is a nonlinear problem, that can be solved through direct nonlinear integration (*see* Section 1.3.2), or can be tackled with the help of amplitude equations formalism (Section 1.3.4). However, basic pulsation properties emerge from simple linear analysis (Section 1.3.1).

1.3.1 Linear analysis

The simplest approach to the radial pulsation problem, first used by EDDINGTON (1918), assumes linear adiabatic oscillations. Such approach describes mechanical aspects of the system and allows to predict pulsation periods in good agreement with observations.

In the framework of linear theory, we consider small, spherically symmetric perturbation of the equilibrium model. Using Lagrangian perturbations, we write for the radius,

$$r = r_0(1 + \zeta), \tag{1.13}$$

where $\zeta = \delta r/r_0$ is relative displacement, and subscript "0" denotes the equilibrium value. Similarly, $p = p_0(1 + \delta p/p_0)$ and $\rho = \rho_0(1 + \delta\rho/\rho_0)$. In the adiabatic approximation, linearized energy equation, (1.4), reduces to,

$$\frac{\delta p}{p} = \Gamma_1 \frac{\delta \rho}{\rho}, \tag{1.14}$$

where Γ_1 is adiabatic exponent. Subscripts indicating equilibrium quantities are not necessary and are dropped. Linearized versions of momentum (1.3) and continuity (1.8) equations are,

$$\frac{\mathrm{d}^2 \delta r}{\mathrm{d}t^2} + \frac{1}{\rho}\frac{\mathrm{d}\delta p}{\mathrm{d}r} - 4g\frac{\delta r}{r} = 0, \tag{1.15}$$

$$\frac{\mathrm{d}\delta r}{\mathrm{d}M_r} = -\frac{\mathrm{d}r}{\mathrm{d}M_r}\left(2\frac{\delta r}{r} + \frac{\delta\rho}{\rho}\right). \tag{1.16}$$

Above, g stands for gravitational acceleration. Assuming a standing wave solution for relative displacement, $\delta r/r = \xi(r)e^{i\omega t}$, and combining above three equations, Linear Adiabatic Wave Equation (LAWE) is obtained,

$$\frac{\mathrm{d}}{\mathrm{d}r}\left(\Gamma_1 p r^4 \frac{\mathrm{d}\xi}{\mathrm{d}r}\right) + \xi\left\{\omega^2 \rho r^4 + r^3 \frac{\mathrm{d}}{\mathrm{d}r}\left[(3\Gamma_1 - 4)p\right]\right\} = 0. \tag{1.17}$$

Detailed derivation can be found *e.g.*, in a book by J.P. COX (1980). LAWE is a second order, ordinary differential equation. With two boundary conditions (resulting from the requirement that δr and $\delta p/p$ should be finite at the center and at the surface) it represents a Sturm-Liuville type problem. Consequently, it has infinite number of solutions, called pulsation modes, labeled with integer index n: ω_n^2, $\xi_n(r)$. Through this thesis, I use convention in which $n = 0, 1, 2, \ldots$. Eigenfunction, $\xi_n(r)$, has n nodes along a stellar radius. It can be multiplied by arbitrary constant, as LAWE is homogeneous and linear in ξ. It means that in linear theory pulsation amplitude is arbitrary. Eigenvalues, ω_n^2, are real, and corresponding pulsation frequencies satisfy,

$$\omega_n > \omega_{n-1}.$$

Pulsation mode of lowest frequency, without nodes along a stellar radius ($n = 0$) is called fundamental mode (F-mode). Consecutive modes of higher frequencies are radial overtones, first ($n = 1$, 1O), second ($n = 2$, 2O), and so on.

It follows from LAWE, that for a sequence of homologous stars, having the same value of Γ_1, pulsation periods satisfy,

$$P_n = \frac{2\pi}{\omega_n} = Q_n\sqrt{\frac{\bar{\rho_\odot}}{\bar{\rho}}}, \tag{1.18}$$

where $\bar{\rho}$ and $\bar{\rho}_\odot$ are mean densities of the star and of the Sun, respectively, and Q_n are called pulsation constants. This is the famous period-mean density relation. Real stars are not homologous, and their adiabatic exponents differ and are not constant along the stellar radius. Thus, Q_n depend on stellar parameters, however, weakly (*see* also Section 1.4.1). Nonadiabaticity and nonlinear effects also do not affect the pulsation periods strongly, and hence, reasonable period estimates can be obtained through the period-mean density relation.

Adiabatic theory tells nothing about pulsation stability. To study the growth or decay of the pulsations, nonadiabatic effects must be considered. Although these are generally expected to be small, they are the source of the phase shifts between pressure and density variations, crucial for the local heat balance. These phase shifts arise from the time derivatives of the energy equation (Eq. 1.4). In case of local heat gains, $\mathrm{d}q/\mathrm{d}t > 0$, maximum pressure comes after maximum density, and hence, δp lags behind $\delta\rho$. Consideration of energy conservation during the pulsation cycle leads to a straightforward conclusion, that the change of the kinetic energy of the star is equal to ordinary pressure work, $p\,\mathrm{d}V$, done by all the (local) mass elements on their surroundings throughout a pulsation period. Thus, the work integral (*see* Appendix A),

$$W = \oint \mathrm{d}t \int \mathrm{d}M\left(p\frac{\mathrm{d}V}{\mathrm{d}t}\right) \qquad (1.19)$$

integrated over the whole envelope, provides the stability information. Its linear version is (*e.g.*, CASTOR 1971, Appendix A),

$$W = -\pi \int \Im\{(\delta p)^*(\delta V)\}\,\mathrm{d}M, \qquad (1.20)$$

Here $\Im$ denotes imaginary part, and * stands for complex conjugate. In case of $W > 0$ we have pulsational instability, while $W < 0$ corresponds to pulsational stability. Locally, the region gaining heat at maximum compression is a driving region, while a region losing heat at maximum compression is a damping region.

Linear nonadiabatic (LNA) problem is much more complicated than adiabatic problem and various numerical methods were developed to solve it. Modern computations treat the LNA equations as eigenvalue problem (*e.g.*, CASTOR 1971). Again, time dependence of variations is assumed to be $e^{i\omega t}$, however, eigenvalues ω_n^2 are no longer real. The real part of ω_n determines the pulsation period, while its imaginary part provides stability information, which is usually expressed as the mode growth rate, γ_n,

$$\gamma_n = -4\pi\Im(\omega_n)/\Re(\omega_n), \qquad (1.21)$$

here expressed as the fractional growth of the kinetic energy per pulsation period.

There are different numerical methods of solving the full LNA problem (*see e.g.*, COX 1980 or UNNO *et al.* 1989). In the convective codes described in the next Chapters, method proposed by GLASNER & BUCHLER (1993) is adopted and details will be given in Chapter 3.

1.3.2 Direct nonlinear integration

The limiting-amplitude pulsation, as is observed in variable stars, can only be studied using nonlinear methods. In direct nonlinear integration methods, stellar model

is divided into several zones. Full set of nonlinear equations, (1.3)–(1.8), is written in the finite-difference form, and calculations are treated as initial value problem. The model is followed forward in time, step by step, till the limiting amplitude pulsation is achieved. The technique is time-consuming. As pulsation growth rates are typically of order of $10^{-2} - 10^{-3}$ (Cepheids), many hundreds of pulsation cycles are necessary to approach the final pulsation state.

Different numerical schemes were developed to conduct the nonlinear integrations. Many codes use simple Lagrangian mesh, with fixed mass zones (*e.g.*, Christy 1964, Stobie 1969a, Stellingwerf 1975a). More sophisticated codes use different variants of adaptive grid (*e.g.*, Aikawa & Simon 1983, Dorfi & Feuchtinger (1991), Buchler, Kolláth & Marom 1997). Details of the Lagrangian scheme for model including convective energy transfer will be presented in Chapter 3.

One of the main drawbacks and problems of purely radiative computations, is the lack of physical viscosity. Consequently, special methods are needed to handle the shocks, developing *e.g.*, in the partial ionization regions. Heat gained during the compression phase is converted into mechanical energy during expansion, pushing the mass zones upward into the atmosphere. The most common method used to deal with shocks, is the inclusion of artificial viscous dissipation into the model, in the form proposed by von Neumann and Richtmyer (Richtmyer 1957), later modified by Stellingwerf (1975a). In this technique artificial viscous pressure, proportional to the square of the relative speed of the consecutive zones, $(\Delta u)^2$, is applied to each zone[6], which makes the shock transition continuous and spread over several mass zones. Unfortunately, numerical results, specially the pulsation amplitudes depend of the artificial viscosity parameters.

1.3.3 Relaxation method

Direct time integration is numerically expensive technique. But its drawbacks are more severe. Even if apparently stable, full amplitude pulsation is developed, the question remains, whether the model will stay in a given state indefinitely. Possible mode switching can be very slow, and it is hard to judge, whether the computed pulsation state is the stable attractor of the model, or the possible switch is imminent. To deal with these difficulties, alternative nonlinear approach was proposed by Baker & von Sengbusch (1969), and later developed by Stellingwerf (1974). The point was to search for strictly periodic solution of the full nonlinear system given by Eqs. (1.3)–(1.8).

Baker & von Sengbusch proposed to solve iteratively for the four unknowns (radius, velocity, temperature and volume) in all the model zones at each time step. If the model is divided into N mass zones and period is divided into K time steps, there are $4NK$ equations to be solved. The number of unknowns is larger however, and equal to $4NK + 4N + 1$, as the period and $4N$ initial values at the beginning of the period are not known *a priori*. $4N$ periodic boundary conditions allow to solve the full set of nonlinear equations through a sophisticated Newton-Rhapson iterations. Unknown period is derived simultaneously as the eigenvalue of the nonlinear equations.

---

[6]if this relative speed exceed some arbitrary limit, *see* Section 3.3.3 for details

Instead of solving the large set of $4NK$ nonlinear equations, STELLINGWERF (1974) evolves the model for one period using standard direct time integration hydrocode. Initial values of dependent variables are guessed, together with initial value for the period (*e.g.*, from LNA computations). The final values of variables at the end of the period are different than the initial guess, and comparison allows to correct both the initial values and the period. Procedure is repeated, till corrections are sufficiently small and strict periodicity (limit cycle) is achieved. This method of computing nonlinear stellar pulsations is called relaxation technique/scheme. Numerical details can be found in STELLINGWERF (1974). Relaxation scheme allows to find limit cycles of different modes. In addition, it provides information about limit cycle stability, through the Floquet stability analysis (*e.g.*, CHICONE 1999, STELLINGWERF 1974). Stability of the limit cycle of mode j, against perturbation in mode i, is described by the Floquet coefficient, $\eta_{i,j}$. If $\eta_{i,j} > 0$, mode j is unstable against perturbation in mode i, and would tend to switch into this mode in direct time integration. The value of the Floquet coefficient provides information about rate of the mode switching. Hence, the other name of the Floquet coefficients – the switching rates.

Relaxation technique proved to be a very powerful method allowing for fast computations of extensive model surveys, studying the light/radial velocity curve shapes, and modal selection, at once.

1.3.4 Amplitude equations formalism

Although direct time integration or relaxation scheme allow to model the full amplitude behaviour of real stars, the underlying physics remains hidden, and difficult to extract from the hydrodynamical evolution of the model. Other way to study the nonlinear pulsations is offered by the amplitude equations (AEs) formalism. In this approach, partial differential equations, (1.3)–(1.8), are reduced to ordinary differential equations for the amplitudes of the excited modes. The assumptions underlying the formalism are weak nonadiabaticity and weak nonlinearity, which allows to describe the nonlinear behaviour in terms of the modes. Both assumptions are rather well satisfied for pulsators populating the classical instability strip. The form of the AEs depends on whether the resonances occur between the linear modes of oscillation. Without resonances, non-resonant AEs describe the saturation of the pulsation instability through the self- and cross-saturation of the pulsation modes. The physics describing these nonlinear effects is contained in the nonlinear saturation coefficients. Usually AEs are truncated at the cubic nonlinearities (in amplitudes), which allows to capture the essential behaviour of the system. If resonances are present between pulsation modes, additional terms, describing the coupling between interacting modes are present in AEs.

Derivation and theory of the AEs formalism can be found *e.g.*, in TAKEUTI & AIKAWA (1981), DZIEMBOWSKI (1982), BUCHLER & GOUPIL (1984). Numerous applications to radial stellar pulsations are by *e.g.*, DZIEMBOWSKI & KOVÁCS (1984), BUCHLER & KOVÁCS (1986a,b), KOVÁCS & BUCHLER (1989), MOSKALIK & BUCHLER (1989). More detailed discussion is postponed to Chapter 6, where AEs will be applied to the problem of non-resonant double-mode Cepheid pulsations.

1.4 Era of radiative computations

The first numerical computations of radial pulsation date to early sixties of the twentieth century. BAKER & KIPPENHAHN (1962) were the first to conduct a linear survey of Cepheid models. The pioneering nonlinear computations were performed by CHRISTY (1964). These early computations suffered from poor spatial resolution and long-lasting computations on the first computers. But soon they became one of the most important tools for studying stellar interiors and physics underlying stellar pulsation.

For many years computed models were purely radiative. Efficiency of convection decrease toward the higher effective temperatures and it was expected that effects of convection should be small, at least close to the blue edge of pulsation instability strip. On the other hand, radiative models couldn't predict the red edge of the instability strip, as models were unstable even for very low effective temperatures. Inclusion of mixing length convection in the structure of the models by BAKER & KIPPENHAHN (1965) led to reduced growth rates for low effective temperatures, and two dimensional computations of DEUPREE (1977a) including dynamical convection confirmed that indeed, convection is responsible for the stabilization of the modes at the red edge. On the other hand, its overall effect on pulsation periods and light/radial velocity curves was found to be small (DEUPREE 1977b).

Convection was disregarded not only because it was considered to be unimportant across the significant part of the instability strip, but also because suitable time-dependent convection models were not available. Early time-dependent models of GOUGH (1965) and UNNO (1967), although quite successfully applied to linear pulsations, were difficult to implement in the nonlinear case. Suitable convection models were developed in the early eighties (STELLINGWERF 1982a), and had to await several years when faster computers allowed for more extensive model surveys.

Below, I briefly describe the problems encountered in modeling of radial stellar pulsation with radiative pulsation hydrocodes. I focus on classical Cepheids, as these are the main subject of this thesis. For other types of radial pulsators, I refer the reader to a review by BUCHLER (1998). The exciting problem of Cepheid mass discrepancy (Section 1.4.1) was entirely solved within the framework of radiative computations. Purely radiative models also satisfactorily reproduced the light and radial velocity curves of fundamental mode Cepheids, although they failed to do so, in case of the first overtone pulsators (Section 1.4.2). Radiative models didn't succeed in reproducing the observed modal selection. Particularly, modeling of double-mode pulsations appeared to be impossible (Section 1.4.3), and motivated the inclusion of time-dependent convection into pulsation hydrocodes (Chapter 2). The problem of modeling the double-mode behaviour in classical Cepheids is still very challenging, and is extensively tackled in this thesis (Chapters 6, 7 and 8).

1.4.1 Mass discrepancy problem

Pulsation theory allows for estimation of Cepheid masses, through several methods. So-called pulsation masses, M_Q, are computed through the period-mean density relation, making use of the known period and radius of the star. Radius can be derived from photometric estimation of luminosity and effective temperature (or

directly from Baade-Wesselink method, which leads to Wesselink masses).

Other method, suitable for determination of double-mode Cepheid masses was established by PETERSEN (1973). Period-mean density relation implies that pulsation period depends mostly on mass and radius of the pulsator. Linear computations (*e.g.,* COX, KING & STELLINGWERF 1972, PETERSEN & JORGENSEN 1972) confirmed that indeed, for a given chemical composition and given mass and radius, pulsation constant, Q, is practically independent of luminosity. Hence, a fitting formulae for pulsation constants of fundamental and first overtone modes, Q_F and Q_{1O}, depending on mass and radius, can be obtained from linear computations. Formulae of COX, KING & STELLINGWERF (1972) were used by PETERSEN (1973) to plot the lines of constant masses on the period ratio *vs.* period plot – nowadays known as the Petersen diagram. Two periods observed for double-mode Cepheid precisely determine its location on the Petersen diagram. So-called beat-mass can be derived from comparison with theoretical lines.

The bump Cepheids also offer an opportunity to estimate the Cepheid masses. As pointed out by STOBIE (1969b), phase of the bump in theoretical light curves depends mostly on the mass to luminosity ratio, M/L, and shows little sensitivity to chemical composition. Thus, two observables, period, and phase of the bump allow to derive the so-called bump-masses of fundamental mode Cepheids, through comparison with nonlinear models. Since the suggestion of SIMON & SCHMIDT (1976) that the occurrence of bumps is connected with the $P_2/P_0 = 0.5$ resonance, and observation that their location depend on the value of P_2/P_0 period ratio, bump-masses could be derived based on linear theory, in a similar way as masses of double-mode Cepheids were derived.

The mass-discrepancy problem can be summarized as follows: all masses being somehow related to the pulsation theory are significantly smaller than evolutionary masses, derived for the same luminosity through the evolutionary $M - L$ relation. Discrepancies were first noted by COGAN (1970) and RODGERS (1970) for pulsation masses, by CHRISTY (1966c) and STOBIE (1969b) for the bump masses, and by PETERSEN (1973) for beat-masses. Revision of cluster distance scale and Cepheid reddenings, led to reconciliation of pulsation masses by the end of 1980 (*e.g.,* A.N. COX 1980). Also Wesselink masses were reconciled (for extensive review on the subject, I refer the reader to review article by A.N. COX 1980), and only beat- and bump-mass discrepancies remained. To reconcile these discrepancies, reduction of period ratios, P_1/P_0 and P_2/P_0, for beat- and bump-masses, respectively, was necessary. Hence, all the proposed mechanisms served to increase P_0 more than P_1 and P_2.

One of the solutions considered, was the possibility that the linear period ratios might differ from those corresponding to full amplitude pulsation. However, analysis of stable double-mode pulsations of RR Lyrae model (STELLINGWERF 1975b) and mode-switching pulsations of Cepheid models (COX, HODSON & KING 1978) showed that linear and nonlinear period ratios agree very well.

Other models to reconcile the mass discrepancy assumed the changes in the envelope structure induced by convection, rotation, inhomogeneous composition or magnetic fields. COGAN (1977) suggested that efficient convection deep in the envelope, would produce less steep density gradient, reducing the P_1/P_0 ratio. However, as discussed by COX *et al.* (1977), required amount of convection was very

high, and in principle could stabilize the pulsations. Effects of rotation on period ratios were studied *e.g.*, by CARSON & STOTHERS (1976) and COX *et al.* (1977). However, only very large rotation rates, not observed in Cepheid variables, might have significant effect on period ratios. COX *et al.* (1977) showed that the mass discrepancies can be removed if helium enriched layer is present in the outer parts of the envelope. Such layer lowers the envelope density gradient, and hence, the linear period ratios. The helium enriched layer was presumed to be due to a helium deficient wind blowing away more hydrogen than helium. Although numerical results were very promising, the perspectives for observational validation of helium enriched layers were poor (*e.g.*, SONNEBORN, KUZMA & COLLINS 1979). Also, inherent to this theory were problems of stability of such enhanced layer against downward mixing.

Another promising, yet hard to verify theory, to reconcile the mass discrepancy, was proposed by STOTHERS (1979). In his theory, lower density gradient, reducing the relevant period ratios, is assured by the tangled magnetic field. The pressure support is partly due to magnetic pressure, allowing for lower densities, and lower density gradient. Nonlinear computations of STOTHERS (1982), including the effects of magnetic field showed that bump-mass discrepancy can be largely reduced. Stothers showed however, that significantly different strengths of magnetic fields were necessary to reconcile the beat-mass discrepancy, which was not satisfactory.

Almost all of the beginning pulsation computations used so-called Los Alamos or Cox-Stewart opacities (COX & STEWART 1965, COX & TABOR 1976). FRICKE, STOBIE & STRITTMATTER (1971) analysed the uncertainties in opacity data, and concluded that opacity changes by reasonable factors strongly affect the inferred masses. Independent opacity computations were done by CARSON (1976). In comparison to Cox-Stewart opacities, Carson opacities are higher by factor ~ 2 in the second helium ionization zone. Using Carson opacities, VERMURY & STOTHERS (1978) computed several models of bump Cepheids and claimed that their models reproduced the bumps at the correct periods and phases. Their conclusion however, was disallowed by SIMON & DAVIES (1983) who performed a quantitative comparison of Vermury & Stothers models with observations, using Fourier decomposition parameters. Also, Carson opacities were invalidated, as it was shown that unrealistic approximations were made in the opacity codes used in their computation (CARSON *et al.* 1984).

SIMON (1982) suggested that the opacities should be revised. He showed that the increase of the opacity due to heavy elements by a factor $\approx 2 - 3$, leads to observed period ratios (for beat- and bump-Cepheids) for masses and luminosities satisfying evolutionary constraints. Similar modification of opacity data was proposed earlier by STELLINGWERF (1978), to excite, otherwise stable, β Cephei stars. Ideas of Simon, although initially criticized by atomic physicists claiming that substantial revision of opacities is not possible (MAGEE, MERTS & HUEBNER 1984), were not abandoned. Extensive parameter study by ANDREASEN (1988) corroborated the results of Simon. Stimulated research of the atomic physics underlying the opacity computations (IGLESIAS, ROGERS & WILSON 1990), soon confirmed that indeed, contribution of the heavy elements to the opacity was underestimated in two temperature domains (one of them, roughly between $10^5 - 10^6$ K was advocated by Simon). Linear and nonlinear computations of MOSKALIK, BUCHLER & MAROM

(1992), adopting new opacity tables (IGLESIAS & ROGERS 1991) showed that beat- and bump-mass discrepancies are largely resolved. Hence, all the mass discrepancies were reconciled within the framework of purely radiative computations.

1.4.2   Modeling of light/radial velocity curves

Pioneering nonlinear models of radial pulsators were computed by CHRISTY (1964). He conducted a large survey of RR Lyrae models (CHRISTY 1966a) and also performed some computations for W Wirginis model (CHRISTY 1966b) and for classical Cepheids (CHRISTY 1966c). In this last paper, he constructed the models of η Aquilae and δ Cephei. Taking their observed parameters (radii, effective temperatures and luminosities), he adjusted the masses of the models to reproduce the observed periods. As a result, he drew some conclusions about possible pulsation modes excited in these stars. The first systematic survey of nonlinear Cepheid models was computed by STOBIE (1969b). He constructed several sequences of models running horizontally across the HR diagram, corresponding to the blue loop evolution. Masses and luminosities were bound by evolutionary computations. Stobie studied the effects of different chemical compositions, as well as impact of numerical details, such us zoning or artificial viscosity on the model properties. Models were initialized not only in the fundamental mode, but also in the first two overtones. In the light and velocity curves of many of his fundamental mode models, a prominent secondary bump was visible. The presence of such bumps was expected, as Hertzsprung bump progression was described already in 1926 (HERTZSPRUNG 1926). However, only nonlinear computations could shade some light on the physical nature of the bumps. WHITNEY (1956), and later CHRISTY (1968), suggested that the bumps are the result of an *echo*, caused by the pressure wave reflected from the stellar core. Other explanation was proposed by SIMON & SCHMIDT (1976). They computed linear nonadiabatic periods corresponding to nonlinear models of STOBIE (1969b) and found that the location of the bump is strongly connected with the ratio of the second overtone period to the fundamental mode period, P_2/P_0. Bump on the ascending branch of the model curves was present when $0.48 \geq P_2/P_0 \geq 0.46$, and it was on the descending branch for $0.53 \geq P_2/P_0 \geq 0.50$. When P_2/P_0 was close to 0.5 or slightly less the bump was located close to the maximum. Hence, Simon & Schmidt concluded that the presence of the bumps is connected with the resonance between the fundamental and second overtone modes, $P_2/P_0 = 0.5$.

The bump visible in the computations of Christy and Stobie, although expected, appeared at wrong phase (at a given pulsation period) as compared to observations. STOBIE (1969b) concluded that only reduction of model masses by factor ~ 2, can bring the phase of the bump into agreement with observations. This notification of so-called bump-mass discrepancy (*see* previous Section) led him to construction of models obeying *pulsation* mass-luminosity relation, with masses at given luminosity equal to half of the evolutionary mass (STOBIE 1969c). Stobie concluded that his new models agree satisfactorily with observations. This conclusion was based on qualitative comparison of such features like amplitudes, light curve asymmetries or presence and phase of the bumps. Similar conclusions were reached by *e.g.*, DAVIS & DAVISON (1978), VERMURY & STOTHERS (1978) and HODSON & COX (1980), who constructed sequences of fundamental mode Cepheid models mostly to study

the bump-mass discrepancy. That such "eyeball" comparisons can be misleading was demonstrated by SIMON & DAVIS (1983) who compared the model and observed light and radial velocity curves in terms of the Fourier decomposition parameters, as proposed by SIMON & LEE (1981). They showed that theoretical models have some serious defects, and do not reproduce quantitatively the characteristic runs of Fourier parameters, φ_{21} and R_{21}, in spite of apparent qualitative agreement with observations. They also showed that the model run of φ_{21} *versus* period ratio, P_2/P_0, has characteristic bell shape centered at $P_2/P_0 = 0.5$, supporting the resonance hypothesis of SIMON & SCHMIDT (1976). The strongest evidence in favour of this theory was provided by BUCHLER & KOVÁCS (1986a), who studied the effects of a 2:1 resonance in nonlinear pulsation, using the amplitude equations formalism. On purely theoretical grounds they showed that the characteristic shape of the Fourier parameters progression is indeed caused by the 2:1 resonance between the fundamental and linearly damped second overtone. Further on, KOVÁCS & BUCHLER (1989) analysed the sequence of hydrodynamical Cepheid models of BUCHLER, MOSKALIK & KOVÁCS (1990) and showed that the nonlinear results are not only qualitatively, but also quantitatively well captured by the amplitude equations, assuming the 2:1 resonance.

The Cepheid model survey of Buchler, Moskalik & Kovács was performed with the codes originally written by STELLINGWERF (1975a), with slight modifications introduced by KOVÁCS & BUCHLER (1988). These codes were extensively used to model all types of pulsators exhibiting radial modes. Faster computers allowed for large model surveys and finer mesh resolution, fully exploiting the possibilities of radiative models. The results of MOSKALIK, BUCHLER & MAROM (1992), who used the revised opacities of IGLESIAS & ROGERS (1991), finally solving the mass discrepancies, showed the great success of radiative models in reproducing the radial velocity curves and moderate success in modeling the light curves. In the latter case, although qualitative agreement between theoretical and observed Fourier parameters is remarkable, models display systematically higher values of low order Fourier phases and amplitude ratios.

Overtone Cepheids didn't attract as much theoretical attention as fundamental mode ones. Their light and radial velocity curves, computed already by CHRISTY (1966c) and more extensively by STOBIE (1969b,c), were quite regular and didn't display significant bumps, so important in their fundamental mode counterparts. On the other hand, observational status of the overtone Cepheids was not clear at the time of early nonlinear pulsation computations. Short period Cepheids with nearly sinusoidal light curves (so-called *s*-Cepheids) were suspected to pulsate in the first overtone. They were established as a separate class of first overtone pulsators by ANTONELLO, PORETTI AND REDUZZI (1990), who showed that the progression of their photometric Fourier phase, φ_{21}, with pulsation period is distinct and well separated from the corresponding fundamental mode progression. The run of photometric φ_{21} values *versus* the period for *s*-Cepheids was studied earlier by ANTONELLO & PORETTI (1986). They noted the presence of two different trends separated by discontinuity near period of 3 days (also referred as "Z"-shape in the literature), and suggested that such behaviour may be caused by the 2:1 resonance between the first and fourth overtones, centered around this period.

Many computations of nonlinear overtone Cepheid models were done with TGRID

code of AIKAWA & SIMON (1983). AIKAWA, ANTONELLO & SIMON (1987) performed some computations to model the short period Cepheid SU Casiopeae, however, didn't obtain satisfactory results. More extensive model surveys, intended to check the resonance hypothesis of ANTONELLO & PORETTI (1986), were done by ANTONELLO & AIKAWA (1993, 1995). At linear level, the authors demonstrated that their models cross the resonance center, however, their nonlinear results were far away from reproducing the observed progressions of photometric φ_{21} and R_{21}. First of all, the variation of model photometric φ_{21} was not as large and sharp as observed. Similar results were obtained by Shaller & Buchler (1994, unpublished) with different hydrocode. Another argument against the resonance operating in the vicinity of 3 days was raised by BUCHLER *et al.* (1996) who showed that single mass-luminosity relation cannot simultaneously reproduce the location of resonance shaping the Hertzsprung progression at 10 days, and the hypothetical resonance at 3 days. The situation was clarified by KIENZLE *et al.* (1999) who showed that indeed, the $P_4/P_1 = 0.5$ resonance is operational in overtone Cepheids, however, it is centered at longer period, ≈ 4.6 days, and it manifests in radial velocity curves, giving rise to a bell shape structure in φ_{21} progression, centered at period of 4 days. In fact, the agreement between model and observed Fourier parameter progressions for radial velocity curves is quite satisfactory, despite the fact that radiative hydromodels completely fail to reproduce the observed overtone Cepheid light curves.

1.4.3 Modal selection and problem of modeling the double-mode behaviour

The problem of mode selection in radial pulsators is longstanding. One of the arguments against hypothesis that Cepheids pulsate, raised by the advocates of the binary hypothesis (*e.g.*, JEANS 1925), was, that according to pulsation theory, many modes, including higher order overtones, should be observed in a single variable. To the contrary, in most of the Cepheid variables, only single periodicity was observed. Already EDGAR (1933) showed that overtone modes suffer from much greater dissipation than the fundamental mode and hence, will not be observed. First numerical stability computations (*e.g.*, KING *et al.* 1973, BAKER & KIPPENHAHN 1965) showed that indeed, only fundamental mode and first and second overtones may be unstable, higher order overtones being firmly stable.

The modal selection problem is simple, if only one mode is linearly unstable. Full amplitude pulsation in this mode will develop. However, if two modes are simultaneously linearly unstable, the question arises, which one (or maybe both) of the modes will be present in the nonlinear regime, at large amplitude pulsation. The problem under discussion is similar for two types of large amplitude pulsators populating the classical instability strip, RR Lyrae stars and classical Cepheids. Therefore, the results for both groups are complementary and will be discussed below.

Large amplitude behaviour cannot be inferred from linear computations. KING *et al.* (1973) noted that for some of their models, in which both F and 1O were simultaneously linearly unstable, stable finite amplitude pulsation in either mode was possible, depending on the way nonlinear integrations were initialized (physically depending on the direction of evolution). First nonlinear computations also

revealed mixed-mode states (*e.g.*, STOBIE 1969b), however, limited computer resources, didn't allow for long-lasting computations and for a definite statements, whether they could correspond to the observed double-mode pulsation or to a transient. From the very beginning the double-mode pulsators attracted much attention. Pulsation period depends mostly on stellar mass and radius (period-mean density relation). Hence, two periods of the simultaneously excited modes can be used to derive the stellar parameters with high precision (*e.g.*, PETERSEN 1973). Clearly, understanding of the double-mode pulsation (multimode in general) was and still is one of the most interesting and outstanding problems of stellar pulsation theory.

STELLINGWERF (1975a) was the first, who developed the phenomenological theory of modal selection. Using relaxation technique (STELLINGWERF 1974, *see* Section 1.3.3) he analysed the stability of the fundamental and first overtone limit cycles (FLC and OLC, respectively) with respect to the perturbation in the other mode. He described four possible pulsation states. Depending on the stability of the individual limit cycles these are: (*a*) fundamental mode only, if FLC is stable against perturbation in 1O, and OLC is unstable against perturbation in F, $\eta_{1,0} < 0$, $\eta_{0,1} > 0$; (*b*) first overtone only, if the reverse is true, $\eta_{1,0} > 0$, $\eta_{0,1} < 0$; (*c*) either-or (F/1O) pulsation domain, in which pulsation in either mode is possible, if both FLC and OLC are stable, $\eta_{1,0} < 0$, $\eta_{0,1} < 0$; (*d*) double-mode pulsation (DM), if both FLC and OLC are simultaneously unstable, $\eta_{1,0} > 0$, $\eta_{0,1} > 0$. KING *et al.* (1973) computations for classical Cepheids and STELLINGWERF (1975a) computations for RR Lyrae stars yielded essentially the same picture. As one crosses the instability strip from its hot, blue side toward the cooler, red side, first, the 1O pulsation domain appears. Next, the either-or domain emerges, and finally at the red side of the instability strip, fundamental mode pulsation domain is present. In addition, the coolest RR Lyrae models of STELLINGWERF (1975a) were found to have both limit cycles simultaneously unstable. The direct numerical integration of particular models by STELLINGWERF (1975b), led to the development of stable double-mode pulsation. His results however, were not confirmed with other hydrocodes (*e.g.*, HODSON & COX 1976; COX, HODSON & KING 1978), and it is believed that the first nonlinear double-mode models were numerical artifacts, resulting from too shallow envelope.

The modal selection was also analysed in detail by SIMON, COX & HODSON (1980), who used for this purpose the iterative theory of SIMON (1972). They arrived at the same four pulsation classes as established by STELLINGWERF (1975a). They also analysed the SIMON'S (1979) hypothesis that double-mode pulsation is a resonant phenomenon. Based on the observation that the period ratios found in double-mode variables are confined to a very narrow range, Simon suggested that the three-mode resonance, namely $\omega_1 + \omega_0 = \omega_3$ may be crucial in bringing up the double-mode behaviour. He also pointed out that some role can be played by a 2:1 resonance, $2\omega_0 = \omega_2$. Nonlinear computations of SIMON, COX & HODSON (1980) however, failed to confirm the role of the three-mode resonance in promoting the double-mode behaviour.

Physics underlying the double-mode pulsation can be studied with amplitude equations formalism. As already discussed (*see* Section 1.3.4) the form of the AEs differ for non-resonant and resonant cases. In the former case pulsation modes compete with each other to saturate the linear pulsation instability of both modes.

It was shown by DZIEMBOWSKI & KOVÁCS (1984) that the double-mode behaviour arises, if the dominant role is played by self-saturation effects. In this case none of the modes is able to stabilize the other, and simultaneous excitation of both modes is possible. Essentially the same results were obtained by BUCHLER & KOVÁCS (1986b). Dziembowski & Kovács also analysed the resonant mode interaction and found that the three-mode resonance, proposed by Simon as the cause of double-mode pulsation, actually stabilizes the single-mode solution and shouldn't play a role in double-mode phenomenon (which explains the negative result of SIMON, COX & HODSON 1980, concerning the three-mode resonance). To the contrary, the 2:1 resonance between one of the two linearly unstable modes and a higher order linearly damped overtone can cause a double-mode pulsation. The amplitude of the unstable resonant mode is limited, allowing the growth of the second linearly unstable mode.

Results of DZIEMBOWSKI & KOVÁCS (1984) were confirmed by the computations of KOVÁCS & BUCHLER (1988). Using relaxation technique, they found a double-mode RR Lyrae models caused by the resonance between the fundamental mode and the third overtone, $2\omega_0 = \omega_3$. BUCHLER, MOSKALIK & KOVÁCS (1990) found radiative, double-mode Cepheid models, connected with the 2:1 resonance shaping the Hertzsprung progression, $2\omega_0 = \omega_2$. The same resonance is operational in radiative, double-mode Cepheid models found by the author (SMOLEC 2009, *see* Chapter 7). All these models however, are not relevant from practical point of view, because their periods are far from the observed ones.

Extensive computations of non-resonant RR Lyrae models with standard numerical and physical parameters by KOVÁCS & BUCHLER (1988) showed, that stable double-mode pulsation is not possible. Very fast after crossing its linear blue edge, fundamental mode limit cycle becomes stable against perturbation in the first overtone. Contrarily, stability of the first overtone limit cycle slowly varies with effective temperature. First overtone limit cycle is firmly stable at high temperatures, and becomes unstable at very low temperatures. Instead of double-mode domain, a relatively wide either-or domain is present. KOVÁCS & BUCHLER (1988) indicated that double-mode, non-resonant pulsation can be obtained with purely radiative hydrocodes, however, only assuming non-standard model parameters (low M/L ratio) or decreased artificial viscosity. An extensive survey of RR Lyrae models with reduced artificial dissipation was computed by KOVÁCS & BUCHLER (1993). Modal stability along a sequence of models was analysed with the help of the relaxation technique. It was demonstrated that in less dissipative models, the double-mode pulsation with the observed periods is possible. However, models of Kovács & Buchler had higher amplitudes as compered to observations (due to reduced dissipation) and were sensitive to numerical details. In the conclusions of their paper, authors stressed the need for development of less dissipative codes with physical source of viscosity instead of artificial one. Indeed, it was inclusion of convection into pulsation hydrocodes that offered a solution to the problem of modeling the double-mode phenomenon (*see* next Chapter).

Chapter 2

Treatment of convection

Convection plays important role in almost all types of stars. Under stellar conditions, convection is accompanied by strong turbulence and as such is impossible to model in Earth's laboratories. Convective zones affect the overall structure of the stars, transporting energy, as well as being responsible for mixing of the atomic species. Detailed computation of these effects is very difficult and for more than fifty years a very simple mixing length prescription of Böhm-Vitense is used for this purpose (Section 2.1). In case of pulsating variable stars problem becomes even more difficult. Pulsation induced, large-scale motion of the gas, interacts with smaller-scale turbulent convective motions. Theories attempting to describe this interaction are called time-dependent convection theories/models. Some general remarks concerning assumptions underlying these models and basic idea of derivation are presented in Section 2.2. For the purpose of nonlinear computations, which are the subject of this thesis, simple one-equation, non-local models are best suited. Of these, two models are most commonly used – the Stellingwerf model (Section 2.3) and the Kuhfuß model (Section 2.4). Kuhfuß model has several advantages over the Stellingwerf one (Section 2.5) and hence, it was adopted in pulsation hydrocodes with which the results of this thesis were obtained. Therefore, this model is described in more detail. Finally, the results obtained up to date with convective pulsation hydrocodes are summarized in Section 2.6.

2.1   Mixing Length Theory

The mixing length theory (MLT) was originally formulated by VITENSE (1953) and BÖHM-VITENSE (1958), based on the early work of Prandtl (*see* PRANDTL 1952). Modern reviews can be found in HANSEN, KAWALER & TRIMBLE (2004) and in COX & GIULI (1968), who provide extensive discussion and derivations. Here, I summarize the theory focusing on the physical picture, particularly on convective instability criterion.

In mixing length theory, the stellar fluid is assumed to be composed of identifiable gas elements, eddies, or blobs. The buoyant forces drive the motions of eddies from regions of high heat content to the regions of lower heat content, thus leading to convective heat transport through the fluid. After traveling the characteristic distance ℓ, the mixing length, eddies lose their identity and merge with the surrounding fluid. Hotter eddies rise, while cooler eddies sink, leading to the net outward heat

transport. It is assumed that the mixing length is much shorter than any length scale associated with the structure of the star (*e.g.*, pressure scale height). Characteristic dimensions of the eddies are of the same order as ℓ. During the motion, eddies maintain the pressure equilibrium with surrounding material and the fluid is assumed to be incompressible. Hence, density variations can be neglected, except those giving rise to buoyancy effects (Boussinesq approximation; *see* next Section).

There are different variations of the MLT, introducing different parametrization, concerning *e.g.*, the eddy shape. Here, I summarize the main results of a classic version, detailed derivation of which can be found in Cox & Giuli (1968). Below, the mixing length, ℓ, is assumed to be some fraction of the pressure scale height, $\ell = \alpha_{\mathrm{MLT}} H_p$.

Criterion for convective instability can be derived through considering the temperature variations during the eddy motion, within the eddy, and in the surrounding material. Let T', ρ' and p' denote the temperature, density and pressure within the convective eddy. The temperature gradient in the surrounding material is,

$$\frac{\mathrm{d}T}{\mathrm{d}r} = -\frac{T}{H_p}\nabla = -\beta, \tag{2.1}$$

where H_p is a pressure scale height,

$$H_p = -\frac{\mathrm{d}r}{\mathrm{d}\ln p}, \tag{2.2}$$

and ∇ is a temperature gradient,

$$\nabla = \frac{\mathrm{d}\ln T}{\mathrm{d}\ln p}. \tag{2.3}$$

Assuming that the eddy moves adiabatically, temperature variation within the eddy is,

$$\frac{\mathrm{d}T'}{\mathrm{d}r} = \left(\frac{\mathrm{d}T'}{\mathrm{d}r}\right)_{\mathrm{a}} = -\frac{T}{H_p}\nabla_{\mathrm{a}} = -\beta_{\mathrm{a}}, \tag{2.4}$$

where ∇_{a} is adiabatic temperature gradient,

$$\nabla_{\mathrm{a}} = \left(\frac{\mathrm{d}\ln T}{\mathrm{d}\ln p}\right)_{\mathrm{a}}. \tag{2.5}$$

Suppose now, that due to some perturbation the eddy starts to rise. If its temperature drops adiabatically below the temperature of the surrounding material, the eddy has negative buoyancy and tends to sink. To the contrary, if its temperature decreases more slowly than the temperature of the surrounding material it will continue to rise due to buoyancy effects. In this case the fluid is convectively unstable. Noting that β and β_{a} are positive, criterion for convective instability (also known as Schwarzschild criterion) can be expressed as

$$\beta > \beta_{\mathrm{a}}, \tag{2.6}$$

or,

$$\nabla > \nabla_{\mathrm{a}}. \tag{2.7}$$

It is convenient to express the above criteria through the superadiabatic gradient (dimensionless entropy gradient), $\mathcal{Y}$,

$$\mathcal{Y} = \nabla - \nabla_{\mathrm{a}} = -\frac{H_p}{c_p}\frac{\mathrm{d}s}{\mathrm{d}r}. \tag{2.8}$$

Stellar layers in which $\mathcal{Y} > 0$ are convectively unstable.

The excess temperature of the rising element, ΔT, can now be easily determined. It follows from Eqs. (2.1) and (2.4) that after traveling the distance ℓ, the excess temperature is,

$$\Delta T(\ell) = \ell\frac{T}{H_p}\mathcal{Y} = \alpha_{\mathrm{MLT}}T\mathcal{Y}. \tag{2.9}$$

The heat released by the eddy upon dissolution is, $\rho c_p \Delta T(\ell)$. Convective flux, transported by the upward moving elements, F_{c}, is equal to the rate of heat release,

$$F_{\mathrm{c}} = \frac{1}{2}u_{\mathrm{c}}\rho c_p\Delta T(\ell) = \frac{1}{2}\alpha_{\mathrm{MLT}}u_{\mathrm{c}}\rho c_p T\mathcal{Y}, \tag{2.10}$$

Detailed derivation of this and following formulae can be found in Cox & Giuli (1968). Above, u_{c} is the average speed of convective elements given by,

$$u_{\mathrm{c}} = \alpha_{\mathrm{MLT}}\left(\frac{1}{8}Tc_p\nabla_{\mathrm{a}}\right)^{1/2}\mathcal{Y}^{1/2}. \tag{2.11}$$

Above formulae for convective flux and velocity are true, if convective eddies move adiabatically. In reality, as temperatures of the convective eddy and its surroundings differ, heat is exchanged. Allowing for radiative leakage, superadiabatic gradient, $\mathcal{Y}$, entering the above two formulae for convective flux and convective velocity, should be replaced by $\nabla - \nabla'$. Temperature gradients are then bound by,

$$\frac{\nabla - \nabla'}{\nabla' - \nabla_{\mathrm{a}}} = \frac{2\alpha_{\mathrm{MLT}}H_p c_p \rho u_{\mathrm{c}}}{9k_{\mathrm{r}}}, \tag{2.12}$$

where k_r is radiation diffusion coefficient (Eq. 1.7).

In the framework of MLT, total energy flux, F_{tot}, is carried by radiative and convective fluxes,

$$F_{\mathrm{tot}} = F_{\mathrm{c}} + F_{\mathrm{r}} = k_{\mathrm{r}}\frac{T}{H_p}\nabla_{\mathrm{rad}}, \tag{2.13}$$

where ∇_{rad} is radiative temperature gradient, defined by the above equation, that is the gradient which would exist if all the energy were transported by radiation. Radiative flux is given by the diffusion law (*cf.* Eq. 1.6), with actual temperature gradient, ∇,

$$F_{\mathrm{r}} = k_{\mathrm{r}}\frac{T}{H_p}\nabla. \tag{2.14}$$

Thus, in convectively unstable regions we have,

$$\nabla_{\mathrm{a}} < \nabla < \nabla_{\mathrm{rad}}. \tag{2.15}$$

For the purpose of further comparison with time-dependent models, it is useful to write down the momentum equation governing the eddy motion. This equation is,

$$\ddot{r} = -g - \frac{1}{\rho}\frac{\partial p}{\partial r} = -g\frac{\Delta\rho}{\rho}, \tag{2.16}$$

where $\Delta\rho = \rho' - \rho$ is excess density of the rising element. The excess density can be expressed through the excess temperature,

$$\frac{\Delta\rho}{\rho} = -\mathcal{Q}\frac{\Delta T}{T}, \tag{2.17}$$

where $\mathcal{Q}$ is the coefficient of thermal expansion,

$$-\mathcal{Q} = \left(\frac{\partial\ln\rho}{\partial\ln T}\right)_{\mu,p} + \left(\frac{\partial\ln\rho}{\partial\ln\mu}\right)_{T,p}\left(\frac{\partial\ln\mu}{\partial\ln T}\right)_p. \tag{2.18}$$

Using Eq. (2.17) and equation of hydrostatic equilibrium (to eliminate g), momentum equation becomes,

$$\ddot{r} = -\frac{1}{\rho}\frac{\partial p}{\partial r}\mathcal{Q}\frac{\Delta T}{T} = \frac{p\mathcal{Q}}{\rho H_p}\frac{\Delta T}{T}. \tag{2.19}$$

Above equation can be used to estimate the eddy acceleration after traveling the distance ℓ, a_{MLT}. Using Eq. (2.9), this acceleration is,

$$a_{\mathrm{MLT}} = \alpha_{\mathrm{MLT}}\frac{p\mathcal{Q}}{\rho H_p}\mathcal{Y}. \tag{2.20}$$

2.2   Time-dependent models – introduction

mixing length theory, as well as all its time-dependent extensions, is based on the Boussinesq approximation to the equations of motion. In this approximation, the gas is taken to be incompressible, except for the essential buoyancy effects. Boussinesq approximation is valid, if characteristic length scale of convection, ℓ, is much smaller than the scale of pulsation motions. Although Boussinesq approximation is well suited for describing the turbulent fluctuations, it cannot be used for pulsations, for which compressibility is essential. Therefore, physical variables as well as hydrodynamical equations are decomposed into mean and fluctuating parts. For example for temperature we have,

$$T(r,t) = T'(r,t) + \langle T(r,t)\rangle, \tag{2.21}$$

and similarly for other variables. Mean quantities, enclosed in $\langle\rangle$, are averages over a spherical shells and depend on the radial coordinate only. Hydrodynamical equations decouple into mean (pulsation) equations and fluctuating (turbulent) equations. Equations are linearized in the fluctuating parts, retaining the nonlinear terms in the velocities. This procedure is called anelastic approximation (*e.g.*, GOUGH 1968), and implies that all fluid velocities are small compared with the speed of sound. Mean and fluctuating equations are coupled by second order correlations, such as Reynolds stress tensor or correlation entering the convective flux, $\langle u'T'\rangle$.

The above procedure is common for almost all the time-dependent convection models. They differ in subsequent assumptions concerning the treatment of second order correlations and fluctuating equations.

The first time-dependent theories were developed by Gough (1965) and Unno (1967). These models are time-dependent extensions of the MLT, adopting different physical pictures, to justify the model equations and assumptions. Differences are extensively discussed by Gough (1977). Both models are local, just as MLT, which means that turbulent quantities at a given point are determined solely by the conditions existing at that point. Local treatment is the source of serious problems in numerical computations. If turbulent pressure is included in the mean equations, singularities appear at the boundaries of the convective zone (Stellingwerf 1976, Gough 1977). Another consequence of the local treatment are the oscillations in the thermal variables, deep in the convective zone (Baker & Gough 1979, Gonczi & Osaki 1980).

Despite the mentioned difficulties, both Gough and Unno models were successfully applied to the linear pulsations (Baker & Gough 1979, Gonczi & Osaki 1980). The local nature and complexity retained in fluctuating equations, makes these models inapplicable for nonlinear pulsations, however. Nonlinear computations require relatively simple, numerically inexpensive models, to allow long-lasting integrations, and numerically robust models, to avoid singularities during the model evolution. Therefore, in the nonlinear hydrocodes, simple one-equation non-local models are adopted. Fluctuating equations are reduced to one equation for turbulent energy, $e_t = \langle (u')^2 \rangle / 2$. In order to close the system, second order correlations need to be modeled. The procedure introduces several dimensionless, order of unity, free parameters. Their values are not determined by the theory, but should be adjusted to match the observational constraints. Non-locality is achieved by the presence of a diffusion terms for the turbulent energy in the equations. In non-local models, turbulent quantities at a given point depend not only on the conditions existing at that point, but also on the conditions at the neighboring points. Hence, turbulent energies can be nonzero even in convectively stable regions, provided they are close enough to the unstable regions. This is so-called overshooting.

Two one-equation models are in common use. These are the models based on the work of Stellingwerf (1982a) and Kuhfuss (1986). Below, I describe both models in more detail. Comparison is provided in Section 2.5, in which the arguments in favour of Kuhfuß model, adopted in this thesis, are presented.

2.3   Stellingwerf models

Stellingwerf (1982a) proposed a simple one-equation model for time-dependent turbulent convection, based on the work of Castor (1968, unpublished). Castor derived fluctuating equations for u' and T', and three moment equations for following averages, $\langle (u')^2 \rangle / 2$, $\langle u'T' \rangle$ and $\langle (T')^2 \rangle / 2$. Although Stellingwerf's derivation is different, it is equivalent to truncating the three moment equations of Castor, into one equation for turbulent energy, $e_t = \langle (u')^2 \rangle / 2$, and applying closure relations for other correlations.

The form of equations and quantities below, is based on the work of Bono & Stellingwerf (1994) (with typos corrected), however, to assure a consistent notation through this thesis, somewhat different variables are used. In the Stellingwerf

model, turbulent energy equation is,

$$\frac{\mathrm{d}\omega}{\mathrm{d}t} = \frac{1}{r^2}\frac{\partial}{\partial r}\left(r^2 l_{\mathrm{ovs}}\omega^{1/2}\frac{\partial\omega}{\partial r}\right) + \frac{\omega^{1/2}}{l}\omega_0 - \frac{\omega^{1/2}}{l}\omega - \frac{2\omega}{r^2}\frac{\partial}{\partial r}\left(ur^2\right),\qquad(2.22)$$

where $\omega = \langle(u')^2\rangle = 2e_t$. First term on the right-hand side of the above equation, is diffusion term, responsible for the non-local character of the model (after slight manipulation it can be represented as a divergence of the turbulent flux). The second term describes the generation of the turbulent energy, and hence, is referred as a source (or driving) function, S, in the following. This term is given by,

$$S = \frac{\omega^{1/2}}{l}\omega_0 = \frac{\omega^{1/2}}{l}2l\mathcal{Q}\frac{pV}{H_pT}\frac{\langle u'T'\rangle}{\langle(u')^2\rangle}.\qquad(2.23)$$

The third term in Eq. (2.22) describes the decay of the turbulent energies and the last term describes the coupling between turbulent field and mean, pulsation induced gas motion. In the momentum equation, turbulent (p_t) and eddy-viscous (p_ν) pressures appear, while in the total energy equation, corresponding pressure works and convective (F_c) and turbulent (F_t) fluxes are present,

$$\frac{\mathrm{d}u}{\mathrm{d}t} = -\frac{1}{\rho}\frac{\partial}{\partial r}(p + p_t + p_\nu) - \frac{GM_r}{r^2},\qquad(2.24)$$

$$\frac{\mathrm{d}}{\mathrm{d}t}(E + e_t) + (p + p_t + p_\nu)\frac{\mathrm{d}V}{\mathrm{d}t} = -\frac{1}{\rho}\frac{\partial\big[r^2(F_r + F_c + F_t)\big]}{r^2\partial r}.\qquad(2.25)$$

Convective fluxes are defined as,

$$F_c = \rho c_p\langle u'T'\rangle,\qquad(2.26)$$

$$F_t = \frac{1}{2}\rho\langle(u')^2u'\rangle.\qquad(2.27)$$

The Reynolds stress tensor, entering the equations, $\langle\rho\rangle u_i'u_j'$ was truncated by Stellingwerf to the diagonal part, yielding the turbulent pressure,

$$p_t = \rho\langle u'u'\rangle \approx \rho\langle(u')^2\rangle = \rho\omega.\qquad(2.28)$$

To model the small-scale turbulent dissipation, eddy-viscous pressure was introduced in an *ad hoc* manner,

$$p_\nu = -\rho l_{\mathrm{ev}}\omega^{1/2}\frac{\partial u}{\partial r}.\qquad(2.29)$$

In the above formulae, $\langle u'T'\rangle$ average, entering the source term and expression for the convective flux, as well as $\langle(u')^2u'\rangle$ term, entering the turbulent flux, need to be modeled. For the latter average, Stellingwerf adopted the diffusion approximation,

$$\langle(u')^2u'\rangle \approx -l_{\mathrm{ovs}}\langle u'\rangle\nabla\langle(u')^2\rangle = -l_{\mathrm{ovs}}\omega^{1/2}\nabla\omega,\qquad(2.30)$$

while for the former average, MLT motivated closure relation was adopted,

$$\langle u'T'\rangle = \omega\left(\frac{T'}{u'}\right)_{\mathrm{MLT}}.\qquad(2.31)$$

Resulting expressions for convective fluxes and the source term are following,

$$F_{\rm t} = -\frac{1}{2}\rho l_{\rm ovs}\omega^{1/2}\frac{\partial\omega}{\partial r}, \tag{2.32}$$

$$F_{\rm c} = \rho c_p\omega\left(\frac{2T^2}{pV\mathcal{Q}}\mathcal{Y}\right)^{1/2} \sim e_t\mathcal{Y}^{1/2}, \tag{2.33}$$

$$S = 2\omega\left(\frac{pV\mathcal{Q}}{H_p^2}\mathcal{Y}\right)^{1/2} \sim e_t\mathcal{Y}^{1/2}. \tag{2.34}$$

In the presented equations, three model parameters are present. They are hidden in the length-scales, the mixing length, l, the scale for eddy-viscous dissipation, $l_{\rm ev}$, and in the scale for turbulent diffusion, $l_{\rm ovs}$. They are all assumed to be some fraction of the local pressure scale height, H_p.

In the **original Stellingwerf model** (Stellingwerf 1982a), $\langle u'T'\rangle \sim \mathcal{Y}^{1/2}$ and hence, both S and $F_{\rm c}$, are restricted to positive values only. In convectively stable regions, $S = F_{\rm c} = 0$. Potential problems, connected with such treatment, concerning mostly the extent of overshooting, were pointed out by Kuhfuss (1986) and Gehmeyr & Winkler (1992a,b) (*see* Section 2.5 for extensive discussion). Correction to the model, overcoming the mentioned problem, was introduced by Bono & Stellingwerf (1992, 1994), who adopted the following patch,

$$\langle u'T'\rangle = \mathrm{sgn}(\mathcal{Y})\langle|u'T'|\rangle. \tag{2.35}$$

Hence, in this **modified Stellingwerf model**, as I will call it in the following, both convective flux and source function are negative in convectively stable regions.

2.4   Kuhfuß model

Another one equation model for time-dependent convection was developed by Kuhfuss (1986). He also truncated fluctuating equations into one equation for turbulent energy, however, consistently applying diffusion-type closure relations. His model included composition changes due to nuclear reactions and effects of molecular viscosity. This effects are not important for stellar pulsation problems (molecular viscosity is negligible compared to turbulent viscosity and considered pulsation time-scales are small, as compared to the nuclear reaction time scale for pulsators populating the classical instability strip). On the other hand, much less attention was payed to the treatment of radiation. Kuhfuß model was reformulated (and extended, see Sections 2.4.1 and 2.4.2) by Wuchterl & Feuchtinger (1998) and Feuchtinger (1999a) specifically for the use in the stellar pulsation hydrocodes. Much of the notation used below, comes from these two papers. In the following, radiation is treated in the diffusion approximation.

The complete set of equations consists of turbulent energy equation,

$$\frac{{\rm d}e_t}{{\rm d}t} + p_t\frac{{\rm d}V}{{\rm d}t} = -\frac{1}{\rho}\frac{\partial\left(r^2F_{\rm t}\right)}{r^2\partial r} + E_q + (S - D), \tag{2.36}$$

and momentum and internal energy equations,

$$\frac{{\rm d}u}{{\rm d}t} = -\frac{1}{\rho}\frac{\partial}{\partial r}(p + p_t) + U_q - \frac{GM_r}{r^2}, \tag{2.37}$$

$$\frac{\mathrm{d}E}{\mathrm{d}t} + p\frac{\mathrm{d}V}{\mathrm{d}t} = -\frac{1}{\rho}\frac{\partial\left[r^2(F_\mathrm{r} + F_\mathrm{c})\right]}{r^2\partial r} - (S - D). \tag{2.38}$$

Turbulent and internal energy equations can be added to yield the total energy equation,

$$\frac{\mathrm{d}(E + e_t)}{\mathrm{d}t} + (p + p_t)\frac{\mathrm{d}V}{\mathrm{d}t} = -\frac{1}{\rho}\frac{\partial\left[r^2(F_\mathrm{r} + F_\mathrm{c} + F_\mathrm{t})\right]}{r^2\partial r} + E_q. \tag{2.39}$$

Reynolds stress tensor is decoupled into trace part, corresponding to turbulent pressure,

$$p_t = \alpha_p \rho e_t, \tag{2.40}$$

and trace-free part leading to turbulent viscosity terms, U_q and E_q, which are viscous momentum and energy transfer rates, respectively. Explicit expressions for these terms are following,

$$U_q = \frac{1}{\rho r^3}\frac{\partial}{\partial r}\left[\frac{4}{3}\mu_q r^3\left(\frac{\partial u}{\partial r} - \frac{u}{r}\right)\right], \tag{2.41}$$

$$E_q = \frac{4}{3}\frac{1}{\rho}\mu_q\left(\frac{\partial u}{\partial r} - \frac{u}{r}\right)^2. \tag{2.42}$$

Kinetic turbulent viscosity is denoted by μ_q,

$$\mu_q = \alpha_m \rho \Lambda e_t^{1/2}, \tag{2.43}$$

and Λ stands for the mixing length, assumed to be some fraction of pressure scale height, $\Lambda = \alpha H_p$.

Turbulent kinetic energy flux is modeled through the diffusion approximation, just as was done by Stellingwerf, which leads to,

$$F_\mathrm{t} = -\alpha_t \rho \Lambda e_t^{1/2}\frac{\partial e_t}{\partial r}. \tag{2.44}$$

Convective flux is physically enthalpy flux,

$$F_\mathrm{c} = \left\langle u'(\rho h)'\right\rangle, \tag{2.45}$$

where h is specific enthalpy, $\mathrm{d}h = T\,\mathrm{d}s + V\,\mathrm{d}p$. Under anelastic approximation, fluctuating enthalpy can be expressed as fluctuating entropy, $h' = Ts'$. Similarly for the source (driving) function, arising from the buoyant forces,

$$S = -\left\langle u'\left(\frac{1}{\rho}\nabla p\right)'\right\rangle = -\left\langle u'\frac{\nabla p}{\rho^2}\rho'\right\rangle, \tag{2.46}$$

anelastic approximation yields,

$$\rho' = -\frac{\rho^2\nabla_\mathrm{a}T}{p}s'. \tag{2.47}$$

Therefore, for both convective flux and source function, entropy flux, $\left\langle u'(\rho s)'\right\rangle$ needs to be modeled. Using diffusion approximation, Kuhfuß arrived at,

$$\left\langle u'(\rho s)'\right\rangle = -\alpha_s \Lambda e_t^{1/2}\rho\frac{\mathrm{d}s}{\mathrm{d}r} = \rho\Pi. \tag{2.48}$$

Correlation Π,

$$\Pi = -\alpha_s \Lambda e_t^{1/2} \frac{\mathrm{d}s}{\mathrm{d}r} = \alpha \alpha_s e_t^{1/2} c_p \mathcal{Y}, \tag{2.49}$$

enters the expressions for both F_c and S, which become,

$$F_c = \frac{\alpha_c}{\alpha_s} \rho T \Pi \sim e_t^{1/2} \mathcal{Y}, \tag{2.50}$$

$$S = \frac{p\mathcal{Q}}{\rho c_p H_p} \Pi \sim e_t^{1/2} \mathcal{Y}. \tag{2.51}$$

The form of the turbulent dissipation term, D, is exactly the same as in Stellingwerf's model,

$$D = \alpha_d \frac{e_t^{3/2}}{\Lambda}. \tag{2.52}$$

It is convenient to join the turbulent source and turbulent dissipation functions into single term, C,

$$C = S - D, \tag{2.53}$$

coupling the turbulent and internal energy equations.

Detailed description of the convective parameters (alphas) entering the model, is presented in Section 2.4.3.

It is useful to provide a more physical insight into turbulent energy equation and quantities entering it. This equation has a non-local character, due to the diffusive term containing the turbulent flux. In the Kuhfuß model, this term is the sole cause of the overshooting of the convective eddies into convectively stable regions. Turbulent energies do not vanish at the boundaries of the convective zone, but are diffused into convectively stable regions, carrying the negative convective flux. The coupling term, C, appears in both turbulent and internal energy equations, however, with reverted sign. Hence, the local gains of the turbulent energy correspond to the local losses of the internal energy, and *vice versa*. Turbulent dissipation term, D, is always positive and hence, brakes the turbulent energies, pumping up the internal energy. In fact, this term is intended to model the turbulent cascade, that is the continuous decay of the turbulent eddies into smaller scales, down to molecular scale, were turbulent energy is dissipated. The turbulent source function, S, describes the buoyant acceleration of the convective eddies. Comparison of the expression for the turbulent source (Eq. 2.51) with the MLT expression for the buoyant acceleration (Eq. 2.20), yields,

$$S = \alpha_s e_t^{1/2} a_{\mathrm{MLT}}. \tag{2.54}$$

Hence, the source function is proportional to the eddy acceleration caused by the buoyant forces. Source function may drive, as well as damp the convective energies, depending on the sign of the superadiabatic gradient. In convectively unstable regions it drives the turbulent motions, while in convectively stable regions it is responsible for slowing down the overshooted eddies, through negative buoyancy. The interplay between turbulent field and mean gas motion is described by the eddy-viscous terms. The viscous energy transfer rate, E_q, is always positive. Thus, this term describes the generation of turbulence at the cost of mean, pulsation induced gas motion. Resulting eddy-viscous dissipation is important factor limiting the pulsation amplitude.

2.4.1 Extensions of the model – radiative cooling

In the original Kuhfuß model, the radiative cooling of the convective elements was not considered. This important effect, specially in the envelope convective zones, was introduced into the model in two different ways by WUCHTERL & FEUCHTINGER (1998) and by BUCHLER & KOLLÁTH (2000).

BUCHLER & KOLLÁTH (2000) considered the run of the Péclet number, Pe, across the Cepheid model. This number provides a measure of the radiative cooling of the convective elements, being the ratio of convective to radiative diffusion coefficients,

$$Pe = \frac{\mathcal{D}_c}{\mathcal{D}_r}. \tag{2.55}$$

Buchler & Kolláth approximated these coefficients by,

$$\mathcal{D}_c = \Lambda e_t^{1/2}, \tag{2.56}$$

$$\mathcal{D}_r = \frac{4}{3} \frac{acT^3}{\kappa \rho^2 c_p}. \tag{2.57}$$

Radiative cooling is unimportant in the regime of high Péclet numbers, that is for efficient convection. However, close to the surface and in the second helium ionization region, Péclet number was found to be small. To account for radiative cooling and improve the description of inefficient convection, Buchler & Kolláth proposed to limit both the convective flux and source term by a Péclet factor, f_{pec},

$$f_{pec} = \frac{1}{1 + \alpha_r Pe^{-1}}. \tag{2.58}$$

Order of unity, free parameter, α_r, resulted from somewhat arbitrary definition of the Péclet number. Proposed form of correction is equivalent to more sophisticated interpolation scheme arising from 5-equation model of turbulent convection by CANUTO & DUBOVIKOV (1998).

A simpler modification was proposed by WUCHTERL & FEUCHTINGER (1998). To account for the radiative energy exchange between the eddy and surrounding material, they modified the energy equations by introducing additional dissipation term for the turbulent energy, D_r, which entered the coupling term (Eq. 2.53),

$$C = S - D - D_r. \tag{2.59}$$

Radiative cooling term was modeled through the relaxation approximation,

$$D_r = \frac{e_t}{\tau_r}, \tag{2.60}$$

with τ_r being radiation diffusion cooling time scale for the convective elements,

$$\tau_r = \frac{c_p \kappa \rho^2 \Lambda^2}{acT^3 \gamma_r^2}. \tag{2.61}$$

Hence, D_r can be expressed as,

$$D_r = \frac{3}{4} \frac{\gamma_r^2}{\Lambda} e_t^{3/2} Pe^{-1}, \tag{2.62}$$

and has the strongest contribution to the coupling term for small Péclet numbers.

2.4.2 Extensions of the model – flux limiter

Computations of WUCHTERL & FEUCHTINGER (1998) indicated the possible problem of the original Kuhfuß model connected with the violation of the diffusion approximation used to model the correlation between velocity and entropy fluctuations (Π, Eq. 2.48). Their reasoning was following. As convective flux is physically enthalpy flux, one can write (Eq. 2.50),

$$F_c = \rho T \Pi = \rho h u_h, \tag{2.63}$$

where u_h is diffusion velocity for the enthalpy carried by convective eddies, and dimensionless parameters entering the convective flux were dropped. Hence,

$$u_h = \frac{T\Pi}{h}. \tag{2.64}$$

Wuchterl & Feuchtinger compared this velocity with the average speed of the convective elements, u_c,

$$u_c = \left(\frac{2}{3}e_t\right)^{1/2}, \tag{2.65}$$

and noted that the ratio u_h/u_c can exceed unity. In this case, enthalpy is transported with velocities larger, than the speed of the convective elements, indicating that the diffusion approximation is violated. To fix the problem they introduced the convective enthalpy flux limiter, by modifying the correlation Π. Equation (2.64) is reverted to yield,

$$\Pi = \frac{h}{T}u_h, \tag{2.66}$$

and u_h is limited by u_c through setting,

$$\Pi = \frac{h}{T}u_c F_L\left(\frac{u_h}{u_c}\right). \tag{2.67}$$

$F_L(x)$ is flux limiter function, linear for $x < 1$, and equal 1 for $x > 1$. Numerically, smooth connection in between is necessary. u_h entering the above equation is computed from Eq. (2.64) using original definition of Π (Eq. 2.49).

2.4.3 Model parameters

Described Kuhfuß model contains eight, order of unity, free parameters. These are α, α_m, α_p, α_s, α_c, α_d, α_t and γ_r (or α_r depending on the adopted model for radiative cooling). Theory provides no guidance for their values, however, some standard values are in use. In principle, all parameters should be adjusted to match as many observational constraints as possible. This is however, a daunting task, and as was shown by YECKO *et al.* (1998), resulting set of parameters may not be unique, as the same numerical results can be obtained using different combinations of the convective parameters.

Parameters α_p and α_c were introduced by YECKO *et al.* (1998), and are not present in the original KUHFUSS (1986) paper, in which $\alpha_p = 2/3$ and $\alpha_c \equiv \alpha_s$. Standard values for α_s and α_d can be derived through comparison of the local

($\alpha_t = 0$) static solution ($u \equiv 0$, $\mathrm{d}/\mathrm{d}t \equiv 0$) of Eqs. (2.36)–(2.38), with MLT results. Exact correspondence can be obtained if radiative losses are neglected. Local static version of Eq. (2.36) is,

$$C = S - D = 0. \tag{2.68}$$

Using relations (2.51) and (2.52) in the above equation, static value for convective velocity (Eq. 2.65) is derived,

$$u_{c,0} = \left(\frac{2}{3}\right)^{1/2} e_{t,0}^{1/2} = \left(\frac{2}{3}\right)^{1/2} \left(\frac{\alpha^2 \alpha_s}{\alpha_d} \frac{p\mathcal{Q}}{\rho} \mathcal{Y}\right)^{1/2}. \tag{2.69}$$

Comparison with MLT value, given by Eq. (2.11) yields,

$$\frac{\alpha_s}{\alpha_d} = \frac{3}{16}, \tag{2.70}$$

where equivalence between α and α_{MLT} was assumed. Comparing the static value for the convective flux (Eq. 2.50),

$$F_{c,0} = \alpha \alpha_s \rho c_p T e_{t,0}^{1/2} \mathcal{Y} = \alpha \alpha_s \rho c_p T \left(\frac{3}{2}\right)^{1/2} u_{c,0} \mathcal{Y}, \tag{2.71}$$

with the MLT value (Eq. 2.10), and again identifying α with α_{MLT}, the standard value for α_s is obtained,

$$\alpha_s = \frac{1}{2}\left(\frac{2}{3}\right)^{1/2}. \tag{2.72}$$

Use of the above value in Eq. (2.70), provides the standard value for α_d,

$$\alpha_d = \frac{8}{3}\left(\frac{2}{3}\right)^{1/2}. \tag{2.73}$$

If radiative losses are included in the model, exact MLT solution cannot be reproduced. However, following three equation model of KUHFUSS (1987) (*cf.* also WUCHTERL & FEUCHTINGER 1998), standard value for γ_r is taken to be $2\sqrt{3}$.

For further reference, convective parameters entering the described model, together with standard values for some of them are collected in Table 2.1.

2.5   Stellingwerf's *vs.* Kuhfuß models

Detailed comparison of the Stellingwerf's and Kuhfuß models was done by GEHMEYR & WINKLER (1992b). Some important points can also be found in a review article by BAKER (1987) and in the work of KUHFUSS (1986). Comparison of numerical results obtained using different convective recipes was also performed by BUCHLER & KOLLÁTH (2000), however, these results should be treated with caution, as Stellingwerf model was compared with modified Kuhfuß model, in which negative buoyancy effects are neglected (*see* description of the Florida-Budapest code in Section 2.6). Here, I summarize the crucial differences, clearly favouring the original Kuhfuß model.

quantity	α	standard value
mixing length	α	-
eddy viscosity	α_m	-
turbulent pressure	α_p	$2/3$
turbulent source	α_s	$1/2\sqrt{2/3}$
turbulent dissipation	α_d	$8/3\sqrt{2/3}$
convective flux	α_c	$1/2\sqrt{2/3}$
turbulent flux	α_t	-
radiative losses	γ_r	$2\sqrt{3}$

Table 2.1: Summary of the convective parameters entering the Kuhfuß model. In the third column standard values for the relevant parameters are given.

A comparison of derivation of equations of both models, shows two weak points of the Stellingwerf model as compared to the Kuhfuß model. This concern the treatment of the eddy-viscous terms, emerging from the Reynolds tensor, and modeling of the second-order correlations, entering the turbulent source and convective flux.

Considering the Reynolds tensor, Stellingwerf neglects its trace-free part, and puts the eddy-viscous pressure into the model in an *ad hoc* manner. To the contrary, in the Kuhfuß model eddy-viscous terms result from first-order modeling of the Reynolds tensor and are not represented by a single pressure term. Consequences of these different forms of eddy viscosity were not studied up to date. However, as I will show in Chapter 5 (*see* also SMOLEC & MOSKALIK 2008a), numerical results are qualitatively the same when using both forms of eddy viscosity.

Considering the modeling of second-order correlations, differences between the two discussed models are more severe. In the Stellingwerf model, closure relations for the second-order correlations are motivated by the static and local MLT. Such closure relations lead to not differentiable formulations for the source function and convective flux. These are proportional to the square root of the superadiabatic gradient (Eqs. 2.34, 2.33), which results in numerical problems at the edges of the convective zone. What is more important, negative buoyancy effects have to be neglected in the original Stellingwerf model. Convective eddies that overshoot into convectively stable regions, or turbulent energies that remained in the zones that became convectively stable during pulsation, cannot be effectively damped. This was already noted by KUHFUSS (1986). As was shown by GEHMEYR & WINKLER (1992b) characteristic time-scales for the growth and decay of turbulent eddies cannot be reasonably defined in the Stellingwerf model. Time-scale for decay is substantially longer than in the Kuhfuß model, in which negative buoyancy effectively brakes the convective motions in layers that became convectively stable. Consequently, overshooting distance can be very large in the Stellingwerf model (although the term overshooting can be misleading in this context, *see* discussion in Chapter 5). The patch adopted in the modified Stellingwerf model (Eq. 2.35) overcomes the mentioned problems. However, the origin of formula used to compute the superadiabatic gradient in convectively stable regions (Eq. 2.35) is not clear.

In the Kuhfuß model, described problems do not appear. Diffusion motivated closure relations lead to fully differentiable formulation. Source term and convective

flux are proportional to the superadiabatic gradient (Eqs. 2.51, 2.50), which allow to account for the negative buoyancy without difficulty. Consequently physical and numerical behaviour of the model is robust.

2.6   Application of turbulent convection recipes

2.6.1   Convective pulsation hydrocodes

Several nonlinear convective hydrocodes, adopting different convective models, were developed in recent years. However, only three were used extensively to compute several sequences of both RR Lyrae and Cepheid models. These are Italian code adopting the Stellingwerf's convection model and Vienna and Florida-Budapest hydrocodes, adopting Kuhfuß-based convection recipes. Below, I briefly describe essential features of these codes, to be compared later with the code described in this thesis. It is also worth to mention that Kuhfuß model was implemented by OLIVIER & WOOD (2005) to study the pulsations of red giants.

Italian code

The original Stellingwerf model was implemented by STELLINGWERF (1982a) to study the pulsation stability at the red side of the instability strip and properties of the convective RR Lyrae models (STELLINGWERF 1982b, 1984a,b,c). These Lagrangian codes, with radiation treated in the diffusion approximation, were later modified by BONO & STELLINGWERF (1992, 1994), who implemented the modified Stellingwerf model, as described at the end of Section 2.3. Their code will be called **Italian code** in the following. It was used extensively to study the convective RR Lyrae and Cepheid models.

Vienna code

Kuhfuß model was reformulated for the use in stellar pulsation hydrocodes by WUCHTERL & FEUCHTINGER (1998) and implemented by FEUCHTINGER (1999a). This code, called the **Vienna code** in the following, is based on the earlier radiative codes of the Vienna group (*e.g.*, DORFI & FEUCHTINGER 1991, 1995). In this very sophisticated code, adaptive grid algorithm is implemented to resolve the sharp ionization features and shocks. Time-dependent radiative transfer is computed in the gray approximation, using two equation model (radiation energy and radiation momentum equations). For convective energy transfer, Kuhfuß model, as described in Section 2.4 is implemented. Radiative cooling of the convective elements is treated through the radiative cooling term, D_r (Section 2.4.1).

Florida-Budapest code

Starting from 1998, different convective recipes were tried by the Florida-Budapest group. In the linear computations of YECKO *et al.* (1998) and nonlinear models of KOLLÁTH *et al.* (1998) a mixed Stellingwerf-Kuhfuß formulation was adopted. Convective flux was proportional to superadiabatic gradient, as in Kuhfuß model (Eq. 2.50), while for the turbulent source term, a Stellingwerf prescription, $\sim \mathcal{Y}^{1/2}$

(Eq. 2.34) was adopted. This mixed formulation was later on dropped (KOLLÁTH *et al.* 2002), and Kuhfuß description was consistently adopted for both convective flux and turbulent source, however, with one important difference. Superadiabatic gradient, entering these terms was truncated to positive values only,

$$\mathcal{Y} = \left(- \frac{H_p}{c_p} \frac{\partial s}{\partial r} \right)_+ \tag{2.74}$$

Hence, $F_c \sim \mathcal{Y}_+$ and $S_c \sim \mathcal{Y}_+$ are equal to 0 in convectively stable zones. Such treatment of turbulent source function accounts to neglecting the negative buoyancy effects. Resulting convection model, although similar to the Kuhfuß model, is substantially different. Therefore, the claim of KOLLÁTH *et al.* (2002) that their convection model is essentially that of Kuhfuß is not justified. This was not realized and not discussed in the literature up to date. In the following, I will refer to the convection model adopted by the Florida-Budapest group, as modified Kuhfuß model. Consequences of truncating the superadiabatic gradient to positive values only, were not discussed so far, and, as I show in this thesis (Chapters 5 and 6, *see* also SMOLEC & MOSKALIK 2008a,b; SMOLEC 2008), are severe.

Another departure from the original Kuhfuß model, is in the treatment of eddy-viscous terms. In the Florida-Budapest code, E_q and U_q terms are dropped, and eddy-viscous pressure in the form similar to that of Stellingwerf (*cf.* Eq. 2.29),

$$p_\nu = -\frac{4}{3} \alpha_m \rho \Lambda e_t^{1/2} r \frac{\partial}{\partial r} \left(\frac{u}{r} \right), \tag{2.75}$$

appears in the model equations, (2.36)–(2.38), exactly as turbulent pressure, p_t, does.

For the radiative cooling of the convective elements Péclet correction is implemented (Section 2.4.1). Radiation is treated in a simple diffusion approximation. Although the code is supplemented with the adaptive grid algorithm, in most of the computations of the group, simple Lagrangian mesh was used.

2.6.2 Results

The earliest application of convection recipes into pulsation hydrocodes was by BAKER & KIPPENHAHN (1965). They applied the MLT to compute the model structure. In linear analysis, however, they ignored the perturbation of convective quantities. This approach is called the frozen-in approximation and is often used in pulsation computations, specially in pulsation codes coupled with evolutionary codes, in which MLT is most commonly used. Considering the modal stability, little progress was achieved, by including frozen-in mixing length convection. At the red side of the instability strip models became more stable in comparison to purely radiative models, however, were not stabilized.

Original Stellingwerf model, was applied by STELLINGWERF (1982b,1984a,b,c) to study the RR Lyrae models, using Lagrangian code, with radiation treated in the diffusion approximation (predecessor of the Italian code). Stellingwerf concluded that indeed, convection is responsible for quenching the pulsations at the red edge (STELLINGWERF 1982b). More interestingly, he found that convection also affects

the stability of the hottest models, shifting the blue edges toward higher temperatures, as compared to radiative results (STELLINGWERF 1984a). Concerning the full amplitude behaviour, STELLINGWERF (1984b,c) found that artificial viscosity played no role in the convective models, and the main factor limiting the pulsation amplitude was eddy-viscous damping.

Original Stellingwerf model was also adopted by GEHMEYR (1992a). His more sophisticated code, using adaptive grid and two equation model for radiation hydrodynamics, was applied to RR Lyrae models close to the red edge (GEHMEYR 1992b, 1993). Besides producing smooth light and radial velocity curves, his results confirmed the earlier Stellingwerf's work.

Hundreds of nonlinear models of both Cepheids (*e.g.*, BONO, MARCONI & STELLINGWERF 2000) and RR Lyrae (*e.g.*, BONO *et al.* 1997) stars were computed with the Italian code implementing the modified Stellingwerf model. Although plenty of light curves were displayed in the cited papers, quantitative comparison with observations, using for example Fourier decomposition parameters, was not performed. Hence, based on their results, it is hard to judge, whether inclusion of convection led to any substantial improvement in comparison to radiative models.

The Vienna code, implementing the Kuhfuß convection model, was successfully used in nonlinear computations of RR Lyrae (FEUCHTINGER 1999b) and first overtone Cepheids (FEUCHTINGER, BUCHLER & KOLLÁTH 2000). In case of the overtone Cepheids, observed Fourier decomposition parameters of the light curves, particularly the "Z" shape in the φ_{21} progression (*cf.* Sections 1.2 and 1.4.2), were reproduced. It is worth to notice that models presented in the paper of Feuchtinger *et al.* were computed using both the Vienna and Florida-Budapest hydrocodes, yielding consistent results.

Many convective models were computed by the Florida-Budapest group. YECKO *et al.* (1998) studied in detail the linear properties of the convective Cepheid models. They showed that the same topology of the instability strip can be obtained using various combinations of the convective parameters. This important result indicates that the absolute calibration of the convective parameters entering the model computations may not be possible. Linear convective models were also applied to derive the metallicity of the observed F/1O double-mode Cepheids. Convective models allow to determine the domains of simultaneous instability of both modes in the theoretical HR diagram, for different metallicities. As a result, allowed metallicity range corresponding to each point at the Petersen diagram can be derived (BUCHLER & SZABÓ 2007 and BUCHLER 2008). The method was successfully applied to double-mode Cepheids observed in the M33 galaxy, allowing to determine metallicity gradient in this galaxy (BEAULIEU *et al.* 2006). Also, metallicities of double-mode LMC Cepheids were derived using this method (MARQUETTE *et al.* 2009). Many nonlinear models were computed by the Florida-Budapest group. Their work however, focused on modeling the double-mode phenomenon and main results will be presented in the next Section.

2.6.3 Double-mode phenomenon

Purely radiative hydrocodes failed to reproduce the double-mode phenomenon in classical pulsators (Section 1.4.3). Since the works of KOVÁCS & BUCHLER (1988,

1993), a lot of hope was connected with inclusion of turbulent convection into pulsation hydrocodes.

Already in 1993, an exciting result, concerning the nonlinear multimode behaviour, was reported by BONO & STELLINGWERF (1993) in a conference proceedings. Using original Stellingwerf model, they demonstrated stable multimode (three-mode) behaviour in one RR Lyrae model (possibly connected with the resonance). However, no further details appeared later on, in any paper of these authors. Interestingly, hundreds of models, of both Cepheids and RR Lyrae stars, were computed by the group led by Giuseppe Bono, using modified Stellingwerf model implemented in the Italian code (*e.g.*, BONO *et al.* 1997, BONO, MARCONI & STELLINGWERF 2000). No signs of double-mode behaviour were reported.

First robust, convective double-mode models were reported in 1998, independently by the Vienna (FEUCHTINGER 1998) and the Florida-Budapest (KOLLÁTH *et al.* 1998) groups. FEUCHTINGER (1998) analysed the RR Lyrae model sequence of constant mass and luminosity. In a very narrow temperature range ($< 20\,\mathrm{K}$) he found the F/1O double-mode behaviour. For one model, long term stability of the pulsation amplitudes of both modes was demonstrated. This is a strong indication that indeed, computed double-mode behaviour is stable, however, in principle long-lasting mode-switching cannot be excluded. Except the paper of Feuchtinger, no other analysis of double-mode behaviour computed with the Vienna code was published.

Results of the Florida-Budapest group leave no doubt that the computed double-mode behaviour is stable. KOLLÁTH *et al.* (1998) computed a sequence of Cepheid models of constant luminosity and proved that in particular temperature range the double-mode behaviour is the only stable solution (attractor) of the system. They considered the modal amplitude phase-space and demonstrated that trajectories corresponding to nonlinear integrations started with different initial conditions converge toward one double-mode attractor. Their conclusions were supported by the Floquet stability analysis. In later publication, KOLLÁTH *et al.* (2002) improved their methods for analyzing the stability of nonlinear convective models by coupling the hydrodynamical results with amplitude equation analysis. These methods are also used in this thesis and will be extensively described in the next Chapters. KOLLÁTH *et al.* (2002) also found that stable double-mode solution can coexist with stable single-mode solution (hysteresis), the case not discussed earlier in the literature and demanding inclusion of quintic terms in the amplitude equations in order to capture the hydrodynamical behaviour of the models (*see* discussion in Chapter 6). SZABÓ, KOLLÁTH & BUCHLER (2004) analysed in detail the modal selection across the HR diagram for RR Lyrae models. Similar work was done for Cepheid models, and presented by Buchler during the conference held in Paris[1].

Although, as noted by KOLLÁTH *et al.* (2002), double-mode solution appeared quite naturally, once turbulent convection was included in the hydrocodes, the underlying physics remained obscure. Already KOLLÁTH *et al.* (1998) showed that the double-mode behaviour they computed, arose due to non-resonant mode coupling. In their models self-saturation exceeded the cross-saturation, thus, fulfilling the necessary condition for double-mode behaviour (*see* Section 1.4.3; DZIEMBOWSKI

---

[1] *Nonlinear Stellar Hydrodynamics*, Paris, July 2007; proceedings to be published in the EAS Publication Series

& Kovács 1984). The either-or domain computed with radiative hydrocodes, in which cross-saturation effects dominated, was replaced by the double-mode domain, with dominant self-saturation. However, the specific ingredient of turbulent convection model, responsible for such change, was not identified.

It is also worth to notice that detailed comparison of the light and radial velocity curves of the computed double-mode models with observations was not performed.

Chapter 3

Convective code for radial stellar pulsation

In this Chapter, I present the details of the convective codes for radial stellar pulsation, used in the computations presented in this thesis. Basic assumptions concerning the numerical and physical foundations of these codes are presented in Section 3.1. Model equations are summarized in Section 3.2, while details of numerical implementation are provided in Section 3.3. Basic tests of the code will be described in the following Chapter. More concise description of the codes is provided in SMOLEC & MOSKALIK (2008a).

3.1 Basic assumptions

Three basic assumptions underlie every convective pulsation hydrocode. These concern the treatment of energy transfer by convection and by radiation (physical assumptions) and the treatment of numerical mesh (numerical assumption). They determine the numerical methods to be used and largely, the computer time necessary to perform nonlinear computations. In the described codes, simple solutions are preferred to more sophisticated, whenever the latter strongly increase the numerical costs, without providing substantially better results. This assures that the codes contain the essence of the best physics available up to date and are fast enough to perform the extensive model surveys.

For the convective energy transfer Kuhfuß model is adopted. Its advantages over the Stellingwerf model, motivating the choice, were presented in Section 2.5. Radiative losses are treated through the radiative dissipation term (Eq. 2.60), which is arbitrary choice. As an option, eddy-viscous pressure, in the form used by the Florida-Budapest group (Eq. 2.75) is implemented.

Radiative energy transfer is treated in a simple diffusion approximation. This assumption works well through the significant, optically thick layers of the model. In the outermost layers, a better description would be desirable and is offered by the time-dependent radiation hydrodynamics. Such treatment however, gives essentially the same results as simple diffusion approximation (KOVÁCS & KANBUR 1998, FEUCHTINGER, BUCHLER & KOLLÁTH 2000), being numerically much more expensive. Therefore, instead of increasing numerical costs, simple diffusion approximation is implemented here.

To describe the model structure, fixed Lagrangian mass zones are used. No doubt, adaptive mesh is a better solution, as it allows to resolve the sharp features, such as partial ionization regions and allows to trace the ionization fronts and shocks, as they move through the model, during the nonlinear evolution. Adaptive mesh algorithms were described by many authors (*e.g.*, DORFI & FEUCHTINGER 1995, BUCHLER, KOLLÁTH & MAROM 1997), and in principle, their implementation is not very difficult. However, simple Lagrangian description is adopted here, for the same reasons that motivated the use of diffusion approximation for the radiative energy transfer. Inclusion of adaptive mesh algorithms into pulsation hydrocodes didn't lead to any substantial improvement of the obtained results. Computed light curves were smoother, which satisfied the eye, however, their overall shape, as described by Fourier decomposition parameters, remained the same, as in case of the simple Lagrangian mesh. This was shown for both radiative (BUCHLER 1998) and convective (FEUCHTINGER *et al.* 2000) computations. Also, stability properties of the models, do not depend on the treatment of numerical mesh. The drawback of the adaptive hydrocodes is the necessity to solve the additional mesh equation. This makes the computations slow, disallowing the extensive model surveys.

The codes described in this thesis are based on radiative, Lagrangian hydrocodes, originally written by STELLINGWERF (1975a), with some minor modifications (KOVÁCS & BUCHLER 1988). Inclusion of turbulent convection into the nonlinear code is laborious, but straightforward, as numerical methods remain largely the same. In case of model builder and linear code, the task in not so simple. The envelope cannot be constructed by simple inward integration of the model equations, alone, as is possible in the radiative case. Some iterative techniques are necessary. Hence, model builder was, to a large extent, written anew (Section 3.3.1). Also, linear nonadiabatic code was written anew, as completely different solution method to the linear problem was implemented (Section 3.3.2). The new equation of state procedures, allowing to compute the necessary second order derivatives, were written (Section 3.3.4).

3.2 Physical formulation of the model

Below, I briefly summarize the model equations and expressions for particular terms entering the model. These were already given and extensively discussed in the previous Chapter. Here, they are collected together at one place, for further, convenient reference. They are also rewritten in the Lagrangian version, and particular expressions are given in the form, in which they are implemented in the hydrodynamical codes.

Momentum and energy equations are given by (Eqs. 2.37, 2.38, 2.36),

$$\frac{\mathrm{d}u}{\mathrm{d}t} = -4\pi r^2 \frac{\partial}{\partial M_r}(p + p_t) + U_q - \frac{GM_r}{r^2}, \tag{3.1}$$

$$\frac{\mathrm{d}E}{\mathrm{d}t} + p\frac{\mathrm{d}V}{\mathrm{d}t} = -\frac{\partial(L_\mathrm{r} + L_\mathrm{c})}{\partial M_r} - C, \tag{3.2}$$

$$\frac{\mathrm{d}e_t}{\mathrm{d}t} + p_t\frac{\mathrm{d}V}{\mathrm{d}t} = -\frac{\partial L_\mathrm{t}}{\partial M_r} + E_q + C. \tag{3.3}$$

Sum of the last two equations form the total energy equation (Eq. 2.39),

$$\frac{d(E + e_t)}{dt} + (p + p_t)\frac{dV}{dt} = -\frac{\partial(L_r + L_c + L_t)}{\partial M_r} + E_q. \tag{3.4}$$

Fluid velocity is time derivative of radius,

$$u = \frac{dr}{dt}. \tag{3.5}$$

Turbulent pressure and eddy-viscous terms are (Eqs. 2.40, 2.41, 2.42),

$$p_t = \alpha_p \rho e_t, \tag{3.6}$$

$$U_q = \frac{1}{\rho r^3}\frac{\partial}{\partial r}\left[\frac{4}{3}\alpha_m \rho \Lambda e_t^{1/2} r^3 \left(\frac{\partial u}{\partial r} - \frac{u}{r}\right)\right] = \frac{4\pi}{r}\frac{\partial \mathcal{X}}{\partial M}, \tag{3.7}$$

$$E_q = \frac{4}{3}\alpha_m \Lambda e_t^{1/2}\left(\frac{\partial u}{\partial r} - \frac{u}{r}\right)^2 = 4\pi \mathcal{X}\frac{\partial(u/r)}{\partial M}, \tag{3.8}$$

where numerically convenient variable $\mathcal{X}$ is given by,

$$\mathcal{X} = \frac{16}{3}\pi\alpha_m \Lambda e_t^{1/2} r^6 \rho^2 \frac{\partial(u/r)}{\partial M}. \tag{3.9}$$

Quantities entering the coupling term, C, are (Eqs. 2.51, 2.52, 2.62),

$$S = \frac{TpQ}{c_p H_p}\Pi, \tag{3.10}$$

$$D = \alpha_d \frac{e_t^{3/2}}{\Lambda}, \tag{3.11}$$

$$D_r = \frac{4\sigma\gamma_r^2}{\alpha^2}\frac{T^3 V^2}{c_p \kappa H_p^2}e_t. \tag{3.12}$$

Above, numerically convenient version of the thermal expansion coefficient, Q, was used,

$$Q = \left(\frac{\partial V}{\partial T}\right)_p = \frac{\mathcal{Q}V}{T}. \tag{3.13}$$

Correlation Π is given by (Eq. 2.49),

$$\Pi = \alpha\alpha_s e_t^{1/2} c_p \mathcal{Y}. \tag{3.14}$$

Finally for the fluxes, following expressions are used (Eqs. 2.50, 2.44, 1.6),

$$F_c = \frac{\alpha_c}{\alpha_s}\rho T\Pi = \alpha\alpha_c \rho T c_p e_t^{1/2}\mathcal{Y}, \tag{3.15}$$

$$F_t = -\alpha_t 4\pi r^2 \rho^2 \Lambda e_t^{1/2}\frac{\partial e_t}{\partial M}, \tag{3.16}$$

$$F_r = -\frac{4\sigma}{3}4\pi r^2 \frac{1}{\kappa}\frac{\partial T^4}{\partial M}. \tag{3.17}$$

Corresponding luminosities are given by $L = 4\pi r^2 F$. The expression for the radiative flux results from the diffusion approximation to the radiative energy transfer. Radiation energy, E_r, and radiation pressure, p_r, are included in p and E together with gas contribution,

$$p = p_g + p_r, \tag{3.18}$$

$$E = E_g + E_r, \tag{3.19}$$

where,

$$p_r = \frac{1}{3} a T^4, \tag{3.20}$$

$$E_r = a T^4 V. \tag{3.21}$$

3.3   Numerical implementation

In the following Sections, I describe the numerical schemes and methods implemented in the hydrocodes, allowing to solve the full set of Eqs. (3.1)–(3.5). Model builder, constructing the static envelope, is described in Section 3.3.1. Linear nonadiabatic code is described in Section 3.3.2, and nonlinear direct time integration hydrocode in Section 3.3.3. All three codes use the same equation of state and opacity subroutines, briefly described in Section 3.3.4. Also, exactly the same numerical mesh, as well as exactly the same numerical representation of all model equations and quantities is used. This is very important, as it allows to interpret the nonlinear results in terms of *e.g.,* linear period ratios (*see* Section 4.1).

3.3.1   Static model builder

Static model builder constructs the static envelope, that is solves the full set of Eqs. (3.1)–(3.5), with time derivatives and fluid velocity set to zero ($d/dt \equiv 0$, $u \equiv 0$). The model to be constructed is specified by its mass, M, luminosity, L, effective temperature, T_{eff}, and chemical composition, hydrogen mass fraction, X, and heavy element mass fraction, Z. Also, the convective parameters entering the model (Table 2.1) need to be specified. In principle, all parameters can be chosen independently, particularly, we are not bound by the evolutionary tracks in choosing the model mass and luminosity.

The structure of the mesh is the same as in case of the original radiative Stellingwerf's hydrocodes (*see e.g.,* KOVÁCS & BUCHLER 1988). The total number of zones is set to N. Of these, N_a outer zones have equal masses, DMN, down to the anchor zone, in which the temperature is fixed to T_a. Below anchor zone, masses of the remaining $N - N_a$ zones increase geometrically inward, with common ratio, h. The bottom boundary of the envelope is fixed by a given temperature, T_{in}. The anchor temperature is chosen to be around $11000\,K$, which assures that at least one zone is located at the center of the hydrogen partial ionization region (PIR). Such mesh structure was necessary in the early radiative computations with coarse mesh, to assure the smooth variation of the mode growth rates along a sequence of models (*e.g.,* for models of constant L and varying T_{eff}). Nowadays, linear computations with much denser mesh are very fast. Also, convection smears the PIRs. However, best (smooth) results are obtained with anchor preserved in the mesh.

The model is divided into N mass zones, separated by the interfaces. All variables are defined either at the zones (thermodynamic variables, T, p, V, κ) or at the interfaces (luminosities, velocities, radii) and are labeled with integer indices, just as is shown in Figure 3.1. Outermost zone, as well as outermost interface have index N. Mass interior to interface i is denoted by M_i, mass of the zone i by DM_i, and mass associated with the interface i, $DM2_i$, is defined as,

$$DM2_i = 0.5(DM_i + DM_{i+1}).$$

$$
\begin{array}{ll}
\underline{\hspace{3cm}} \quad i+1 & \\
\quad i+1 & \\
\underline{\hspace{3cm}} \quad i & \quad M,\ DM2,\ u,\ r,\ H_p,\ \mathcal{Y},\ L_{\mathrm{r}},\ L_{\mathrm{c}},\ L_{\mathrm{t}},\ U_q \\
\quad i & \quad DM,\ T,\ V,\ Q,\ c_p,\ \kappa,\ p,\ p_t,\ E_q,\ S,\ D,\ D_{\mathrm{r}} \\
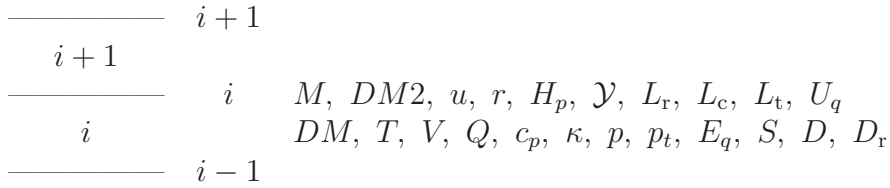\underline{\hspace{3cm}} \quad i-1 &
\end{array}
$$

Figure 3.1: Notation used in the numerical scheme and summary of zone and interface quantities.

For discrete numerical scheme, one has to define the spatial averages of model quantities, denoted by curly brackets {}, as well as spatial differences, denoted by Δ, which are numerical representation of the derivatives. Spatial average (spatial difference) of the zone quantity is defined at the interface and spatial average (spatial difference) of the interface quantity is defined at the zone. Examples below illustrate the notation,

$$\{T\}_i = 0.5(T_i + T_{i+1}),$$
$$\{r\}_i = 0.5(r_{i-1} + r_i),$$
$$\Delta p_i = p_{i+1} - p_i,$$
$$\Delta L_i = L_i - L_{i-1}.$$

In order to construct the envelope, momentum (Eq. 3.1), total energy (Eq. 3.4) and turbulent energy (Eq. 3.3) equations need to be solved. Numerical representation of their static, equilibrium versions are following,

$$0 = \mathcal{M}_i = -4\pi r_i^2 \frac{\Delta p_i + \Delta p_{t,i}}{DM2_i} - \frac{GM_i}{r_i^2}, \tag{3.22a}$$

$$0 = \mathcal{E}_i = \frac{L_{\mathrm{r},i}}{L} + \frac{L_{\mathrm{c},i}}{L} + \frac{L_{\mathrm{t},i}}{L} - 1, \tag{3.22b}$$

$$0 = \mathcal{Z}_i = -\frac{\Delta L_{\mathrm{t},i}}{DM_i} + C_i. \tag{3.22c}$$

Note that the total energy equation reduces to luminosity conservation condition, and that eddy-viscous terms do not enter the static model computations. Above, $\mathcal{M}_i$, $\mathcal{E}_i$ and $\mathcal{Z}_i$ denote the left-hand-sides of the momentum, total energy and turbulent energy equations, respectively, which for static model should be equal to zero for all model zones/interfaces.

Construction of the static envelope proceed in two steps. In the first step, initial model is constructed, without turbulent pressure and without turbulent flux ($\alpha_p =$

$\alpha_t = 0$), with turbulent energy (and coupling term) defined at the interfaces. This can be done by direct integration of the static equilibrium equations (Eqs. 3.22) from surface inward. In the second step, the final model, with turbulent pressure and turbulent flux included and with turbulent energies redefined at the zones, is constructed. This is done through the multivariate Newton-Rhapson iterations, called the envelope relaxation in the following (*see e.g.*, YECKO *et al.* 1998). Below, both steps are briefly described.

Inward integration. Turbulent pressure and turbulent flux are neglected in Eqs. (3.22). Initial surface conditions for the inward integration are following. Outer pressure is set equal to 0,

$$p_{\text{out}} = 0, \tag{3.23}$$

radius of the outermost interface, r_N, is set to,

$$r_N = \sqrt{\frac{L}{4\pi\sigma T_{\text{eff}}^4}}, \tag{3.24}$$

and temperature of the outermost zone is equal,

$$T_N^4 = fT_{\text{eff}}^4. \tag{3.25}$$

For f value $1/2$, resulting from the Eddington approximation is used by default.

With the guessed value for the mass of the outermost zone, DMN, and with conditions (3.23) and (3.24), the value of p_N is derived from the momentum equation (Eq. 3.22a). Then, for a given p_N and T_N (Eq. 3.25), EOS yields the value of the specific volume, V_N. From continuity equation, the value of r_{N-1} (r_{i-1}, in general) is computed,

$$r_{N-1} = \left(r_N^3 - \frac{3V_N DM_N}{4\pi}\right)^{1/3}.$$

For the interior zones masses are set according to,

$$M_{i-1} = M_i - DM_i,$$

with $DM_i = DMN$ above the anchor and $DM_{i-1} = hDM_i$, below. Momentum equation immediately yields p_{N-1} (p_{i-1}). For zone $N-1$, and all interior zones, energy equations need to be solved. T_{N-1} (T_{i-1}) is guessed. EOS and opacity tables yield, V_{N-1} and κ_{N-1} (V_{i-1} and κ_{i-1}), which allow to compute the luminosities and check the luminosity conservation condition (Eq. 3.22b). T_{N-1} (T_{i-1}) is changed iteratively until this condition is fulfilled. Integrations continue till the anchor zone is reached. With initial guess for the DMN, temperature in the anchor zone is different than T_{a}. All computations are repeated, with DMN successively changed to yield T_{a} in the anchor zone.

The whole procedure is repeated for integrations below the anchor, however, now h is successively changed to yield the given inner boundary temperature, T_{in}.

Envelope relaxation. At this step, turbulent pressure and turbulent flux are included in the model. Turbulent energies, as well as coupling terms, are redefined at the zones. Below, numerical representation of all model quantities entering the

equilibrium model is given. For the quantities entering the coupling term we have (Eqs. 3.10, 3.11, 3.12),

$$S_i = \frac{T_i p_i Q_i}{c_{p,i}} \left\{ \frac{\Pi}{H_p} \right\}_i e_{t,i}^{1/2}, \tag{3.26}$$

$$D_i = \frac{\alpha_d}{\alpha} \frac{e_{t,i}^{3/2}}{\{H_p\}_i}, \tag{3.27}$$

$$D_{\mathrm{r},i} = \frac{4\sigma\gamma_r^2}{\alpha^2} \frac{T_i^3 V_i^2}{c_{p,i}\kappa_i\{H_p^2\}_i} e_{t,i}. \tag{3.28}$$

Correlation Π is given by,

$$\Pi_i = \alpha\alpha_s\{c_p\}_i \mathcal{Y}_i. \tag{3.29}$$

Note that in comparison to Eq. (3.14), the term $e_t^{1/2}$ was dropped above. Now, it appears separately in the expression for turbulent source function, S_i, and below, in the expression for convective flux, where it is averaged at the interface. The motivation for such treatment is to assure that all quantities entering the coupling term in zone i, C_i, depend only on the turbulent energy in this zone, $e_{t,i}$. Hence, the only non-local (in e_t) term in the turbulent energy equation is the diffusive term containing the turbulent flux.

Numerical representations of the luminosities (Eqs. 3.15, 3.16, 3.17) are,

$$L_{\mathrm{c},i} = 4\pi r_i^2 \frac{\alpha_c}{\alpha_s} \left\{ \frac{T}{V} \right\}_i \Pi_i \{e_t^{1/2}\}_i, \tag{3.30}$$

$$L_{\mathrm{t},i} = -\frac{2}{3}\alpha\alpha_t(4\pi r_i^2)^2 H_{p,i} \left\{ \frac{1}{V^2} \right\}_i \frac{e_{t,i+1}^{3/2} - e_{t,i}^{3/2}}{DM2_i}, \tag{3.31}$$

$$L_{\mathrm{r},i} = -\frac{4\sigma}{3} \frac{(4\pi r_i^2)^2}{DM2_i} \frac{T_{i+1}^4/\kappa_{i+1} - T_i^4/\kappa_i}{1 - \frac{\log(\kappa_{i+1}/\kappa_i)}{\log(T_{i+1}^4/T_i^4)}}. \tag{3.32}$$

Averaging scheme in the expression for radiative luminosity comes from STELLING-WERF (1975a). Finally, turbulent pressure (Eq. 3.6) is given by,

$$p_{t,i} = \frac{\alpha_p e_{t,i}}{V_i}. \tag{3.33}$$

Pressure scale height and superadiabatic gradient entering above formulae are represented as,

$$H_{p,i} = \frac{r_i^2}{GM_i}\{pV\}_i, \tag{3.34}$$

$$\mathcal{Y}_i = \frac{4\pi r_i^2}{DM2_i} \frac{H_{p,i}}{\{V\}_i} \left(\left\{ \frac{Q}{c_p} \right\}_i (\Delta p_i) - (\log T_{i+1} - \log T_i) \right). \tag{3.35}$$

Expression for the superadiabatic gradient is based on the formula given by STELLING-WERF (1982a).

The whole system of Eqs. (3.22) is solved through the multivariate Newton-Rhapson iterations. For the turbulent energy equation, $\varpi = e_t^{1/2}$ is used as a basic

variable. The correction equations form a linear, band system of bandwidth eleven,

$$
\begin{pmatrix}
\frac{\partial \mathcal{E}_1}{\partial T_1} & \frac{\partial \mathcal{E}_1}{\partial \varpi_1} & \frac{\partial \mathcal{E}_1}{\partial r_1} & \frac{\partial \mathcal{E}_1}{\partial T_2} & \cdots \\
\frac{\partial \mathcal{Z}_1}{\partial T_1} & \frac{\partial \mathcal{Z}_1}{\partial \varpi_1} & \frac{\partial \mathcal{Z}_1}{\partial r_1} & \frac{\partial \mathcal{Z}_1}{\partial T_2} & \cdots \\
\frac{\partial \mathcal{M}_1}{\partial T_1} & \frac{\partial \mathcal{M}_1}{\partial \varpi_1} & \frac{\partial \mathcal{M}_1}{\partial r_1} & \frac{\partial \mathcal{M}_1}{\partial T_2} & \cdots \\
\frac{\partial \mathcal{E}_2}{\partial T_1} & \frac{\partial \mathcal{E}_2}{\partial \varpi_1} & \frac{\partial \mathcal{E}_2}{\partial r_1} & \frac{\partial \mathcal{E}_2}{\partial T_2} & \cdots \\
\cdots & \cdots & \cdots & \cdots
\end{pmatrix}
\begin{pmatrix}
\delta T_1 \\
\delta \varpi_1 \\
\delta r_1 \\
\delta T_2 \\
\cdots
\end{pmatrix}
= -
\begin{pmatrix}
\mathcal{E}_1 \\
\mathcal{Z}_1 \\
\mathcal{M}_1 \\
\mathcal{E}_2 \\
\cdots
\end{pmatrix}
\tag{3.36}
$$

Initial values for iterations are taken from the first step of model construction (inward integration). During iterations outer temperature is constrained to,

$$
T_N^4 = \frac{fL}{4\pi\sigma r_N^2},
\tag{3.37}
$$

and free adjustment of the outer radius, r_N, is allowed. Iterations are treated as converged, if relative corrections to the radii, temperatures and turbulent energies are smaller than 10^{-10}, in all model zones/interfaces. In a resulting model, temperature in the anchor zone is not equal to T_a. Hence, to preserve the mesh structure, iterations are repeated several times with DMN and h being successively changed. DMN is adjusted to match the desired temperature in the anchor zone. Then, to assure a smooth transition from the upper part (zones above the anchor) to the lower part (zones below the anchor) of the envelope, h need to be changed. This is done in such a way that the total mass of the envelope below the anchor is not changed. As a result, the temperature of the innermost zone is slightly different from T_{in}, but only by several Kelvins.

3.3.2 Linear analysis

In the linear nonadiabatic analysis (LNA), the full set of equations, (3.1)–(3.5), is considered. Below they are rewritten in a convenient form, with time derivatives of basic variables, for which we pick r, u, T and e_t, left alone on the left hand side,

$$
\begin{aligned}
\frac{\mathrm{d}r}{\mathrm{d}t} &= u, \\
\frac{\mathrm{d}u}{\mathrm{d}t} &= -4\pi r^2 \frac{\partial(p + p_t)}{\partial M_r} - \frac{GM_r}{r^2} + U_q, \\
c_V \frac{\mathrm{d}T}{\mathrm{d}t} &= -\left(p + \left(\frac{\partial E}{\partial V}\right)_T\right)\frac{\mathrm{d}V}{\mathrm{d}t} - \frac{\partial(L_r + L_c)}{\partial M_r} - C, \\
\frac{\mathrm{d}e_t}{\mathrm{d}t} &= -p_t\frac{\mathrm{d}V}{\mathrm{d}t} - \frac{\partial L_t}{\partial M_r} + C.
\end{aligned}
\tag{3.38}
$$

In case of the internal energy equation, thermodynamic identity,

$$
\frac{\mathrm{d}E}{\mathrm{d}t} = c_V \frac{\mathrm{d}T}{\mathrm{d}t} + \left(\frac{\partial E}{\partial V}\right)_T \frac{\mathrm{d}V}{\mathrm{d}t},
$$

was used to yield the time derivative of the temperature. c_V in a formulae above, is specific heat at constant volume,

$$
c_V = \left(\frac{\partial E}{\partial T}\right)_V.
\tag{3.39}
$$

Numerical representations of the left-hand side derivatives, entering Eqs. (3.38), are,

$$
\bar{\mathcal{V}}_i = \frac{\mathrm{d}r_i}{\mathrm{d}t} = u_i
$$

$$
\bar{\mathcal{M}}_i = \frac{\mathrm{d}u_i}{\mathrm{d}t} = -\frac{4\pi r_i^2}{DM2_i}(\Delta p_i + \Delta p_{t,i}) - \frac{GM_i}{r_i^2} + U_{q,i}
$$

$$
c_{V,i}\bar{\mathcal{E}}_i = c_{V,i}\frac{\mathrm{d}T_i}{\mathrm{d}t} = -\left(p_i + \left(\frac{\mathrm{d}E}{\mathrm{d}V}\right)_{T,i}\right)\frac{4\pi}{DM_i}\left(r_i^2 u_i - r_{i-1}^2 u_{i-1}\right) - \frac{\Delta L_{\mathrm{r},i} + \Delta L_{\mathrm{c},i}}{DM_i} - C_i
$$

$$
\bar{\mathcal{Z}}_i = \frac{\mathrm{d}e_{t,i}}{\mathrm{d}t} = -p_{t,i}\frac{4\pi}{DM_i}\left(r_i^2 u_i - r_{i-1}^2 u_{i-1}\right) - \frac{\Delta L_{\mathrm{t},i}}{DM_i} + C_i
$$

$$(3.40)$$

To express the time derivative of the specific volume, following identity was used,

$$
\mathrm{d}V_i = \frac{4\pi}{3DM_i}\,\mathrm{d}(r_i^3 - r_{i-1}^3).
$$

$\bar{\mathcal{V}}$, $\bar{\mathcal{M}}$, $\bar{\mathcal{E}}$ and $\bar{\mathcal{Z}}$ denote the time derivatives of the basic variables, r, u, T and e_t, respectively. Numerical representation of all model quantities is exactly the same as provided in the previous section (Eqs. 3.26–3.35). In addition, eddy-viscous term, U_q (Eq. 3.7), enters the linear analysis. Its numerical representation is given below,

$$
U_{q,i} = \frac{4\pi}{r_i}\frac{\mathcal{X}_{i+1} - \mathcal{X}_i}{DM2_i},
$$

$$(3.41)$$

where,

$$
\mathcal{X}_i = \frac{16}{3}\pi\alpha\alpha_m\frac{1}{V_i^2}e_{t,i}^{1/2}\{H_p\}_i\{r^6\}_i\frac{u_i/r_i - u_{i-1}/r_{i-1}}{DM_i}.
$$

$$(3.42)$$

Although the viscous energy transfer rate, E_q (Eq. 3.8), does not enter the LNA computations (since it is $\sim u^2$), its numerical representation is also given below, for completeness,

$$
E_{q,i} = 4\pi\mathcal{X}_i\frac{u_i/r_i - u_{i-1}/r_{i-1}}{DM_i}.
$$

$$(3.43)$$

The static, not perturbed model is constructed by the model builder. Very small turbulent energies are filtered out, through setting $e_t = e_f$ if $e_t < e_f$. This is necessary to avoid numerical havoc in the computed work integrals in the deep model zones, which appear, if very small turbulent energies ($e_t < 10^{-4}\,\mathrm{erg/g}$) are retained. With $e_f = 1\,\mathrm{erg/g}$ results are satisfactory and do not depend on the exact value of e_f (at least in a reasonable range, $e_f \in (10^{-4}, 10^6)\,\mathrm{erg/g}$). The system (3.40) is linearized around equilibrium, and time dependence of the form $\sim \exp(\sigma t)$ is assumed for the perturbed quantities. The compact form of the resulting eigenvalue problem is,

$$
\begin{pmatrix}
\frac{\partial\bar{\mathcal{V}}_1}{\partial r_1} & \frac{\partial\bar{\mathcal{V}}_1}{\partial u_1} & \frac{\partial\bar{\mathcal{V}}_1}{\partial T_1} & \frac{\partial\bar{\mathcal{V}}_1}{\partial e_{t,1}} & \frac{\partial\bar{\mathcal{V}}_1}{\partial r_2} & \cdots \\
\frac{\partial\bar{\mathcal{M}}_1}{\partial r_1} & \frac{\partial\bar{\mathcal{M}}_1}{\partial u_1} & \frac{\partial\bar{\mathcal{M}}_1}{\partial T_1} & \frac{\partial\bar{\mathcal{M}}_1}{\partial e_{t,1}} & \frac{\partial\bar{\mathcal{M}}_1}{\partial r_2} & \cdots \\
\frac{\partial\bar{\mathcal{E}}_1}{\partial r_1}k_1 & \frac{\partial\bar{\mathcal{E}}_1}{\partial u_1}k_1 & \frac{\partial\bar{\mathcal{E}}_1}{\partial T_1}k_1 & \frac{\partial\bar{\mathcal{E}}_1}{\partial e_{t,1}}k_1 & \frac{\partial\bar{\mathcal{E}}_1}{\partial r_2}k_1 & \cdots \\
\frac{\partial\bar{\mathcal{Z}}_1}{\partial r_1} & \frac{\partial\bar{\mathcal{Z}}_1}{\partial u_1} & \frac{\partial\bar{\mathcal{Z}}_1}{\partial T_1} & \frac{\partial\bar{\mathcal{Z}}_1}{\partial e_{t,1}} & \frac{\partial\bar{\mathcal{Z}}_1}{\partial r_2} & \cdots \\
\frac{\partial\bar{\mathcal{V}}_2}{\partial r_1} & \frac{\partial\bar{\mathcal{V}}_2}{\partial u_1} & \frac{\partial\bar{\mathcal{V}}_2}{\partial T_1} & \frac{\partial\bar{\mathcal{V}}_2}{\partial e_{t,1}} & \frac{\partial\bar{\mathcal{V}}_2}{\partial r_2} & \cdots \\
\cdots & \cdots & \cdots & \cdots & \cdots &
\end{pmatrix}
\begin{pmatrix}
\delta r_1 \\
\delta u_1 \\
\delta T_1 \\
\delta e_{t,1} \\
\delta r_2 \\
\cdots
\end{pmatrix}
= \sigma
\begin{pmatrix}
\delta r_1 \\
\delta u_1 \\
\delta T_1 \\
\delta e_{t,1} \\
\delta r_2 \\
\cdots
\end{pmatrix}, \quad (3.44)
$$

where $k_i = c_{V,i}^{-1}$.

As suggested by Glasner & Buchler (1993), the system is solved using the canned eigenvalue solver. Two numerical subroutines are implemented in the code, namely RG from the EISPACK library (Dongarra & Moler 1983), and DGEEV from the LAPACK library (Anderson *et al.* 1999). By default EISPACK/RG is used.

Linear code allows to compute the mode periods, growth rates, as well as associated linear eigenfunctions, mode energies and work integrals. Below, formulae for these quantities are summarized.

Mode growth rates and frequencies. Growth rate of the mode, γ, is defined as fractional growth of the kinetic energy per pulsation period,

$$\gamma = 4\pi \frac{\Re(\sigma)}{\omega}, \tag{3.45}$$

where,

$$\omega = \Im(\sigma), \tag{3.46}$$

is the mode frequency. In case of radiative computations the LNA system generates N thermal ($\Im(\sigma) = 0$) and N vibrational ($\sigma^i = (\sigma^j)^*$, for associated eigenvalues) eigenmodes. In convective case, additional turbulent energy equation generates a new family of N modes. Some of them are of vibrational character. These are extremely damped, with typical growth rates, $\gamma < -1$, and hence, are not expected to cause any troubles in nonlinear computations (*see* also, Yecko *et al.* 1998).

Linear eigenvectors. Radius, temperature and turbulent energy eigenvectors, δr_i , δT_i and $\delta \varpi_i$ ($i = 1, \ldots, N$), are simply returned by the eigenvalue solver. They are normalized by,

$$\mathcal{K} = r_N / \delta r_N,$$

to yield following definitions of the complex, linear and normalized eigenvectors of the radius and temperature,

$$f_{r,i} = \frac{\delta r_i}{r_i} \mathcal{K},$$

$$f_{T,i} = \frac{\delta T_i}{T_i} \mathcal{K},$$

For the luminosity eigenvector we write,

$$f_{L,i} = \left(\frac{\partial L}{\partial r_*} \delta r_* + \frac{\partial L}{\partial T_*} \delta T_* + \frac{\partial L}{\partial \varpi_*} \delta \varpi_* \right) \mathcal{K} / L_0,$$

where L denotes the total luminosity, L_0 its static value, and asterisks denotes all the relevant indices (value of luminosity at a given zone, depends on physical conditions in the neighboring zones). Amplitudes and phases are simply defined as in example below,

$$\mathrm{abs}(f_{r,i}) = |f_{r,i}|,$$

$$\mathrm{ph}(f_{r,i}) = \mathrm{atan}\left(\frac{\Im(f_{r,i})}{\Re(f_{r,i})} \right).$$

Mode energies and work integrals. Kinetic energy of a pulsation mode is defined as,

$$E_K = 0.5 \int \omega^2 |\delta r|^2 \, \mathrm{d}M. \tag{3.47}$$

Numerically we have,

$$E_K = 0.5 \sum_i DM2_i \Big(\Im(\sigma) \mathrm{abs}(\delta r_i \mathcal{K}) \Big)^2$$

The ordinary gas pressure work done in particular zone i, $W_{g,i}$, can be expressed as (*e.g.*, CASTOR 1971; Appendix A, Eq. A.14),

$$W_{g,i} = -\pi DM_i \Im\big((\delta p_i)^* \delta V_i \big).$$

Hence, the gas pressure work integral, $W_g(M_r)$, is simply,

$$W_g(M_r) = -\pi \int_{M_0}^{M_r} \Im\{ (\delta p)^* (\delta V) \} \, \mathrm{d}M, \tag{3.48}$$

where integration is extended over the mass of the envelope. Specific volume and gas pressure perturbations are computed as,

$$\delta V_i = \left(\frac{\partial V_i}{\partial r_*} \delta r_* \right) \mathcal{K}$$

$$\delta p_i = \frac{\partial p_i}{\partial V_i} \delta V_i + \frac{\partial p_i}{\partial T_i} \delta T_i \mathcal{K}$$

Turbulent pressure work integral has exactly the same form as gas pressure work integral, however, with p replaced by p_t.

Expression for eddy-viscous work integral, $W_{EV}(M_r)$, is following (Eq. A.14),

$$W_{EV}(M_r) = \pi \int_{M_0}^{M_r} \Im\left\{ (\delta X)^* \left[\frac{\delta V}{r^3} - \frac{3V}{r^3} \frac{\delta r}{r} \right] \right\} \mathrm{d}M. \tag{3.49}$$

Derivation of the above formula (SMOLEC & MOSKALIK 2008a) is presented in Appendix A.

3.3.3   Direct time integration nonlinear hydrocode

In nonlinear, direct time computations, full nonlinear set of equations, (3.1)–(3.5), is solved as initial value problem. Static model, computed by the model builder, is initialized (kicked) with the scaled linear velocity eigenvector, and evolved forward in time, step by step. At a given instant of time (time step), the model is fully specified by the values of velocities and radii of all model interfaces and temperatures and turbulent energies in all model zones. In the following, the value of some quantity Z, in the i-th zone/interface of the model, at a time step n, will be denoted by, $Z_i^{(n)}$. Thus, the basic step of the nonlinear hydrocode is to perform the time evolution,

$$\left(u_i^{(n)}, \ r_i^{(n)}, \ T_i^{(n)}, \ \varpi_i^{(n)} \right) \rightarrow \left(u_i^{(n+1)}, \ r_i^{(n+1)}, \ T_i^{(n+1)}, \ \varpi_i^{(n+1)} \right)$$

In the following, I will present the finite difference form of the full nonlinear model equations. Then, I will discuss the time averages that appear in them. Finally, the solution method will be given.

Finite difference equations

Equations, (3.1), (3.4), (3.3) and (3.5) are written in a finite difference form, with $\varpi = e_t^{1/2}$, being the basic variable,

$$\frac{Du_i}{DT} + 4\pi \langle r_i^2 \rangle \frac{\Delta(\langle p_i \rangle + \langle p_{t,i} \rangle)}{DM2_i} + GM_i \left\langle \frac{1}{r_i^2} \right\rangle - \langle U_{q,i} \rangle = 0, \qquad (3.50)$$

$$D(E_i + \varpi_i^2) + (\langle p_i \rangle + \langle p_{t,i} \rangle) DV_i + \frac{DT}{DM_i} \Delta(\langle L_{r,i} \rangle + \langle L_{c,i} \rangle + \langle L_{t,i} \rangle) - DT \langle E_{q,i} \rangle = 0, \qquad (3.51)$$

$$D\varpi_i^2 + \langle p_{t,i} \rangle DV_i + \frac{DT}{DM_i} \Delta \langle L_{t,i} \rangle - DT \langle E_{q,i} \rangle - DT \langle C_i \rangle = 0, \qquad (3.52)$$

$$r_i^{(n+1)} = r_i^{(n)} + DT \langle u_i \rangle. \qquad (3.53)$$

In the above equations, $\langle \rangle$ denote the time average over a time step, capital D is used for the time difference, and DT stands for the value of the time step. Time differences are calculated as in the following example,

$$Du_i = u_i^{(n+1)} - u_i^{(n)}.$$

For the boundary conditions we use similar expressions as in radiative computations discussed in Section 1.3. For the outer boundary, vanishing external pressure is assumed,

$$p_{\text{out}} = 0. \qquad (3.54)$$

Turbulent energy is set to zero in the outermost model zone,

$$\varpi_N = 0, \qquad (3.55)$$

and for the outgoing luminosity we write (*cf.* Eq. 3.37),

$$L_N = 4\pi r_N^2 f^{-1} \sigma T_N^4. \qquad (3.56)$$

At the inner boundary a rigid core,

$$u_0 = 0, \qquad (3.57)$$

of constant luminosity is assumed, and turbulent energy is set to zero in the innermost zone,

$$\varpi_1 = 0, \qquad (3.58)$$

(and practically, also in several innermost zones, as deep interior of the models, discussed in this thesis, is purely radiative).

Numerical representation of all model quantities is **exactly** the same as discussed in the previous Sections, namely Eqs. (3.41)–(3.43) are used for eddy-viscous terms, and Eqs. (3.26)–(3.35) for the remaining quantities. However, turbulent energy dissipation term is slightly modified, to deal with a somewhat troubling nature of the turbulent energy equation. Note that in this equation, all terms depend on e_t in some power. Therefore, $e_t = 0$ is always a solution. Once e_t becomes zero in some zone it will stay equal zero, even if convective instability arises. The problem was

extensively discussed by GEHMEYR & WINKLER (1992b), who proposed numerical scheme to overcome the problem. Different scheme was adopted by YECKO *et al.* (1998), and very similar scheme is used here. A small non-zero term is added in the turbulent energy equation, by slight modification of the turbulent dissipation term (Eqs. 3.11, 3.27),

$$D_i = \frac{\alpha_d}{\alpha} \frac{e_{t,i}^{3/2} - e_0^{3/2}}{\{H_p\}_i}, \tag{3.59}$$

where e_0 is a small, non-zero, constant turbulent energy, for which we set $e_0 = 10^4 \, \mathrm{erg/g}$. The way in which this correction works, will be described in Section 5.2.2, based on numerical examples.

In the nonlinear scheme also artificial viscous pressure is included. Artificial viscosity (AV) is necessary in radiative computations to handle shocks developing mostly in the PIRs. It acts as ordinary pressure, spreading the shock through several mass zones. Unfortunately, it is also main factor limiting the pulsation amplitude of radiative models (*see* Section 1.3.2). In convective hydrocodes, artificial viscosity is, in principle, not necessary. Eddy-viscous terms provide physical source of dissipation, and numerical problems are usually not encountered. However, for consistency AV is preserved in all convective hydrocodes (BONO & STELLINGWERF 1994, FEUCHTINGER 1999a) and also in the code described here. Modified von Neumann-Richtmyer formula for AV (STELLINGWERF 1975a), containing two free parameters, C_Q and α_{cut}, is used here. Additional AV pressure, p_{av}, is computed in the following way,

$$p_{\mathrm{av},i} = C_Q p_i \left(\frac{u_{i-1} - u_i}{\sqrt{p_i V_i}} - \alpha_{\mathrm{cut}} \right)^2 \tag{3.60}$$

AV pressure turns on, only if relative speed of the consecutive approaching zones exceeds a given fraction, α_{cut}, of a local sound speed. By default, $C_Q = 4$ is used, just as in radiative computations. Cut-off parameter is set to very high value, $\alpha_{\mathrm{cut}} = 0.1$. This choice assures that AV turns on only exceptionally. It never plays a role in full amplitude pulsation. Note also, that as AV pressure is proportional to the square of the relative velocity, it does not enter the static model computation, nor LNA analysis.

Time averages

To solve the finite difference equations (3.50)–(3.53), time averages over a time step, of several quantities, need to be calculated. Usually time average of some quantity Z is expressed as,

$$\langle Z_i \rangle = \xi Z_i^{(n+1)} + (1 - \xi) Z_i^{(n)},$$

with $\xi = 1$ corresponding to fully implicit treatment and $\xi = 0$ corresponding to fully explicit treatment. The exact value of ξ results from energy conservation considerations. In case of radiative hydrocodes appropriate averaging scheme was given by FRALEY (1968). In case of convective hydrocode described in this thesis, averaging scheme is derived in Appendix B. Below, summary of resulting expressions is provided.

In order to preserve the total energy, $\langle r_i^2 \rangle$ and $\langle 1/r_i^2 \rangle$ entering the momentum equation, have to be calculated as (Eqs. B.10 and B.8),

$$\langle r_i^2 \rangle = \frac{1}{3}\left(r_i^{2\ (n+1)} + r_i^{(n+1)}r_i^{(n)} + r_i^{2\ (n)}\right), \tag{3.61}$$

$$\left\langle \frac{1}{r_i^2} \right\rangle = \frac{1}{r_i^{(n)}r_i^{(n+1)}}. \tag{3.62}$$

For the velocity average in Eq. (3.53), time-centered scheme is necessary (Eq. B.9),

$$\langle u_i \rangle = \frac{1}{2}u_i^{(n+1)} + \frac{1}{2}u_i^{(n)}. \tag{3.63}$$

These are exactly the same expressions as required in purely radiative hydrocodes. In case of convective model adopted in the hydrocode under discussion, the way time averages of eddy-viscous terms are calculated, is also determined by the energy conservation, and is following (Eqs. B.16, B.17),

$$\langle U_{q,i} \rangle = \frac{4\pi}{\langle r_i \rangle} \frac{\langle \mathcal{X}_{i+1} \rangle - \langle \mathcal{X}_i \rangle}{DM2_i}, \tag{3.64}$$

$$\langle E_{q,i} \rangle = 4\pi \langle \mathcal{X}_i \rangle \frac{\langle u_i \rangle / \langle r_i \rangle - \langle u_{i-1} \rangle / \langle r_{i-1} \rangle}{DM_i}, \tag{3.65}$$

$$\langle \mathcal{X}_i \rangle = \theta_u \mathcal{X}_i^{(n+1)} + (1 - \theta_u)\mathcal{X}_i^{(n)}, \tag{3.66}$$

$$\langle r_i \rangle = \beta r_i^{(n+1)} + (1 - \beta)r_i^{(n)}. \tag{3.67}$$

Values of θ_u and β are not restricted by energy conservation. For radius averaging, $\langle r_i \rangle$, it is natural to adopt the time-centered definition ($\beta = 1/2$), as it enters the quotients with time centered velocity average. For $\langle \mathcal{X}_i \rangle$ fully implicit scheme ($\theta_u = 1$) is used, which, as was checked experimentally, assures fast convergence in nonlinear iterations.

The way pressures and luminosities are averaged, has no effect on the energy conservation. Following definitions are adopted,

$$\langle p_i \rangle = \theta p_i^{(n+1)} + (1 - \theta)p_i^{(n)}, \tag{3.68}$$

$$\langle p_{t,i} \rangle = \theta_t p_{t,i}^{(n+1)} + (1 - \theta_t)p_{t,i}^{(n)}, \tag{3.69}$$

$$\langle L_{r,i} \rangle = w_r L_{r,i}^{(n+1)} + (1 - w_r)L_{r,i}^{(n)}, \tag{3.70}$$

$$\langle L_{c,i} \rangle = w_c L_{c,i}^{(n+1)} + (1 - w_c)L_{c,i}^{(n)}, \tag{3.71}$$

$$\langle L_{t,i} \rangle = w_t L_{t,i}^{(n+1)} + (1 - w_t)L_{t,i}^{(n)}, \tag{3.72}$$

with $\theta = \theta_t = 1/2$ and $w_r = w_c = w_t = 2/3$. The quoted values of θ and w_r assure greater numerical stability of radiative computations. The same values are adopted for turbulent pressure and convective fluxes.

Turbulent energy equation alone, does not enter the energy conservation analysis (*see* Appendix B). For the coupling term following average is used,

$$\langle C_i \rangle = \gamma C_i^{(n+1)} + (1 - \gamma)C_i^{(n)}, \tag{3.73}$$

and by default fully implicit treatment ($\gamma = 1$) is adopted, which assures fast convergence in nonlinear iterations.

Solution

Numerical scheme adopted to solve Eqs. (3.50)–(3.53), is based on the original radiative version of the code (STELLINGWERF 1975a). Multivariate Newton-Rhapson method is used to solve Eqs. (3.50), (3.51) and (3.52). The concise form of the linear iteration equations is following,

$$
\begin{pmatrix}
\frac{\partial \tilde{\mathcal{M}}_0}{\partial r_0} & \frac{\partial \tilde{\mathcal{M}}_0}{\partial T_1} & \frac{\partial \tilde{\mathcal{M}}_0}{\partial \varpi_1} & \frac{\partial \tilde{\mathcal{M}}_0}{\partial r_1} & \frac{\partial \tilde{\mathcal{M}}_0}{\partial T_2} & \cdots \\
\frac{\partial \tilde{\mathcal{E}}_1}{\partial r_0} & \frac{\partial \tilde{\mathcal{E}}_1}{\partial T_1} & \frac{\partial \tilde{\mathcal{E}}_1}{\partial \varpi_1} & \frac{\partial \tilde{\mathcal{E}}_1}{\partial r_1} & \frac{\partial \tilde{\mathcal{E}}_1}{\partial T_2} & \cdots \\
\frac{\partial \tilde{\mathcal{Z}}_1}{\partial r_0} & \frac{\partial \tilde{\mathcal{Z}}_1}{\partial T_1} & \frac{\partial \tilde{\mathcal{Z}}_1}{\partial \varpi_1} & \frac{\partial \tilde{\mathcal{Z}}_1}{\partial r_1} & \frac{\partial \tilde{\mathcal{Z}}_1}{\partial T_2} & \cdots \\
\frac{\partial \tilde{\mathcal{M}}_1}{\partial r_0} & \frac{\partial \tilde{\mathcal{M}}_1}{\partial T_1} & \frac{\partial \tilde{\mathcal{M}}_1}{\partial \varpi_1} & \frac{\partial \tilde{\mathcal{M}}_1}{\partial r_1} & \frac{\partial \tilde{\mathcal{M}}_1}{\partial T_2} & \cdots \\
\frac{\partial \tilde{\mathcal{E}}_2}{\partial r_0} & \frac{\partial \tilde{\mathcal{E}}_2}{\partial T_1} & \frac{\partial \tilde{\mathcal{E}}_2}{\partial \varpi_1} & \frac{\partial \tilde{\mathcal{E}}_2}{\partial r_1} & \frac{\partial \tilde{\mathcal{E}}_2}{\partial T_2} & \cdots \\
\cdots & \cdots & \cdots & \cdots & \cdots &
\end{pmatrix}
\begin{pmatrix}
\delta r_0 \\
\delta T_1 \\
\delta \varpi_1 \\
\delta r_1 \\
\delta T_2 \\
\cdots
\end{pmatrix}
= -
\begin{pmatrix}
\tilde{\mathcal{M}}_0 \\
\tilde{\mathcal{E}}_1 \\
\tilde{\mathcal{Z}}_1 \\
\tilde{\mathcal{M}}_1 \\
\tilde{\mathcal{E}}_2 \\
\cdots
\end{pmatrix},
\qquad (3.74)
$$

where $\tilde{\mathcal{M}}$, $\tilde{\mathcal{E}}$ and $\tilde{\mathcal{Z}}$ are left hand sides of Eqs. (3.50), (3.51) and (3.52), respectively. The matrix on the left hand side is band matrix of bandwidth 13 and dimension $3N + 1$, as inner boundary condition is implemented in the first equation. The system is solved using either LAPACK procedures (DGBTRF+DGBTRS, ANDERSON *et al.* 1999), or LINPACK procedures (DGBFA+DGBSL, DONGARRA *et al.* 1979). The former are adopted by default, as they are significantly faster.

Temperatures, radii and turbulent energies at time step (n) (time t) provide initial guess, and values at time step $(n + 1)$ $(t + DT)$ are iterated. To avoid convergence problems, emerging corrections need to be limited by undercorrection factor, just as in radiative case (*see e.g.*, STELLINGWERF 1975a). Velocities are derived during the iterations through Eq. (3.53), rewritten in the following form (Eq. 3.63 is also used),

$$
u_i^{(n+1)} = -u_i^{(n)} + \frac{2}{DT}\left(r_i^{(n+1)} - r_i^{(n)}\right). \qquad (3.75)
$$

At the beginning of the computations $(t = 0)$ the static model, as computed by the model builder, is initialized with arbitrary velocity profile. For this purpose a scaled LNA radius eigenvector of a given mode, or a superposition of eigenvectors corresponding to different modes, is used. Constant time step, corresponding to 600 steps per pulsation cycle, is adopted by default. Iterations are treated as converged if relative corrections, $\delta T_i/T_i$ and $\delta \varpi_i/\varpi_i$, are smaller than 10^{-6} in all model zones. If convergence is not achieved in less than 60 iterations, computations are restarted with halved time step. Model integration proceed for a given number of pulsation cycles, and can be restarted later on from continuation file.

3.3.4   Material properties

All the codes described in this Chapter, model builder, LNA code and nonlinear hydrocode, use exactly the same equation of state (EOS) and opacity subroutines.

By default, analytical EOS described in the Appendix of STELLINGWERF (1982a) is used. In this EOS, equilibrium mixture of H, H^+, He, He^+, He^{++}, M and M^+ is considered. M stands for fictional metal with ionization potential of 7.6eV, used to model the ionization of heavier elements. The input variables for this EOS are

temperature and specific volume, which is very convenient, as also opacities are usually computed as a function of these variables. EOS returns the values of energy and pressure (gas+radiation), as well as all thermodynamic derivatives (first and second order) necessary in the described numerical schemes (c_p, c_V, Q, derivatives of pressure and energy with respect to temperature and volume).

The analytical EOS is very simple and consequently very fast, which makes it suitable in nonlinear computations. Still, it is sufficiently accurate and leads to qualitatively the same results, as obtained with more sophisticated tabular EOS of the OPAL group (EOS2001, ROGERS 2000). This was checked numerically. The tabular OPAL EOS was implemented into the codes as an option. The original subroutines from the OPAL web page, were slightly modified by the author. Original table interpolation scheme was changed and made suitable for envelope computations (fixed chemical composition). In the modified procedures, external code generates a single table for given X and Z (instead of a table for given Z, only). This table is interpolated by the modified OPAL procedures implemented directly into hydrodynamical codes, and supplemented with driver subroutines yielding the relevant quantities and derivatives as a function of T and V. The comparison between simple analytical EOS and tabular OPAL EOS was performed for several sequences of models. Almost the same results were obtained, concerning both linear and nonlinear results. Here, just for example, results for one particular Cepheid model are briefly summarized. The model is characterized by $M = 4.5 M_\odot$, $L = 1143.40 L_\odot$, $T = 5793.6 K$, $X = 0.7$ and $Z = 0.02$. This model will be extensively described in the next Chapter, and more details are given there. Table 3.1 provides the periods and linear growth rates for three pulsation modes, computed with analytical and tabular EOS. Results are almost the same. In Figure 4.3, in the next Chapter, thin blue lines correspond to quantities (∇_a, $\mathcal{Y}$, F_c, F_t and e_t) computed with the tabular EOS (black lines are computed with analytical EOS). Again, very similar results are obtained with both EOS. Black and blue lines almost overlap, differences being barely visible. This fully justifies the use of analytical EOS, which is by more than 40 per cent faster than the tabular EOS in typical model computations.

Quantity	analytical EOS	tabular EOS
P_0 [d]	3.6884	3.6981
P_1 [d]	2.5724	2.5791
P_2 [d]	1.9976	2.0011
γ_0	$0.505 \cdot 10^{-2}$	$0.513 \cdot 10^{-2}$
γ_1	$0.144 \cdot 10^{-1}$	$0.131 \cdot 10^{-1}$
γ_2	$-0.408 \cdot 10^{-1}$	$-0.429 \cdot 10^{-1}$

Table 3.1: Linear periods and growth rates for the three consecutive pulsation modes, computed with analytical and tabular EOS.

To compute the opacity and opacity derivatives, subroutines used in Warsaw-New Jersey stellar evolutionary code (*e.g.*, PAMYATNYKH 1999) are adopted[1]. The external program is used to compute the opacity tables for a given composition,

---

[1]The codes are kept up-to-date by A.A. Pamyatnykh, who kindly provides the most recent version to the author

X and Z, and for a given chemical mixture. Then, numerical procedure incorporated in the hydrocodes, interpolates the opacity and opacity derivatives for a given temperature and specific volume.

Chapter 4

Tests of the Code

In this Chapter, I present some basic tests of the described convective hydrocodes. They concern modeling of fundamental (Section 4.1), as well as first overtone (Section 4.2) Cepheids. Described tests show how model builder, LNA code, and nonlinear hydrocode work. Results prove that the computed models are reliable and numerically robust. The tests provide a background for further discussion concerning the double-mode phenomenon, as the same sets of convective parameters as adopted in this Chapter, will also be adopted in the following Chapters.

Considering the scientific results, in Section 4.1 I display the Fourier progression for radial velocity curves of fundamental mode Cepheid models and compare them with observations. Although plenty of such models were computed by Italian group (*e.g.*, BONO, MARCONI & STELLINGWERF 2000), no quantitative comparison with observations was done. In Section 4.2, I show the Fourier progression for radial velocity curves of first overtone Cepheid models. The focus in these computations was to reproduce the longest observed period for overtone Galactic Cepheid, 7.57 d (V440 Persei). These models, computed by myself, are described in the paper of BARANOWSKI *et al.* (2009), and impose interesting constraints on convective parameters entering the model.

Some convective models of β Cephei stars were also computed with the described codes (SMOLEC & MOSKALIK 2007), however, details and results will not be given in this thesis.

4.1 Fundamental mode Cepheid models

Computations presented in this Section were done for test purposes, and were not intended for detailed modeling of real stars. In particular, convective parameters entering the model, were not tuned to match all observational constraints. Two sets of convective parameters discussed in this Section are given in Table 4.1. Set A represents the simplest convective model, without turbulent pressure, turbulent flux and radiative losses ($\alpha_p = \alpha_t = \gamma_r = 0$). In set B effects of turbulent pressure and turbulent flux are turned on[1]. Table 4.1 provides also parameters of set C including radiative losses, that will be discussed in the next Section.

---

[1] These two effects are usually studied together, for stability reasons. If turbulent pressure is turned on without turbulent flux, convergence difficulties are encountered in nonlinear integrations. This was also noted for red giant models by OLIVIER & WOOD (2005).

Set	α	α_m	α_s	α_c	α_d	α_p	α_t	γ_r
A	1.5	0.20	1.0	1.0	1.0	0.0	0.0	0.0
B	1.5	0.25	1.0	1.0	1.0	1.0	0.01	0.0
C	1.5	0.50	1.0	1.0	1.0	0.0	0.0	1.0

Table 4.1: Three sets of convective parameters considered in this and in following Chapters. Parameters α_s, α_c, α_d, α_p and γ_r are given in the units of standard values (*see* Table 2.1).

All models described in this Section are characterized by Galactic chemical composition, $X = 0.7$, $Z = 0.02$. OPAL opacities are used (IGLESIAS & ROGERS 1996), at the low temperatures supplemented with the ALEXANDER & FERGUSSON (1994) opacity data. Opacities were generated for the solar mixture of GREVESSE & NOELS (1993). Model parameters are constrained by the $M - L$ relation given by SZABÓ *et al.* (2007), $\log(L/\mathrm{L}_\odot) = 3.56 \log(M/\mathrm{M}_\odot) + 0.7328$.

The mesh parameters are, total number of zones, $N = 150$, anchor location, $N_\mathrm{a} = 50$, inner boundary temperature, $T_\mathrm{in} = 2.5 \cdot 10^6 \,\mathrm{K}$. For the temperature in the anchor zone different values were used for models of set A and B. For models of set A, $T_\mathrm{a} = 11000 \,\mathrm{K}$ was adopted, just as in radiative computations. However, for models of set B, higher temperature is necessary, $T_\mathrm{a} = 15000 \,\mathrm{K}$, to assure smooth behaviour of mode growth rates along a sequence of models. With lower temperature in the anchor zone, growth rates are not smooth, which is numerical effect, resulting from poor spatial resolution. In test computations with dense mesh ($N = 300$), growth rates are smooth independently of T_a value (provided it is reasonable). The problem appears for models in which turbulent pressure is included, and hence, for all such models considered later on in this thesis, higher anchor temperature is adopted.

Instability strips computed for models of both sets of convective parameters are depicted in Figure 4.1, in which the theoretical HR diagrams are presented. The overall structure of the instability strips computed for sets A and B is very similar. In case of set A, instability strips (both F and 1O) are slightly narrower than in case of set B, and are shifted by $\approx 200 \,\mathrm{K}$ toward higher temperatures. For the fundamental mode, width of the IS at $\log(L/\mathrm{L}_\odot) = 3.0$ is equal to $\approx 830 \,\mathrm{K}$ for set A, and $\approx 1020 \,\mathrm{K}$ for set B. In case of set A instability strip for the first overtone extends toward slightly higher luminosities. In both cases, the 2:1 resonance between the fundamental and second overtone crosses the instability strip at periods slightly lower than 10 days indicated by observations (*see* later on in this Section).

For detailed discussion of static and full amplitude model properties, one model of set B was picked. Its mass is $4.5\mathrm{M}_\odot$, and it lays $300 \,\mathrm{K}$ away from blue edge of the fundamental mode IS. Its location is shown with black circle in the right panel of Figure 4.1. The model is unstable in the fundamental and in the first overtone. Higher order overtones are stable. Linear nonadiabatic period of the fundamental mode is $\approx 3.69^\mathrm{d}$ (*see* second column of Table 3.1 for exact values of LNA periods and growth rates for this model).

Static model structure is depicted in Figures 4.2 and 4.3. Upper panel of Figure 4.2 demonstrates the envelope mesh structure. The outermost part of the envelope, above the anchor, consists of 50 zones of equal mass. It contains very little
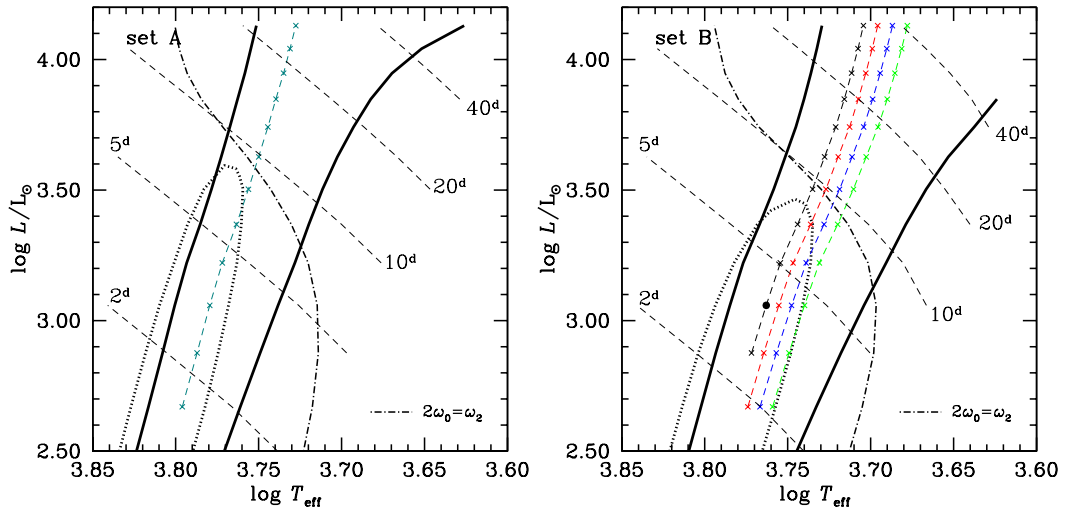
Figure 4.1: Instability strips in the theoretical HR diagram, computed for convective parameters of set A (left panel) and B (right). Solid and dotted black lines limit the fundamental mode and first overtone instability strips, respectively. Dashed black lines correspond to constant fundamental mode periods indicated in the Figures. Dash-dotted lines show the center of the 2:1 resonance shaping the Hertzsprung bump progression ($2\omega_0 = \omega_2$). Coloured lines show the location of nonlinear model sequences described in this Section and displayed in Figures 4.10 and 4.11.

mass, as compared to total stellar mass ($\approx 5 \cdot 10^{-5} M$), and extends over slightly less than 1 per cent of the stellar radius. Cepheids are giant stars, characterized by high central mass concentration. Indeed, the whole envelope under discussion contains ≈ 23 per cent of the total mass extending along 86 per cent of the total radius. The run of basic thermodynamic variables, temperature, pressure and specific volume (density), is plotted in the lower panel of Figure 4.2 Temperature decrease monotonically toward the outer model layers. Pressure decreases in the inner most layers, then, just above the anchor is stays roughly constant for more than 20 mass zones, and drops off fast close to the surface. Specific volume increase outward the model, except the hydrogen partial ionization region (above the anchor zone), where density inversion is observed.

In Figure 4.3 the crucial variables determining the convective structure of the model and model stability, are plotted *versus* the zone temperatures. Zone scale is provided at the top axis for reference. Upper panel shows the run of opacity, $\log \kappa$, and opacity derivative, $\kappa_T = (\partial \log \kappa / \partial \log T)_V$. Three opacity bumps are clearly visible. The innermost bump (Z bump, iron bump) is produced by fine-structure transitions in iron-group elements. It is located at $\log T \approx 5.3$. Helium (He) and hydrogen (H) opacity bumps are connected with partial ionization regions. They are located closer to the surface, at $\log T \approx 4.65$ and $\log T \approx 4.05$, respectively. Each opacity bump is connected with the bump in the run of opacity derivative, which is crucial for determining the driving properties of the model zones (*see* discussion of the work integrals in the following). Convective zones of the model develop in the outermost regions of the envelope, in the hydrogen-helium partial ionization regions.
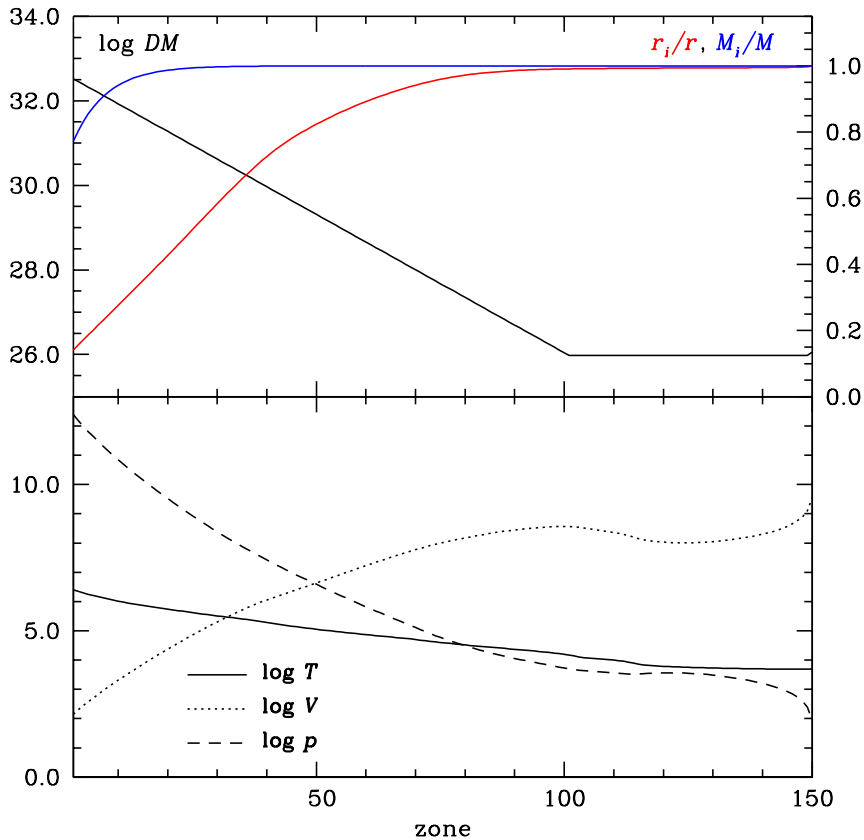
Figure 4.2: Structure of the static mesh for $4.5 M_\odot$ model of set B, discussed in the text. In the upper panel the fractional mass (blue line), fractional radius (red line) and logarithm of the zone mass (black line) are plotted *versus* the zone number. In the lower panel, logarithms of basic thermodynamic variables, temperature, specific volume and pressure (solid, dotted and dashed lines, respectively) are plotted.

These are best visible in the plot of the adiabatic gradient presented in the middle panel of Figure 4.3. PIRs are accompanied by minima of the adiabatic gradient. Red vertical bars, close to the minima of ∇_a, show the locations at which ionization fraction of the relevant element is equal to 0.5. Hydrogen and both helium PIRs are clearly resolved with the described mesh. Convective stability of a particular zone is determined by the value of superadiabatic gradient, $\mathcal{Y} = \nabla - \nabla_a$, which is also displayed in the middle panel of Figure 4.3. Zones in which $\mathcal{Y} > 0$ are convectively unstable. The lower panel of the discussed Figure displays the profiles of turbulent energy and convective and turbulent fluxes. Two convective zones, separated by small radiative region, are clearly visible. The outer convective zone is connected with the combined hydrogen and first helium ionization zones (hydrogen-helium convective zone in the following). At the center of this zone more than 90 per cent of the total flux is carried by convection. Slightly below, less pronounced second convective zone, is visible (helium convective zone in the following). Only up to 20 per cent of the total flux is carried by convection in this zone. Also turbulent

energies are smaller than in the hydrogen-helium zone. Turbulent flux is always very small. In the discussed model, it carries less than 0.3 per cent of the total flux. It is negative if turbulent energy increases outward, and positive in the reverse case. Physically, turbulent flux smears the turbulent energy profile, and in the discussed convection model it is the sole cause of the overshooting of the convective eddies into convectively stable zones. Indeed, turbulent energy does not vanish in convectively stable regions, although the extent of overshooting is very small, and the effect is barely visible in Figure 4.3. Note also, that thin blue lines in this Figure correspond to model computations with sophisticated tabular EOS instead of simple analytical EOS used by default. As already discussed in Section 3.3.4, lines corresponding to different EOS almost overlap, justifying the choice of fast analytical EOS.

In Figure 4.4 linear differential work integral (or work per zone) and linear work integral for the fundamental mode of the discussed model are presented. Work integrals are plotted *versus* the zone number to allow further comparison with nonlinear work integrals. In the upper frame of this Figure, the run of opacity and opacity derivatives, copied from Figure 4.3, is plotted for reference. Computed work integrals are normalized by the kinetic energy of the fundamental mode. Hence, the total work at the surface is equal to the growth rate of the mode, and is positive in the discussed case. Cepheid pulsations are driven through the κ mechanism (Section 1.1), which is purely radiative. The envelope region in which specific combination of opacity derivatives, of which κ_T plays a decisive role, increases outward, contributes to the driving of pulsations (*see e.g.*, DZIEMBOWSKI 1994 or PAMYATNYKH 1999 for the detailed discussion of the κ mechanism). Hence, with each opacity bump, the driving region is connected. In the innermost zones of the discussed model, a small driving region connected with the Z bump is visible (around zone 42, $\log T \approx 5.25$). However, through the most of the inner parts of the envelope pulsations are damped. The main driving regions are connected with the hydrogen-helium opacity bumps, located close to the surface. Driving in these regions exceed the internal radiative damping (lower panel of Figure 4.4), and hence, the model is pulsationaly unstable. In comparison to radiative models (*see* work integrals in *e.g.*, BUCHLER 1990), the local driving connected with the hydrogen opacity bump (around zone 100, $\log T \approx 4.15$) is much less pronounced. In this region most of the flux is carried by convection (Figure 4.3) and consequently, κ mechanism is not effective. Close to the red edge, when almost whole energy transfer is due to convection, κ mechanism is quenched and so are pulsations. Considering eddy-viscous work, it always contributes to the damping of pulsations. As discussed in Section 2.4, eddy-viscous terms build up the turbulent energies at the cost of kinetic energy of pulsations. Turbulent pressure work can contribute to driving as well as to damping of pulsations, depending on the relative phase between the turbulent energy and density perturbations. For the discussed model its overall contribution is neutral.

Linear computations tell nothing about final pulsation state, its amplitude, light/radial velocity curves and mode selected (if more than one are linearly unstable). To study these problems, nonlinear computations have to be conducted. However, linear properties of the model, particularly period ratios indicating the possible proximity to the resonances, are useful in interpreting the nonlinear results. Therefore, it is important to assure that linear and nonlinear codes are consistent with each other. For this reason, all the codes described in the previous Chapter use
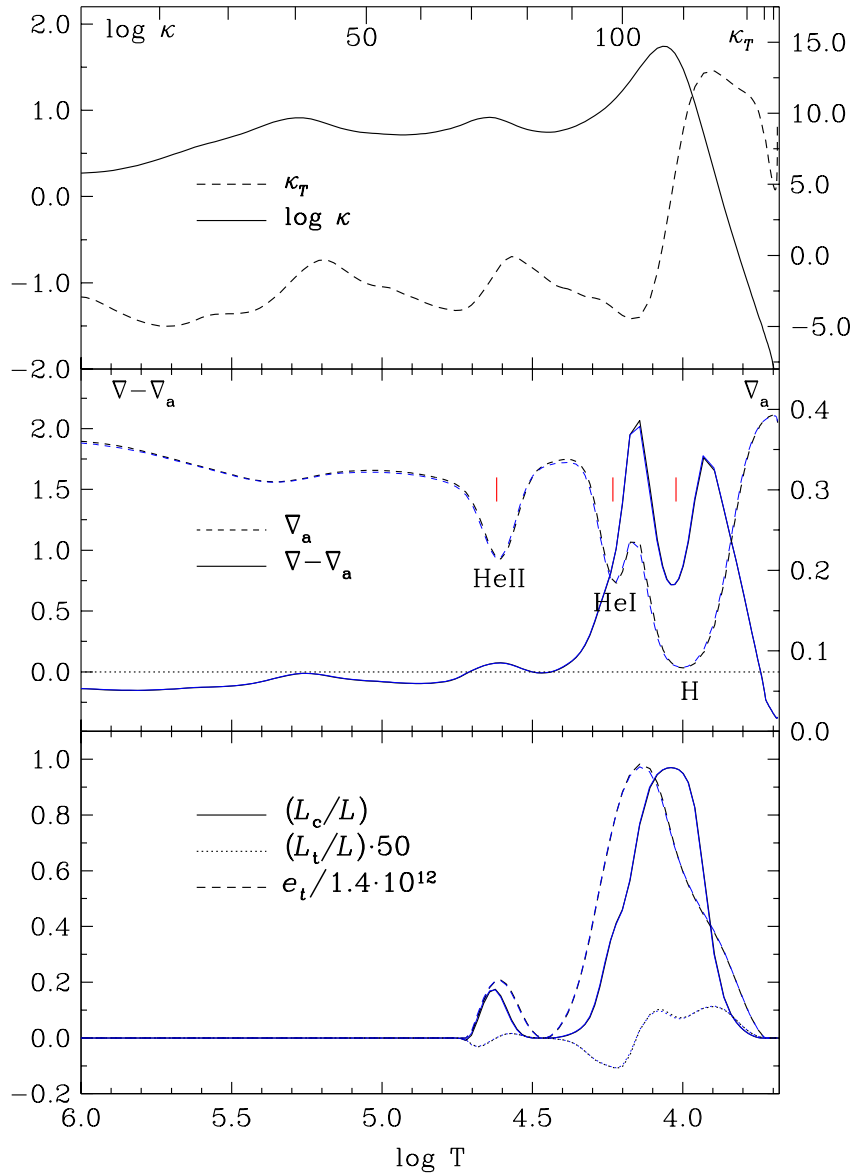
Figure 4.3: Static structure for 4.5M$_\odot$ model of set B, discussed in the text. All variables are plotted against the zone temperatures (the zone number scale is also provided at the top axis). In the upper panel logarithm of the opacity (solid line, left scale) and opacity derivative, κ_T (dashed line, right scale) are plotted. In the middle panel adiabatic, ∇_a, and superadiabatic, $\mathcal{Y} = \nabla - \nabla_a$, gradients are plotted. Minima of ∇_a connected with PIRs are labeled. In addition, red vertical lines mark the locations at which ionization fraction of the relevant element is equal to 0.5. In the bottom panel, relative convective and turbulent fluxes are plotted, together with scaled turbulent energy profile. Thin blue lines correspond to model computed with tabular OPAL EOS (*see* Section 3.3.4 for details).
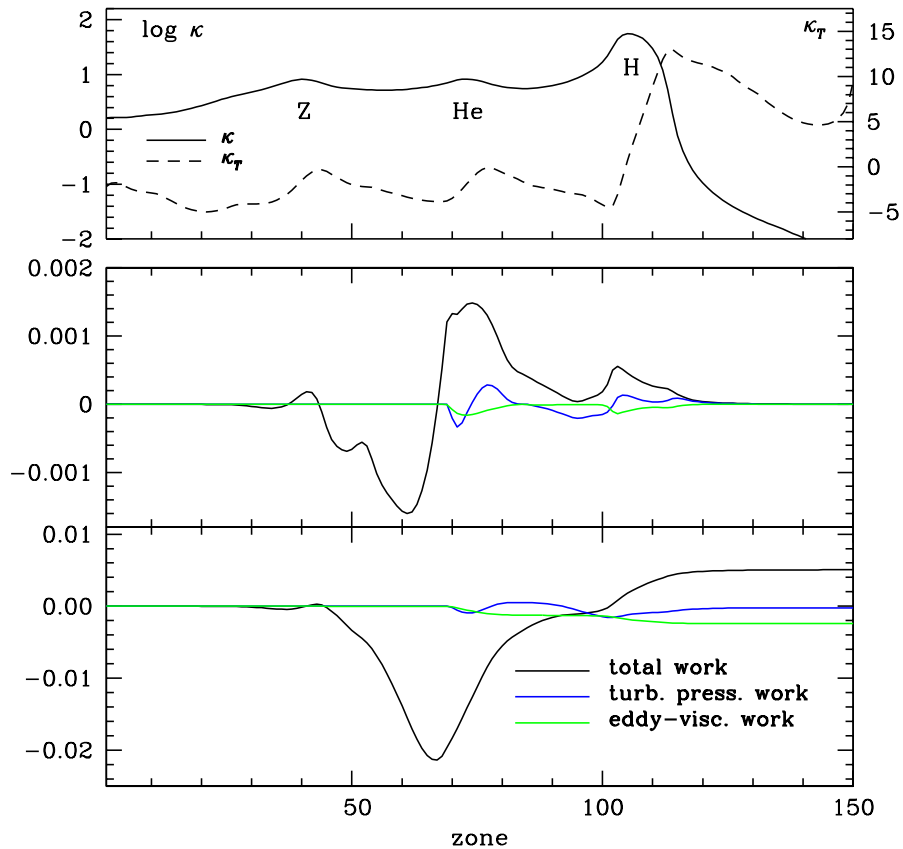
Figure 4.4: Linear differential work integral (middle panel) and linear work integral (bottom panel) *versus* the zone number, for the fundamental mode of $4.5\mathrm{M}_\odot$ model of set B, discussed in the text. In the upper panel variation of opacity and opacity derivative copied from Figure 4.3 is presented.

the same numerical mesh, EOS/opacity subroutines and numerical representation of all the quantities entering the model. In practice, consistency can be checked, by comparing nonlinear periods and nonlinear growth rates, computed at small amplitude pulsations, with linear periods and linear growth rates. Such comparison was conducted for the fundamental mode models of sets A and B, running parallel to the fundamental mode blue edge. Nonlinear computations were initialized with linear velocity eigenvector scaled to surface velocity equal to $0.1\,\mathrm{km/s}$. Nonlinear periods were derived through the simple Fourier transform. Relative difference between nonlinear and linear periods is always smaller than 10^{-4}. Nonlinear growth rates, γ_n, were computed, as the average total envelope work over several initial pulsation cycles. Such determination suffers from unclean initialization – in addition to the desired mode, also high order, strongly damped parasite modes are present at the initial phase of model integration. Nevertheless, for both sequences of models adopting convective parameters of set A and B, the agreement between linear and nonlinear growth rates is satisfactory as is presented in Figure 4.5. Relative difference between the growth rates is usually smaller than 5 per cent.
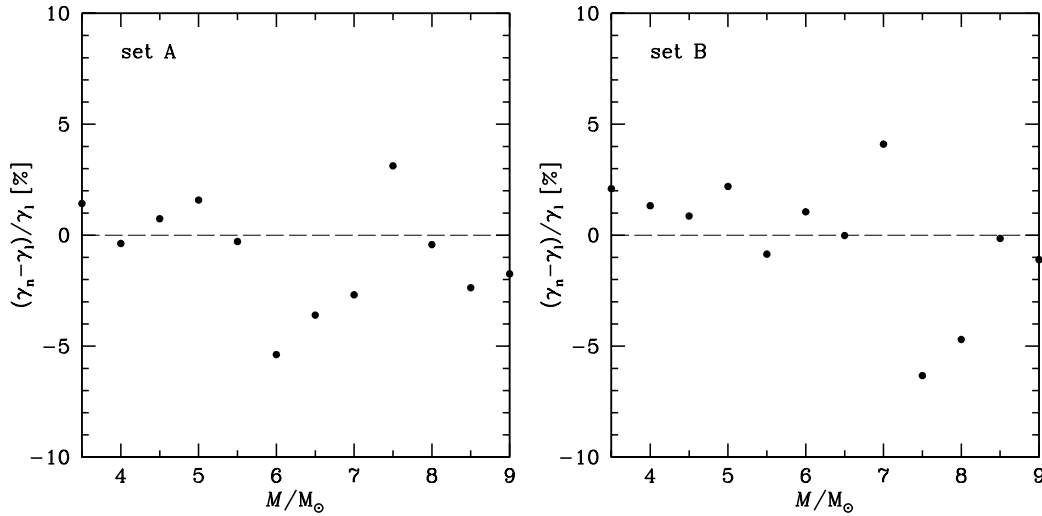
Figure 4.5: Relative difference between nonlinear, γ_n, and linear, γ_l, growth rates of the fundamental mode for the sequence of convective models of set A (left panel) and B (right panel). Models run parallel to the blue edge of the fundamental mode instability strip, 300 K apart from it.

Before discussing the overall properties of the nonlinear model sequences, I provide more detailed discussion of the $4.5 M_\odot$ model under discussion in this Section. Its full amplitude light and radial velocity curves are plotted in blue in Figure 4.9.

In Figure 4.6 nonlinear work integrals are plotted (*see* Appendix A). This Figure should be compared with the linear counterpart, Figure 4.4. Note, that the total work at the surface is equal to zero. This indicates that the model approached the limit cycle, and that pulsation instability is saturated. In comparison to linear work integrals two differences are clearly visible. First, the sharp features visible in the linear work integrals are widened, being smeared by the motion of ionization fronts through the Lagrangian zones of the model. Second, the eddy-viscous damping is much stronger in the nonlinear case. In fact, eddy-viscous terms can be used to control the model amplitude, through the adjustment of α_m parameter. Eddy viscosity provides physical source of dissipation in the model, which is lacking in radiative models, were artificial viscosity has to be used.

Time-dependent convective structure of the model during one cycle of full amplitude pulsation is presented in Figures 4.7 and 4.8. In Figure 4.7 profiles of turbulent energy are plotted. The two panels highlight internal and external parts of the model. Internal parts of the model, below zone 70, are convectively stable. Turbulent energies are extremely small, smaller than 10^{-10} erg/g. They are nonzero because of the correction term described in Section 3.3.3 (Eq. 3.59). Such small energies are completely negligible from physical point of view, however, they are numerically necessary, as they allow to built up convective zone if convective instability arises. At the center of convective zones, turbulent energies are of order of 10^{13} erg/g and span from 30 to more than 70 model zones (during the compression phase). Displayed profiles are smooth. Subtle differences in the level of turbulent energy in the hydrogen-helium and helium convective zones are clearly visible. These
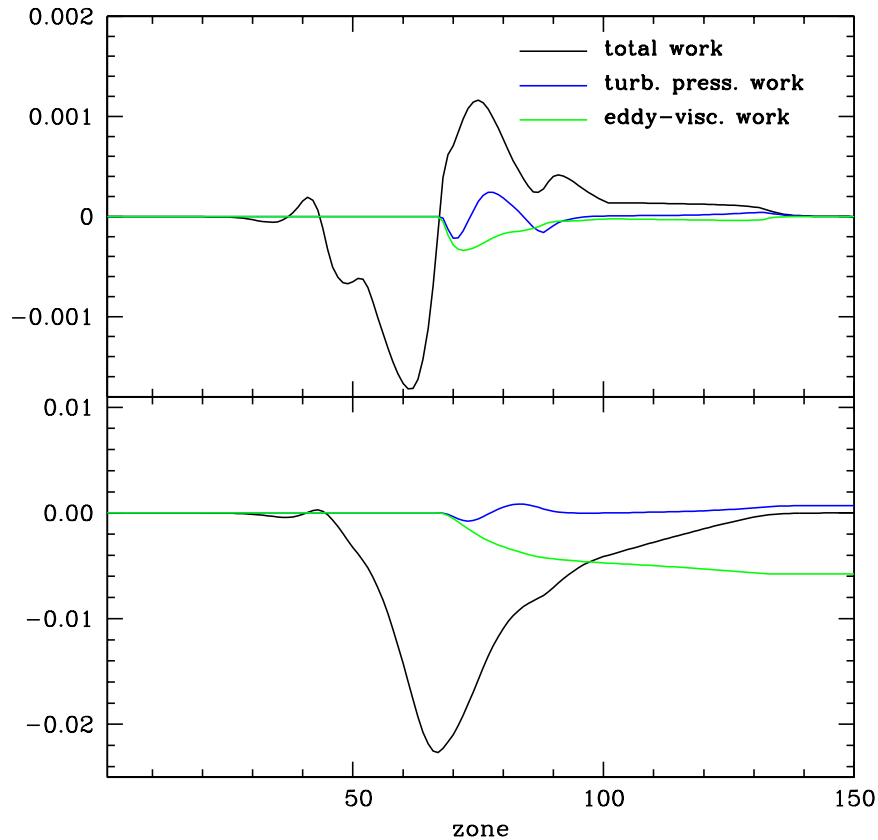
Figure 4.6: Nonlinear differential work integral (upper panel) and work integral (lower panel) *versus* the zone number, for the fundamental mode, full amplitude pulsation of $4.5M_\odot$ model of set B, discussed in the text.

two zones merge at pulsation phase ≈ 0.5.

In Figures 4.8 the profiles of convective, radiative and turbulent fluxes are plotted as two dimensional maps, with the relative contribution of a particular flux coded with colours. Structure and time evolution of convective zones are clearly visible. Two convective zones are present in the model. In the deeper, helium convective zone, up to 40 per cent of the total flux (during compression phase) is carried by convection. This zone is thin and almost merges with the hydrogen-helium zone at the maximum compression (phase 0.5). In hydrogen-helium convective zone almost entire energy transport is due to convection. This zone sweeps through the Lagrangian zones of the model, entering the sub-surface zones at the phase of maximum compression, and extending over more than 50 model zones at that time. During the expansion phase, convective zone shrinks, moving inward the model. At pulsation phases between 0.6 and 0.8, the outer convective zone is barely resolved. The picture for radiative flux (middle panel of Figure 4.8) is reversed. Turbulent flux plays a minor role in the energy transfer. Numerically, its computation requires high spatial resolution as it contains the gradient of rapidly varying turbulent energy. As is well visible in the bottom panel and in the whole Figure 4.8, adopted mesh and
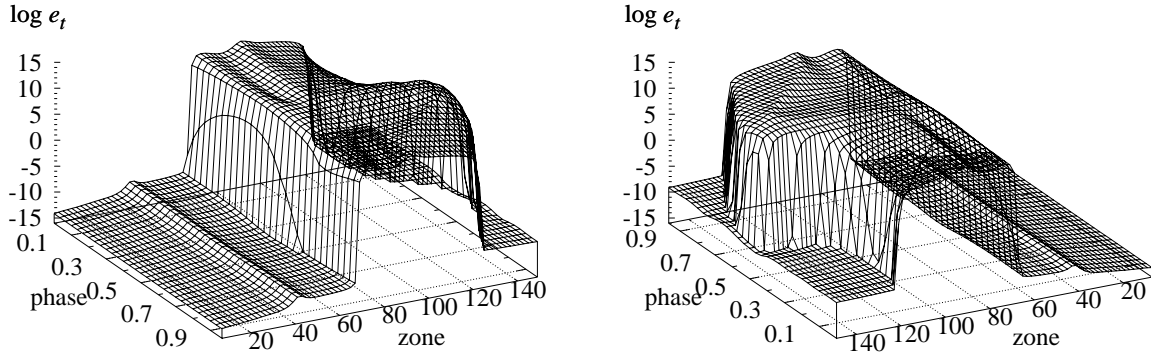
Figure 4.7: Turbulent energy profiles during one pulsation cycle, for the fundamental mode, full amplitude pulsation of $4.5 M_{\odot}$ model of set B discussed in the text. Two panels highlight the internal (left) and external (right) parts of the model.

time step assure smooth spatial and temporal variation of the model quantities.

Now, I will briefly describe the overall properties of nonlinear model sequences. Fundamental mode light and radial velocity curves were computed for all models marked with crosses in Figure 4.1, located at constant distance, ΔT, from the blue edge of the fundamental mode instability strip. For set A one sequence of models with $\Delta T = 300\,\mathrm{K}$ was computed, while for set B four sequences located at $\Delta T = 300\,\mathrm{K}$, $400\,\mathrm{K}$, $500\,\mathrm{K}$ and $600\,\mathrm{K}$ were computed. In Figure 4.9 individual light and radial velocity curves for model sequence of set B and $\Delta T = 300\,\mathrm{K}$ are plotted. Curves are labeled with fundamental mode period and P_2/P_0 period ratio, characterizing the proximity to the $2\omega_0 = \omega_2$ resonance center. As described in Section 1.4.2, this resonance shapes the Hertzsprung bump progression. The progression is best visible for radial velocity curves. Starting from short periods, the bump first appears on the descending branch, and then, as period ratio decreases, it moves toward the ascending branch. At periods around 10 days the bump appears as a double-peaked maximum in the velocity curves, and single more or less symmetric maximum in the bolometric light curves. Displayed radial velocity curves are smooth. In case of bolometric light curves, a series of wiggles appears on the descending branch. This is connected with the just described poor spatial resolution in the thin hydrogen-helium convective zone moving inward the model at the end of the expansion phase.

Quantitative comparison between computed radial velocity curves and observations is provided in Figures 4.10 and 4.11, in which low order Fourier decomposition parameters of radial velocity curves are plotted. In Figure 4.10 the run of amplitude, A_1 (scaled by constant projection factor, 1.4), amplitude ratio, R_{21}, and Fourier phase, φ_{21}, is shown for four model sequences of set B, located at different distances from the fundamental mode blue edge. The Fourier bump progression is clearly reflected by theoretical models. At around 10 days, amplitudes are significantly lower, as parasite second overtone is resonantly excited at the cost of the
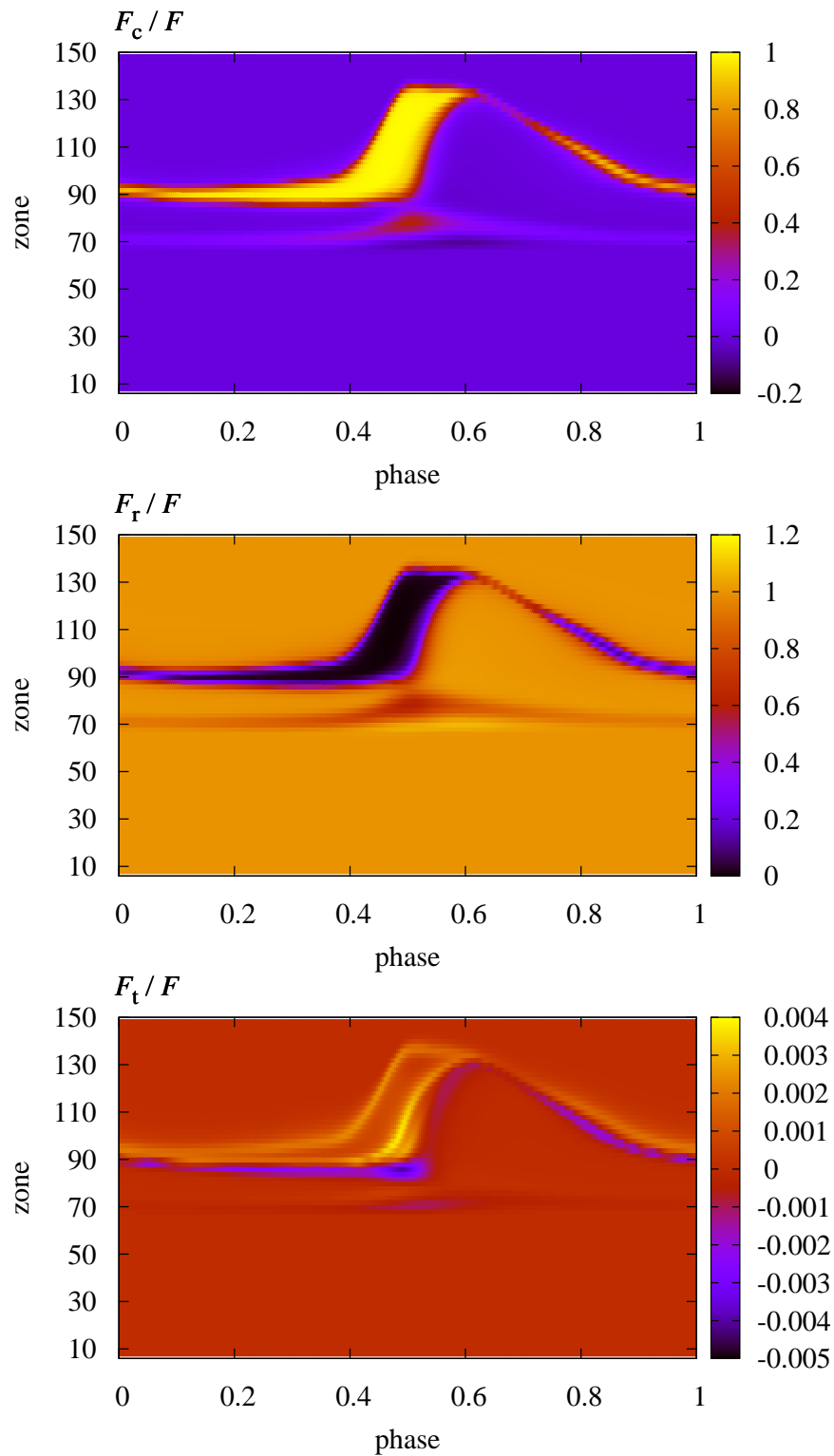
Figure 4.8: Convective, radiative and turbulent flux profiles during one pulsation cycle, for the fundamental mode, full amplitude pulsation of $4.5 M_\odot$ model of set B discussed in the text. Relative contribution of the fluxes to the total energy transfer is colour coded.
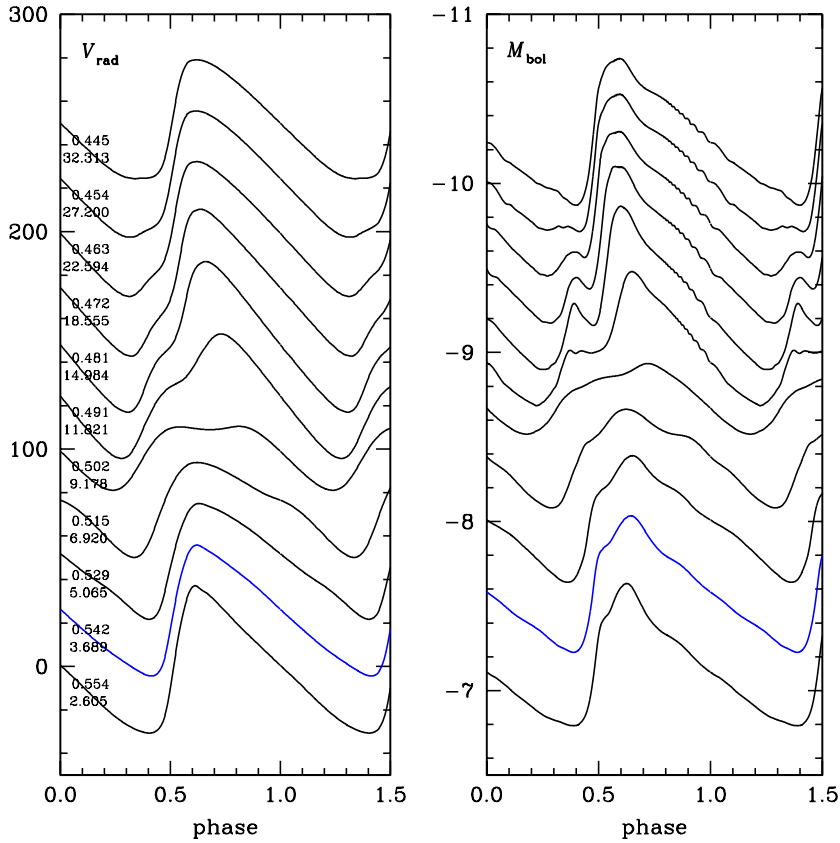
Figure 4.9: Individual bolometric light (right panel) and radial velocity (left panel) curves for models of set B, running parallel to the fundamental mode blue edge ($\Delta T = 300$ K). Model masses increase from $4\mathrm{M}_\odot$, at the bottom of the Figure, up to $9\mathrm{M}_\odot$ at the top with $0.5\mathrm{M}_\odot$ step. Consecutive radial velocity curves are shifted by 25 km/s to allow comparison. Curves are labeled with linear fundamental mode period, P_0, and linear period ratio, P_2/P_0.

fundamental mode. Connected drop in the amplitude ratio is well visible. Models also reproduce the characteristic bell-shape progression of φ_{21} also caused by the $2\omega_0 = \omega_2$ resonance.

Despite the fact that the convective parameters entering the model were not adjusted to match the observational constraints, the overall agreement between models and observations is satisfactory. Probably the most severe problem concerns the R_{21} ratio. Models do not reproduce the sharp increase of R_{21} for periods below 10 days. The φ_{21} progression is reproduced very well. Model curves are shifted toward slightly shorter periods as compared to observations, which can be easily explained. The characteristic run of φ_{21} is connected with the location of the $2\omega_0 = \omega_2$ resonance center, which falls at around 10 days, as indicated by observations. Numerically, location of the resonance center depends mostly on the adopted mass-luminosity relation, metallicity and, to a lesser extend, on the adopted convective parameters. As is visible in Figure 4.1, for the adopted $M-L$ relation and convective parameters
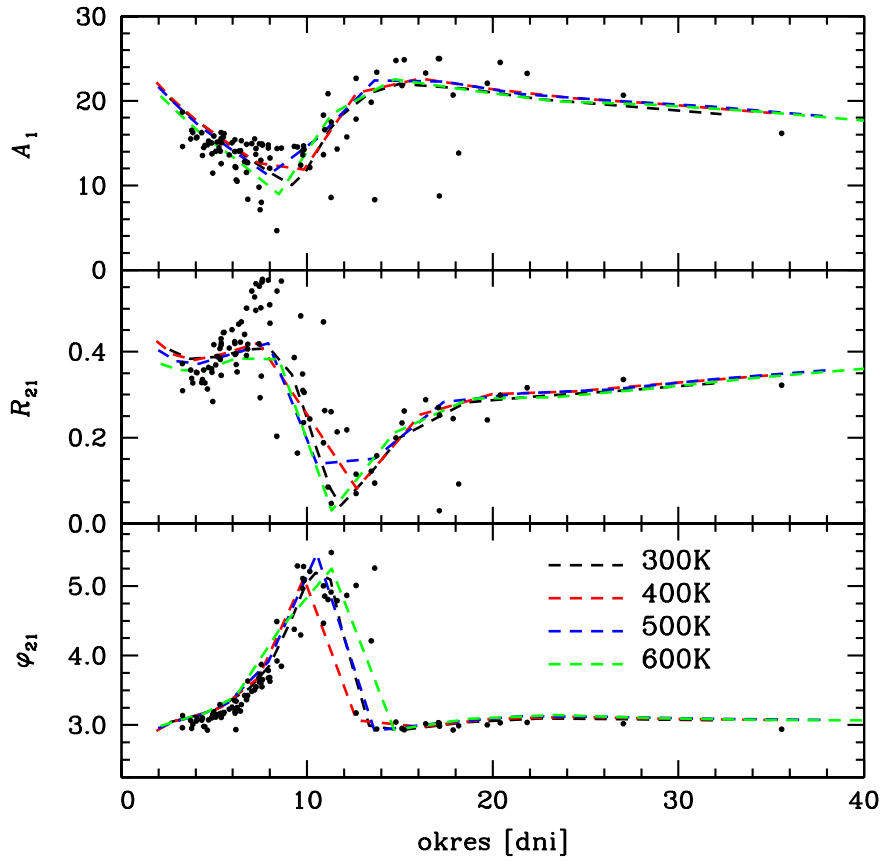
Figure 4.10: Fourier decomposition parameters of radial velocity curves for fundamental mode Cepheid models of set B, running parallel to the fundamental mode blue edge at distances, $\Delta T = 300\,\mathrm{K}$, $400\,\mathrm{K}$, $500\,\mathrm{K}$ and $600\,\mathrm{K}$. Model locations in the HR diagram are shown in the right panel of Figure 4.1 with dashed lines of the same colours. Amplitudes are scaled by constant projection factor equal 1.4. Individual curves for model sequence located at $\Delta T = 300\,\mathrm{K}$ are plotted in Figure 4.9. Dots represent observational data (*see* Figure 1.4 for references).

of set B, resonance center crosses the fundamental mode instability strip for periods lower than 10 days, which explains the shift.

In Figure 4.11 Fourier decomposition parameters of radial velocity curves for models of sets A and B (and also C, *see* Section 4.3) are compared. Despite rather dramatic change in the convective parameters (*cf.* Table 4.1), overall progressions are very similar for both sets. Model progressions computed for set A are shifted toward slightly lower periods, which is again connected with the resonance location. Although the $M - L$ relation is the same for models of sets A and B, displayed in the Figure, instability strip computed with convective parameters of set A is shifted toward higher temperatures. Consequently, in case of set A, the resonance crosses the fundamental mode instability strip for periods shorter, than in case of set B, which is clearly visible in Figure 4.1.
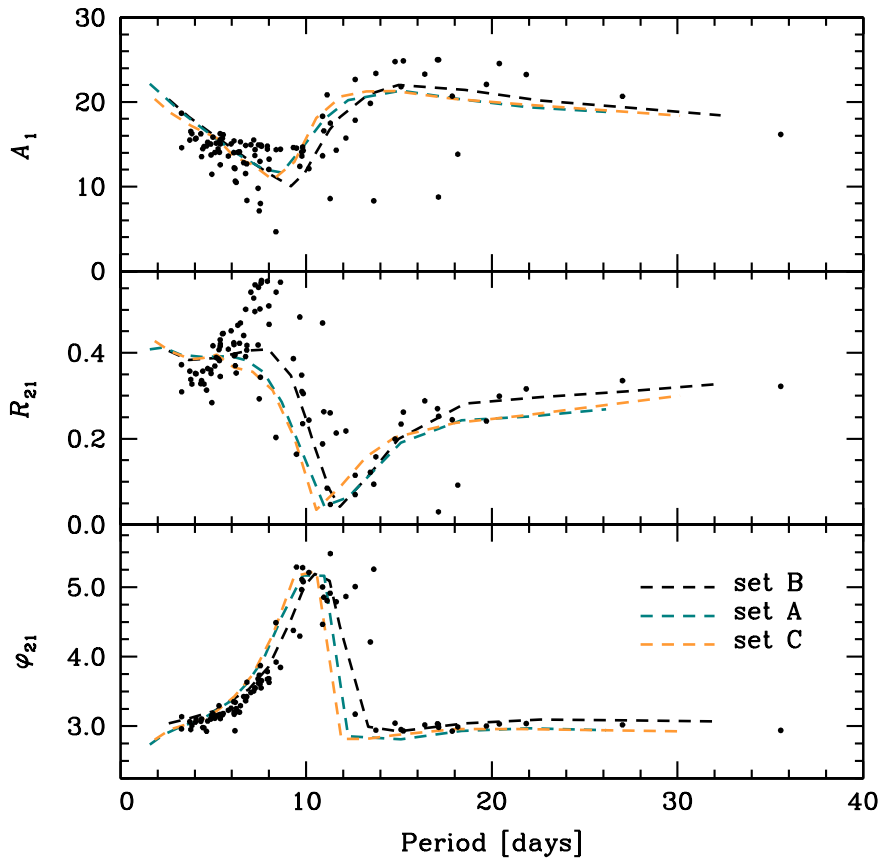
Figure 4.11: Fourier decomposition parameters of radial velocity curves for fundamental mode Cepheid models of sets A, B and C, running parallel to the fundamental mode blue edge at distance, $\Delta T = 300$ K. Model locations in the HR diagram are shown in Figures 4.1 (sets A and B) and 4.12 (set C) with dashed lines of the same colours. Amplitudes are scaled by constant projection factor equal 1.4. Dots represent observational data (*see* Figure 1.4 for references).

4.2 First overtone Cepheid models

Models to be described in this Section were presented in the paper of BARANOWSKI *et al.* (2009), reporting the observations of V440 Persei. Hydromodels presented therein, supported the hypothesis that V440 Per is an overtone Galactic Cepheid ($P_1 = 7.57\,\mathrm{d}$).

Parameters of the first overtone Cepheid models described below, are similar to those of fundamental mode Cepheids, discussed in the previous Section. Envelope is deeper ($T_{\mathrm{in}} = 4 \cdot 10^6\,\mathrm{K}$), which allows for better determination of overtone modes periods (which penetrate deeper into the envelope than the fundamental mode). Different $M - L$ relation, resulting from SCHALLER *et al.* (1992) evolutionary calculations, $\log(L/\mathrm{L_\odot}) = 3.56\log(M/\mathrm{M_\odot}) + 0.79$, is used. This relation has slightly higher zero point, as compared to $M - L$ relation used in the previous Section. For the convective parameters set C of Table 4.1 is adopted. In this set, turbulent flux and turbulent pressure are neglected, just as in set A, and radiative losses are turned on. As I show in the paper of BARANOWSKI *et al.* (2009), inclusion of radiative losses is necessary in order to model such long overtone periods (*see* general comment on convective parameters in the next Section). Here, I focus on the comparison between the computed and observed Fourier parameters of radial velocity curves, showing that model computations reproduce basic properties of the observed Fourier progressions.

The theoretical HR diagram computed with set C of convective parameters is presented in Figure 4.12, while in Figure 4.13 comparison between the model and observed Fourier parameters is provided. Nonlinear model sequences were computed at constant distances from the first overtone blue edge, $\Delta T = 25\,\mathrm{K}$, $75\,\mathrm{K}$, $125\,\mathrm{K}$ and $175\,\mathrm{K}$. Their location is showed with dashed coloured lines in Figure 4.12. For all these models fundamental mode is stable. The most luminous models entering the fundamental mode instability strip (not shown in Figure 4.12) switched into fundamental mode pulsation.

The characteristic progression connected with the 2:1 resonance between the first overtone, and linearly damped fourth overtone (Section 1.4.2) is clearly visible in both models and observations. The overall agreement between model and observed progressions is satisfactory, although some problems are apparent. Part of the visible discrepancies can be attributed, just as in case of the fundamental mode Cepheid models, to the location of the 2:1 resonance. As was shown by KIENZLE *et al.* (1999), the resonance center falls around 4.6 days. In the presented computations it crosses the overtone instability strip for periods around 4 days (Figure 4.13). The change in the zero point of the $M - L$ relation can shift the resonance center toward longer periods. However, the problem is more complicated. As is visible in the model run of φ_{21}, the computed width of the characteristic bell shape is too high. The width is affected by both zero point and slope of the adopted $M - L$ relation. Hence, to match the observations, both zero point and slope should be adjusted. This is not an easy task, requiring much numerical work, and was not performed within this thesis. Nevertheless, amplitudes and amplitude ratios agree satisfactorily with observations. The most severe problem concerns the Fourier phase, φ_{21}, at short period range. Model values are too high as compared to observations.
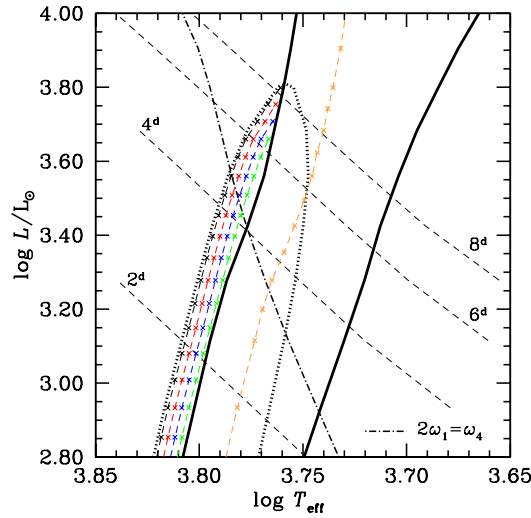
Figure 4.12: Instability strips in the theoretical HR diagram, computed for convective parameters of set C. Solid and dotted black lines limit the fundamental mode and first overtone instability strips, respectively. Dashed black lines are lines of constant, first overtone period indicated in the Figure. Dash-dotted line shows the center of the 2:1 resonance, $2\omega_1 = \omega_4$. Coloured lines show the location of nonlinear model sequences described in this and in the next Section and displayed in Figures 4.11 and 4.13.

4.3   Note on convective parameters

In the previous Sections, different sets of convective parameters were used to model fundamental and first overtone Cepheids. It is important to check, whether with convective parameters of set C, adopted to model the first overtone Cepheids, fundamental mode Cepheid models still agree satisfactorily with observations. The answer is provided in Figure 4.11, where Fourier progression for fundamental mode Cepheid models adopting convective parameters of set C, are plotted with orange, dashed lines. Despite rather dramatic differences between convective parameters of sets A, B and C, computed Fourier progressions for fundamental mode Cepheids are very similar. Hence, among convective parameters a kind of degeneracy is present – different sets of convective parameters lead to roughly the same results. This was first observed by YECKO *et al.* (1998) in their linear Cepheid model survey. However, a caution is necessary. Similar results, concerning *e.g.*, Fourier decomposition coefficients, obtained with different sets of convective parameters, do not indicate that results concerning the modal selection will be similar, too. This is the case with three parameter sets discussed here. Inclusion of radiative losses is necessary to model such long period as observed for an overtone pulsator V440 Persei.

Then, other question is, which parameters are the best. The most desired set should satisfy all constraints implied by observations of Cepheids pulsating in different modes and in stellar systems of different metallicities. Such calibration of the convective model, even if possible, would be a daunting task, as number of model parameters and observational constraints is enormous. But most likely, such calibration is simply not possible. It is hard to expect that such simple convective model,
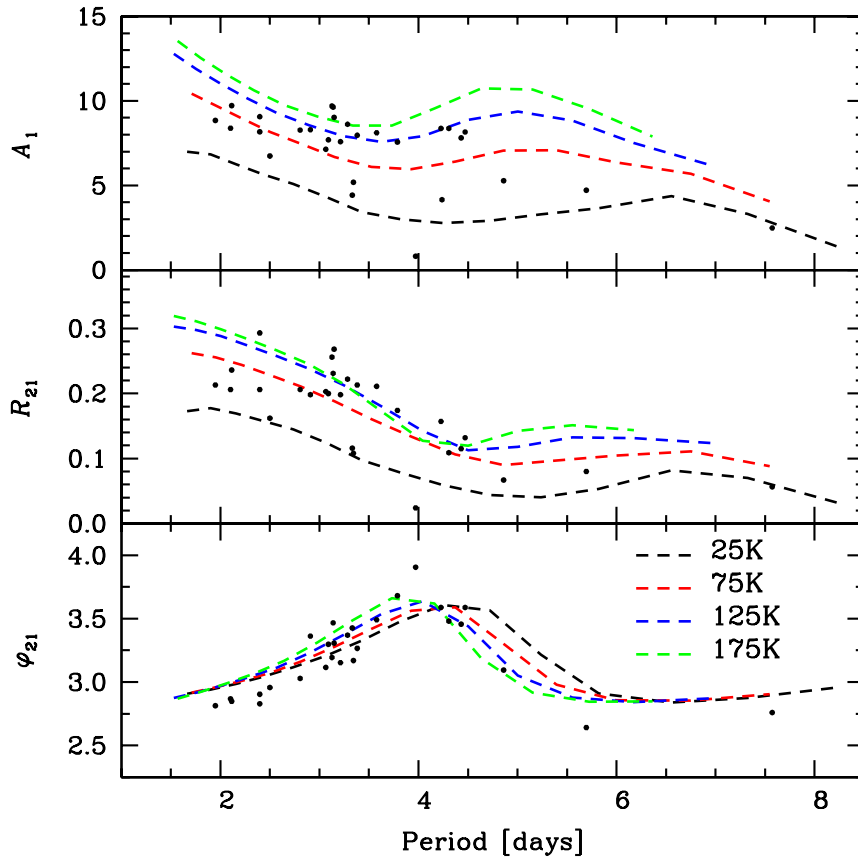
Figure 4.13: Fourier decomposition parameters of radial velocity curves for first overtone Cepheid models of set C, running parallel to the first overtone blue edge at distances, $\Delta T =$ 25 K, 75 K, 125 K and 175 K. Model locations in the HR diagram are shown in Figure 4.12 with dashed lines of the same colours. Amplitudes are scaled by constant projection factor equal 1.4. Dots represent observational data (*see* Figure 1.4 for references).

as discussed here, can do the thing. Hence, the choice of convective parameters is always somewhat arbitrary.

In this thesis, simple sets are our first choice. In these sets, some effects are simply neglected (*e.g.*, turbulent flux and turbulent pressure in sets B and C, radiative losses in sets A and B), which speeds up the computations. Then, the effects are turned on, separately, to see their effect on model computations. Such approach will be adopted in Chapter 6, where model surveys with many sets of convective parameters will be conducted. This is not always possible. In Chapter 8, concerning the modeling of double-overtone (1O/2O) Cepheids, only one set of convective parameters is adopted. In this case, growth rates of low mass models considered are very small, and computed models have dense numerical mesh, making the computations extremely slow. Therefore, the one adopted set was carefully chosen. It is set C of Table 4.1, which, as was shown in this Chapter, leads to reliable models of both fundamental and first overtone Cepheids.

Chapter 5

Comparison with other hydrocodes

In this Chapter, I discuss the approximations adopted in different convective pulsation hydrocodes, and their effect on the computed single-mode Cepheid models. These approximations concern the treatment of eddy-viscous terms (Section 5.1) and the treatment of turbulent source function in convectively stable regions (Section 5.2). Hydrocodes adopting different formulation, than the default discussed in Chapter 3, are not publicly available. However, some of the approximations and formulations adopted in these codes, can be easily implemented in the codes described in this thesis (as an option), allowing for detailed comparison. Discussion in this Chapter is limited to the codes adopting the Kuhfuß-based convection models, mainly to the Florida-Budapest hydrocode.

It turns out that the treatment of eddy viscosity has only a minor effect on the computed models. However, different assumptions concerning the turbulent source function, lead to qualitatively different results, which has severe consequences for the double-mode models (Chapter 6).

5.1   Treatment of eddy viscosity

In this Section, I compare the results computed adopting different treatments of eddy-viscous terms. In the default formulation adopted in the codes described in this thesis, eddy-viscous terms result from first order modeling of the Reynolds stress tensor (Section 2.4). As a result, viscous momentum (U_q) and energy (E_q) transfer rates are present in the momentum and energy equations (Eqs. 3.1, 3.3–3.4). This formulation, called Kuhfuß eddy viscosity in the following, is also adopted in the Vienna code (Section 2.6.1). However, in other codes (Italian code, Florida-Budapest code, *see* Section 2.6.1), the eddy-viscous pressure, introduced in an *ad hoc* way, is used. In the formulation used in the Florida-Budapest code, eddy-viscous pressure is given by (Eq. 2.75),

$$p_\nu = -\frac{4}{3}\alpha_m \rho \Lambda e_t^{1/2} r \frac{\partial}{\partial r}\left(\frac{u}{r}\right),$$

and enters the model equations in the same way turbulent pressure does. This formulation, called Kolláth eddy viscosity in the following, was adopted in the codes

presented in Chapter 3 as an option. In this formulation, model equations are following,

$$\frac{\mathrm{d}u}{\mathrm{d}t} = -4\pi r^2 \frac{\partial}{\partial M_r}(p + p_t + p_\nu) - \frac{GM_r}{r^2},$$

$$\frac{\mathrm{d}E}{\mathrm{d}t} + p\frac{\mathrm{d}V}{\mathrm{d}t} = -\frac{\partial(L_\mathrm{r} + L_\mathrm{c})}{\partial M_r} - C,$$

$$\frac{\mathrm{d}e_t}{\mathrm{d}t} + (p_t + p_\nu)\frac{\mathrm{d}V}{\mathrm{d}t} = -\frac{\partial L_\mathrm{t}}{\partial M_r} + C.$$

In comparison to momentum and turbulent energy equations adopting the default formulation (Eqs. 3.1 and 3.3), terms, $-(3V/r)p_\nu$, and, $(3V/r)p_\nu u$, were dropped above, respectively.

The effects of using different forms of eddy viscosity were checked for linear and nonlinear fundamental mode Cepheid models, adopting convective parameters of sets A and B (Table 4.1). Models adopting the Kuhfuß eddy viscosity are exactly the same as discussed in Section 4.1.

In Figure 5.1 instability strips computed with different forms of eddy viscosity are compared. Models adopt convective parameters of set A (left panel) and set B (right panel). Instability strips computed with the Kolláth eddy viscosity (green lines) are slightly narrower than those computed with the Kuhfuß eddy viscosity (black lines). This reflects the general property of individual models – those computed with Kolláth eddy viscosity are slightly less unstable (have smaller growth rates). The described effect can be compensated, by lowering α_m in the models adopting Kolláth eddy viscosity, while keeping other alphas fixed. Considering the periods, or loci of the resonances, they are almost identical for both forms of eddy viscosity (hence, separate lines of constant period are not plotted in Figure 5.1, as they would overlap). This is because periods are mostly determined by the static structure of the model, and this is entirely independent of eddy viscosity.
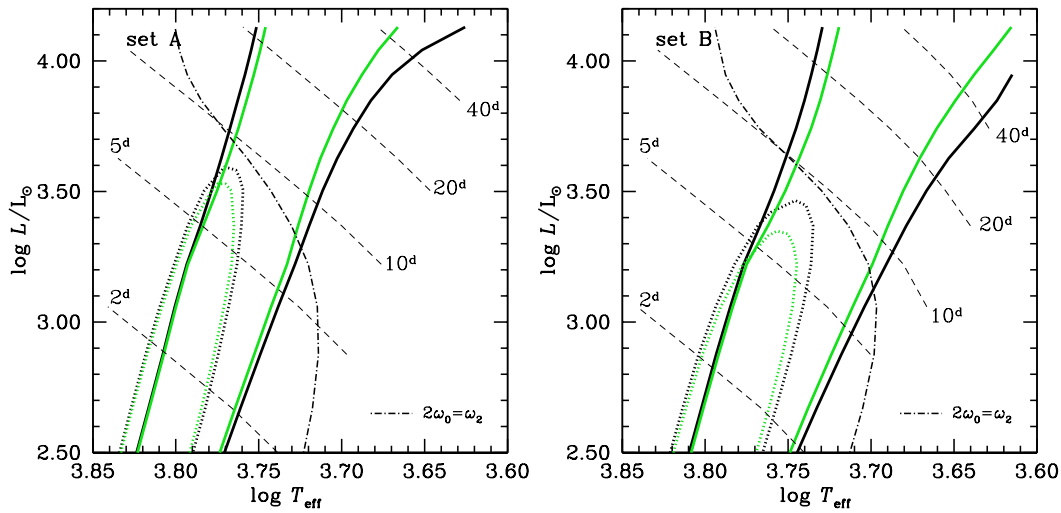

Figure 5.1: Instability strips in the theoretical HR diagram, computed for convective parameters of set A (left panel) and B (right panel). Black and green lines correspond to models computed with Kuhfuß and Kolláth forms of eddy viscosity, respectively.

Comparison of nonlinear models can be done in several ways. Here, computations were conducted for model sequences running parallel to the fundamental mode blue edges ($\Delta T = 300\,\mathrm{K}$), computed adopting two eddy viscosity forms discussed. Therefore, effective temperatures of models of the same mass slightly differ. Results for convective parameters of set B are presented in Figure 5.2, in which Fourier decomposition parameters of radial velocity curves are plotted. In agreement with linear expectations, amplitudes, and consequently R_{21} ratios are slightly smaller for models computed with Kolláth eddy viscosity. Considering the Fourier phase, φ_{21}, results are almost identical. Again, small decrease of α_m in models adopting the Kolláth eddy viscosity, should bring the results for both treatments of eddy viscosity into perfect agreement.
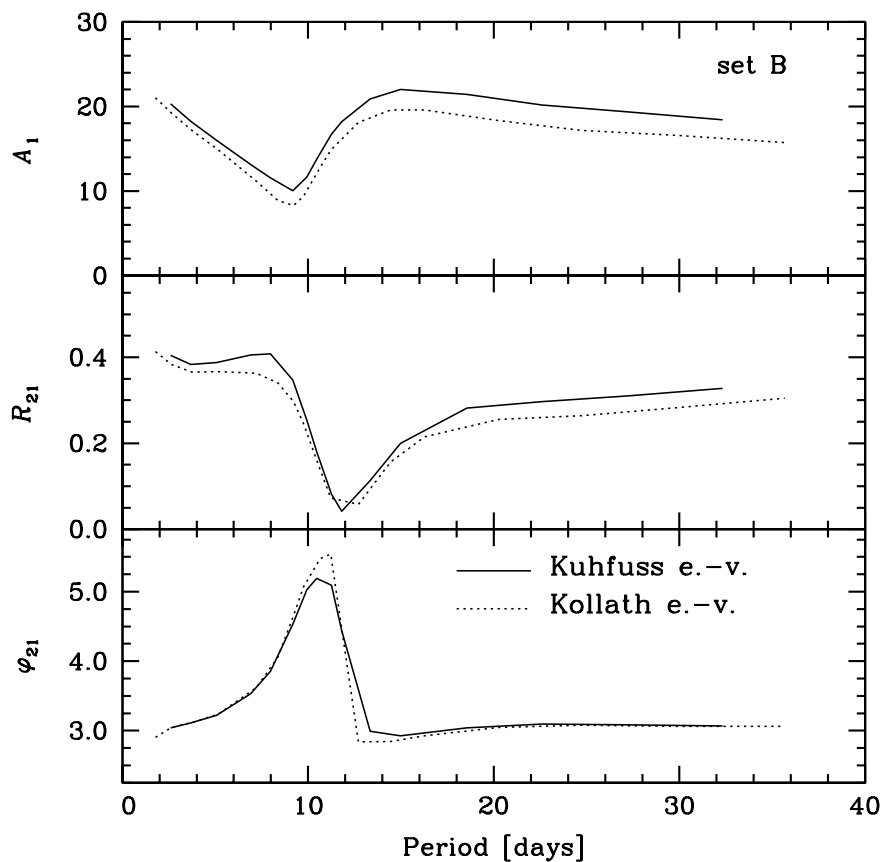

Figure 5.2: Fourier decomposition parameters of radial velocity curves for fundamental mode Cepheid models of set B, running parallel to the fundamental mode blue edge, at distance, $\Delta T = 300\,\mathrm{K}$. Amplitudes are scaled by constant projection factor equal 1.4. Solid lines for models adopting Kuhfuß eddy viscosity, dotted lines for models computed with Kolláth eddy viscosity.

5.2   Treatment of the turbulent source function

Many of the convective Cepheid and RR Lyrae models, particularly almost all double-mode models, were published by the Florida-Budapest group. Their code adopts a convective model based on the work of Kuhfuß, however, with different treatment of the convectively stable regions. As already discussed in Section 2.6.1, in Florida-Budapest codes superadiabatic gradient is restricted to positive values only (Eq. 2.74),

$$\mathcal{Y} = \left(- \frac{H_p}{c_p} \frac{\partial s}{\partial r} \right)_+ \qquad (5.1)$$

Consequently, turbulent source function and also convective flux are equal to zero in convectively stable regions. Resulting convective model is different from Kuhfuß model and was called modified Kuhfuß model in Section 2.6.1. Reasons motivating approximation expressed by Eq. (5.1), were never discussed by the Florida-Budapest group. Possible consequences were not studied, neither, and these can be significant as may be inferred from the papers by BUCHLER & KOLLÁTH (2000) and GEHMEYR & WINKLER (1992b). Buchler & Kolláth compared the results of model computations (both linear and nonlinear) adopting different expressions for the turbulent source function and convective flux. These expressions were ($S \sim \sqrt{\mathcal{Y}}$, $F_c \sim \sqrt{\mathcal{Y}}$), which corresponded to the original Stellingwerf model (*see* Section 2.3), ($S \sim \sqrt{\mathcal{Y}}$, $F_c \sim \mathcal{Y}_+$), which was formulation adopted in the initial papers of the Florida-Budapest group (YECKO *et al.* 1998, KOLLÁTH *et al.* 1998) and, ($S \sim \mathcal{Y}_+$, $F_c \sim \mathcal{Y}_+$), which was the default formulation adopted in the Florida-Budapest hydrocodes. Let me note that the last formulation is called Kuhfuß model by the Florida-Budapest group, which is not justified. BUCHLER & KOLLÁTH (2000) showed that if convective parameters entering the three mentioned models were recalibrated accordingly, computed models, both linear and nonlinear were qualitatively the same. In particular, it means that the Stellingwerf and Florida-Budapest models lead to essentially the same results. If indeed, the Florida-Budapest formulation is equivalent to Kuhfuß formulation, this result would be in contradiction to the analytical studies by GEHMEYR & WINKLER (1992a,b), described in Section 2.5. These authors compared the Stellingwerf and original Kuhfuß model, in which ($S \sim \mathcal{Y}$, $F_c \sim \mathcal{Y}$), and found significantly different model behaviour, as discussed in Section 2.5.

Therefore, it seems useful and necessary to compare the full hydrodynamical models adopting different formulations. This is the goal of the following Sections. Models in which superadiabatic gradient is restricted to positive values (Florida-Budapest formulation, modified Kuhfuß model, or simply PP model in the following), will be compared with models computed using original Kuhfuß formulation, adopted by default in the codes described in this thesis (NN model in the following). To this aim, PP convection model was implemented into the codes described in Chapter 3 as an option. This is very easy and straightforward modification. I stress that the models described in this and following Chapters were computed with hydrocodes described in Chapter 3, however, adopting different treatment of convectively stable regions (PP model instead of NN model).

In the following Sections, linear as well as nonlinear model sequences are computed adopting the two described formulations (Section 5.2.1). Explanation for the

observed differences is provided in Section 5.2.2, based on the detailed comparison of individual models. In Section 5.2.3 it is shown that it is the different treatment of turbulent source function, being responsible for the observed differences between NN and PP models, treatment of convective flux playing a minor role. In Section 5.2.4 short remark concerning the numerical behaviour of NN and PP models is made, and finally, in Section 5.2.5, the criticism of the PP formulation is done.

5.2.1 PP *versus* NN models – linear and nonlinear model surveys

The models to be compared adopt convective parameters of sets A and B, from the previous Chapter (Table 4.1). Models are constructed exactly as described in Section 4.1, and all the results computed with NN convection model were described in the previous Chapter. Here, I conduct their comparison with the PP models.

Linear results (periods, growth rates, model structure) are almost identical for both PP and NN convection models. Respective edges of the instability domains in Figure 4.1, for NN and PP models would overlap, as they are shifted with respect to each other by less than 1K. The same is true for lines of constant period, or lines showing the loci of the resonances. Qualitatively and quantitatively, linear results computed with NN and PP convection models are the same. Nevertheless, nonlinear results differ significantly.

Full nonlinear computations were conducted for the fundamental mode Cepheid models running parallel to the fundamental mode blue edge ($\Delta T = 300$ K). Models to be compared have exactly the same physical parameters (masses, luminosities, chemical compositions) as well as numerical (mesh structure) and convective parameters (alphas). The only difference is in the treatment of convectively stable regions (NN *versus* PP models). Figures 5.3 and 5.4 display the Fourier decomposition parameters of radial velocity curves, for models adopting convective parameters of sets A and B, respectively. In each Figure NN and PP models are compared. Model progressions for NN models are exactly the same as displayed in Figure 4.11 (although some additional models are present in Figures 5.3 and 5.4). The striking differences between NN and PP models are visible in the run of amplitudes and amplitude ratios. Amplitudes of the models computed with PP convection are significantly lower, than amplitudes of the same models computed with NN convection. Consequently, also R_{21} ratios are smaller for PP models. Differences are largest at short periods. To the contrary, the run of Fourier phase, φ_{21}, is almost the same for both NN and PP models. Results are qualitatively the same for sets A and B. In the following Section, I explain the described differences between NN and PP models.

5.2.2 Explanation of the differences between PP and NN models

To explain the differences between NN and PP nonlinear model sequences, we focus our attention on one particular model of set A, with the mass of $4.5M_\odot$. Its location is shown with arrows in Figure 5.3. The model is the simplest possible convection model, without turbulent pressure, turbulent flux and without radiative losses (*cf.* Table 4.1). Discrepancies between NN and PP models, noted in the previous Section,
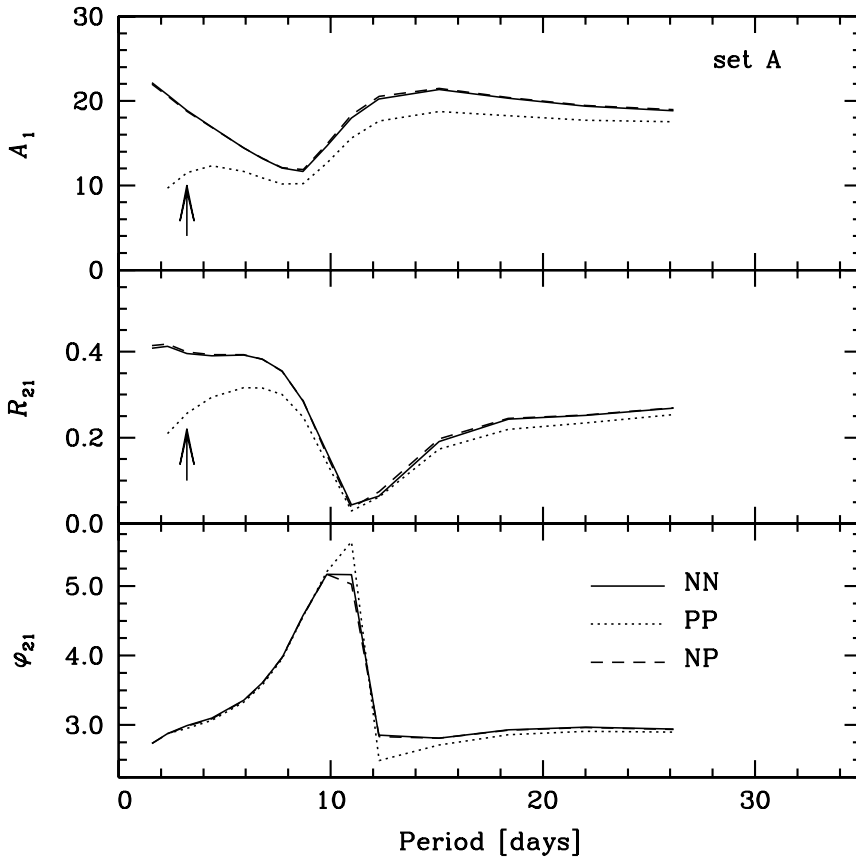
Figure 5.3: Fourier decomposition parameters of radial velocity curves for fundamental mode Cepheid models of set A, running parallel to the fundamental mode blue edge ($\Delta T = 300\,\mathrm{K}$). Amplitudes are scaled by constant projection factor equal 1.4. Solid lines for NN models, dotted lines for PP models and dashed lines for NP models (*see* Section 5.2.3). Arrow marks the location of the model discussed in Section 5.2.2.

are very similar for set A and set B which includes more complicated effects (p_t, F_t). Therefore, it is natural to focus attention on set A first, as additional effects due to turbulent pressure and turbulent flux, are not expected to play significant role in rising up the discrepancies.

Figures 5.5 and 5.6 are crucial to understand the differences between NN and PP models. In Figure 5.5, profiles of superadiabatic gradient, $\mathcal{Y} = \nabla - \nabla_a$, together with profiles of turbulent energy, e_t, during one pulsation cycle are plotted, for both NN and PP models. In case of turbulent energy profiles, two viewpoints are provided for each model, highlighting internal and external zones. In Figure 5.6 nonlinear differential work integrals of these two models are plotted (NN model in the upper, PP model in the lower panel).

Comparing the turbulent energy profiles (Figure 5.5), striking differences are visible in convectively stable regions, in which $\mathcal{Y}$ is negative (NN model) or set equal to zero (PP model). In both the discussed models, main convective zone extends down to zone ≈ 70 (upper panels of Figure 5.5). Interior zones are convectively stable. In NN model, turbulent energies are extremely small in these zones, of
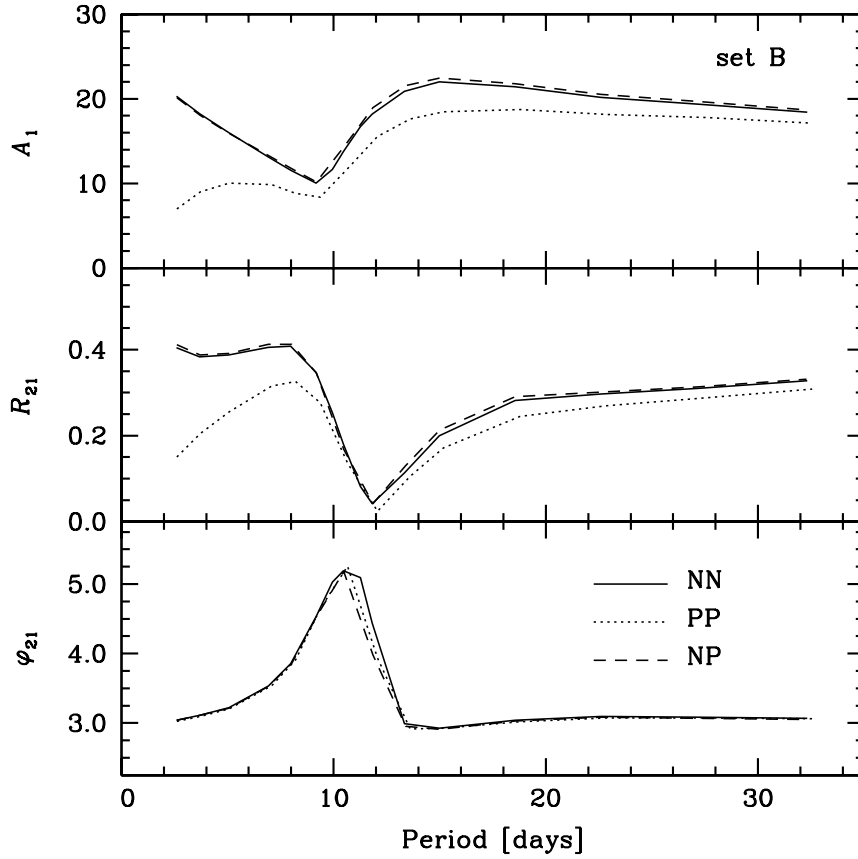
Figure 5.4: Fourier decomposition parameters of radial velocity curves for fundamental mode Cepheid models of set B, running parallel to the fundamental mode blue edge ($\Delta T = 300\,\mathrm{K}$). Amplitudes are scaled by constant projection factor equal 1.4. Solid lines for NN models, dotted lines for PP models and dashed lines for NP models (*see* Section 5.2.3).

order of $10^{-14}\mathrm{erg/g}$. To the contrary, in PP model, turbulent energies are by many orders of magnitude higher. In zones 40–70, they are of order of $10^9 - 10^{10}\mathrm{erg/g}$, which is only three orders of magnitude smaller than in the center of the convective zone. In these zones, the whole energy transfer is due to radiation, as convective flux in convectively stable regions of PP model is equal to zero, by definition ($F_c \sim \mathcal{Y}_+$). Also turbulent flux is turned off in set A, and significant turbulent energies cannot arise due to overshooting. Whatever is the source of such high turbulent energies in PP model, they cause the significant eddy-viscous dissipation in the internal, convectively stable zones of the model, clearly visible in the differential work integral displayed in the lower panel of Figure 5.6. Negative contribution to the work integral is present below zone 70 and extends down to zone ≈ 30. In NN model, eddy viscosity does not contribute to the work integral in convectively stable regions, as turbulent energies are extremely small there. As a consequence of internal eddy-viscous damping, amplitude is lower for the PP model, which is clearly visible in Figure 5.3. Described mechanism is qualitatively the same for all the models presented in Figures 5.3 and 5.4.

Now, I will explain the reasons behind very different turbulent energy profiles
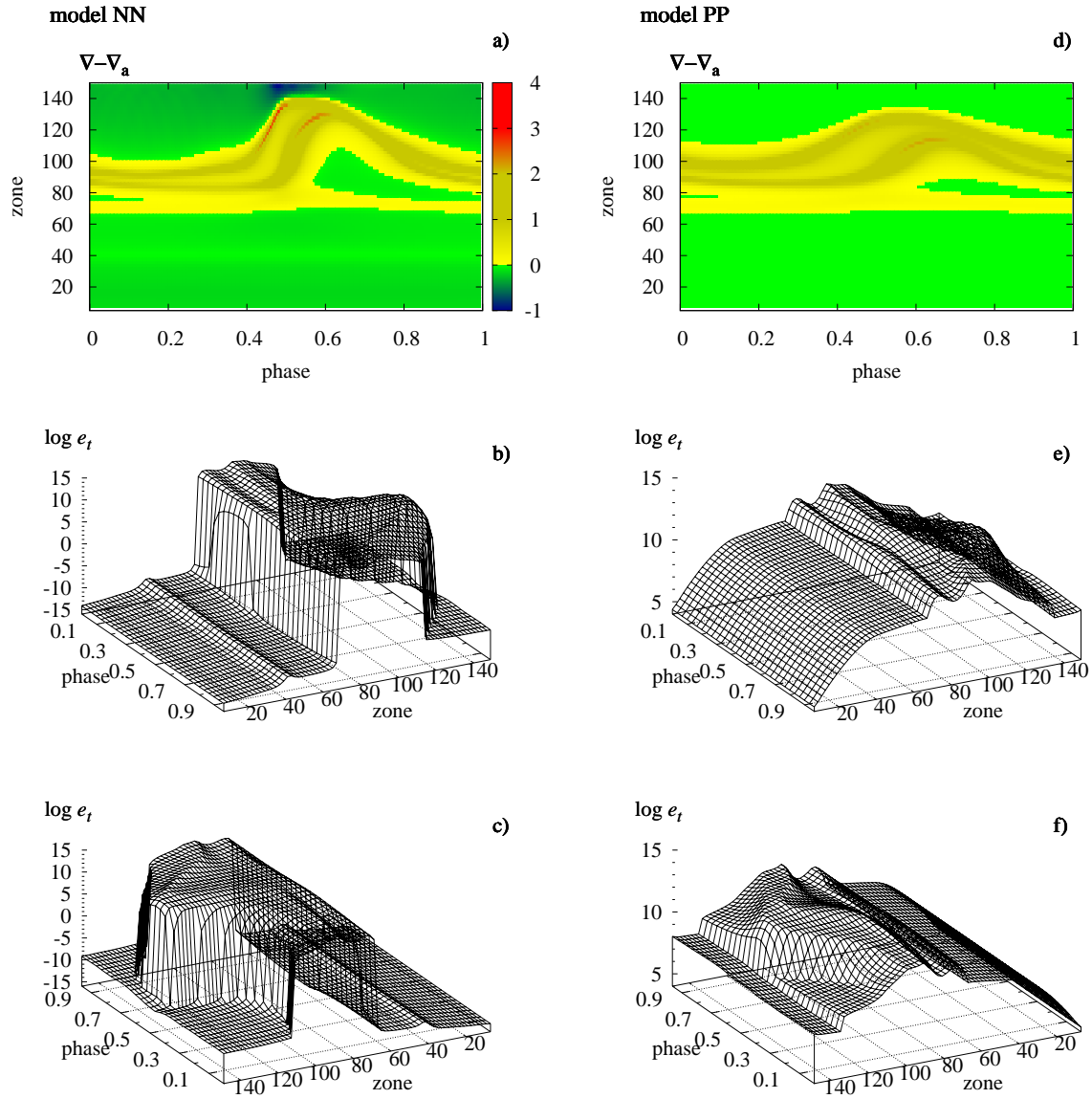
Figure 5.5: Profiles of superadiabatic gradient (top panels) and turbulent energy profiles (middle and bottom panels) during one pulsation cycle for NN (left panels) and PP models (right panels), adopting convective parameters of set A. For the turbulent energy profiles, middle panels highlight the internal, while bottom panels the external parts of the model. Note different scale on vertical, logarithmic axes for NN and PP models.

in NN and PP models. To achieve this goal, turbulent energy equation has to be analysed. In case of set A considered at the moment (turbulent flux and turbulent pressure neglected) it can be written as (Eqs. 3.3, 3.59),

$$\frac{de_t}{dt} = \underbrace{S}_{S-\text{term}} \underbrace{-\alpha_d \frac{e_t^{3/2}}{\Lambda}}_{D-\text{term}} \underbrace{+\alpha_d \frac{e_0^{3/2}}{\Lambda}}_{e_0-\text{term}} \underbrace{+E_q}_{E_q-\text{term}} \ . \qquad (5.2)$$
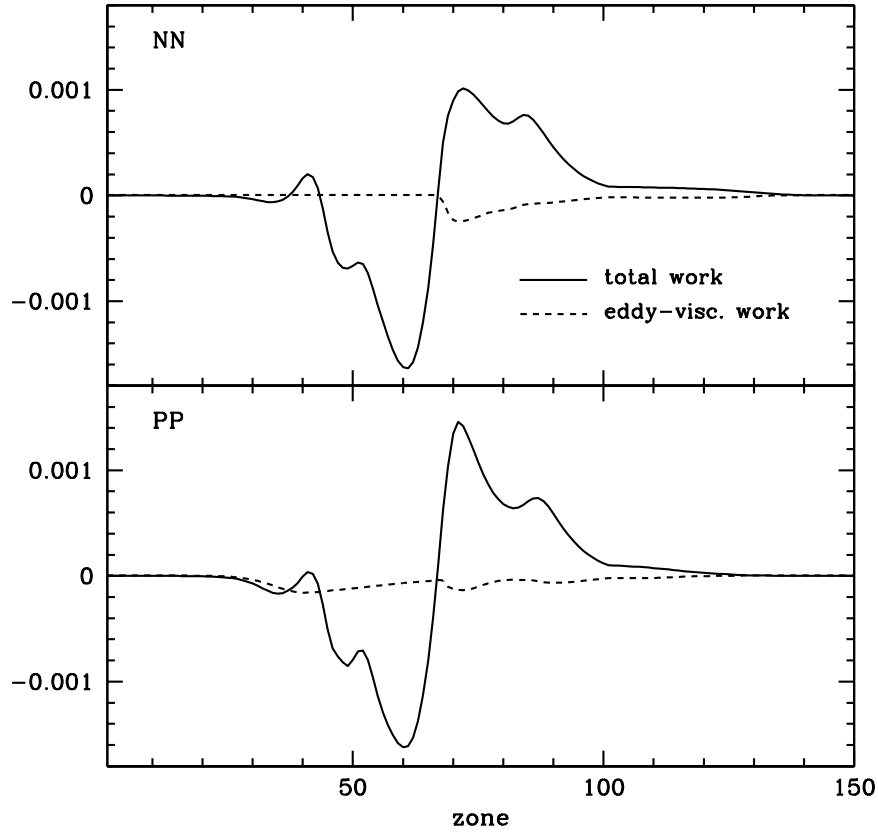
Figure 5.6: Nonlinear, differential work integrals plotted *versus* the zone number for $4.5M_\odot$ model discussed in the text. Upper panel for NN model, lower panel for PP model.

Several terms contribute to the generation/decay of turbulent energies. These are the turbulent source term (S-term), turbulent dissipation term (D-term), correction term (e_0-term) and eddy-viscous energy transfer rate (E_q-term). The last two terms are always positive and contribute to the driving of turbulent energies. Turbulent dissipation term is always negative and thus, always contributes to the decay of turbulent energy. The source term may drive as well as damp the turbulent energies, depending on the sign of the superadiabatic gradient in NN model, and can only drive the turbulent energies in PP model, in which it is restricted to non-negative values. For the further discussion, it is important to note how do these terms depend on turbulent energy. S and E_q terms depend on e_t like $\sim e_t^{1/2}$, while D-term depends like $\sim e_t^{3/2}$. The whole picture is summarized in the scheme below, in which red terms are positive and contribute to the driving of turbulent energies and blue terms are negative, contributing to the decay of turbulent energies. It is useful to consult this scheme during the following discussion.

	NN model	PP model
$\mathcal{Y} > 0$	$\frac{de_t}{dt} = S(e_t^{1/2}) - D(e_t^{3/2}) + E_q(e_t^{1/2}) + e_0$	$\frac{de_t}{dt} = S(e_t^{1/2}) - D(e_t^{3/2}) + E_q(e_t^{1/2}) + e_0$
$\mathcal{Y} < 0$	$\frac{de_t}{dt} = S(e_t^{1/2}) - D(e_t^{3/2}) + E_q(e_t^{1/2}) + e_0$	$\frac{de_t}{dt} = -D(e_t^{3/2}) + E_q(e_t^{1/2}) + e_0$

It is clearly visible that the model equations differ in convectively stable regions, only.

Now we focus our attention around zone ≈ 70, at which superadiabatic gradient changes its sign (Figure 5.5). Here, the crucial and drastic discrepancy in turbulent energy profiles of NN and PP models arises. Below, I describe the processes shaping these profiles, first in NN and then, in PP models.

- **NN model.** As superadiabatic gradient, $\mathcal{Y}$, changes its sign, S-term becomes negative. Together with turbulent dissipation term, they damp the turbulent energies very effectively. Around zone ≈ 70 turbulent energies fall by roughly 25 orders of magnitude, to a very small level. This rapid damping is caused mostly by the source term and its $\sim e_t^{1/2}$ dependence on e_t. It easily overcomes the turbulent energy driving due to E_q-term. In a physical description, turbulent eddies are effectively braked by the negative buoyancy represented in the source term. The effect is much stronger than the generation of turbulent energy at the cost of pulsation, through the eddy-viscous forces, represented in the E_q-term. Turbulent energies fall very fast, however, not to zero, but to a very small level which is assured by the e_0-term. This term is not a physical ingredient of the Kuhfuß model, but was introduced for numerical reasons (*see* Section 3.3.3). As all the terms entering the turbulent energy equation depend on e_t in some power, $e_t = 0 \, \mathrm{erg/g}$ is a solution to this equation. Once turbulent energy is equal to zero in some zone, it will stay zero, even if convective instability arises. Therefore, e_0-term is necessary and acts as a seed for turbulent energies at the onset of convective instability.

  In all the interior zones of the NN model, turbulent energies are extremely small. They are set by the balance between the S, E_q and e_0 terms. Turbulent dissipation term (D-term) is not significant with its $\sim e_t^{3/2}$ dependence on e_t. The relative distribution of turbulent energies is shaped by the physics, represented in the S-term. Hence, a small bump in the turbulent energy profile around zone 40 – result of the iron opacity bump. However, the overall level of turbulent energies, of order of $10^{-12} - 10^{-14} \, \mathrm{erg/g}$, makes them entirely not significant from physical point of view. This small level is set mainly by the value of e_0 constant ($e_0 = 10^4 \, \mathrm{erg/g}$). Still, these small turbulent energies are sufficient to rebuilt the convective zone, if convective instability arises. This is clearly visible in the bottom-left panel of Figure 5.5, highlighting the external zones of the model. Here, convective zone sweeps through several Lagrangian zones of the model, during the pulsation cycle.

  It is important to stress that e_0-term plays only a numerical role and does not affect the physical behaviour of the model. It is not responsible for the steep fall of turbulent energies at the base of the convective zone, as it always drives the turbulent energies. It only prevents the turbulent energies from falling to zero.

- **PP model.** The restriction of superadiabatic gradient to positive values in PP model, is responsible for completely different distribution of turbulent energies in convectively stable regions. As $\mathcal{Y}$ becomes negative, the turbulent source function is set equal to zero. This is equivalent to the neglect of neg-

ative buoyancy effects. The only term that contributes to the decay of turbulent energies is the turbulent dissipation term, which models the decay of the turbulent eddies through the turbulent cascade. This term is responsible for the fall of turbulent energies at the base of the convective zone, but only by three orders of magnitude, from 10^{13} erg/g in the center of the convective zone, to 10^{10} erg/g just below it (middle-right panel of Figure 5.5). Further fall is prevented by the eddy-viscous energy transfer (E_q-term), which pumps up the turbulent energies at the cost of kinetic energy of pulsations. E_q-term depends on turbulent energy like $\sim e_t^{1/2}$, while the D-term like $\sim e_t^{3/2}$. As turbulent energies fall, the damping strength of the D-term falls more rapidly than the driving strength of the E_q-term. In the absence of the damping turbulent source term ($\sim e_t^{1/2}$), the balance between the D and E_q terms sets the turbulent energies at relatively high level. In more than thirty zones below the base of the convective zone (zones $40-70$), turbulent energies are of order of $10^9 - 10^{10}$ erg/g. In the innermost zones (below zone 40), turbulent energies gently decrease, which reflects the vanishing amplitude of the fundamental mode, as one moves inward the model. In fact close to the inner boundary, $e_t \approx e_0 = 10^4$ erg/g, as only D and e_0 terms are significant there. However, through the almost whole envelope, e_0-term is small and insignificant as compared to E_q-term. It has no effect on the turbulent energy distribution below the convective zone. Even more, no numerical problems are encountered if e_0-term is dropped during the full amplitude pulsation. Non-zero turbulent energies are maintained by the eddy-viscous driving (E_q-term).

Although below the convective zone turbulent energies are smaller than in the center of the convective zone, they are high enough to produce a significant eddy-viscous damping, clearly visible in the differential work integrals displayed in the lower panel of Figure 5.6, in between zones ≈ 40 and ≈ 70. This range corresponds to more than 6 local pressure scale heights. Eddy-viscous damping in such a large region is responsible for the lower amplitudes of the PP models visible in Figure 5.3.

Significant turbulent energies can be present in convectively stable zones of the model due to the overshooting. However, in the discussed models, turbulent flux, the sole cause of the overshooting in the discussed convective recipes (*see* Section 2.4) is turned off. In convectively stable regions of the NN model, turbulent energies are rapidly damped by the negative buoyancy. As expected, no traces of overshooting are visible in this model. To the contrary, high turbulent energies are present in convectively stable regions of the PP model. They are driven at the cost of pulsations through the eddy-viscous forces and cannot be damped by the negative buoyancy, which is neglected. Hence, the effect has nothing to do with the overshooting. Note also, that the region with significant turbulent energies is very large, as it covers more than 6 local pressure scale heights.

As described above, viscous energy transfer is crucial in bringing up the high turbulent energies in convectively stable zones of the PP model. It can be easily checked numerically by computing the models neglecting the eddy viscosity (parameter α_m set equal to zero). In this case, nonlinear models adopting NN and PP formulation are almost the same, particularly have equal amplitudes. This is be-

cause now, in both NN and PP models turbulent energies are small in convectively stable regions. In case of NN model, situation does not change much. Turbulent energies are extremely small, being effectively damped through the negative source term. In case of PP model, turbulent energies are constant and equal to e_0, which is a solution of Eq. (5.2), when turbulent source and eddy-viscous terms are equal to zero. Turbulent energies equal 10^4 erg/g are negligible as compared to the values present in the center of the convective zone (10^{13} erg/g). Of course no eddy-viscous damping is present in the models. If eddy viscosity is neglected, results are the same for both NN and PP models.

Above considerations also explain why linear results computed with NN and PP convective models are the same. This is simply because eddy-viscous terms do not enter the static model computations at all. Static structure of the models is almost the same for both NN and PP convection models. Also, eddy-viscous terms that appear in the energy equations do not enter the linear nonadiabatic analysis. Described effect is purely nonlinear.

The form of the eddy viscosity used (Kuhfuß or Kolláth, *see* Section 5.1) is not important in the above considerations. If Kolláth form is used instead of Kuhfuß, E_q-term is replaced by, $-p_\nu(\,\mathrm{d}V/\,\mathrm{d}t)$. This term plays exactly the same role – it generates the turbulent energies at the cost of pulsation.

Presented results do not depend on the exact values of convective parameters (alphas) and effects included/neglected in the model. Particularly, inclusion of turbulent flux into the model, does not change the presented discussion. As already discussed (compare Figures 5.3 and 5.4) qualitatively the same differences are observed between NN and PP model sequences, computed with convective parameters of sets A and B. In the latter set, effects of turbulent pressure and turbulent flux are turned on. Figure 5.7 shows the profiles of turbulent energy during one cycle of full amplitude pulsation for $4.5 M_\odot$ model of set B computed with NN and PP convection. Profiles are qualitatively the same as displayed in the middle and bottom panels of Figure 5.5. They are just more smooth, as sharp features are diffused by the gradient of turbulent flux. In the PP model the whole envelope is turbulent and physical overshooting, as a cause of turbulent energies in convectively stable regions, is not important anyway. In the NN model, on the other hand, the range of physical overshooting is always very small (much less than one pressure scale height), as negative buoyancy effectively damps the turbulent energies in convectively stable regions of the model.

5.2.3 The crucial role of the turbulent source function

Discussion presented in the previous Section clearly shows the crucial role played by the neglect of turbulent source function in convectively stable regions. The exact form of the source function is not important. This was checked by BUCHLER & KOLLÁTH (2000), as discussed at the beginning of Section 5.2. They compared the models adopting the original Stellingwerf prescription, in which $S \sim \sqrt{\mathcal{Y}}$, with PP models, obtaining qualitatively the same results. In both models, negative buoyancy is absent, and does not damp the turbulent energies in convectively stable regions. Hence, in both models strong eddy-viscous damping, extending over few pressure scale heights below the convective zone is present. This is clearly visible in the lower
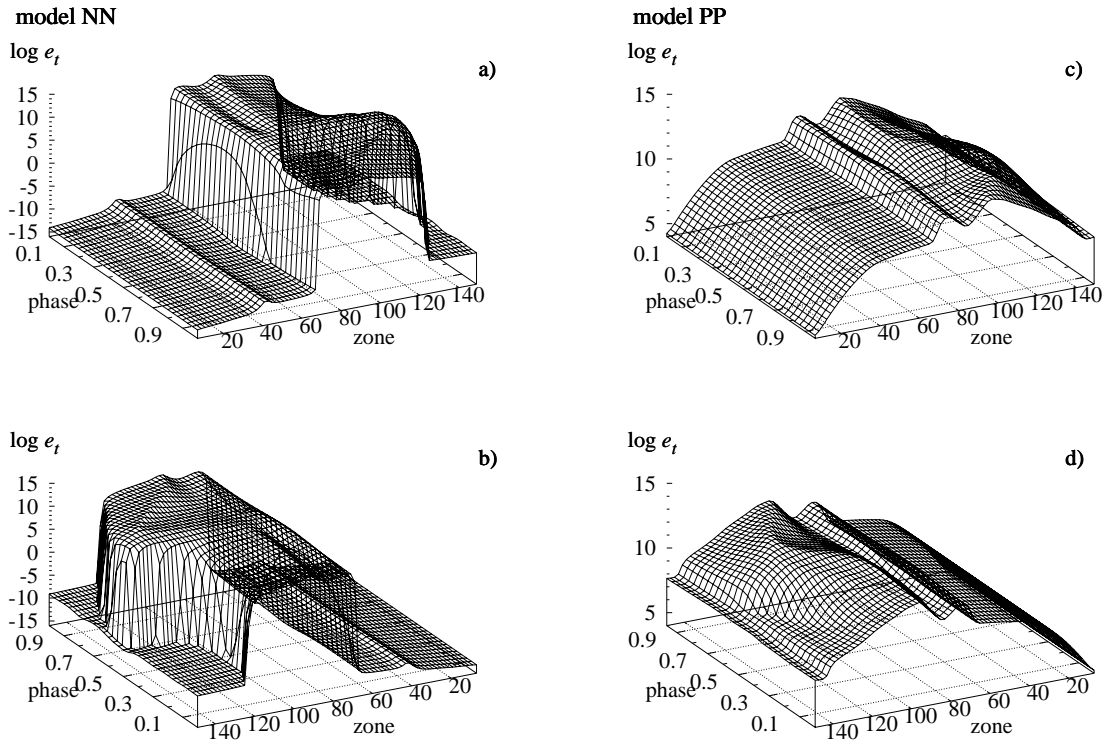
Figure 5.7: Turbulent energy profiles during one pulsation cycle for NN model (left panels) and PP model (right panels), adopting convective parameters of set B (including overshooting). Top panels highlight the internal, while bottom panels the external parts of the model. Note different scale on vertical, logarithmic axes for PP and NN models.

panel of Figure 5.6, and in the work integrals published in the paper of Buchler & Kolláth.

If negative buoyancy is included in the model, internal eddy-viscous dissipation is not present. This is true, again, independently of the form of the source function. In the work integrals published by the Italian group (*e.g.*, BONO, MARCONI & STELLINGWERF 1999), eddy-viscous damping is not present in the internal model zones, just as in case of our NN model (upper panel of Figure 5.6). In their computations the modified Stellingwerf model is adopted in which $S \sim \mathrm{sgn}(\mathcal{Y})\sqrt{|\mathcal{Y}|}$ (*see* Section 2.3). Hence, in convectively stable regions turbulent energies are effectively damped, just as in NN model.

Restriction of superadiabatic gradient to positive values, affects not only the source function, but also the convective flux, which is always positive in PP model. However, almost the whole difference between the NN and PP models can be attributed to the different treatment of the source function. Convective flux plays only a minor role, which is easy to understand. In convectively stable regions of the PP model, convective flux is equal to zero by definition. In NN model, on the other hand, turbulent energies are negligible in convectively stable regions, or very small and extending over a very limited range if overshooting is turned on in the model. Hence, also negative convective flux ($F_c \sim e_t^{1/2}\mathcal{Y}$) is always very small as compared

to the total flux. These considerations are fully supported by model computations in which convective flux is restricted to positive values only ($F_{\rm c} \sim \mathcal{Y}_+$), but negative buoyancy effects are included in the model ($S \sim \mathcal{Y}$). Nonlinear results for such NP convective model are presented in Figures 5.3 (set A) and 5.4 (set B). As expected, model curves for NP model almost overlap the corresponding curves for NN model. Slightly larger differences are visible in case of models adopting convective parameters of set B. In these models overshooting leads to higher turbulent energies in convectively stable zones, and consequently, effects of negative convective flux are stronger.

5.2.4   Numerical behaviour of the PP and NN models

Besides the physical differences in the properties of the computed models adopting NN and PP convection, there are also strictly numerical consequences of choosing one of these two treatments. Model computations adopting the PP convection are much faster. Nonlinear iterations converge fast and without problems. Price to pay for the inclusion of negative buoyancy effects is greater numerical cost. Comparison of turbulent energy profiles in PP and NN models displayed in Figures 5.5 and 5.7 tells why. In PP model, turbulent energy is slowly varying function of both time and spatial coordinate. During the integration of PP model, turbulent energy vary only by few orders of magnitude, and no sharp falls or increases are visible. To the contrary, in NN model we deal with changes in turbulent energy by several orders of magnitude. These are caused by the negative buoyancy, leading to steep fall of turbulent energies at the boundaries of the convective zone. Also, as convective instability arises, turbulent energies have to be rebuilt from a low level. Consequently, nonlinear iterations converge slower than in PP models, particularly, during the compression phase, when convective zone sweeps through the outer layers of the model. Sometimes it is necessary to change the time step into smaller value. In case off PP model, constant time step can be used through the whole model integration, without any problems.

5.2.5   Criticism of the PP formulation

The PP formulation, in which superadiabatic gradient, and consequently turbulent source function and convective flux, are restricted to positive values, was not derived within any convective model. It was introduced, without any explanation, in the code of the Florida-Budapest group (Kolláth *et al.* 2002). Although it is claimed that their convection model is essentialy that of Kuhfuß, it is not.

At any point of derivation of the Kuhfuß model, there is no need to truncate the superadiabatic gradient to non-negative values. The whole Kuhfuß formulation is differentiable, and in principle, no serious numerical problems were encountered in implementing it into pulsation hydrocodes. As discussed by Kuhfuss (1986), and later on by Gehmeyr & Winkler (1992b), the advantage of the Kuhfuß model over original Stellingwerf model results from the more correct treatment of convectively stable regions, namely from the inclusion of negative buoyancy effects. Both negative source function and negative convective flux have clear physical interpretation, which I briefly recall below (*see* also Sections 2.4, 2.5)

Physical interpretation of turbulent source function was given in Section 2.4. A simple comparison with MLT theory, shows that the source function is proportional to buoyant acceleration of the convective eddies (Eq. 2.54). In convectively stable regions, this acceleration does not vanish, it becomes negative. Buoyant force is now a restoring force, and slows down the motion of the overshooted eddies, leading to convective stability. By restricting the turbulent source function to positive values only, negative buoyancy is neglected. This is unphysical, and, as shown in this Chapter, has a serious consequences. At the absence of negative buoyancy, turbulent energies are driven through the eddy-viscous forces to significant values, and extend over few pressure scale heights below the main convective zone. Resulting eddy-viscous dissipation, cannot be regarded as physical effect.

Convective eddies that overshoot into convectively stable zones carry both kinetic and thermal energy. Convective eddy overshooted downward from the convective zone is hotter than the surrounding medium. Eddy that overshoots up is cooler. In both cases, the net convective flux is directed downward and hence, is negative. By setting the convective flux to zero, the heat transfer by the overshooted eddies is neglected, too.

Chapter 6

Modeling of double-mode F/1O Cepheid pulsation

In this Chapter, I describe the results concerning the modeling of double-mode F/1O Cepheid pulsation. Search for stable double-mode models is not an easy task, and method of mode selection analysis, adopted in this thesis, will be described in Section 6.1. Then, interesting new results will be presented in Sections 6.2 and 6.3. These results indicate that the success of convective hydrocodes in solving the long-standing problem of modeling the double-mode phenomenon was superficial and the problem remains still open.

6.1 Mode selection analysis

To search for stable double-mode solution, some mode selection analysis method needs to be employed. Such method must be based on nonlinear computations, as linear results can only indicate which full amplitude pulsation states are possible. For many years, a very powerful relaxation technique was used for this purpose (Section 1.3.3). It allows for fast computation of single-mode limit cycles and their stability, in terms of the Floquet stability coefficients. In particular, double-mode pulsation is unavoidable, if two single-mode limit cycles of interest, are simultaneously unstable to perturbation in the other mode. Relaxation technique, working well for radiative computations, fails to predict all the possible solutions that can be found with convective computations. Nonlinear computations of *e.g.*, Kolláth *et al.* (2002) show that stable double-mode solution can coexist with stable single-mode solution (DM/F hysteresis in their computations). In this case, one of the Floquet coefficients is negative, and existence of the double-mode solution cannot be inferred from the stability analysis of single-mode limit cycles. Hence, another method of mode selection analysis, not restricted to study of single-mode solutions, has to be adopted. Such method was proposed by the Florida-Budapest group (*e.g.*, Kolláth *et al.* 2002), and is also adopted in this thesis. It is based on the coupling of direct nonlinear integrations, analysed with analytical signal method, with amplitude equation formalism. This procedure allows to find all the possible pulsation states and allows to determine their stability. Here, the method is briefly described, based on numerical examples.

Single, direct time integration of the model doesn't tell a lot about modal selec-

tion for two reasons. First, the apparently stable full amplitude pulsation can be a transient state. Mode switching time scales can be extremely long, and even long-lasting, seemingly steady pulsations, emerging from the hydrocode, do not prove that the pulsation is indeed stable. Second, there can be more than one stable full amplitude solution, a situation called hysteresis. This is illustrated in Figure 6.1, in which time variation of the surface velocity of the same model, integrated with two different initial conditions, is presented. This model is unstable in both fundamental and first overtone modes, higher order overtones being stable. Integrations were initialized with scaled mixture of the linear velocity eigenvectors, as described in the Figure. Initial phases of model integration are shown in the left panels. Beating between the two initialized modes is clearly visible. After computing of several thousands of pulsation cycles, single-mode pulsation is observed for both integrations, however, with different periods, amplitudes and radial velocity curves. Shorter period, lower amplitude pulsation in the upper panel of Figure 6.1, corresponds to first overtone pulsation, while in the lower panel of that Figure, fundamental mode pulsation is visible. Hence, a hysteresis is present – final pulsation state differs, depending on the initial conditions. Physically, pulsation state depends *e.g.*, on the direction of stellar evolution across the instability strip. Still, one cannot be sure, whether computed single-mode pulsations are the only solutions, and even whether they are stable.

To search for other possible solutions and to determine their stability, one can run the pulsation hydrocode with several initial conditions. Results of such integrations can be represented best in amplitude-amplitude phase-space, in which time evolution of the mode amplitudes is plotted. There are many techniques to extract the time variation of the amplitudes of the individual modes from the hydrodynamical computations. One of them is time dependent Fourier analysis adopted by KOVÁCS, BUCHLER & DAVIS (1987) in their analysis of radiative models. However, much better results are obtained with analytical signal method. This rather old numerical technique (GABOR 1946) was reformulated and applied to stellar pulsation problems by the Florida-Budapest group (*see e.g.*, KOLLÁTH *et al.* 2002). Here, a brief summary of the method, focused on the numerical aspects, is provided. The multi-periodic time series to be analysed, is the relative radius variation, $h(t) = r(t)/r$, computed with the pulsation hydrocode. We are interested in one particular component of frequency ω_k, which is represented as the product of long-term variation and fast oscillation, $A_k(t)e^{i\omega_k t}$. The long-term variation is extracted by following transformation of the input signal, $h(t)$,

$$A_k(t) = \frac{1}{\pi} \int_0^\infty d\omega G(\omega - \omega_k) e^{i\omega t} \int_{-\infty}^\infty dt' h(t') e^{-i\omega t'} \qquad (6.1)$$

First, the Fourier transform of $h(t)$ is computed, then, a desired frequency component is filtered, through a Gaussian window centered on the frequency ω_k, $G(\omega - \omega_k)$. Finally, long term variation of the desired component is extracted through the one-sided reverse Fourier transform.

Analytical signal method extracts smooth time dependence of the pulsation amplitudes of the modes considered, $A_0(t)$ and $A_1(t)$. With such data, results of hydrodynamical direct time integration can be represented as a trajectory in the
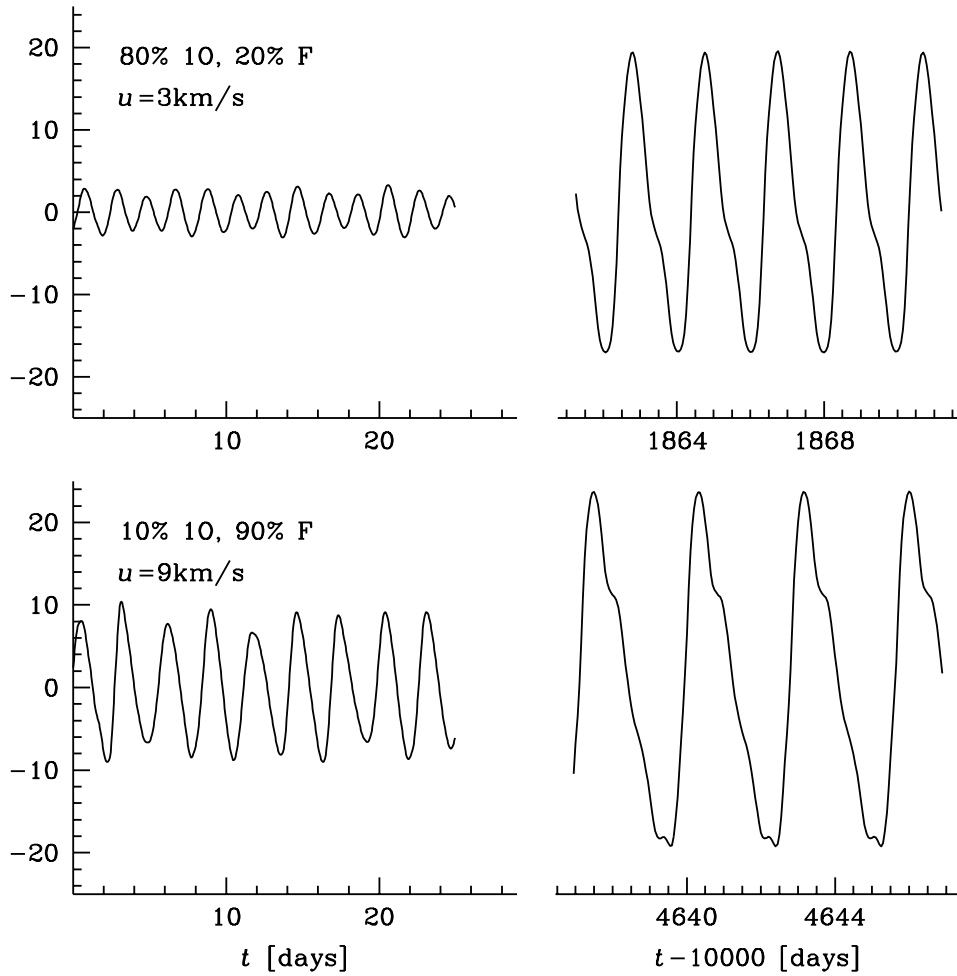
Figure 6.1: Time evolution of the radial velocity of the same model initialized with two different initial conditions (scaled mixtures of the fundamental and first overtone linear velocity eigenvectors) indicated in the Figure (top and bottom panels). Initial phases of integration are shown (left panels), as well as seemingly steady pulsations after computing many thousands of pulsation cycles (right panels).

amplitude-amplitude phase-space. This is illustrated in Figure 6.2 in which several trajectories, corresponding to integrations of the same model with different initial conditions, are plotted. This is the same model, for which time variation of radial velocity is plotted in Figure 6.1. All trajectories run away from the origin ($A_0 = 0$, $A_1 = 0$), as both fundamental and first overtone modes are linearly unstable for the discussed model. After initial fast evolution, trajectories slowly evolve along an arc. Four leftmost trajectories evolve toward first overtone attractor ($A_0 = 0$, $A_1 \neq 0$), remaining three, evolve toward fundamental mode attractor ($A_0 \neq 0$, $A_1 = 0$). Figure 6.2 indicates that two stable single-mode solutions are possible. However, one may still doubt, whether a double-mode solution was not missed in between the fourth and fifth trajectory in this Figure.

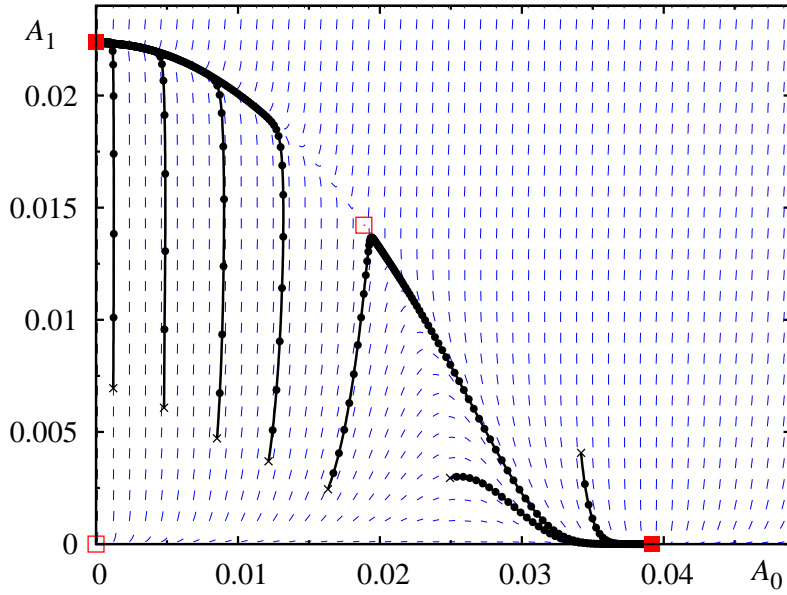To disperse these doubts, and to extract more quantitative information from

Figure 6.2: Results of hydrodynamical integrations of the same model with seven different initial conditions (crosses). Trajectories (solid black lines) were extracted through the analytical signal method. Solid dots along each trajectory are equidistant in time, providing information about evolution speed. Red filled/open squares show the location of the stable/unstable fixed points computed through the AEs. Short blue lines visualize the normalized flow field, $(\dot{A}_0, \ \dot{A}_1)$.

Figure 6.2, amplitude equations (AEs) can be employed to describe the hydrodynamical results. As discussed in Section 1.3.4, AEs describe the time evolution of the mode amplitudes through the set of ordinary differential equations. Their form depends on whether resonances between pulsation modes are present or not. As in the period range occupied by the double-mode F/1O Cepheids no resonances between pulsation modes are found, non-resonant AEs are considered in this Chapter. Truncated at the quintic terms, they are following,

$$
\begin{aligned}
\dot{A}_0 &= \left(\gamma_0 + q_{00}A_0^2 + q_{01}A_1^2 + r_{00}A_0^4 + r_{01}A_1^4 + s_0 A_0^2 A_1^2\right)A_0, \\
\dot{A}_1 &= \left(\gamma_1 + q_{10}A_0^2 + q_{11}A_1^2 + r_{10}A_0^4 + r_{11}A_1^4 + s_1 A_0^2 A_1^2\right)A_1.
\end{aligned}
\tag{6.2}
$$

These equations are part of the general complex amplitude equations system, which, in non-resonant case, can be decoupled into real part for amplitudes (above equations) and imaginary part yielding equations for phases (not relevant in these considerations). In the above equations, $\dot{A}_0$ and $\dot{A}_1$ are time derivatives of the amplitudes of the fundamental and first overtone modes, A_0 and A_1. Linear growth rates of the modes are denoted by γ_i, q_{ii} and q_{ij} are cubic self- and cross-saturation coefficients, r_{ij} and s_i are quintic saturation coefficients.

The use of quintic AEs in necessary to capture the reach topology of solutions found with convective hydrocodes, particularly the coexistence of stable double-mode solution with stable single-mode solution. However, it is not necessary to retain all the quintic coefficients. In the analysis of BUCHLER *et al.* (1999), *r*-terms

were retained, while KOLLÁTH *et al.* (2002) retained *s*-terms only, claiming that they allow for better representation of hydrodynamical results. We follow the latter choice here.

Linear growth rates and saturation coefficients are functions of model parameters; mass, luminosity, effective temperature, chemical composition and depend on the physics put into the model (convective parameters and opacities). Linear growth rates can be computed using linear hydrocode. Situation is much worse for the saturation coefficients. In principle, they can be computed using the static structure of the model and linear eigenvectors. In practise, this is too complicated and cannot be done quantitatively, without invoking some simplifying assumptions. However, hydrodynamical computations allow to determine all the coefficients entering the AEs in a simple and straightforward way. Analytical signal method provides time dependence of mode amplitudes, $A_0(t)$ and $A_1(t)$, from which their time derivatives, $\dot{A}_0$ and $\dot{A}_1$, can be computed at any time of the model evolution. These data can be used to derive the saturation coefficients (and linear growth rates) through a simple linear fitting of amplitudes and their derivatives with Eqs. (6.2). Once saturation coefficients are known, AEs can be analysed, providing the complete mode selection information.

Time independent, constant amplitude solutions of the AEs are called fixed points. They can be easily found numerically (or analytically for the case discussed here) and their stability can be checked through the Hurwitz criteria (HURWITZ 1964). In particular, for a single-mode solutions we have,

$$
\begin{aligned}
A_0 &= \sqrt{-\gamma_0/q_{00}}, \quad A_1 = 0, \\
A_1 &= \sqrt{-\gamma_1/q_{11}}, \quad A_0 = 0,
\end{aligned}
\tag{6.3}
$$

for the fundamental and first overtone fixed points, respectively. Linear stability of these solutions (with respect to perturbation in the other mode) is determined by the values of stability coefficients,

$$
\begin{aligned}
\gamma_{1,0} &= \gamma_1 + q_{10}A_0^2 = \gamma_1 - \gamma_0\frac{q_{10}}{q_{00}}, \\
\gamma_{0,1} &= \gamma_0 + q_{01}A_1^2 = \gamma_0 - \gamma_1\frac{q_{01}}{q_{11}},
\end{aligned}
\tag{6.4}
$$

for the fundamental and first overtone fixed points, respectively. Negative value of the above coefficients means that respective fixed points are stable. In case of quintic AEs consider here (with *s*-terms only), analytical expressions for the two possible double-mode solutions can be given, too. Stable fixed points are attractors of the system, and trajectories evolve toward them. Unstable fixed points repel the trajectories.

Fixed points correspond to steady nonlinear pulsations. Stable, single-mode fixed points correspond to stable limit cycle pulsations. Stability coefficients given in Eqs. (6.4), are directly related to the Floquet coefficients of the limit cycles. Red filled squares in Figure 6.2 correspond to stable fixed points, while open squares to unstable fixed points. Their location was computed based on the values of saturation coefficients derived from fitting the AEs to the seven visible trajectories. No doubt is left that only two stable, single-mode solutions are possible for the model under discussion. The only double-mode solution is unstable and repels the trajectories.

Blue, short lines in Figure 6.2, visualize the normalized flow field ($\dot{A}_0$, $\dot{A}_1$) computed through the AEs. At each point these lines show the expected direction of evolution. A close inspection of Figure 6.2 shows that AEs provide a very good description of the hydrodynamical results.

Described methods can be used for detailed study of the modal selection along a sequence of models, *e.g.*, of constant mass/luminosity and varying effective temperature. To this purpose, hydrodynamical computations are performed for several models of different T_{eff} along the sequence. Next, amplitude equations are fitted to the hydrodynamical trajectories computed through the analytical signal method, yielding the values of saturation coefficients and linear growth rates for these models. Then, simple interpolation can be used to obtain the values of saturation coefficients and linear growth rates, and consequently to establish the modal selection at any temperature along a sequence. The numerical pipeline to perform this analysis was written by the author. To compute the Fourier transforms entering Eq. (6.1), subroutines from the FFTPACK5 library (SWARZTRAUBER 1984) are used.

6.2   Double-Mode F/1O Cepheid Models – Revisited

In this Section, I present the revision of the current knowledge concerning the modeling of the double-mode F/1O Cepheids. The new results indicate that the great success of convective hydrocodes in modeling the double-mode behaviour (*see* Section 2.6.3) was superficial, and resulted form incorrect assumptions made in PP model. Short motivation behind the computations presented in this Chapter is given in Section 6.2.1. Detailed comparison of modal selection along a sequences of NN and PP models is provided in Section 6.2.2. Resulting explanation of the double-mode behaviour computed with PP convection is given in Section 6.2.3. Short discussion of these new and unexpected results, putting the problem of modeling the double-mode behaviour in new light is contained in Section 6.4.

6.2.1   Motivation

Several papers were published concerning convective double-mode Cepheid and RR Lyrae models. All these models are non-resonant. Except of a single RR Lyrae model computed with the Vienna code (FEUCHTINGER 1998), they were all computed with the Florida-Budapest code. Published surveys of double-mode pulsation focused on dynamical aspects of the phenomenon. Except more detailed analysis of RR Lyrae models (SZABÓ *et al.* 2004), no detailed comparison of the theoretical models with observations was done. In case of Cepheid models, even the theoretical Petersen diagram was not published for the nonlinear models. Light and radial velocity curves were not compared, neither, although the amplitudes of the models are claimed to be smaller than observed (KOLLÁTH & BUCHLER 2001). Extensive model surveys computed by the Florida-Budapest group indicated that stable double-mode solutions appeared quite naturally as soon as turbulent convection was included in the model. Also, the presence of such solutions did not depend strongly on the exact values of convective parameters and specific effects included in the

model. Location of the double-mode domain in the HR diagram depended on these factors, but not its existence (KOLLÁTH *et al.* 2002). The modal selection was found to depend on the strength of the eddy viscosity. For the lowest values of the eddy-viscous parameter, double-mode domain didn't exist. For higher values of eddy viscosity it appeared first coexisting with stable fundamental mode solution (DM/F hysteresis), and then, being the only stable solution in some particular domain in the HR diagram (KOLLÁTH *et al.* 1998, KOLLÁTH & BUCHLER 2001).

Despite extensive work of the Florida-Budapest group, still many questions remained unanswered. Probably the most important is, how turbulent convection brings up stable double-mode solutions. Turbulent convection has to be crucial, as purely radiative models fail to reproduce the double-mode behaviour. However, it was not analysed which factor of turbulent convection is essential. KOLLÁTH *et al.* (2002) pointed out that turbulent convection brings up the double-mode solutions, through modification of the stellar structure, in such a way, that self-saturation exceeds the cross-saturation. This is however, only observation that necessary condition for the double-mode behaviour to arise, is fulfilled (*see* Section 1.4.3, and later in this Chapter), and cannot be regarded as satisfactory explanation of the phenomenon.

To study the nature of the double-mode behaviour and to test the convective codes described in this thesis, extensive search for the double-mode solutions was conducted. Despite the claim of KOLLÁTH *et al.* 2002 that double-mode models are easily found, no sign of double-mode behaviour was noticed. The obvious conclusion was, that differences between convective models adopted in our code and in the Florida-Budapest code can be crucial. Different treatment of radiative losses (Section 2.4.1) seems unimportant, as in many double-mode models published, radiative losses were neglected (*e.g.*, KOLLÁTH *et al.* 1998, 2002). Analysis presented in Section 5.1 indicates that also different treatment of eddy-viscous terms should play a minor role. However, to minimize the differences between Florida-Budapest codes and ours, all the model sequences were computed once again with eddy viscosity in the form of Kolláth (this form of eddy viscosity is used consistently in all the models presented in this Chapter). As expected, double-mode behaviour was still missing. The only remaining difference between the two discussed codes was the different treatment of convectively stable regions (NN convection in our and PP convection in Florida-Budapest codes). Indeed, this difference turned out to be crucial as is shown in the forthcoming Sections.

6.2.2   NN *versus* PP model sequence

The search for stable double-mode behaviour was conducted along a specific sequence of models characterized by constant mass, $M = 4.5 M_\odot$, constant luminosity, $L = 1143.5 L_\odot$ (SZABÓ *et al.* 2007 $M - L$ relation) and Galactic chemical composition, $X = 0.7$, $Z = 0.02$. In all computations OPAL opacities (IGLESIAS & ROGERS 1996) computed for the solar mixture of GREVESSE & NOELS (1993) were used. Such choice of parameters is motivated by the model survey of KOLLÁTH & BUCHLER (2001). According to their survey, in Cepheid model sequence of $4.5 M_\odot$, double-mode domain extends over relatively large range of effective temperatures. For the basic analysis two sets of convective parameters were adopted, namely sets
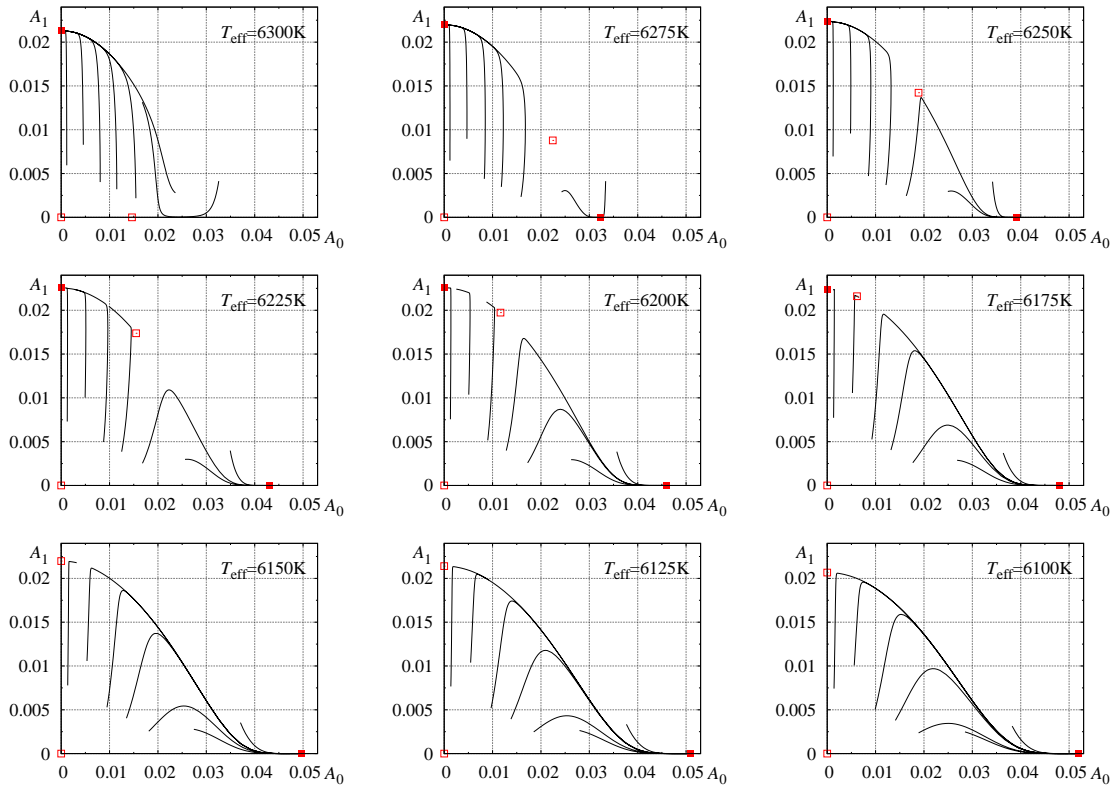
Figure 6.3: Results of hydrodynamical integrations for nine consecutive Cepheid models along a sequence of constant luminosity. Effective temperatures of the models are indicated in each panel. Trajectories were extracted through the analytical signal method. Solid and open squares mark the location of stable and unstable solutions, respectively. These were computed using the saturation coefficients and linear growth rates derived from the fit of the amplitude equations to the hydrodynamical trajectories. Computations for NN convection model adopting convective parameters of set A.

A and B of Table 4.1. In the following, most attention is payed to the simplest convective model, characterized by the parameters of set A, that is without radiative losses, turbulent flux and turbulent pressure. Models are computed either with our standard treatment of convection (NN models) or with turbulent source function and convective flux restricted to non-negative values (PP formulation, adopted in the Florida-Budapest code). To avoid confusion, NN/PP prefix is put in front of the set name, in the following (*e.g.*, we compare model sequences NN-A and PP-A).

Mode selection is analysed along a sequence of models for which both fundamental and first overtone modes are simultaneously unstable. Consecutive models differ in effective temperature by 25 K. For each model in the sequence, several hydrodynamical computations are performed. Results for nine consecutive models of sets NN-A and PP-A are presented in Figures 6.3 and 6.4, respectively.

Modal selection analysis proceed as described in Section 6.1. For each model of Figures 6.3 and 6.4, quintic amplitude equations are fitted to the hydrodynamical trajectories, yielding the values of saturation coefficients and linear growth rates. Values of the former are presented in the upper and in the lower panels of Figure 6.5,
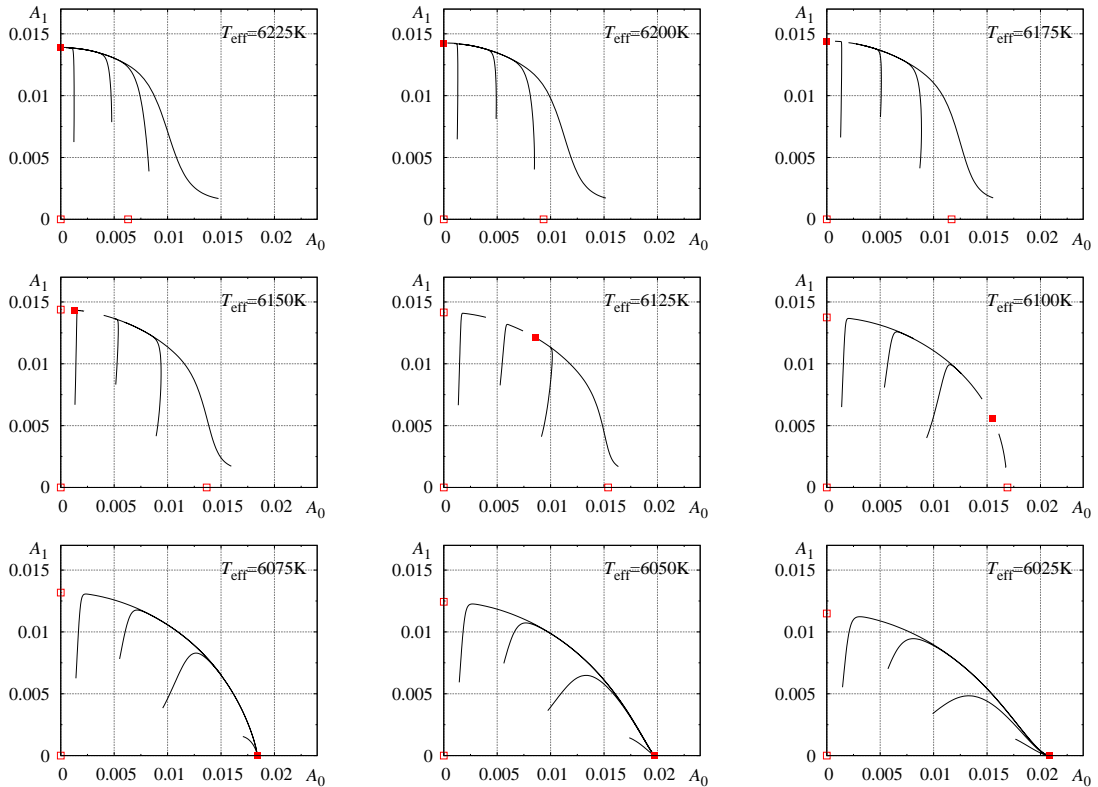
Figure 6.4: Results of hydrodynamical integrations for nine consecutive Cepheid models along a sequence of constant luminosity. Effective temperatures of the models are indicated in each panel. Trajectories were extracted through the analytical signal method. Solid and open squares mark the location of stable and unstable solutions, respectively. These were computed using the saturation coefficients and linear growth rates derived from the fit of the amplitude equations to the hydrodynamical trajectories. Computations for PP convection model adopting convective parameters of set A.

for sets NN-A and PP-A, respectively. All the saturation coefficients vary smoothly along a model sequence. Once the saturation coefficients and linear growth rates are known, all the possible solutions and their stability can be computed. In Figures 6.3 and 6.4 stable solutions are marked with solid squares, while unstable with open squares. Modal selection can be established not only for the computed hydrodynamical models, but also at any temperature along a model sequence. This is done through the linear interpolation of the saturation coefficients and linear growth rates. This allows to find a possibly very narrow (in effective temperature) double-mode domain, *e.g.*, between the models for which direct hydrodynamical computations were done.

Before discussing the modal selection along sequences NN-A and PP-A, a remark concerning the linear growth rates has to be done. Linear growth rates can be derived using above fitting procedure (fitted growth rates, in the following), or they can be computed using linear code (computed growth rates). Comparison of fitted and computed growth rates revealed significant differences, depending on the convection model used (PP or NN) and the order of the amplitude equations considered. In
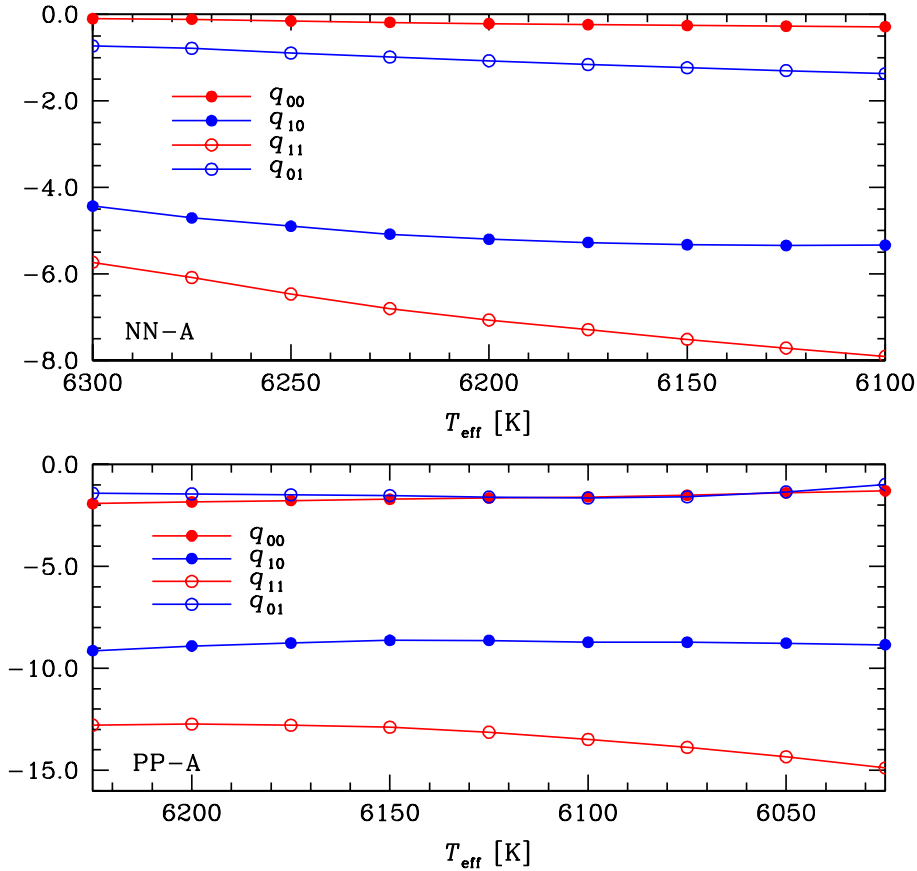
Figure 6.5: Cubic saturation coefficients along a sequence of Cepheid models of constant luminosity. Computations either for NN (upper panel) or PP convection (lower panel). In both cases convective parameters of set A were adopted. Coefficients were derived through fitting the amplitude equations to the hydrodynamical trajectories presented in Figures 6.3 (NN models) and 6.4 (PP models).

case of NN convection, and quintic amplitude equations, as described in Section 6.1, computed and fitted growth rates of the first overtone mode agree very well ($\pm 5\%$), which is not the case for the fundamental mode. Here a systematic difference is noted – fitted growth rates are on average higher by 15 per cent than the computed ones. Such difference is not unexpected. Fitted growth rates result from the description of hydrodynamical computations through the truncated series of amplitude equations. Consequently, use of the higher order terms in the amplitude equations, should reduce the discrepancy. Indeed, with seventh order aplitude equations, agreement between the fitted and computed growth rates is satisfactory also for fundamental mode of NN models ($\pm 3\%$). Situation is much worse in case of PP models. Even with seventh order amplitude equations, fitted growth rates are systematically smaller (by $\approx 15\%$) for both fundamental and first overtone modes. This is likely caused by the not differentiable nature of the PP model. To study the modal selection, either fitted or computed growth rates can be used. In case of NN models either choice is equally

good. However, in case of PP models, fitted growth rates allow for better description of hydrodynamical trajectories. Therefore, in the following, linear growth rates are fitted. This is the same choice as adopted by the Florida-Budapest group (KOLLÁTH *et al.* 2002, SZABÓ *et al.* 2004).

Now, I will discuss the modal selection along model sequences of sets NN-A and PP-A. Detailed results are displayed in Figures 6.6 and 6.7 for sets NN-A and PP-A, respectively. In the upper panels of these Figures stability coefficients of the single-mode solutions (Eqs. 6.4) are plotted. In the lower panels, amplitudes of all the solutions (stable and unstable) are displayed.

- **NN-A model sequence.** Individual hydrodynamical models for this sequence are displayed in Figure 6.3, while results of detailed mode selection analysis in Figure 6.6. In this model sequence no stable double-mode solution is found. At the highest temperatures, only pulsation in the first overtone is possible. Fundamental mode limit cycle is unstable, however, only in a narrow temperature range to the red of the linear fundamental mode blue edge. Soon after amplitude of the fundamental mode exceeds the amplitude of the first overtone and at temperature $\approx 6290\,\mathrm{K}$, fundamental mode limit cycle becomes stable. As first overtone limit cycle is still stable, unstable double-mode solution must appear. It extends in the temperature range, $\approx 6290 - 6165\,\mathrm{K}$. At the cool edge of this either-or domain, first overtone limit cycle loses stability. Double-mode solution disappears and the only stable solution is fundamental mode pulsation. Through the either-or domain amplitude of the fundamental mode solution is significantly higher than the amplitude of the first overtone solution. Qualitatively, described mode selection is exactly the same as in case of radiative models (Section 1.4.3), and can be inferred from the stability coefficients of the single-mode solutions.

- **PP-A model sequence.** Individual hydrodynamical models for this sequence are displayed in Figure 6.4, while results of detailed mode selection analysis in Figure 6.7. In this model sequence, stable double-mode solutions are visible already in hydrodynamical models (Figure 6.4). In three consecutive models ($T_{\mathrm{eff}} = 6150\,\mathrm{K}$, $6125\,\mathrm{K}$ and $6100\,\mathrm{K}$) double-mode attractors are clearly visible. For these models, they are the only attractors of the system, single-mode solutions being unstable. Double-mode domain extends in the temperature range slightly larger than $50\,\mathrm{K}$ ($\approx 6150 - 6100\,\mathrm{K}$). At higher temperatures only pulsation in the first overtone is possible, while at lower temperatures fundamental mode pulsation domain extends. At each temperature only one solution is stable, no hysteresis is possible. Across the double-mode domain amplitudes of the unstable single-mode limit cycles (fundamental and first overtone modes) are comparable.

Described modal selection scenarios for NN and PP models are typical. In Section 6.3 an extensive survey of NN models with various convective parameters and various physical properties will be presented. In all these model sequences either-or domain is present instead of the double-mode domain.

Considering the PP models, double-mode solutions are easily found, independent of the exact values of convective parameters. For set PP-B (including effects of
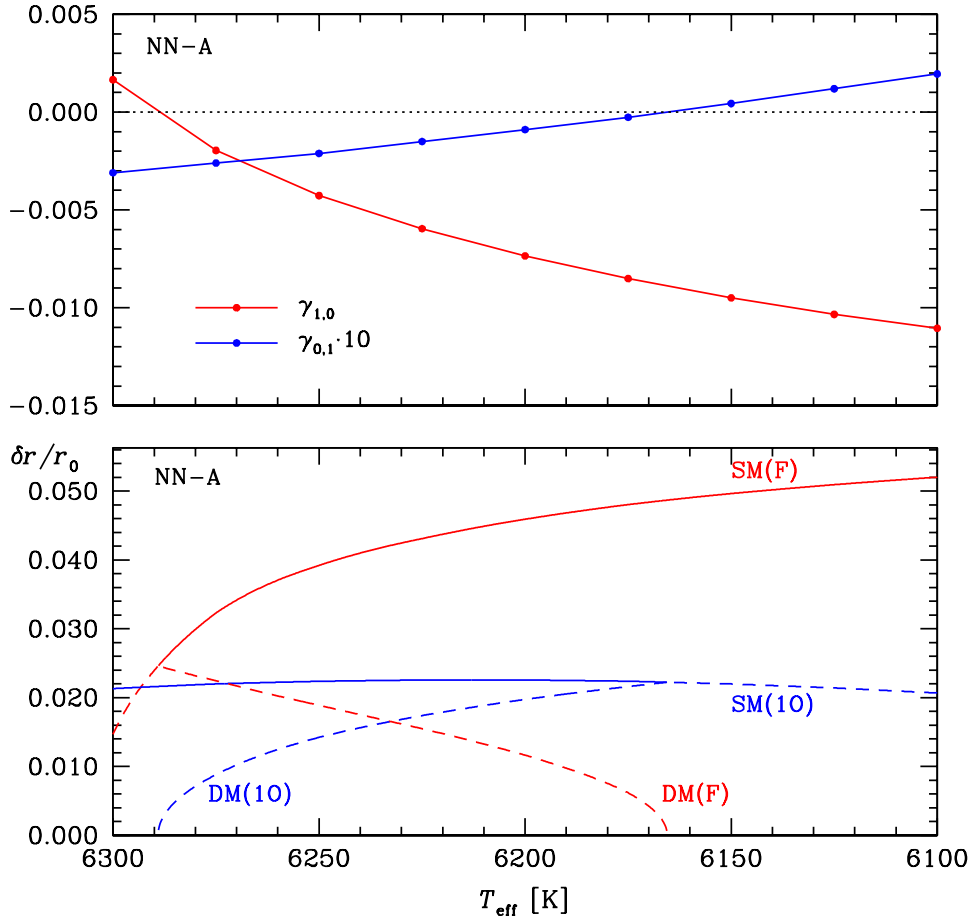
Figure 6.6: Stability coefficients of the single-mode limit cycles (upper panel) and amplitudes of all the possible solutions (lower panel) for a sequence of Cepheid models of constant luminosity. In the lower panel stable solutions are plotted with solid, while unstable solutions with dashed lines. Amplitudes of the fundamental and first overtone modes are plotted with red and blue lines, respectively. Computations for NN convection model adopting convective parameters of set A.

turbulent pressure and turbulent flux), double-mode domain, extending over more than $50\,\mathrm{K}$, is also found. Other sets of convective parameters were examined too, and stable double-mode solutions were a rule, rather than an exception. Detailed results of PP model surveys and their properties, will not be presented here. Qualitatively the same results are found as in the works of the Florida-Budapest group.

Hysteresis models, for which stable double-mode solution coexists with stable fundamental mode solution, are also found. As these solutions are qualitatively different from those presented for sets NN-A and PP-A, it is worth to present these curious models in more detail. They also demonstrate that consideration of the quintic amplitude equations is a must, as such solutions cannot be captured with cubic amplitude equations. Models under consideration adopt convective parameters essentially of set B, however, with lower value of the eddy-viscous parameter ($\alpha_m = 0.15$ instead of $\alpha_m = 0.25$), set H in the following. Hysteresis is clearly visible
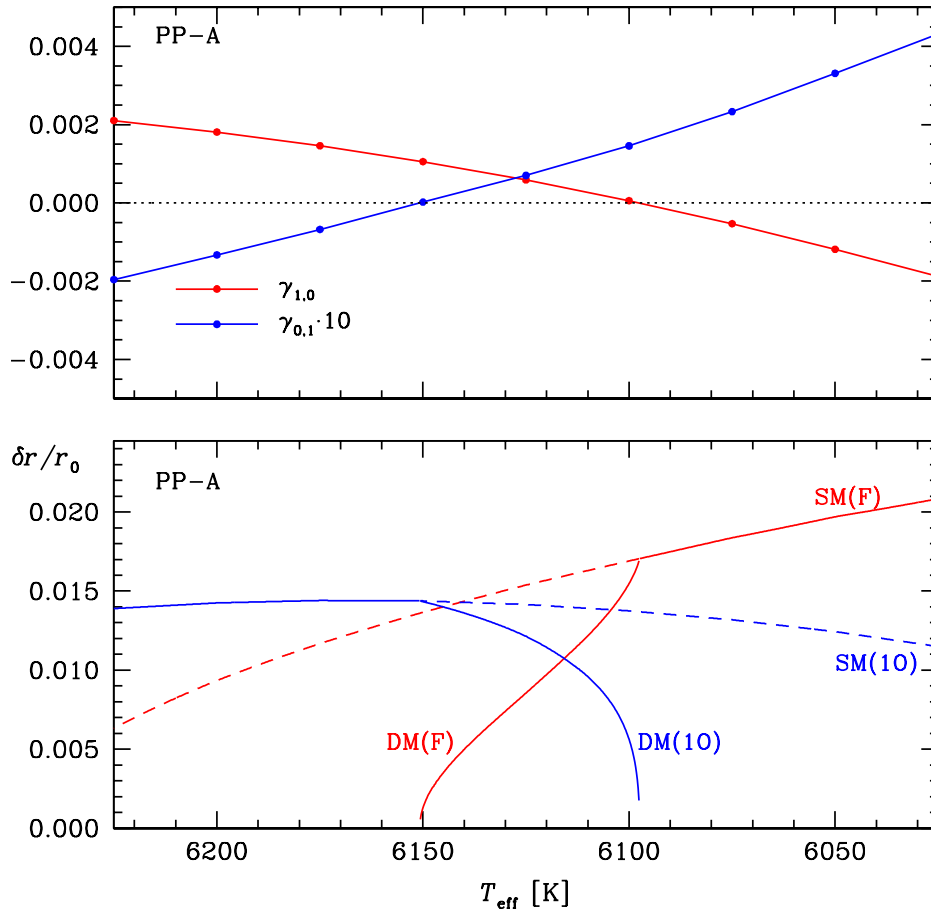
Figure 6.7: Stability coefficients of the single-mode limit cycles (upper panel) and amplitudes of all the possible solutions (lower panel) for a sequence of Cepheid models of constant luminosity. In the lower panel stable solutions are plotted with solid, while unstable solutions with dashed lines. Amplitudes of the fundamental and first overtone modes are plotted with red and blue lines, respectively. Computations for PP convection model adopting convective parameters of set A.

for model of temperature $5775\,\mathrm{K}$, and results of hydrodynamical integrations for this model are presented in Figure 6.8. Two leftmost trajectories evolve toward stable double-mode attractor, one of them from the left and other from the right. The third trajectory evolves toward fundamental mode solution. Necessarily, second unstable double-mode solution must be present between the two stable attractors. In Figure 6.9 amplitudes of all stable and unstable solutions are plotted, together with stability coefficients of the single-mode solutions, for the entire sequence of models. Moving from high temperatures toward lower ones, first, only pulsation in the first overtone is possible. As fundamental mode limit cycle becomes stable ($\approx 5785\,\mathrm{K}$), unstable double-mode solution appears. A narrow either-or F/1O domain is present in a temperature range $\approx 5785 - 5778\,\mathrm{K}$. At the cool edge of this domain ($\approx 5778\,\mathrm{K}$) first overtone limit cycle loses its stability. First overtone still can saturate the pulsation instability, however, not alone. Extremely narrow double-mode domain appears

in a temperature range $\approx 5778 - 5769\,\mathrm{K}$. At the same temperatures stable fundamental mode solution is also possible. At the temperature $\approx 5769\,\mathrm{K}$, both double-mode solutions (stable and unstable) meet and disappear. For lower temperatures only fundamental mode pulsation is possible. For the discussed case, the presence of the double-mode domain cannot be inferred from the values of stability coefficients of single-mode solutions (upper panel of Figure 6.9). At no temperature, both single-mode limit cycles are simultaneously unstable. However, it is worth to notice that across the DM/F hysteresis domain, fundamental mode limit cycle is only weakly stable (it was unstable just $10\,\mathrm{K}$ to the blue).
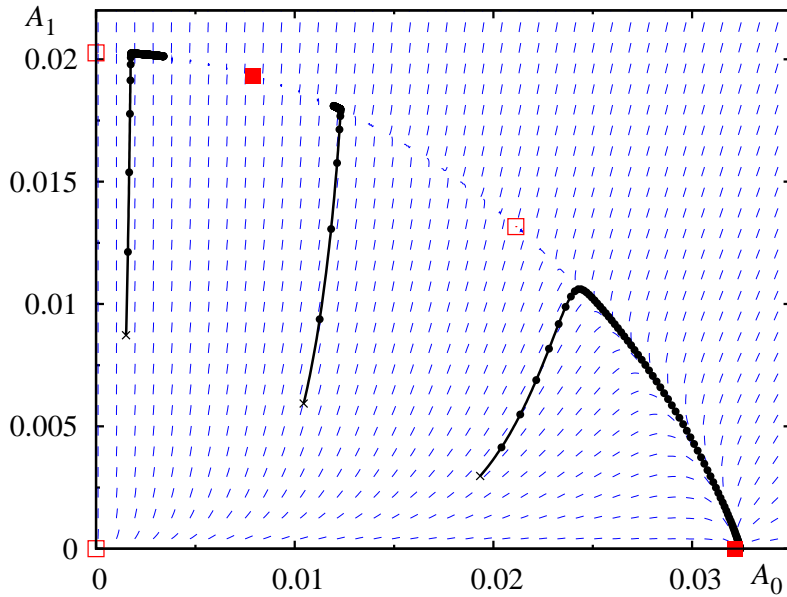

Figure 6.8: Results of hydrodynamical integrations, illustrating the DM/F hysteresis. Symbols and lines as in Figure 6.2. Computations for PP convection model adopting convective parameters of set H.

6.2.3   Explanation for the double-mode behaviour observed in PP models

There are two physical mechanisms that can be responsible for the double-mode pulsation, resonant and non-resonant. In case of the double-mode F/1O Cepheids, the latter mechanism has to be responsible for most of the observed double-mode variables, as no low order resonances are found in the period range occupied by the double-mode variables. All the models discussed in this Chapter are non-resonant. In non-resonant scenario double-mode pulsation arises due to feed-back effect of pulsation on mean radial structure of the star. In the language of saturation coefficients, the effects of mode self-saturation must exceed the effects of cross-saturation, so neither of the modes can saturate the pulsation instability alone. Some useful conditions can be derived through considering the amplitude equations. Using cubic amplitude equations, DZIEMBOWSKI & KOVÁCS (1984) (*see* also BUCHLER &
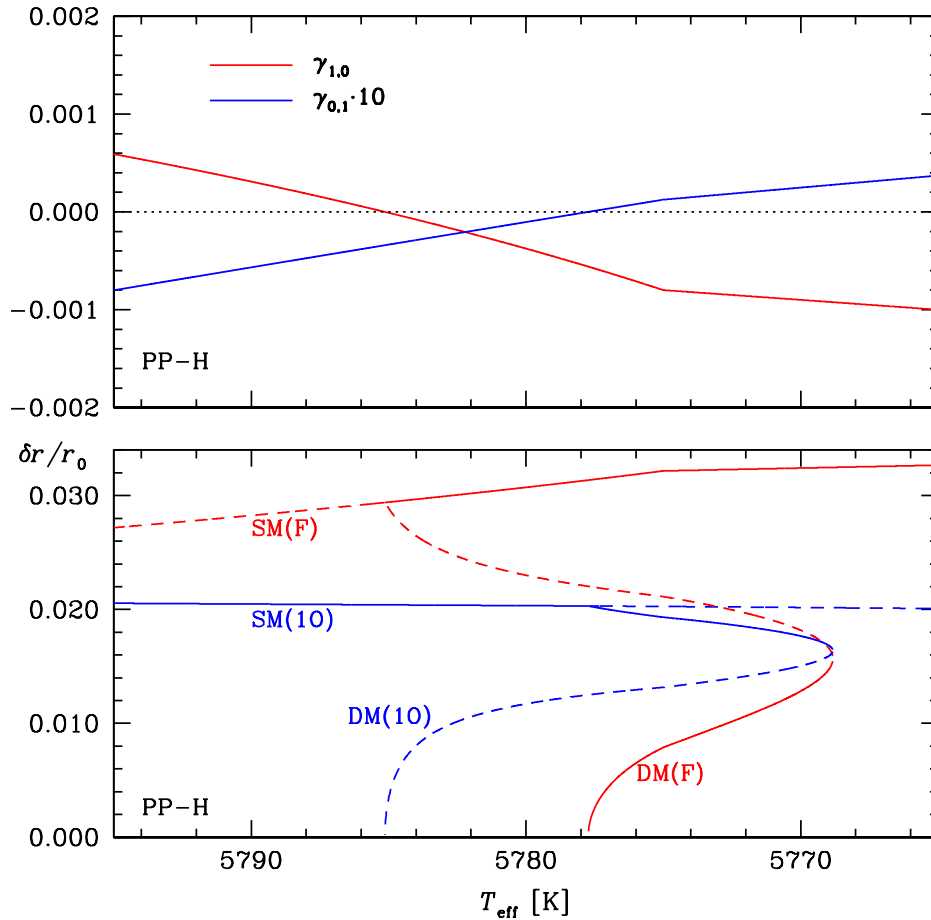
Figure 6.9: The same as Figure 6.7, but for models computed with convective parameters of set H.

KOVÁCS 1986b) showed that necessary condition for the F/1O double-mode pulsation to occur, is the positive value of the following discriminant,

$$\mathcal{D} = q_{00}q_{11} - q_{01}q_{10}. \tag{6.5}$$

Here, we consider quintic amplitude equations, however, the physical picture behind the above condition remains unchanged. Detailed inspection of the values of saturation coefficients displayed in Figure 6.5 shows that indeed, $\mathcal{D} > 0$ for PP model sequence, while $\mathcal{D} < 0$ for NN models. This was noticed already by KOLLÁTH *et al.* (1998). Later, KOLLÁTH *et al.* (2002) gave two reasons for the occurrence of double-mode pulsation in convective model computations. First reason was the increase of self-saturation coefficients relative to cross-saturation coefficients, which leads to $\mathcal{D} > 0$. However, this is just the claim that necessary condition for the double-mode behaviour to occur is fulfilled in the convective models. Second reason was the necessity to include the quintic terms in amplitude equations to describe the hydrodynamical results. This prevents overlooking double-mode solution coexisting with stable single-mode solution. Again, this is not an explanation, but claim of the fact that topology of solutions computed with convective hydrocodes can be richer,

than in case of radiative computations.

The surveys of double-mode models computed with PP convection published by the Florida-Budapest group, as well as test computations described in this Chapter indicate that neither ingredient of the turbulent convection model is crucial in bringing up the stable double-mode solutions. They appear quite naturally in the expected period range, independent of the exact values of the convective parameters and specific effects included in model computation (KOLLÁTH *et al.* 2002). Hence, the existence of stable double-mode solutions is inherent property of PP convection model.

The analysis how PP convection increases the self-saturation effects relative to cross-saturation effects was never done. In practise, it is difficult to perform such analysis, as saturation coefficients are very complicated functions of the model structure. Therefore, it is hard to uncover the cause of the double-mode pulsation, based on PP model sequence, alone. However, comparison with NN model sequence leads to a simple, but disappointing explanation. Double-mode behaviour in PP models results from the neglect of negative buoyancy effects, and hence, its cause is artificial.

Double-mode F/1O Cepheid pulsations are found only in PP models. They are not found in NN models, which have exactly the same model parameters (masses, luminosities, chemical composition, convective parameters, mesh parameters) as PP models, but include the effects of negative buoyancy. As this is the only difference between NN and PP models, it is natural to assume that the neglect of negative buoyancy effects in PP models is crucial for the double-mode behaviour to arise. Indeed, more detailed comparison of NN and PP models presented below, confirms this hypothesis.

In Chapter 5, the differences in fundamental mode Cepheid models computed with NN and PP convection were described and explained. Models computed adopting PP convection have lower amplitudes. Comparison of Figures 6.6 and 6.7, as well as comparison of corresponding models displayed in Figures 6.3 and 6.4 shows that indeed, amplitudes of both fundamental and first overtone modes in PP models are reduced as compared to NN models, however, not by the same factor. Amplitude of the fundamental mode is reduced much more than the amplitude of the first overtone mode. This is clearly visible in Figure 6.10, in which results of hydrodynamical integrations conducted with NN and PP convection, for one particular model ($T_{\mathrm{eff}} = 6125\,\mathrm{K}$) of set A, are compared. Amplitudes of both single-mode solutions are much smaller in case of PP model. Amplitude of the fundamental mode fixed point is reduced by a factor of ≈ 3.3, while amplitude of the first overtone fixed point by factor twice as small, ≈ 1.5.

The reasons behind amplitude reduction in PP models were explained in Section 5.2.2 of the previous Chapter. Due to neglect of negative buoyancy effects, turbulent energies are not damped effectively in convectively stable regions of the model. To the contrary, they are driven to relatively high level through the eddy-viscous forces. This driving occurs at the cost of pulsation, which is reflected in the strong eddy-viscous damping in the internal convectively stable layers of the model. Just described results show that the internal eddy-viscous damping in PP models, acts differentially on pulsation modes, having stronger effect on the fundamental mode. This is clearly visible in the nonlinear eddy-viscous work integrals of the fundamental and first overtone modes. They are displayed in Figure 6.11.
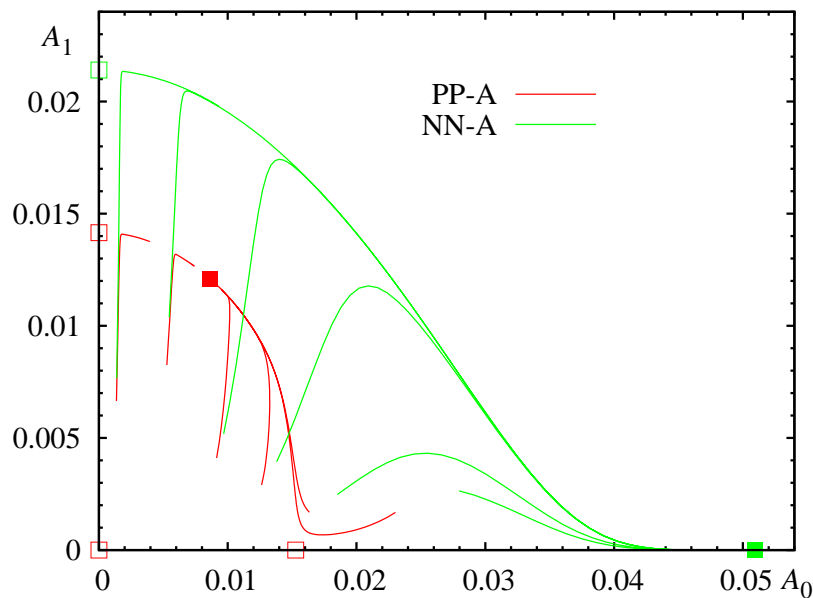
Figure 6.10: Comparison of hydrodynamical trajectories computed with NN (green lines) and PP (red lines) convection models for the same Cepheid model of set A ($T_{\text{eff}} = 6125\,\text{K}$). Solid and open squares mark the location of the computed stable and unstable fixed points, respectively.

For the discussed PP-A model sequence, two stable single-mode solutions cannot coexist. The domain of stable fundamental mode pulsation is separated from the domain of first overtone pulsation by the double-mode domain, in which both single-mode solutions are unstable. Therefore, work integrals are plotted for two models of different effective temperatures, lying on both sides of the double-mode region (*see* Figure 6.4). Fundamental mode work integrals are plotted for model with $T_{\text{eff}} = 6075\,\text{K}$, while first overtone mode work integrals for model hotter by $100\,\text{K}$ ($T_{\text{eff}} = 6175\,\text{K}$). Work integrals for a single-mode solutions do not vary strongly in such narrow temperature range, and hence, such comparison is justified. In Figure 6.11 internal eddy-viscous damping below the envelope convective zone (below zone ≈ 70) is clearly visible. The range of this damping is different for both modes, however. For the fundamental mode, eddy-viscous damping extends down to zone ≈ 20, while for the first overtone it becomes negligible already at zone ≈ 40, slightly below the first overtone pulsation node. The run of work integrals (lower panel of Figure 6.11) indicate that the different range of eddy-viscous dissipation in the internal zones, for fundamental and first overtone modes, is responsible for differential reduction of their amplitudes, as compared to NN models, in which internal eddy-viscous dissipation is not present, at all.

The different range of the internal eddy-viscous dissipation for the fundamental and first overtone modes is a consequence of different properties of these modes in the deep interior of the model. For the first overtone, pulsation node is located there, which leads to different turbulent energy profile in the internal zones as compared to the model pulsating in the fundamental mode. Turbulent energy profiles for both discussed models are presented in Figure 6.12. Significant turbulent ener-
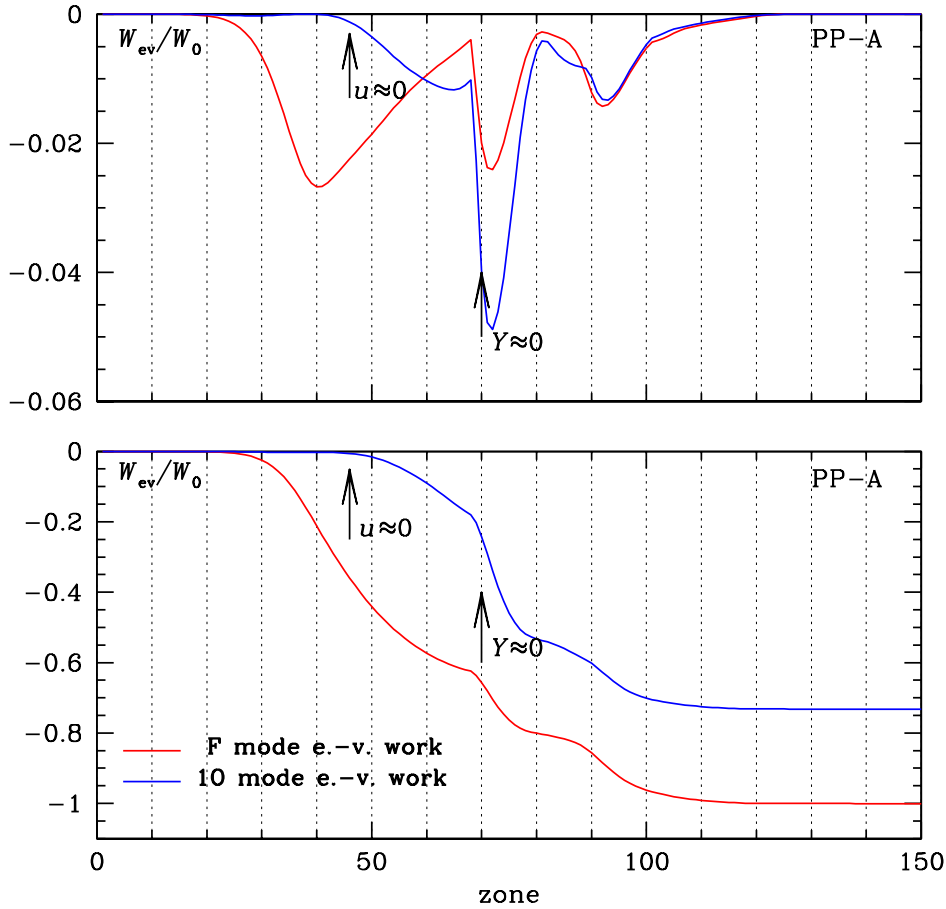
Figure 6.11: Nonlinear eddy-viscous differential work integral (upper panel) and work integral (lower panel), for the fundamental mode and first overtone models discussed in the text. Work integrals are normalized by the same factor, W_0, equal to the surface value of eddy-viscous work integral for the fundamental mode.

gies below envelope convection zone are clearly visible. Turbulent energy profile for the fundamental mode is qualitatively the same as discussed in the previous Chapter. For the first overtone, a drop in the turbulent energies is visible in a region slightly below zone 40. Pulsation node of the first overtone is located few zones above. Reasons behind the fall of turbulent energies below the pulsation node are easy to understand. As described in the previous Chapter, turbulent energies in convectively stable, internal zones of the model, are built up by the eddy-viscous forces. In case of Kolláth eddy viscosity adopted through this Chapter, turbulent energies are driven by the $-p_\nu(\mathrm{d}V/\mathrm{d}t)$ term. Eddy-viscous pressure, p_ν, changes its sign below the pulsation node, at the local maximum of first overtone velocity (see Eq. 2.75). As p_ν and $(\mathrm{d}V/\mathrm{d}t)$ change their sign in opposite direction, the product $-p_\nu(\mathrm{d}V/\mathrm{d}t)$ is non-negative, and approaches to zero below the location of the pulsation node[1]. Consequently, eddy-viscous driving is not effective below the node

---

[1]Described picture is qualitatively the same if Kuhfuß form of eddy viscosity is used. This is

location, and the overall level of turbulent energy in the internal zones is smaller for the model pulsating in the first overtone. This is best visible in Figure 6.13, in which snapshots of turbulent energy profiles for both fundamental and first overtone modes at arbitrary pulsation phase ($\phi \approx 0.5$) are presented (as is well visible in Figure 6.12, turbulent energy profile in the internal zones is almost independent of the pulsation phase). Of course below the envelope convective zone of the PP model, turbulent energy profile and eddy-viscous damping are directly related to each other (as this damping reflects the driving of turbulent energies at the cost of pulsation). Hence, the different turbulent energy profiles for fundamental and first overtone modes, displayed in Figure 6.13, allow to understand the different ranges of the internal eddy-viscous damping for these modes, visible in Figure 6.11. As turbulent energies become lower than $\approx 10^8$ erg/g, eddy-viscous dissipation becomes negligible. Also the drop in the turbulent energy profile of the first overtone model is accompanied by the zero in the differential eddy-viscous work integral (which is however, barely visible in the upper panel of Figure 6.11).
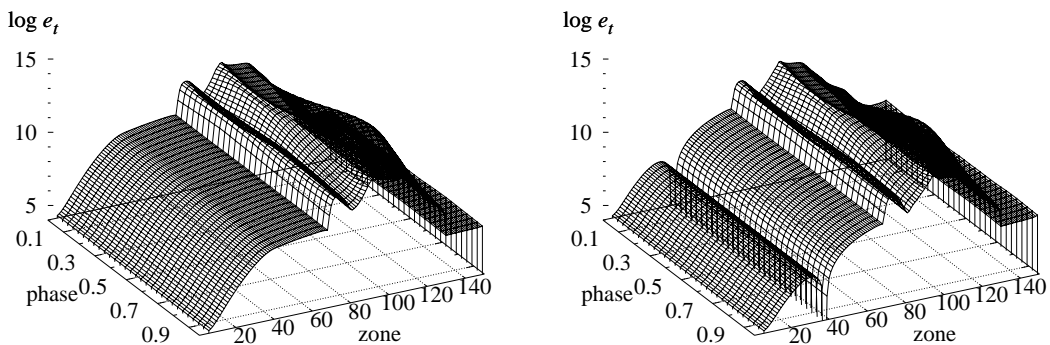

Figure 6.12: Turbulent energy profiles for the fundamental mode (left panel) and first overtone (right panel) models adopting PP convection, discussed in the text.

Reduction of the amplitudes of the fundamental and first overtone modes in the PP models, as compared to NN models, is crucial in bringing up the double-mode behaviour in the former models. As is visible in Eq. (6.4) amplitude of the mode is the main factor related to its stability. Lower the amplitude of the mode, more unstable it is against perturbations in the other modes. Comparison of the NN and PP model sequences shows that the amplitudes of the PP models are reduced, however, by different amount for each pulsation mode. As amplitude of the fundamental mode is reduced much stronger than the amplitude of the first overtone, we expect that fundamental mode would be more unstable in the PP model sequence. This is clearly visible in the upper panel of Figure 6.14, in which stability coefficients of both single-mode limit cycles (or fixed points) are plotted along a sequence of PP-A (black lines) and NN-A models (red lines). It is useful to analyse this Figure together with Figures 6.6 and 6.7, in which amplitudes of all possible solutions are

---

because E_q term, Eq. (3.8), contains the square of the same velocity derivative as p_ν, and hence, E_q also approaches zero below the first overtone pulsation node.
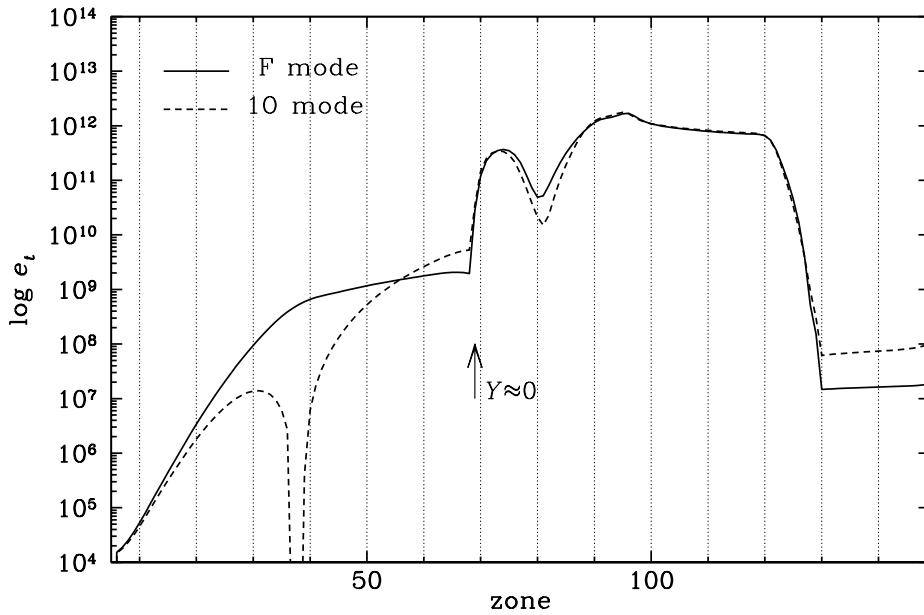
Figure 6.13: Snapshots of turbulent energy profiles displayed in Figure 6.12, at pulsation phase, $\phi \approx 0.5$.

plotted, for NN and PP models, respectively.

Moving across the instability strip from blue to the red, stability of the fundamental mode limit cycle increases ($\gamma_{1,0}$ decreases), while stability of the first overtone limit cycle decreases ($\gamma_{0,1}$ increases). This is a common property of the discussed stability coefficients, well visible in Figure 6.14 for both NN and PP models. The run of stability coefficient of the first overtone mode, $\gamma_{0,1}$, is very similar for both NN and PP models. First overtone limit cycle becomes stable at temperature $\approx 6150\,\mathrm{K}$. To the contrary, considering the stability of the fundamental mode limit cycle, dramatic difference between NN and PP models is visible. In NN model sequence fundamental mode becomes stable at relatively high temperature ($6280\,\mathrm{K}$), soon as its amplitude becomes higher than the amplitude of the first overtone limit cycle (Figure 6.6). For lower temperatures its amplitude is much higher than the amplitude of the first overtone and consequently, it is firmly stable against perturbation in the first overtone. At no temperature along NN model sequence both modes are simultaneously unstable. Nor one of the modes is close to being unstable, while other already is, which would give some hope for stable double-mode solution coexisting with stable single-mode solution (hysteresis, *cf.* Figure 6.9, particularly the run of stability coefficients across the double-mode domain). Stable double-mode pulsation is not possible for NN sequence. Situation is very different for PP sequence. Moving across the instability strip to the red, fundamental mode limit cycle becomes less unstable, that is $\gamma_{1,0}$ decreases, however, much slower than in case of NN sequence. It becomes stable at temperature $\approx 6100\,\mathrm{K}$, cooler by $\approx 200\,\mathrm{K}$ as compared to NN models. For higher temperatures amplitude of the fundamental mode is lower or comparable to the amplitude of the first overtone. As first overtone limit cycle becomes unstable at temperature $\approx 6150\,\mathrm{K}$, in a temperature range from $\approx 6150\,\mathrm{K}$
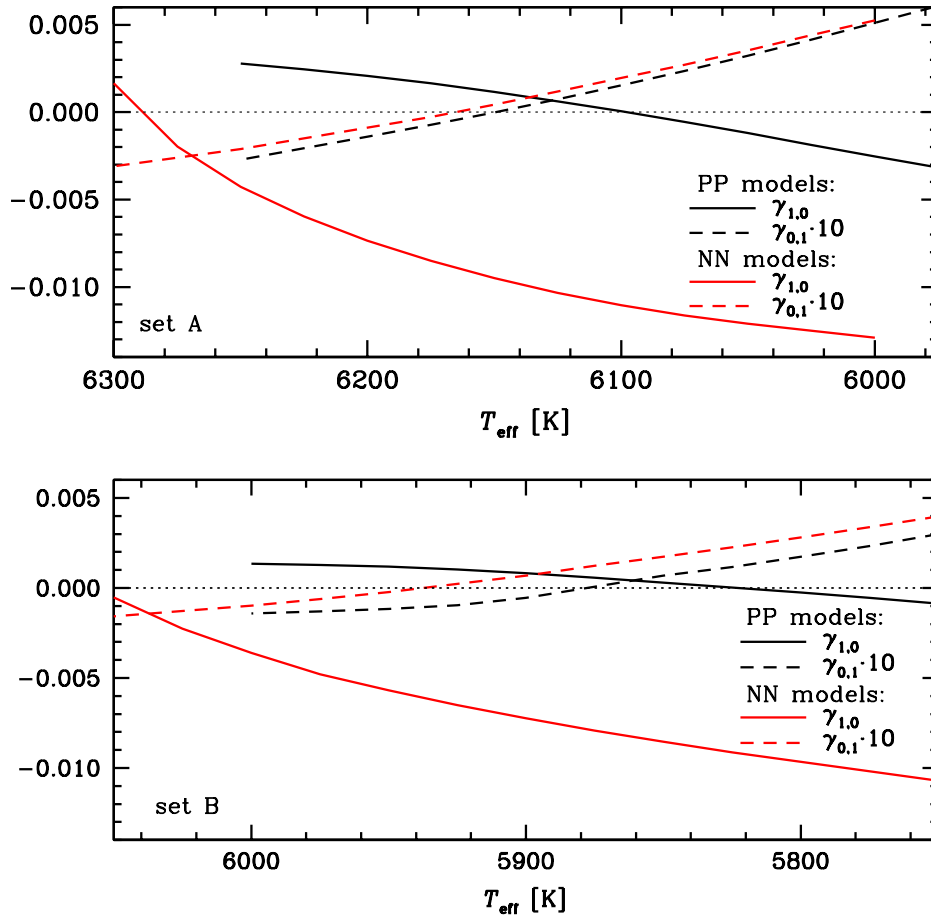
Figure 6.14: The run of stability coefficients of single-mode fixed points, along a sequence of models adopting convective parameters of set A (upper panel) and B (lower panel). In each panel, results obtained with PP (black lines) and NN convection (red lines) are shown.

to $\approx 6100\,\mathrm{K}$, both fundamental and first overtone limit cycles are simultaneously unstable, giving rise to double-mode domain. Existence of stable double-mode solution is possible, because amplitude of the fundamental mode is reduced significantly enough, so it remains unstable in a temperature range in which first overtone is already also unstable.

The above discussion was based on model computations for the simplest possible convective model, with parameters of set A. However, presented results are general and valid independent on exact values of convective parameters. In Chapter 5 it was shown that the internal eddy-viscous damping in convectively stable zones is present independent of model parameters. This damping is the crucial factor giving rise to stable double-mode pulsation. Test computations with different sets of convective parameters fully confirm the results presented for set A. In particular, in the lower panel of Figure 6.14, the run of stability coefficients for NN and PP model sequences, adopting convective parameters of set B (Table 4.1) are presented. Results are qualitatively the same as for set A.

Considerations presented in this Chapter clearly identify the cause of stable double-mode behaviour computed with PP convection by the Florida-Budapest group. The neglect of negative buoyancy effects leads to significant turbulent energies in deep convectively stable layers of the model. These energies are driven at the cost of pulsation through eddy-viscous forces. These forces depend on the pulsation properties of the model, particularly on the pulsation induced velocity field, which is different for the fundamental and first overtone modes. Therefore, turbulent energy profiles and connected eddy-viscous damping are different for the two pulsation modes. Eddy-viscous damping is stronger for the fundamental mode, and consequently its amplitude, as compared to NN models, is reduced much more than the amplitude of the first overtone. Otherwise stable and dominant (in NN models), fundamental mode becomes unstable in PP models, that is it cannot saturate the pulsation instability alone, allowing for simultaneous excitation of the first overtone.

Described explanation is disappointing. Crucial assumption of the PP convection model – the neglect of negative buoyancy effects – is physically not correct, and so are the double-mode F/1O Cepheid models published up to date.

Described mechanism is somewhat similar to the mechanism causing the 2:1 resonant doubly-periodic pulsation. In the resonant mechanism, amplitude of one of the two linearly unstable modes is reduced through the resonant coupling to a linearly damped parasite mode, which acts as an energy sink. Otherwise dominant, resonantly coupled mode, is no longer able to saturate the other linearly unstable mode, allowing its growth. In PP models internal eddy-viscous damping acts similarly to the parasite mode. Although it reduces amplitudes of both of the modes, the effect is much stronger for the fundamental mode.

6.3   Search for stable double-mode behaviour with NN convection

The mechanism leading to stable double-mode pulsation in case of PP models, described in the previous Section, cannot be operational in NN models. In NN treatment, turbulent energies are effectively damped in convectively stable regions through the negative buoyancy effects, and internal eddy-viscous damping is not present. For the discussed two sets of convective parameters, A and B, stable double-mode solution was not found with physically correct NN convection model.

Existence of the double-mode F/1O Cepheids is an observational fact. Physically correct pulsation hydrocode, should reproduce the observed modal selection. Failure to do so, indicates that some important physics is still missing in the code. Therefore, it is extremely important to conduct more extensive search for stable double-mode behaviour with correct NN description. Such model survey, focused on F/1O Cepheids, will be described in this Section.

As already described, search for the stable double-mode phenomenon is not an easy task. First, convective model we use has several free parameters. Stable double-mode solutions can exist only for some specific combination of these parameters. Hence, extensive parameter study is necessary. Second, the domain of physical parameters for which stable double-mode solution may exist, is expected to be narrow, as double-mode pulsators are rather rare as compared to their single-mode coun-

terparts. Therefore, sets with various physical parameters should be considered, too. To avoid overlooking the stable double-mode solution restricted to a narrow temperature range, or coexisting with stable single-mode solution, modal selection analysis, as described in Section 6.1, should be carefully applied. As such computations are extremely time consuming, some special strategy must be used, which is briefly described below.

We consider two sets of model parameters which will be called basic in the following. For convective parameters of these sets we adopt sets A and B of Table 4.1, repeated in Table 6.1 to allow comparison with other sets considered in this Section. I recall, that set A represents the simplest possible convective model, without turbulent pressure, turbulent flux (overshooting) and radiative losses, while in set B, the former two effects are turned on. In all sets considered in this Section, flux limiter is not included, and eddy viscosity in the form of Kolláth (*see* Section 5.1) is used. All model sequences considered here run horizontally across the HR diagram, that is models have constant mass and luminosity and varying effective temperature. For the two basic sets, physical parameters are, $M = 4.5\mathrm{M_\odot}$, $L = 1143.5\mathrm{L_\odot}$ (Szabó *et al.* 2007 $M - L$ relation), and chemical composition corresponding to the Galaxy, $X = 0.7$ and $Z = 0.02$. Such parameters assure that pulsation periods and period ratios fall within the ranges for the observed double-mode variables. By default OPAL opacities (Iglesias & Rogers 1996) computed for the solar mixture of Grevesse & Noels (1993) are adopted.

Our search for stable double-mode solution proceed in two directions. First, we fix the physical parameters of the models and vary the convective parameters, only. Second, we keep convective parameters frozen to the values of sets A and B, and vary the physical parameters of the models. All considered sets of model parameters are collected in Table 6.1. For each model sequence several models, differing in effective temperature by $25\,\mathrm{K}$, are considered. These models have both fundamental and first overtone modes simultaneously linearly unstable. Models lying close to the boundaries of such double-mode instability domain are not computed, except if it is necessary to infer the modal selection. This is because of low growth rates of such models, implying long-lasting computations. In most cases however, the modal selection along the whole instability strip can be inferred without doubt from the computations limited to models occupying its central parts. For each considered sequence, modal selection is established. We analyse not only whether the stable double-mode solution exists for a given model sequence or not, but try to select the most promising set of model parameters. This is done through comparing the stability results (stability coefficients of the single-mode limit cycles, $\gamma_{0,1}$ and $\gamma_{1,0}$) for a given sequence, with results for a corresponding basic set (A or B). Such comparison can be qualitative only, as differences in the convective or physical parameters of the model sequences, lead to the shift of the computed instability domains. Results of the previous Section indicate that sets in which fundamental mode limit cycle is less stable at the hot side of the instability strip are promising. Also model sequences in which one of the limit cycles in unstable, while the other is only marginally stable are wanted, as they give hope for the hysteresis solution.

The described model survey yielded null result. No stable double-mode solution could be found. Below, the results are briefly summarized, first for the model sequences in which convective parameters of the models were varied (Section 6.3.1),

Set	α	α_m	α_s	α_c	α_d	α_p	α_t	γ_r	M	L	X	Z
						Basic sets:						
A	1.5	0.20	1.0	1.0	1.0	0.0	0.00	0.0	4.5	1143.5	0.700	0.020
B	1.5	0.25	1.0	1.0	1.0	1.0	0.01	0.0		. . .		
					Other sets considered:							
A1	1.3	0.20	1.0	1.0	1.0	0.0	0.00	0.0		. . .		
A2	1.7	0.20	1.0	1.0	1.0	0.0	0.00	0.0		. . .		
A3	1.5	0.25	1.0	1.0	1.0	0.0	0.00	0.0		. . .		
A4	1.5	0.25	0.8	1.0	1.0	0.0	0.00	0.0		. . .		
A5	1.5	0.25	1.0	0.8	1.0	0.0	0.00	0.0		. . .		
A6	1.5	0.25	1.0	1.0	1.2	0.0	0.00	0.0		. . .		
A7	1.5	0.25	0.8	0.8	1.2	0.0	0.00	0.0		. . .		
A8	1.5	0.30	1.0	1.0	1.0	0.0	0.00	1.0		. . .		
B1	1.5	0.20	1.0	1.0	1.0	1.0	0.10	0.0		. . .		
B2	1.5	0.20	1.0	1.0	1.0	1.0	0.50	0.0		. . .		
AC1	1.5	0.20	1.0	1.0	1.0	0.0	0.00	0.0	4.5	1143.5	0.716	0.010
AC2				. . .					4.5	1143.5	0.756	0.004
AC3				. . .					4.5	1143.5	0.726	0.004
AC4				. . .					4.5	1143.5	0.700	0.012
AL1				. . .					4.5	902.5	0.700	0.020
AL2				. . .					4.5	404.4	0.700	0.020
AM				. . .					4.0	751.9	0.700	0.020
BC1	1.5	0.25	1.0	1.0	1.0	1.0	0.01	0.0	4.5	1143.5	0.716	0.010
BC2				. . .					4.5	1143.5	0.756	0.004
BL1				. . .					4.5	902.5	0.700	0.020
BL2				. . .					4.5	404.4	0.700	0.020
BM				. . .					4.0	751.9	0.700	0.020
AZ	1.5	0.20	1.0	1.0	1.0	0.0	0.00	0.0	4.5	1143.5	0.700	0.030

Table 6.1: All sets of convective and physical model parameters that were examined in search for stable double-mode pulsation with NN convection model. Convective parameters, α_s, α_c, α_d, α_p and γ_r, are given in the units of standard values (Table 2.1).

and next, for the model sequences with varying physical parameters (Section 6.3.2). The plots of stability coefficients of the single-mode limit cycles for each model sequence under discussion are displayed in Appendix C.

6.3.1   Effects of varying convective parameters

In the upper part of Table 6.1, parameters of the models in which convective parameters were varied, are given. Physical parameters of all the models are the same. Sets A1–A8 neglect the effects of turbulent pressure and turbulent flux, and thus, computed modal stability should be compared with modal stability for basic set A. Turbulent pressure and turbulent flux are included in sets B1–B2, and results of model computations for these sets should be compared to those of set B. In none of the discussed sets stable double-mode solution was found. Trends among stability coefficients of the single-mode solutions are briefly discussed below, and graphically

presented in Figures C.1–C.10 of Appendix C.

- **Effects of varying the mixing length, α.** Effects of varying the mixing length parameter, while keeping other alphas fixed are studied in sets A1 (decreased value of α, $\alpha = 1.3$) and A2 (increased value of α, $\alpha = 1.7$). The comparison of single-mode stability coefficients with those of set A is presented in Figures C.1 and C.2.

  The change in the mixing length parameter shifts the instability strip toward lower (decreased α, set A1) or higher (increased α, set A2) effective temperatures. However, the overall modal selection remains qualitatively the same as for set A. Fundamental mode limit cycle becomes stable at high temperatures, when first overtone limit cycle is still firmly stable.

- **Effects of varying the strength of eddy viscosity, α_m.** In set A3 eddy-viscous parameters is slightly higher than in set A ($\alpha_m = 0.25$ instead of $\alpha_m = 0.2$. Eddy viscosity plays a special role in the discussed models. It can be used to adjust the pulsation amplitude, as it is the main source of dissipation in the model. As discussed (Section 6.2.1), it plays a crucial role in bringing up the stable double-mode behaviour in PP models, having also an effect on the modal selection.

  The comparison of single-mode stability coefficients of set A3 with those of set A is presented in Figure C.3. In comparison to set A, with increased value of α_m we observe that first overtone limit cycle is more unstable. Stability of the fundamental mode limit cycle is very similar as in case of set A. Hence, with further increase of α_m the F/1O either-or domain would shrink, giving some hope for the appearance of stable double-mode solution. However, by increasing the strength of eddy viscosity, models become linearly more stable and stronger increase of α_m would stabilize the first overtone.

- **Effects of varying the α_s, α_c and α_d.** In basic sets A and B, these parameters are set to their standard values (Section 2.4.3), resulting from the comparison of the static, time independent Kuhfuß model with the mixing length theory. In sets A4–A6 values of each of these parameters are varied. The α_s and α_c parameters are decreased by 20 per cent (sets A4 and A5) as compared to set A, while value of α_d is increased by 20 per cent (set A6). These changes imply that convection is less vigorous as compared to models of set A, which is assured through decreased strength of buoyant driving of turbulent energies (set A4), decreased efficiency of the convective heat transfer (set A5) and increased rate of turbulent energy decay through the turbulent cascade (set A6).

  The comparison of single-mode stability coefficients of the discussed sets with those of set A is presented in Figures C.4, C.5 and C.6 for sets A4, A5 and A6, respectively. Qualitatively the same picture is observed for all these sets. Stability of the first overtone limit cycle remains almost unchanged as compared to set A, while fundamental mode limit cycle is more unstable, particularly, it becomes stable at lower temperatures. Described results are promising. Therefore, additional computations were done for set A7, corresponding to

the merged sets A4–A6 ($\alpha_s = 0.8$, $\alpha_c = 0.8$ and $\alpha_d = 1.2$). Unfortunately, stability results for this set (Figure C.7) are qualitatively the same as for set A.

- **Effects of radiative losses, γ_r.** In basic sets A and B effects of radiative cooling of the convective elements are neglected. In set A8 they are turned on. Parameter γ_r is set to its standard value as discussed in Section 2.4.3. Inclusion of radiative losses results in significantly higher model amplitudes, as convection is less efficient. To compensate the effect and to assure reliable model amplitudes, eddy viscosity parameter is increased in set A8 ($\alpha_m = 0.3$).

  The comparison of single-mode stability coefficients of set A8 with those of set A is presented in Figure C.8. The change in convective parameters leads to shift of the instability strip toward lower temperatures for set A8. Qualitatively the same modal selection is observed as for set A, however, first overtone is even more stable, making the double-mode solution more distant.

- **Effects of turbulent pressure and turbulent flux, α_p and α_t.** Effects of turbulent pressure and turbulent flux are studied in sets B, B1 and B2. In all these sets turbulent pressure is turned on at its full strength ($\alpha_p = 2/3$), while effects of turbulent flux are gradually increased ($\alpha_t = 0.01$ in set B, 0.1 in set B1 and 0.5 in set B2). Also, eddy viscosity is slightly lower in sets B1 and B2 as compared to set B.

  Inclusion of turbulent pressure in the models leads to significant shift of the computed instability strips, making the comparison of the models with and without turbulent pressure difficult. However, as already discussed in Section 6.2.3 (Figure 6.14), qualitatively the same modal selection is observed for sets A and B.

  The comparison of single-mode stability coefficients of the sets B1 and B2 with those of set B is presented in Figures C.9 and C.10. Comparing results for sets B and B1, qualitatively and quantitatively the same results are obtained. Stronger increase of the turbulent flux (set B2) leads to more unstable first overtone limit cycle and more stable fundamental mode limit cycle, particularly at higher temperatures, making the appearance of stable double-mode solution less probable.

6.3.2   Effects of varying physical parameters

In the lower part of Table 6.1, parameters of the models in which physical parameters were varied, are given. Convective parameters of all the models remain frozen to the values adopted for sets A or B. In sets AC1–AC4 and BC1–BC2 effects of varying metallicity and opacity data are studied. In sets AL1, AL2, BL1 and BL2, different luminosities are adopted, while keeping the mass of the models fixed. In sets AM and BM mass is changed (and luminosity, according to the adopted $M-L$ relation). In none of the discussed sets stable double-mode solution was found. Trends among stability coefficients of the single-mode solutions are briefly discussed below, and graphically presented in Figures C.11–C.22 of Appendix C.

- **Effects of varying chemical composition.** In sets AC1–AC3, BC1 and BC2, chemical compositions corresponding to stellar systems of lower metallicity are adopted. Metallicity is slightly lower, while hydrogen abundance slightly higher than in the basic sets. In sets AC1 and BC1 we set $X = 0.716$ and $Z = 0.01$, which corresponds to LMC, while in sets AC2 and BC2 we set $X = 0.756$ and $Z = 0.004$ ($\sim$ SMC). Additionally, higher helium abundance is adopted in set AC3, in which $X = 0.726$ and Z is the same as in set AC2 ($Z = 0.004$).

  The comparison of single-mode stability coefficients for the discussed sets with those of sets A and B is presented in Figures C.11–C.13, C.18 and C.19. Emerging picture is the same for all the sets considered. Lower the metallicity, more stable the fundamental mode limit cycle is. At the hot side of the instability strip, where fundamental mode limit cycle is expected to be unstable, first overtone limit cycle would be firmly stable, thus, prohibiting the occurrence of stable double-mode pulsation.

  In set AC4 the effects of adopting new solar mixture of ASPLUND *et al.* (2004) were checked. The new solar metallicity ($Z = 0.012$) was also adopted for this set. Stability of the first overtone limit cycle is the same as in case of basic set A. Fundamental mode limit cycle is more stable, particularly at higher temperatures, making the stable double-mode solution more distant.

- **Effects of varying model mass.** In sets AM and BM, lower model masses, $M = 4M_{\odot}$ are adopted. Luminosity is also lower according to the adopted $M - L$ relation of SZABÓ *et al.* (2007).

  The comparison of single-mode stability coefficients for sets AM and BM with those of sets A and B is presented in Figures C.17 and C.22. As expected, instability strips are shifted toward higher temperatures. Qualitatively the same modal selection is observed as in case of sets A and B. No tendency toward double-mode solution is visible.

- **Effects of varying the mass/luminosity ratio.** In sets AL1, AL2, BL1 and BL2, luminosity is set to lower values, while keeping the model masses unchanged. In sets AL1 and BL1 luminosity is decreased by 0.1 in $\log L$, while luminosities for sets AL2 and BL2, result from ALIBERT *et al.* (1999) $M - L$ relation for the first crossing of the instability strip.

  Considering the sets with slightly decreased luminosity (AL1 and BL1), stability of the first overtone limit cycle is very similar as for sets A and B. However, fundamental mode limit cycle is more stable at higher temperatures, which is not promising in the context of double-mode pulsation. Situation is much worse for the models obeying the mass-luminosity relation for the first crossing. Here, comparison with sets A and B is rather not possible, due to strong shift of the instability strips. However, it is clearly visible that first overtone limit cycle becomes unstable at low temperatures, far from the blue edge of the instability domain. At these temperatures fundamental mode limit cycle is firmly stable, and stable double-mode pulsation is not possible.

6.4   Discussion of results

Results presented in this Chapter are rather disappointing. We considered the modeling of the F/1O double-mode Cepheids. The origin of the double-mode F/1O Cepheid pulsation, computed with the Florida-Budapest hydrocode (PP convection) was explained. Double-mode pulsation in these models, arose due to unphysical assumption concerning the convectively stable regions, namely from the neglect of negative buoyancy effects. Consequently, the cause of the double-mode pulsation is artificial. We cannot claim that with negative buoyancy effects included in the model (NN convection), non-resonant F/1O double-mode Cepheid pulsation is not possible at all. However, results of extensive parameter study presented in the previous Section, leave little hope for the final success. Thus, the problem of modeling the double-mode F/1O Cepheid pulsation remains open.

Florida-Budapest hydrocode was used to model not only F/1O double-mode Cepheids, but also F/1O double-mode RR Lyrae stars (*e.g.*, SZABÓ *et al.* 2004). It was also claimed that double-mode 1O/2O Cepheid models were computed (KOLLÁTH & BUCHLER 2001), but no details of these models were published since. Results presented in this Chapter concern F/1O double-mode Cepheids. However, the described mechanism leading to stable double-mode pulsation should be operational also in F/1O double-mode RR Lyrae models computed with PP convection. In fact, all such models, except one, were published by the Florida-Budapest group, adopting this unphysical treatment of convectively stable layers. The only double-mode RR Lyrae model computed with other hydrocode, was published by FEUCHTINGER (1998) using the Vienna code. This code adopts the Kuhfuß convection model. In the description of this code (WUCHTERL & FEUCHTINGER 1998, FEUCHTINGER 1999a), no special remarks concerning the treatment of convectively stable regions were made. Therefore, it is natural to assume that the original Kuhfuß prescription (NN convection) was adopted. However, the very good agreement of the first overtone Cepheid models computed with the Vienna and Florida-Budapest hydrocodes, claimed by FEUCHTINGER, BUCHLER & KOLLÁTH (2000), leave some doubt whether indeed, NN convection is adopted in the Vienna code. On the other hand, only one double-mode F/1O RR Lyrae model was published. In fact it was not proved beyond doubt, that the computed double-mode state is stable. It was only demonstrated that the fundamental and first overtone amplitudes do not change significantly for few thousands of pulsation cycles. In principle, this is possible for a transient.

It is also worthy to notice that to the best knowledge of the author no double-mode model was published by the Italian group, despite enormous number of computed convective Cepheid and RR Lyrae models. In their code (BONO & STELLINGWERF 1992, 1994; Section 2.6.1), negative buoyancy effects are included, and the described mechanism, bringing up the stable double-mode behaviour in PP models, cannot work. The lack of double-mode models in the computations with the Italian code is not surprising, in the light of results presented in this Chapter.

Situation can be more complicated in case of 1O/2O double-mode Cepheid models. It was claimed that such models were computed with the Florida-Budapest code (KOLLÁTH & BUCHLER 2001), although no details had been given. First and second overtones have pulsation nodes in convectively stable regions of the Cepheid models, and hence, the driving of turbulent energies by the eddy-viscous forces is

not as effective for these modes as it is for the fundamental mode. Consequently, we expect smaller amplitude reduction in comparison to NN models. As a result, stability properties of the overtone modes should not differ significantly between NN and PP treatment. This is exactly what we see for the first overtone mode in Figure 6.14. The search for stable double-mode 1O/2O Cepheid models with NN convection model will be described in Chapter 8.

Although the results presented in this Chapter are rather disappointing – incorrect assumption was identified as a cause of the published double-mode F/1O Cepheid models, and no double-mode models were found with the corrected treatment – they show the direction in which the correct solution has to be searched for. We need a mechanism that would strongly decrease the amplitude of the fundamental mode. However, it is hard to identify such mechanism. Internal eddy-viscous damping, as is observed in PP models is not probable. It requires significant turbulent energies in the internal model zones, below the envelope convection zone. But in these regions, negative buoyancy damps the turbulent motions very effectively. Turbulent motions in the horizontal direction are not affected by the buoyant forces. However, generation of such turbulence through the mean gas motion, is not likely to be strong in slowly rotating, radially pulsating Cepheids and RR Lyrae stars.

Turbulence can be generated in the internal parts of the model in convective zone associated with the iron opacity bump. In this zone, eddy-viscous damping, having strong effect on the fundamental mode might arise. In the discussed models however, the iron opacity bump is too weak to produce a significant convective zone. Possible revision of opacity data can in principle change the situation. To check whether the iron bump induced convective zone can be helpful in bringing up the stable double-mode solution, some models adopting parameters of set AZ (Table 6.1) were computed. This set has the same parameters as set A, except the metallicity which is enhanced ($Z = 0.03$). Indeed, stronger convective zone and associated significant turbulent energies develop in the internal parts of the models. However, they are restricted to a very narrow region, spanning no more than 4 zones of the model. Eddy-viscous damping associated with this layer is present, however, much weaker than the damping in other parts of the model. What is most important, this damping is too weak to affect the mode amplitudes significantly.

The difficulty of modeling the double-mode F/1O Cepheid pulsation can also originate from oversimplified treatment of convection. More sophisticated models are needed. Improvements are necessary not only in the modeling of turbulent correlations entering the model. Also, three dimensional models are needed, as turbulent convection is essentially three dimensional phenomenon. Some attempts to develop more elaborate models were recently made (*e.g.*, STÖKL 2008), however, their numerical implementation is still at its infancy.

As more advanced convective models are not yet available, the best thing to do is to check the possibilities of the best model available – the original Kuhfuß model implemented in the described codes. In Chapter 8 the search for stable double-mode 1O/2O Cepheid pulsation will be conducted. As resonances can play a significant role in these models, first, some interesting resonant multi-mode models will be discussed in the following Chapter.

Chapter 7

Resonant excitation of the doubly-periodic pulsation

In this Chapter, I discuss the resonant mechanism of bringing up stable multi-mode pulsation. Presented models are mainly of theoretical interest, as they either disagree with observations, or their agreement is not satisfactory. Discussed models are radiative, except Cepheid models presented in Section 7.3. This allows to study the modal selection and underlying physical processes with the relaxation scheme, with the help of the Floquet stability coefficients (*see* Sections 1.3.3, 1.4.3). Such analysis is hard to conduct for convective models that are described in Section 7.3 and in the following Chapter. Methods of mode selection analysis presented in Section 6.1 are difficult to implement for the resonant case, as appropriate amplitude equations are much more complex than non-resonant ones. Also, relaxation scheme was not implemented in the convective hydrocodes. Therefore, discussion of resonant radiative models provides a necessary background to understand the resonant convective models. Additionally, radiative models that will be described, represent a very curious cases, not discussed earlier in the literature (spiral attractors, resonant double-mode domain coexisting with non-resonant one).

Two types of resonances will be analysed in this Chapter. In Section 7.1 the 2:1 resonance will be discussed, while in Sections 7.2 and 7.3, some results concerning higher order parametric resonance will be given. Both these resonances can be conductive in bringing up stable 1O/2O multi-mode Cepheid pulsation (Chapter 8).

7.1 Excitation of the multi-mode pulsation through the 2:1 resonance

The effects of the 2:1 resonance on radial stellar pulsation were extensively studied in the literature (*see* Sections 1.4.2, 1.4.3 and references therein). The resonances between the fundamental and the second overtone, $2\omega_0 = \omega_2$, and between the first and fourth overtones, $2\omega_1 = \omega_4$, are crucial in shaping the light and radial velocity curves of fundamental mode and first overtone Cepheids, respectively. The former resonance is responsible for the Hertzsprung bump progression observed in the fundamental mode Cepheids, while the latter for characteristic progression of the Fourier decomposition parameters visible in the first overtone Cepheids (*see*

Section 1.4.2).

In the 2:1 resonant models, linearly damped, higher frequency parasite mode, is excited at the cost of a resonantly coupled linearly unstable lower frequency mode. Due to nonlinear phase lock phenomenon (*e.g.*, DZIEMBOWSKI & KOVÁCS 1984), nonlinear frequencies fulfill the resonance condition exactly, and parasite mode is not visible as a separate frequency, but manifests in the distortion of the singly-periodic light/radial velocity curve. Hence, bump Cepheids are in fact, double-mode but singly-periodic pulsators.

In this Chapter, we consider the effects of resonances on modal selection. The 2:1 resonance can be conductive in exciting the doubly-periodic pulsation, which is of particular interest in this thesis. The relevant mechanism was described in detail by DZIEMBOWSKI & KOVÁCS (1984). Here, we focus on exciting the doubly-periodic F/1O pulsation, but the discussion is general, and applies to double-overtone pulsation (Chapter 8) as well. In the most interesting case, both fundamental and first overtone modes are linearly unstable, while second overtone is linearly damped. At the absence of the resonance, each of the two linearly excited modes (or only one of them) is able to saturate the pulsation instability alone, leading to either-or domain (or single-mode pulsation domain). This is the usual case in the radiative computations, as well as in convective computations with turbulent convection model including the negative buoyancy effects (NN model, Sections 1.4.3 and 6.3). In the resonant scenario, linearly unstable fundamental mode is coupled to the linearly damped second overtone. Due to resonant energy transfer, second overtone is excited at the cost of the fundamental mode. Amplitude of the fundamental mode becomes lower. Consequently, it is no longer able to saturate the pulsation instability alone, allowing for the simultaneous growth of the first overtone. Due to nonlinear phase-lock phenomenon, emerging triple-mode pulsation is apparently doubly-periodic (second overtone is not visible as a separate frequency). Considering the Floquet coefficients (or stability coefficients of the amplitude equation's fixed points), the resonance is responsible for the increase in $\eta_{1,0}$ ($\gamma_{1,0}$), as the fundamental mode limit cycle becomes less stable (and eventually unstable) against perturbation in the first overtone. If the fundamental mode is destabilized in a parameter range at which first overtone limit cycle is also unstable, multi-mode state is unavoidable.

Hydrodynamical models corresponding to the described situation were computed by KOVÁCS & BUCHLER (1988) and by BUCHLER, MOSKALIK & KOVÁCS (1990). These are purely radiative models. Kovács & Buchler found doubly-periodic RR Lyrae models excited through the $2\omega_0 = \omega_3$ resonance (*see* Section 1.4.3). Buchler, Moskalik & Kovács found a doubly-periodic Cepheid model connected with the resonance shaping the Hertzsprung bump progression, $2\omega_0 = \omega_2$. In most cases, however, this resonance does not induce the doubly-periodic pulsation. Typically, the resonance center, and thus, the decreased stability of the fundamental mode, occurs in a temperature range in which first overtone limit cycle is firmly stable. Thus, if fundamental mode limit cycle is destabilized, this will lead to the first overtone pulsation, as was demonstrated by BUCHLER, GOUPIL & PICIULLO (1997). Schematic run of the Floquet coefficients corresponding to this case is presented in the upper panel of Figure 7.1. To excite the simultaneous pulsation in the fundamental and in the first overtone, destabilization of the fundamental mode should occur at lower temperatures, at which first overtone limit cycle is also unstable.

Schematically this is illustrated in the bottom panel of Figure 7.1. Such models were found by the author (SMOLEC 2009) accidentally, while testing the described nonlinear convective hydrocode in the radiative limit (all convective parameters set to zero). The shift of the instability domain of the fundamental mode was caused by the use of nonstandard $M-L$ relation. Apart from direct time integrations, Floquet stability analysis of the limit cycles was conducted, using purely radiative relaxation hydrocode. Computed models are not relevant from observational point of view, as they occur at much longer periods, than are observed in the F/1O double-mode Cepheids. Nevertheless, these models are very interesting from dynamical point of view (spiral triple-mode attractor) and well illustrate the resonant mechanism of exciting the doubly-periodic pulsations. Thus, it is worth to present them in more detail.
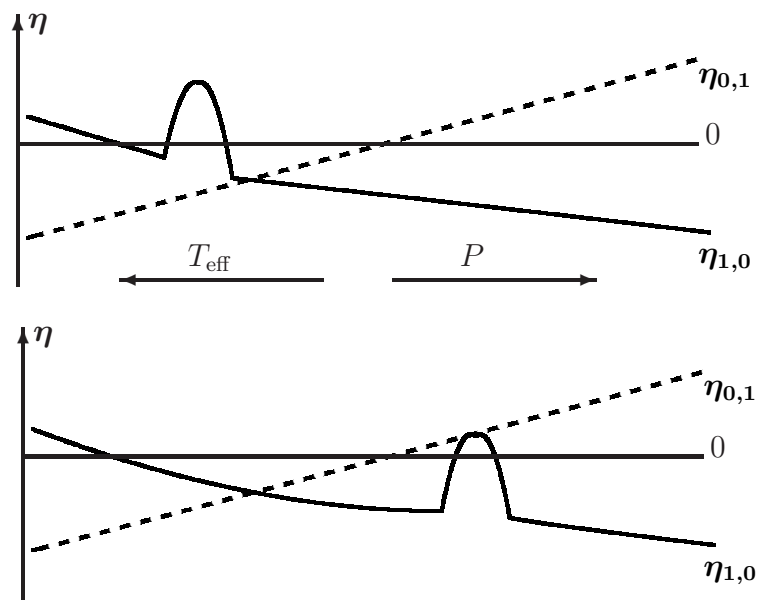
Figure 7.1: Schematic illustration of the effects of the 2:1 resonance on fundamental mode limit cycle stability. In the top panel, situation corresponding to model computations of BUCHLER, GOUPIL & PICIULLO (1997) is presented , while the bottom panel illustrates the situation for the multi-mode case discussed in the text.

The models to be discussed have all equal masses, $M = 5.5 \mathrm{M}_\odot$, and luminosities, $L = 2068.7 \mathrm{L}_\odot$. Chemical composition corresponding to our Galaxy was adopted, $X = 0.7$, $Z = 0.018$. OPAL opacities (IGLESIAS & ROGERS 1996) supplemented with the ALEXANDER & FERGUSSON (1994) opacity data at the lower temperatures, were used in all model computations. Opacities were generated for the solar mixture of GREVESSE & NOELS (1993). Structure of the models is similar as described in Section 4.1. Models have 160 zones, 40 outermost zones have equal mass down to the the anchor zone in which temperature is set to $T_\mathrm{a} = 11000\,\mathrm{K}$. The temperature at the inner boundary is, $T_\mathrm{in} = 4 \cdot 10^6\,\mathrm{K}$. Nonlinear computations were conducted using both relaxation scheme and direct time integration.

In the left panel of Figure 7.2 the Floquet stability coefficients of the fundamental and first overtone limit cycles, $\eta_{1,0}$ and $\eta_{0,1}$, are plotted *versus* the effective temperature of the models. Arrow shows the location of the resonance center, inferred from
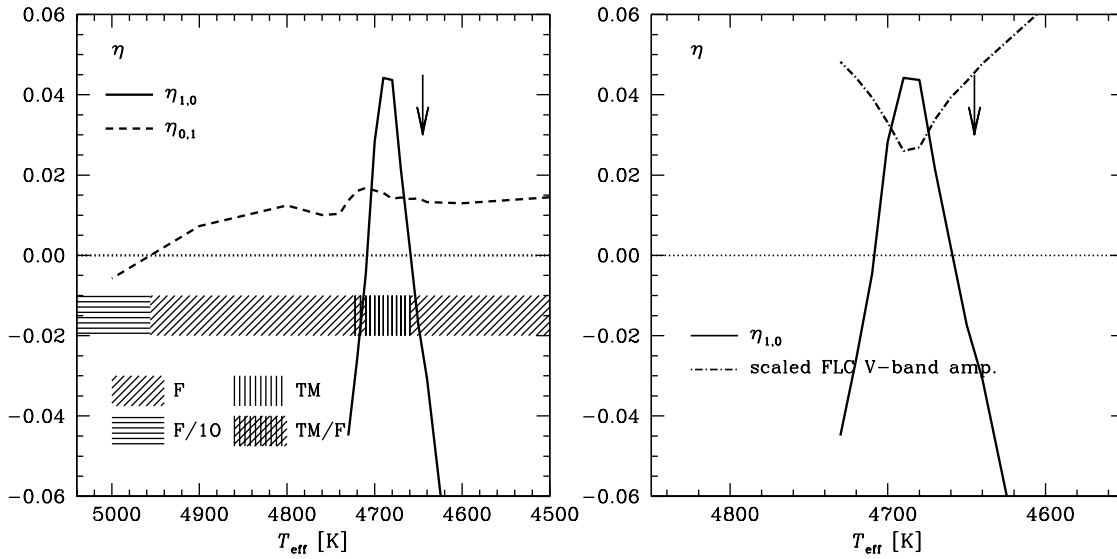
Figure 7.2: The run of the Floquet stability coefficients *versus* the effective temperature of the models, close to the center of the 2:1 resonance, $2\omega_0 = \omega_2$, marked with arrow (left panel). Shaded bar shows the modal selection inferred from the Floquet stability analysis and from the results of hydrodynamical direct time model integration. TM stands for triple-mode (doubly-periodic) pulsation. Correlation between the amplitude of the fundamental mode limit cycle (FLC) and its stability coefficient is demonstrated in the right panel.

the linear computations. Qualitatively the same picture, as is schematically drawn in the bottom panel of Figure 7.1 is visible. Around temperature $T_{\text{eff}} = 4680\,\text{K}$, a prominent peak in the stability coefficient of the fundamental mode limit cycle, $\eta_{1,0}$, is present. As is visible in the right panel of Figure 7.2, the destabilization of the fundamental mode limit cycle is connected with the resonant decrease of its pulsation amplitude. Destabilization occurs far from the blue edge of the instability strip, in a temperature range at which first overtone limit cycle is already unstable. Consequently, triple-mode (F/1O/2O) domain, manifesting in doubly-periodic (F/1O) pulsation, emerges in the middle of the fundamental mode pulsation domain. Stable, triple-mode solution exists also to the blue of this domain, in a narrow temperature range, at which fundamental mode limit cycle is stable ($\eta_{1,0} < 0$). In this domain, triple-mode solution coexists with stable fundamental mode solution. Existence of such domain cannot be inferred from the Floquet analysis. It was found through direct time integration of individual models across the temperature sequence.

Several nonlinear direct time integrations were conducted to approach the triple-mode solution. Hydrodynamical results were analysed through the analytical signal method, as described in Section 6.1. The extracted amplitude, S_1, corresponding to signal at linear frequency of the first overtone, ω_1, is directly related to the amplitude of this mode, $S_1 = A_1$. However, this is not the case for amplitude S_0, which corresponds to signal at linear frequency of the fundamental mode, ω_0. Due to resonant coupling between the fundamental and second overtone modes, S_0 contains

the contribution from the latter mode too (*see e.g.*, KOVÁCS & BUCHLER 1989),

$$S_0 = \Re(a_0 + h_{21}a_0^*a_2). \tag{7.1}$$

Above, a_0 and a_2 are complex amplitudes corresponding to fundamental and second overtone modes, respectively, and h_{21} is a complex coefficient. Computed trajectories are presented in Figures 7.3 and 7.4 in $S_0 - S_1$ plane. Note, that the topology of the solutions in this plane, is exactly the same as in amplitude-amplitude, $A_0 - A_1$, plane.

In Figure 7.3 hydrodynamical trajectories corresponding to models of different effective temperatures are plotted. For each model one trajectory is displayed. However, to probe the whole phase-space, model of each temperature was integrated with several initial conditions. Results for two models of temperatures 4690 K and 4720 K, are presented in Figures 7.4.
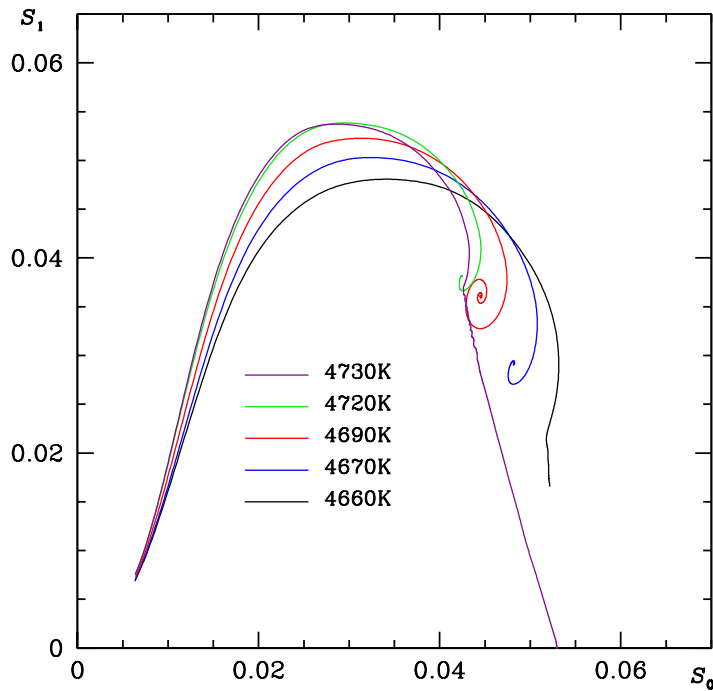
Figure 7.3: Hydrodynamical trajectories in $S_0 - S_1$ plane, for five Cepheid models of different effective temperatures, located close to the $2\omega_0 = \omega_2$ resonance center.

Trajectories visible in the Figures are qualitatively different from those displayed in Figures 6.3 and 6.4, which is caused by the resonant mode interaction. Trajectory for the hottest model in Figure 7.3 evolves toward fundamental mode solution. For slightly cooler model ($T_{\text{eff}} = 4720$ K) triple-mode resonant solution appears. Already for this model, the curious character of the attractor is apparent. It is spiral attractor, which is best visible for model of $T_{\text{eff}} = 4690$ K. Solutions of such character were not encountered in hydrodynamical pulsation modeling, up to date. For cooler models, the spiral becomes less pronounced, and finally disappears. Also triple-mode
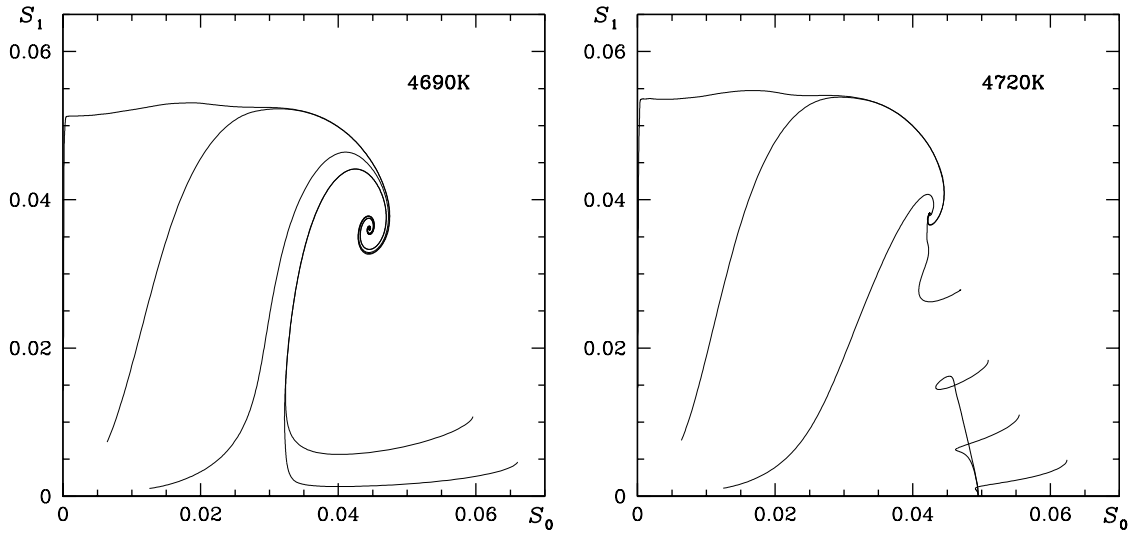
Figure 7.4: Results of hydrodynamical model integrations for two Cepheid models with $T_{\mathrm{eff}} = 4690\,\mathrm{K}$ (left panel) and $T_{\mathrm{eff}} = 4720\,\mathrm{K}$ (right panel). For each model, several trajectories are plotted, corresponding to integrations with different initial conditions. Note that trajectories can cross, as $S_0 - S_1$ is not a full phase-space.

solution is not present for temperatures lower than $4660\,\mathrm{K}$. The doubly-periodic domain extends over more than $60\,\mathrm{K}$ in the middle of the fundamental mode pulsation domain. It is also worthy to notice that at the hot side of this domain, triple-mode solution coexist with stable fundamental mode solution. Hysteresis is clearly visible for model with $T_{\mathrm{eff}} = 4720\,\mathrm{K}$ displayed in the right panel of Figure 7.4. Note also, that trajectories in this Figure intersect themselves. This is because $S_0 - S_1$ (or $A_0 - A_1$) plane is not a full phase-space, as three modes are involved in the pulsations (phase-space is 4-dimensional, *see e.g.,* DZIEMBOWSKI & KOVÁCS 1984). The domain in which hysteresis is possible is narrow, its width is smaller than $20\,\mathrm{K}$. Across this domain fundamental mode limit cycle is stable ($\eta_{1,0} < 0$) and first overtone limit cycle is unstable ($\eta_{0,1} > 0$). For lower temperatures, triple-mode state is the only attractor of the system, and all trajectories evolve toward it, which is clearly visible for model with $T_{\mathrm{eff}} = 4690\,\mathrm{K}$ (left panel of Figure 7.4). In this case both single-mode limit cycles are simultaneously unstable.

Modal selection, as depicted in the left panel of Figure 7.2, was inferred through the Floquet analysis and direct numerical model integration. The more robust method would be to apply the mode selection analysis, as described in Section 6.1. In this case however, resonant amplitude equations should be fitted to hydrodynamical trajectories. For the discussed case, relevant amplitude equations are following,

$$
\begin{aligned}
\frac{da_0}{dt} &= \left(\gamma_0 + Q_{00}a_0^2 + Q_{01}a_1^2 + Q_{02}a_2^2\right)a_0 + \Pi_0 a_0^* a_2 \\
\frac{da_1}{dt} &= \left(\gamma_1 + Q_{10}a_0^2 + Q_{11}a_1^2 + Q_{12}a_2^2\right)a_1 \\
\frac{da_2}{dt} &= \left(\gamma_2 + Q_{20}a_0^2 + Q_{21}a_1^2 + Q_{22}a_2^2\right)a_2 + \Pi_2 a_0^2
\end{aligned}
\tag{7.2}
$$

Above, a_0, a_1 and a_2 are complex amplitudes of the fundamental, first and second overtone modes, respectively. Q_{ij} are complex cubic saturation coefficients and Π_0 and Π_2 are complex coupling coefficients. Non-resonant saturation terms were truncated at cubic nonlinearities. Complex resonant coupling terms are present in the equations for the fundamental and second overtone complex amplitudes. Decoupling of these equations into separate equations for amplitudes and phases, which is possible in non-resonant case, cannot be done here. Linear fitting to the hydrodynamical trajectories is not possible, neither. Also, the parameter space is significantly larger than in non-resonant case (25 parameters instead of 8 in Section 6.1). Therefore, the mode selection analysis as described in Section 6.1 is hard to conduct.

An attempt was made to derive all the parameters entering the resonant AEs, through minimization of the residuals between amplitudes computed from hydrodynamical trajectories and those computed from AEs (Eqs. 7.2), assuming some trial values for saturation and coupling coefficients. To this purpose, genetic algorithm PIKAIA was used (CHARBONNEAU 1995). Unfortunately, no satisfactory solution was found, probably because of complicated properties of the minimized residual function, which appears to have many local minima. Also, extremely large parameter space made the computations very slow.

7.2 Excitation of the multi-mode pulsation through the three-mode resonance − β Cephei models

In the resonance to be discussed in this Section, three consecutive radial modes are involved. Frequency of the middle mode is close to the mean of the remaining two modes: $2\omega_1 = \omega_0 + \omega_2$. The resonance was shortly discussed by KOVÁCS & BUCHLER (1993) in the context of multi-mode RR Lyrae models. It was found to be conductive in bringing up the stable multi-mode behaviour in radiative models of β Cephei stars (SMOLEC & MOSKALIK 2007). These results will be shortly described in this Section. Surprisingly, the same resonance is operational in multi-mode convective Cepheid models that were found accidentally by the author. These results will be described in Section 7.3.

β Cephei stars are main sequence, early B-type pulsators. They are driven through the κ-mechanism acting in the iron opacity bump. Pulsation in non-radial modes is dominant, although in several stars, radial modes had been detected (*see e.g.*, DZIEMBOWSKI 2007, PIGULSKI 2007 for recent reviews). SMOLEC & MOSKALIK (2007) studied the amplitude saturation in β Cephei models by computing the properties of the radial modes with radiative pulsation hydrocode. These models are robust, and independent of artificial viscosity parameters. The use of radiative codes in modeling these stars is fully justified. External hydrogen-helium (H–HeI) convective zone is not present, simply because of high effective temperatures. Helium (HeII) convective zone is located close to the surface and is not important for driving. Convection associated with the iron opacity bump is weak, as in the computed static convective models only up to three per cent of the total flux can be carried by convection (*see* SMOLEC & MOSKALIK 2007). Because of very small growth rates for β Cephei models ($\gamma \approx 10^{-5}$), only relaxation method can be used to conduct extensive model survey. Analysis of the Floquet stability coefficients

of the computed models, revealed two domains in which both fundamental mode and first overtone limit cycles are simultaneously unstable, thus, leading to multi-mode pulsation. These results will be presented in this Section (*see* also SMOLEC & MOSKALIK 2007, SMOLEC 2009).

Models under consideration were computed along the evolutionary tracks obtained with the Warsaw-New Jersey stellar evolutionary codes (*e.g.*, PAMYATNYKH 1999). In these computations Galactic chemical composition ($X = 0.7$, $Z = 0.02$) was adopted. Here, we will discuss the most interesting models computed with the OPAL opacities. Several envelope models, characterized by masses, luminosities and effective temperatures given by the evolutionary code, were constructed. All models consist of 120 mass shells, extending down to $T_{\mathrm{in}} = 3 \cdot 10^7 \, \mathrm{K}$. Anchor is located close to the iron opacity bump at temperature, $T_{\mathrm{a}} = 2.5 \cdot 10^5 \, \mathrm{K}$, 70 zones below the surface. Instability strips emerging from linear stability analysis are shown in the theoretical HR diagram plotted in Figure 7.5. Several models were selected for non-linear computations. They are shown with solid hexagons in Figure 7.5. For each model, fundamental and first overtone limit cycles were computed through the relaxation technique. Values of the Floquet coefficients were used to derive the modal selection coded with colours in Figure 7.5. Except the models located along $10 \mathrm{M}_\odot$ evolutionary track, modal selection is qualitatively the same as observed in radiative models of classical pulsators (Section 1.4.3) – fundamental and first overtone domains are separated by the F/1O either-or domain, in which pulsation in either mode is possible. For models of lowest mass ($8 \mathrm{M}_\odot$, $9 \mathrm{M}_\odot$), as well as for highest mass models ($20 \mathrm{M}_\odot$), only pulsation in the fundamental mode is possible.

The most interesting results are obtained along $10 \mathrm{M}_\odot$ evolutionary track. Here, a double-mode model is found in between the first overtone and fundamental mode pulsation domains. Such location suggests that non-resonant mechanism is operational in bringing up the double-mode behaviour. Analysis of linear periods revealed however, that the center of the $2\omega_1 = \omega_0 + \omega_2$ resonance is also located nearby. The loci of this resonance is drawn with dashed brown line in Figure 7.5. To check the possible effects of this resonance on modal selection, a much denser grid of models was computed along $10 \mathrm{M}_\odot$ evolutionary track. Obtained results are very interesting. Two multi-mode domains are located along this evolutionary track. One of them is resonant, and falls exactly at the resonance center, between the two first overtone models plotted in Figure 7.5. The second domain, in which the single double-mode model plotted in Figure 7.5 is located, has nothing to do with the resonances. This scenario was inferred from values of the Floquet stability coefficients along the discussed sequence of $10 \mathrm{M}_\odot$ models, which are presented in Figure 7.6. Stability coefficients are plotted *versus* the Δ parameter, defined as,

$$\Delta = \frac{2\omega_1}{\omega_0 + \omega_2}, \qquad (7.3)$$

thus, characterizing the proximity to the resonance center.

At the highest temperatures, only pulsation in the first overtone is possible. First overtone limit cycle is stable ($\eta_{0,1} < 0$), while fundamental mode limit cycle is unstable ($\eta_{1,0} > 0$). Then, exactly at the resonance center ($\Delta = 1$), a prominent peak of the switching rate toward fundamental mode, $\eta_{0,1}$, is visible. No doubt, discussed resonance destabilizes the first overtone. Otherwise stable, first overtone
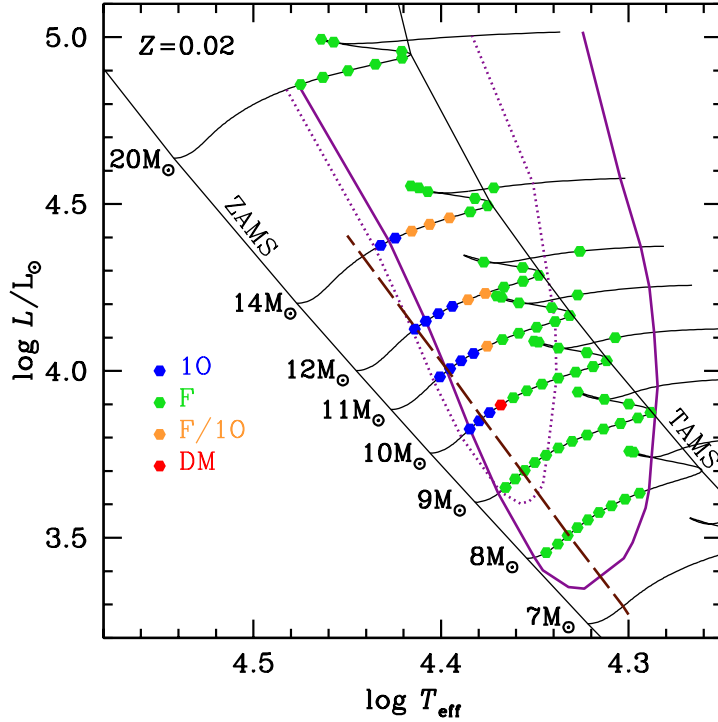
Figure 7.5: Location and modal stability information for the computed nonlinear β Cephei models. Models were computed along evolutionary tracks (black lines) for stars of masses indicated in the Figure. Locations of the zero-age main-sequence (ZAMS) and terminal-age main-sequence (TAMS) are also shown. Solid and dotted violet lines enclose the fundamental and first overtone instability strips, respectively. Dashed line shows the loci of the $2\omega_1 = \omega_0 + \omega_2$ resonance.

becomes unstable ($\eta_{0,1} > 0$) at the resonance center. As fundamental mode is also unstable, resonant triple-mode (damped second overtone is resonantly excited) domain emerges in the middle of the first overtone pulsation domain. The sharp peak of $\eta_{0,1}$ indicates that resonant effects are important only very close to its center. For lower temperatures a monotonic increase of $\eta_{0,1}$ and monotonic decrease of $\eta_{1,0}$ are clearly visible. Both switching rates cross at around $\Delta \approx 1.01$ and are simultaneously positive at the crossing point. Thus, a second double-mode domain emerges, separating the first overtone and fundamental mode pulsation domains. This is exactly what we expect in case of non-resonant mode coupling. It is also worth to mention, that in agreement with theoretical analysis of amplitude equations (KOVÁCS & BUCHLER 1993), discussed resonance has no effect on the stability of the fundamental mode ($\eta_{1,0}$).

Direct nonlinear integrations were not conducted for the resonant models. Due to a very small growth rates, convergence to stable attractors is extremely slow and requires the computations of more than 10^5 pulsation cycles. Four trajectories were computed for the non-resonant case (*see* SMOLEC 2009), however, they just confirm the existence of the stable double-mode attractor, which cannot be reached in reasonable time, even on very fast computers.
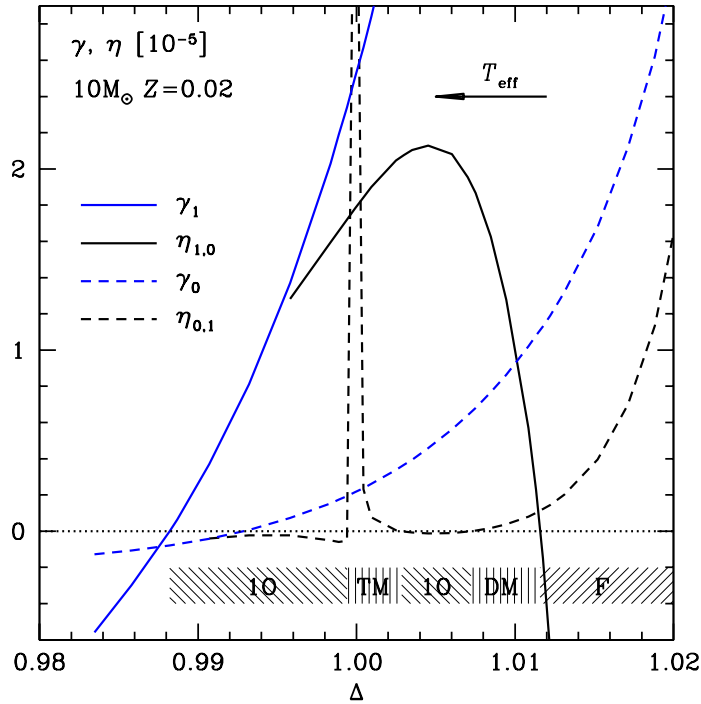
Figure 7.6: Linear growth rates (blue lines) and Floquet stability coefficients (switching rates) plotted against proximity parameter Δ, for β Cephei models along $10\text{M}_\odot$ evolutionary track. Shaded bar shows the emerging modal selection. TM stands for triple-mode (doubly-periodic) pulsation.

Described models are mainly of theoretical interest. In none of the observed β Cephei stars, two radial modes alone are simultaneously observed. In these stars non-radial modes usually dominate, and these were not taken into account in the presented computations. However, computed models clearly illustrate the resonant and non-resonant mechanisms of bringing up stable multi-mode pulsation – at a single evolutionary track.

7.3 Excitation of the multi-mode pulsation through the three-mode resonance $-$ δ Cephei models

Multi-mode models that will be described in this Section were found accidentally during test computations, intended to model the Hertzsprung bump progression. All computations were done with convective hydrocodes described in this thesis, including negative buoyancy effects (NN model). Static models were constructed using the same mesh structure and opacity data as described in Section 4.1. Models were computed along a sequence of constant luminosity and varying effective temperature. Masses and luminosities of the models satisfy the mass-luminosity relation resulting from SCHALLER *et al.* (1992) evolutionary computations. Convective parameters and masses of the models to be discussed, are collected in Table 7.1. Convective
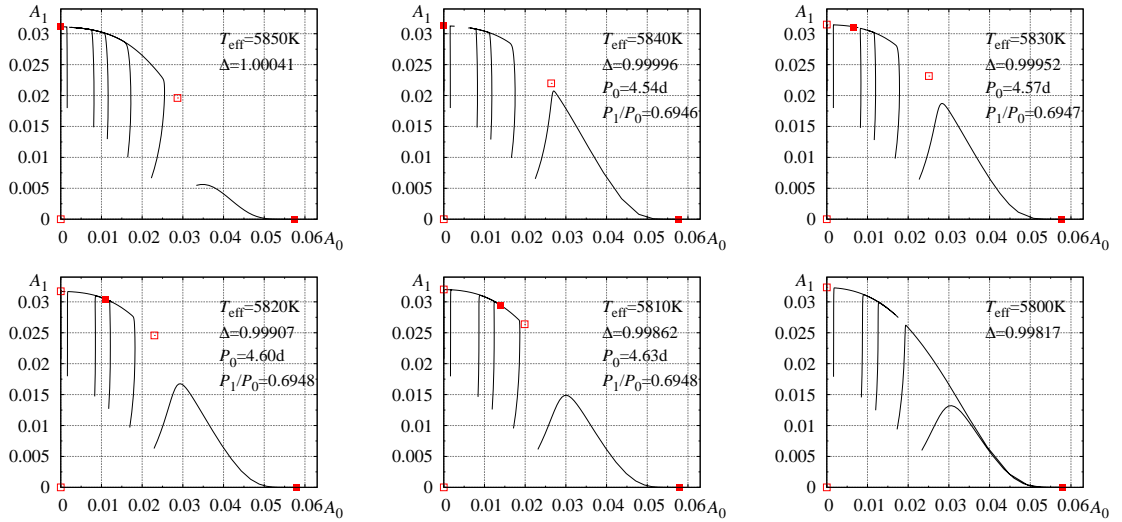
Figure 7.7: Hydrodynamical trajectories for six consecutive Cepheid models of set R2, lying close to the $2\omega_1 = \omega_0 + \omega_2$ resonance center. Model properties are given in each panel. Solid and open squares mark the location of stable and unstable fixed points computed through fitting the hydrodynamical trajectories with non-resonant amplitude equations.

parameters of set R3 are exactly the same as for set C discussed in Chapter 4 (Table 4.1).

Set	α	α_m	α_s	α_c	α_d	α_p	α_t	γ_r	$M[M_\odot]$	$T[K]$	Δ	$P_0[d]$	P_1/P_0
R1	1.5	0.3	1	1	1	1.0	0	0.75	4.50	5755	1.00064	4.21	0.6964
R2	1.5	0.3	1	1	1	0.5	0	1.00	4.75		*see* Figure 7.7		
R3	1.5	0.5	1	1	1	0.0	0	1.00	5.00	5965	1.00009	4.77	0.6929

Table 7.1: Parameters and properties of the multi-mode convective Cepheid models discussed in the text. Convective parameters, α_s, α_c, α_d, α_p and γ_r, are given in the units of standard values (*see* Table 2.1). In the last four columns effective temperature, proximity parameter, fundamental mode period and P_1/P_0 period ratio are given for models for which doubly-periodic solution exists.

The double-mode solution was first found for one model of set R1. Detailed linear analysis revealed that the $2\omega_1 = \omega_0 + \omega_2$ resonance can be involved in the pulsations, as the model was located almost exactly at the resonance center (Table 7.1). This finding motivated the search for doubly-periodic F/1O Cepheid pulsation connected with the discussed three-mode resonance. Such models are hard to find as special conditions are necessary for their occurrence (*see* later in this Section). Multi-mode models were found for sets R2 and R3 of Table 7.1. The widest domain with doubly-periodic solutions exists for set R2. In Figure 7.7 results of hydrodynamical model integrations for six consecutive models of this set are presented.

Modal selection and properties of the models are very similar for all three parameter sets of Table 7.1, and are briefly discussed below.

Modal selection. Mode selection scenario is evident from the hydrodynamical trajectories alone, and is the same for all three parameter sets under discussion.

Doubly-periodic attractor always coexists with stable fundamental mode attractor (*see* Figure 7.7). Hysteresis domain is always very narrow. Close to the resonance center consecutive models were computed in 5 K steps in effective temperature. For sets R1 and R3, doubly-periodic solution was found in only one model (*see* Table 7.1 for its properties), indicating that the interesting domain is narrower than 10 K. Only for models adopting parameters of set R2, doubly-periodic domain is wider, and extends over more than 40 K. For all three model sequences, this domain is located between the F/1O either-or domain (hotter models) and fundamental mode pulsation domain (cooler models). Therefore, from astrophysical point of view, doubly-periodic solution can be reached only during red-ward evolution, by models previously pulsating in the first overtone. During the blue-ward evolution, models pulsate in the fundamental mode, which remains stable.

Origin of multi-periodic pulsation. At first glance, the non-resonant mechanism seems to be the most likely cause of the doubly-periodic (and double-mode, in non-resonant case) pulsation. Doubly-periodic solutions are always located between the fundamental and F/1O either-or domains, which is rather natural for the non-resonant mechanism. In case of typical resonant excitation, doubly-periodic domain emerges in the middle of the single-mode domain – fundamental mode domain, as for the 2:1 resonance discussed in Section 7.1, or first overtone domain, as for the three-mode resonance acting in β Cephei pulsators (Section 7.2). This is because of resonant destabilization of one of the limit cycles. Also, non-resonant amplitude equations seem to capture hydrodynamical results. Solid and open squares in Figure 7.7 correspond to stable and unstable fixed points, computed as described in Section 6.1, through fitting the non-resonant amplitude equations to the hydrodynamical trajectories. Except one model of $T_{\mathrm{eff}} = 5840$ K, location of the fixed points seems consistent with the hydrodynamical data.

Nevertheless, other arguments point toward resonant explanation of the computed doubly-periodic models. First, all the computed doubly-periodic models are very close to the resonance center. Proximity parameters, Δ (Eq. 7.3), are given in Table 7.1 for the two relevant models of sets R1 and R3 and in Figure 7.7 for models of set R2. This is not likely to happen by accident, particularly, for three model sequences of different convective parameters as well as masses and luminosities. Second, extensive survey of models presented in Section 6.3 hasn't revealed any doubly-periodic solutions, particularly, close to the transition line between fundamental and F/1O either-or domains. In all models of Section 6.3, $2\omega_1 = \omega_0 + \omega_2$ resonance was far from the transition line. Also, doubly-periodic models were not found close to the resonance center, if transition line was distant. This indicates that special condition is required to bring up the stable doubly-periodic pulsation – proximity of the models to both the resonance center and discussed transition line. Consequently, doubly-periodic domain is always restricted to a very narrow region in the HR diagram. Also, existence of the doubly-periodic solution depends on the values of convective parameters entering the model computations (*see* next paragraph).

General properties of the models. Periods and period ratios for the computed doubly-periodic models are collected in Table 7.1 (sets R1 and R3) and in Figure 7.7 (set R2). Models occupy a narrow period range. As compared to observations (*see* Petersen diagram in *e.g.*, Moskalik & Kołaczkowski 2009), pe-

riod ratios are slightly smaller. This can be compensated through the decrease of model's metallicity. However, the main drawback of the computed models is their high amplitude. Except for set R3, amplitudes of the single-mode solutions along the computed model sequences, are always higher than are observed for Cepheids. Particularly, amplitudes of the fundamental mode are higher at least by 30 per cent. Similar discrepancy is observed for the first overtone models. Attempt to decrease the model amplitudes by increasing the eddy-viscous dissipation (parameter α_m) were unsuccessful. Doubly-periodic solution simply disappeared. In all three parameter sets of Table 7.1, effects of radiative cooling of the convective elements are turned on. In such models convection is always less vigorous. However, more extensive parameter study is necessary to judge, whether this effect is crucial in bringing up doubly-periodic solutions.

Despite described difficulties, presented models are promising, as they are computed with convective hydrocode including negative buoyancy effects. Certainly, more work is necessary to understand the mechanism bringing up the doubly-periodic behaviour, and to check whether better agreement with observations can be achieved. Such work is planned.

Chapter 8

Hydrodynamical modeling of double-overtone Cepheid pulsation

In this Chapter, search for nonlinear 1O/2O double-overtone Cepheid behaviour is described. Physical parameters of the models are chosen to reproduce the double-overtone Cepheids in the Large Magellanic Clouds. Recently, their number was significantly enlarged by the OGLE team. Observational data are briefly described in Section 8.1. Linear model survey, intended to reproduce the observed Petersen diagram and period-luminosity relation, is conducted in Section 8.2. Finally, in Section 8.3 results of nonlinear model survey are presented and discussed.

8.1   Observational data

A large sample of new Cepheid variables in the Large Magellanic Cloud was discovered in the OGLE data (OGLE-II – UDALSKI *et al.* 1999, OGLE-III – SOSZYŃSKI *et al.* 2008b). Many of these objects are multi-periodic pulsators, including previously unknown double-mode 1O/3O Cepheids, and three new cases of very rare triple-mode Cepheids (SOSZYŃSKI *et al.* 2008a). Also, a new classes of double-mode pulsators were found in the OGLE data, with period ratios either close to unity, or in a range $0.60 - 0.64$ (MOSKALIK, KOŁACZKOWSKI & MIZERSKI 2004, MOSKALIK & KOŁACZKOWSKI 2008, 2009; SOSZYŃSKI *et al.* 2008b). Non-radial modes must be involved in the pulsations of the former class (with period ratio close to unity), and are also suggested as likely explanation for the latter group (period ratios around $0.60 - 0.64$) – *see* MOSKALIK & KOŁACZKOWSKI (2009). These exciting variables lack satisfactory theoretical interpretation.

In this Chapter, we focus on 1O/2O double-overtone Cepheids. They are most frequent class of multi-periodic Cepheids in the LMC. 206 such variables were found in OGLE-III data, to be compared with only 61 F/1O double-mode Cepheids. There are many more single-mode first overtone Cepheids (1238), however, in a period range $0.5\,\mathrm{d} < P_1 < 0.9\,\mathrm{d}$ double-overtone Cepheids are most common type of pulsators among the LMC Cepheids. Surprisingly only 14 variables are confirmed single-mode second overtone pulsators. Hence, second overtone is excited predominantly together with the first overtone.

Observational data for the LMC double-overtone Cepheids are plotted in Figure 8.1. In the upper panel of that Figure, Petersen diagram is plotted. Double-

overtone Cepheids seem to fall into two overlapping groups in this diagram. The first, less numerous group, extends from the shortest periods to periods slightly longer than $P_1 \approx 0.6$ days ($\log P_1 \approx -0.2$). Within this group, one can observe a weak increasing trend in the P_2/P_1 period ratio. Members of the second, more numerous group, extending for longer periods ($P_1 > 0.6$ days) form a well defined sequence with decreasing period ratio. In the lower panel of Figure 8.1, the period-luminosity relation is plotted. On vertical axis, reddening-free Wesenheit index, defined as,

$$W_I = I - 1.55(V - I), \tag{8.1}$$

is plotted. Tight, linear relation between Wesenheit index and logarithm of the first overtone period is clearly visible.
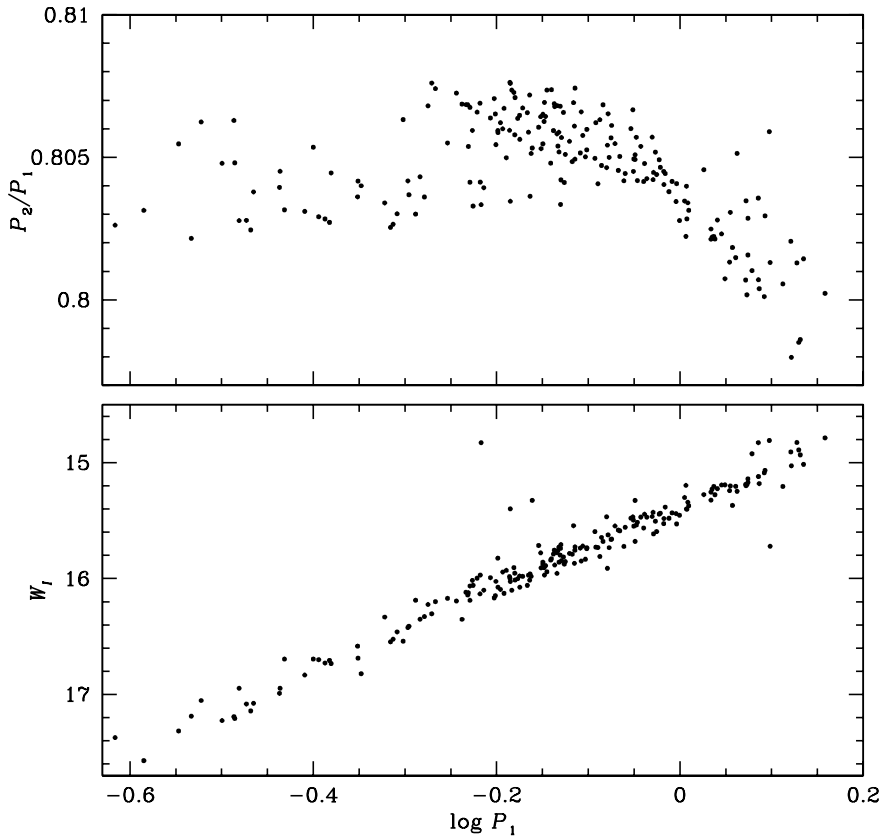
Figure 8.1: Petersen diagram (top panel) and period luminosity relation, $\log P_1 - W_I$ (bottom panel), for the double-overtone Cepheids in the LMC. Data from SOSZYŃSKI *et al.* (2008b).

Data on double-overtone pulsators represent a challenge for stellar evolution and pulsation theories. As was shown by DZIEMBOWSKI & SMOLEC (2009) standard evolutionary computations fail to reproduce the majority of double-overtone Cepheids. In the next Section their conclusions, based on linear pulsation modeling will be briefly summarized.

8.2 Linear modeling of the double-overtone LMC Cepheids

In this Section, we focus on modeling the data visible in Figure 8.1. To this purpose evolutionary computations coupled with linear pulsation modeling were used. Evolutionary tracks were computed with the Warsaw-New Jersey stellar evolutionary code (*see e.g.*, PAMYATNYKH 1999), which allows to compute evolutionary phases before core helium ignition. Computations were conducted for two values of metallicity characteristic to LMC, namely $Z = 0.006$ and $Z = 0.008$. For the hydrogen abundance, $X = 0.72$ was adopted. ASPLUND *et al.* (2004) solar mixture was used in opacity computations. Rotation, as well as overshooting from the convective core, were neglected. Mixing length parameter was set to $\alpha_{\mathrm{MLT}} = 1.5$. Computed tracks for stars of masses $2.5M_\odot$, $3.0M_\odot$ and $3.5M_\odot$, are plotted with solid ($Z = 0.006$) and with dot-dashed lines ($Z = 0.008$) in the theoretical HR diagram displayed in Figure 8.2.
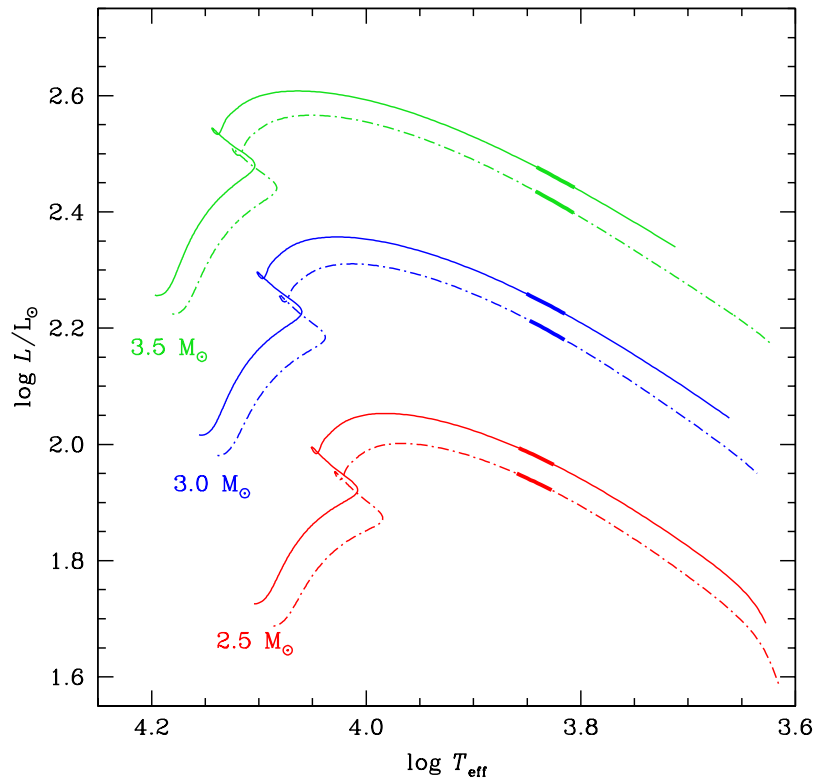
Figure 8.2: Evolutionary tracks for the $2.5M_\odot$, $3.0M_\odot$ and $3.5M_\odot$ models (red, blue and green lines, respectively), computed assuming no overshooting from the convective core. Solid and dot-dashed lines correspond to computations with metallicities of $Z = 0.006$ and $Z = 0.008$, respectively. Thick line segments along each evolutionary track refer to domains of simultaneous instability of the first and second overtones.

Along each evolutionary track, instability domains, in which both first and second overtones are simultaneously unstable ($\gamma_1 > 0$, $\gamma_2 > 0$), were determined with linear

convective pulsation code described in this thesis. They are marked with thick lines along each evolutionary track. Below, some details of linear pulsation models are given.

Modeling of double-overtone pulsation and, more generally, pulsation involving higher order overtones, is not an easy task. Higher the order of pulsation mode, deeper into envelope it penetrates. Hence, to obtain reliable periods and period ratios, model envelopes should be deep and computed with higher resolution in the internal layers, as compared to fundamental mode Cepheid models. The best solution, would be to use the full evolutionary models, including the zones of nuclear burning and regions of non-homogeneous chemical composition. Such models can be computed with the linear code of DZIEMBOWSKI (1977), which is coupled with the Warsaw-New Jersey stellar evolutionary code. However, treatment of convection in this code is very simple (frozen-in MLT). Consequently, it does not allow to compute the red edges of the instability strips. Therefore, the envelope convective code with Kuhfuß convection model (Chapter 3) was used in pulsation modeling. The model structure, zoning and depth of the envelope, were chosen to reproduce the results obtained with the Dziembowski's code as closely as possible. Comparison of model periods and period ratios was conducted either for purely radiative models, or with convection in the frozen-in approximation in both of the codes. In the envelope code, radiative losses, turbulent pressure and turbulent flux were neglected, and other parameters were set to their standard values, which makes static convective Kuhfuß model equivalent to MLT (*see* Section 2.4.3). Resulting mesh structure for the envelope models is following (*see* Section 3.3.1): number of zones is, $N = 200$, of which $N_a = 50$ outer zones have equal mass down to the anchor zone, in which temperature is set to $T_a = 11000 \, \text{K}$. Envelope extends down to temperature $T_{in} = 8 \cdot 10^6 \, \text{K}$. It has to be stressed, that arising periods of the pulsation modes, and period ratios, can be compared with observational data only qualitatively. For detailed asteroseismic modeling, as *e.g.*, conducted by MOSKALIK & DZIEMBOWSKI (2005) for the triple-mode 1O/2O/3O Cepheids, only full evolutionary models are suitable.

In the final model computations convective parameters of set C of Table 4.1 were adopted. Of course, linear model surveys adopting other sets of convective parameters can be conducted relatively fast, however, only this particular set will be considered here, for several reasons. First, in Sections 4.2 and 4.3, it was shown that with parameters of set C reliable models of both fundamental and first overtone single-mode Cepheids are obtained. Second, this set includes effects of radiative cooling of the convective elements. It was claimed that inclusion of this effect was necessary to obtain 1O/2O nonlinear double-mode models with the Florida-Budapest code (BUCHLER & KOLLÁTH 2000). Although the treatment of convection in Florida-Budapest code is significantly different from ours (Chapters 5 and 6), differences may not be as significant in case of 1O/2O models (*see* Section 6.4). Third, the constructed linear models will serve as initial models for nonlinear computations described in the next Section. As we consider low mass models characterized by small growth rates, nonlinear computations are extremely time-consuming and extensive model survey with different convective parameters is hard to conduct. Also, as discussed models are hot, convection is not expected to be very strong, and results should not be very sensitive to the exact values of the convective parameters.

Pulsation models were computed along each evolutionary track visible in the HR diagram displayed in Figure 8.2. Emerging instability domains, in which necessary condition for the double-overtone pulsation is fulfilled ($\gamma_1 > 0$, $\gamma_2 > 0$), are marked with thick lines in Figure 8.2. In Figures 8.3 and 8.4 location of relevant models in the Petersen diagram and in period-luminosity diagram is shown with solid lines, for both metallicities considered. Wesenheit index for the theoretical models was computed using KURUCZ (2004) colour indices and bolometric corrections, and adopting 18.5 mag for the distance modulus to the LMC (SCHAEFER 2008).
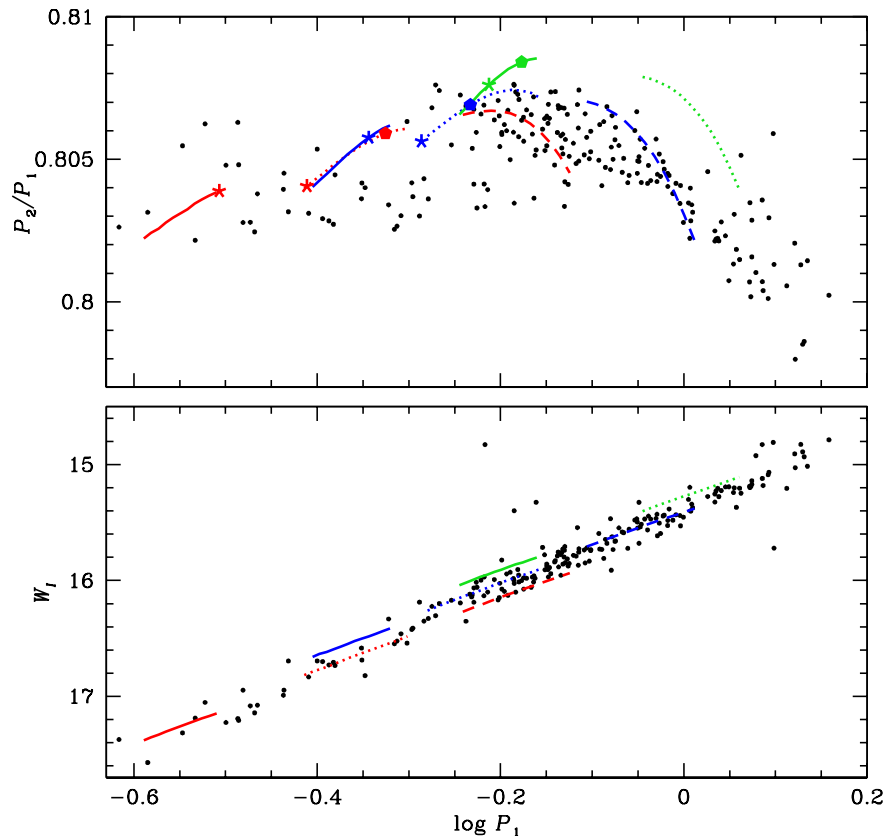
Figure 8.3: Petersen diagram (top panel) and period-luminosity relation (bottom panel) for the computed linear models with first and second overtones simultaneously linearly unstable. Red, blue and green lines correspond to $2.5 M_\odot$, $3.0 M_\odot$ and $3.5 M_\odot$ models, respectively. Solid lines refer to models computed along evolutionary tracks. In models plotted with dotted and dashed lines luminosity is constant and artificially increased by $\Delta \log L \approx 0.2$ and $\Delta \log L \approx 0.4$, relative to evolutionary models. Asterisks and filled pentagons show the location of the $2\omega_1 = \omega_5$ and $2\omega_2 = \omega_1 + \omega_3$ resonance centers, respectively. All computations for $Z = 0.006$. Data are shown with dots.

In addition to models computed along evolutionary tracks corresponding to first crossing of the instability strip, other models crossing the HR diagram horizontally (constant luminosity) were computed. Masses of the models are the same as in evolutionary computations, $2.5 M_\odot$, $3.0 M_\odot$ and $3.5 M_\odot$, however, luminosities are ar-
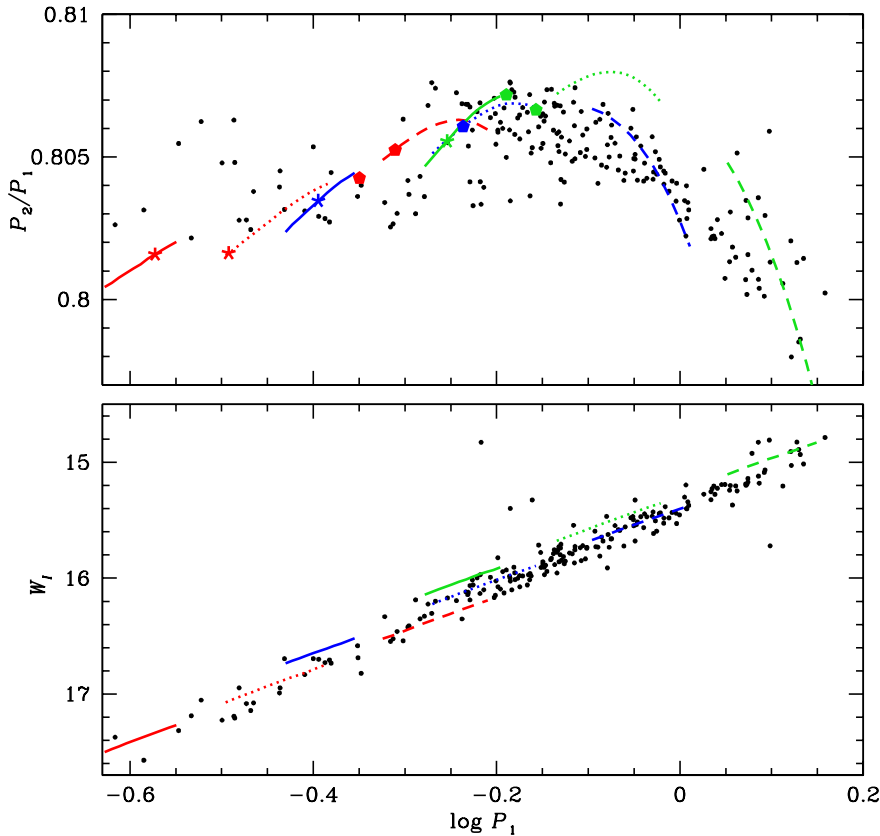
Figure 8.4: The same as Figure 8.3, but for models with metallicity $Z = 0.008$.

tificially increased by $\Delta \log L \approx 0.2$ and $\Delta \log L \approx 0.4$ relative to average luminosity for the first crossing models. Models along these horizontal paths, and within the instability strip ($\gamma_1 > 0$, $\gamma_2 > 0$), are plotted with dotted ($\Delta \log L \approx 0.2$) and dashed ($\Delta \log L \approx 0.4$) lines in Figures 8.3 and 8.4. Adopted luminosity increases can model large convective core overshooting during the main sequence phase or later phases of evolution, second and third crossings of the instability strip, during the core helium burning. Both possibilities disagree with modern evolutionary computations. However, the respective models agree with the observational data. Analysis of results, presented in Figures 8.3 and 8.4, led DZIEMBOWSKI & SMOLEC (2009) to several interesting conclusions, briefly summarized below[1].

(i) Models of constant mass cluster around straight lines in the plot of $\log P_1 - W_I$ relation. Majority of double-overtone Cepheids have masses $3.0 \pm 0.5 M_\odot$.

(ii) Double-overtone Cepheids of shorter periods ($\log P_1 \lesssim -0.2$) are well explained with evolutionary models corresponding to first crossing of the instability strip, computed without overshooting (solid lines in Figures 8.3 and 8.4), or with moderate overshooting during the main sequence evolution (in between solid and

---

[1] All linear computations, presented in Figures 8.3 and 8.4 were done by the author with the convective code described in this thesis. Conclusions regarding evolutionary status of the double-overtone Cepheids, summarized in this Section are due to prof. Dziembowski.

dotted lines in Figures 8.3 and 8.4).

(*iii*) At longer periods, evolutionary models corresponding to first crossing are too luminous as compared to the observational data. At some particular period range, better agreement with the data is obtained for non-evolutionary models of lower mass with highest luminosity excess ($\Delta \log L \approx 0.4$, dashed lines in Figures 8.3 and 8.4). If these are the models crossing the instability strip for the first time, the excess luminosity may be caused by the over-large overshooting during main sequence evolution. If these are objects during the blue loop evolution, inferred masses are lower than necessary to enter this evolution phase according to modern evolutionary computations (*e.g.*, $4.0 \mathrm{M_\odot}$ in GIRARDI *et al.* 2000 computations including overshooting from the convective core, as well as in PIETRINFERNI *et al.* 2004 computations without overshooting; *see* also Section 1.2).

For more details, I refer the reader to DZIEMBOWSKI & SMOLEC (2009). Here, we focus on challenges for pulsation theory, particularly on modeling the double-overtone pulsations.

Detailed analysis of linear periods revealed that two resonances occur within the linear models displayed in Figures 8.3 and 8.4. These are the same resonances as discussed in the previous Chapter, however, involving higher order overtones. The 2:1 resonance between the first and fifth overtones, $2\omega_1 = \omega_5$, was suggested by Dziembowski (*see* SOSZYŃSKI *et al.* 2008b, DZIEMBOWSKI & SMOLEC 2009) as a possible cause shaping the structures visible in Fourier decomposition parameters for short period first overtone Cepheids. Other resonance, $2\omega_2 = \omega_1 + \omega_3$ was not previously discussed in the context of overtone Cepheids. Resonance centers along sequences of computed models are indicated with asterisks (2:1 resonance) and filled pentagons (three-mode resonance) in Figures 8.3 and 8.4. The 2:1 resonance occurs at shorter periods, $\log P_1 \lesssim -0.2$, while three-mode resonance only in intermediate period range around $\log P_1 \approx -0.25$. As was shown in the previous Chapter, both these resonances can be conductive in bringing up stable doubly-periodic pulsations. Results displayed in Figures 8.3 and 8.4 indicate that for shorter periods, double-overtone pulsation can be a resonant phenomenon. At longer periods however, non-resonant mechanism must be operational. Only nonlinear modeling can give more insight into the double-overtone pulsations. This is the subject of the next Section.

8.3 Search for nonlinear models of the double-overtone LMC Cepheids

Extensive nonlinear model survey was conducted for models with metallicity $Z = 0.006$. Similar survey was computed for metallicity $Z = 0.008$, yielding qualitatively the same results. Presented model computations are not yet published.

For metallicity $Z = 0.006$, six nonlinear model sequences were computed. They were chosen to cover the significant part of the Petersen diagram. Three sequences are located within instability domains ($\gamma_1 > 0$, $\gamma_2 > 0$) along evolutionary tracks for stars of masses $2.5 \mathrm{M_\odot}$, $3.0 \mathrm{M_\odot}$ and $3.5 \mathrm{M_\odot}$ (solid lines in Figure 8.3). Other three are located along horizontal paths with artificially increased luminosity ($2.5 \mathrm{M_\odot}$, $\Delta \log L = 0.4$; $3.0 \mathrm{M_\odot}$, $\Delta \log L = 0.4$; $3.5 \mathrm{M_\odot}$, $\Delta \log L = 0.2$). Location of all the

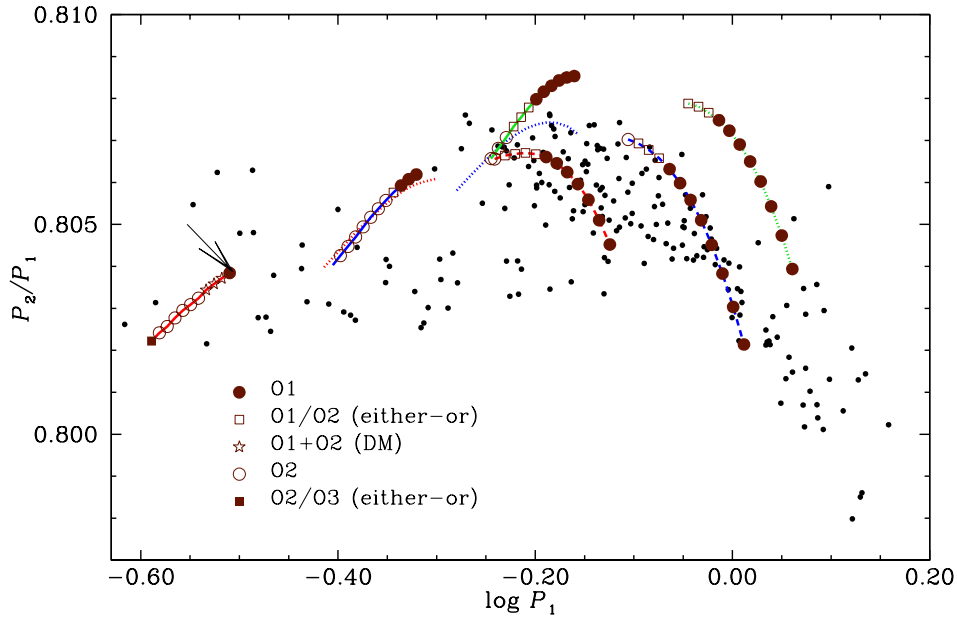computed models is shown with brown symbols in Figure 8.5.

Figure 8.5: Petersen diagram showing the location and stability information for the computed nonlinear convective models. Lines showing the location of linear model sequences are the same as in Figure 8.3. Arrow marks the location of the $2\omega_1 = \omega_5$ resonance center along $2.5M_\odot$ evolutionary path. All computations for metallicity parameter $Z = 0.006$.

For each model five hydrodynamical integrations were conducted, each initialized with different mixture of first and second overtone's velocity eigenvectors. For most of the models integrations were carried over 8000 pulsation cycles. In case of the least massive models located along evolutionary track ($2.5M_\odot$, $\Delta \log L = 0.0$), integrations were twice as long, as growth rates are very small for this model sequence. Individual trajectories are presented in Figures 8.6 ($2.5M_\odot$, $\Delta \log L = 0.0$) and 8.7 ($3.5M_\odot$, $\Delta \log L = 0.4$). Results are particularly interesting for model sequence of $2.5M_\odot$ (Figure 8.6). For other five model sequences results are qualitatively the same as presented in Figure 8.7.

Modal selection information for the computed models is presented in Figure 8.5. It was derived through the analysis of the computed trajectories, visible *e.g.*, in Figures 8.6 and 8.7. Hydrodynamical computations were not analysed with amplitude equations (as it was done in Chapter 6) for following reasons. First, in most of the models, more than two modes are linearly excited and should be taken into account in the amplitude equations. Along each of the paths displayed in Figures 8.3 or 8.5, fundamental mode is linearly unstable at the cool side (higher $\log P_1$). At the hot side, third overtone is unstable in all model paths with overtone period shorter than 0.62 days ($\log P_1 < -0.2$). Although in all the models except one (*see* following paragraph), both fundamental and third overtone modes are not present in full amplitude pulsation (which was checked through the analytical signal method), they are present during the transient evolution. Hence, they have to be taken into account in amplitude equations analysis, in order to derive the modal selection cor-

rectly. Second, in short period range, resonances occur between pulsation modes. Hence, amplitude equations should be supplemented with resonant terms, which makes them much more complex. Their fitting to hydrodynamical results is even more difficult than in case of models discussed in Section 7.1, because of more modes being involved. Nevertheless, interesting and robust results are obtained from the analysis of hydrodynamical trajectories alone, and are described below.
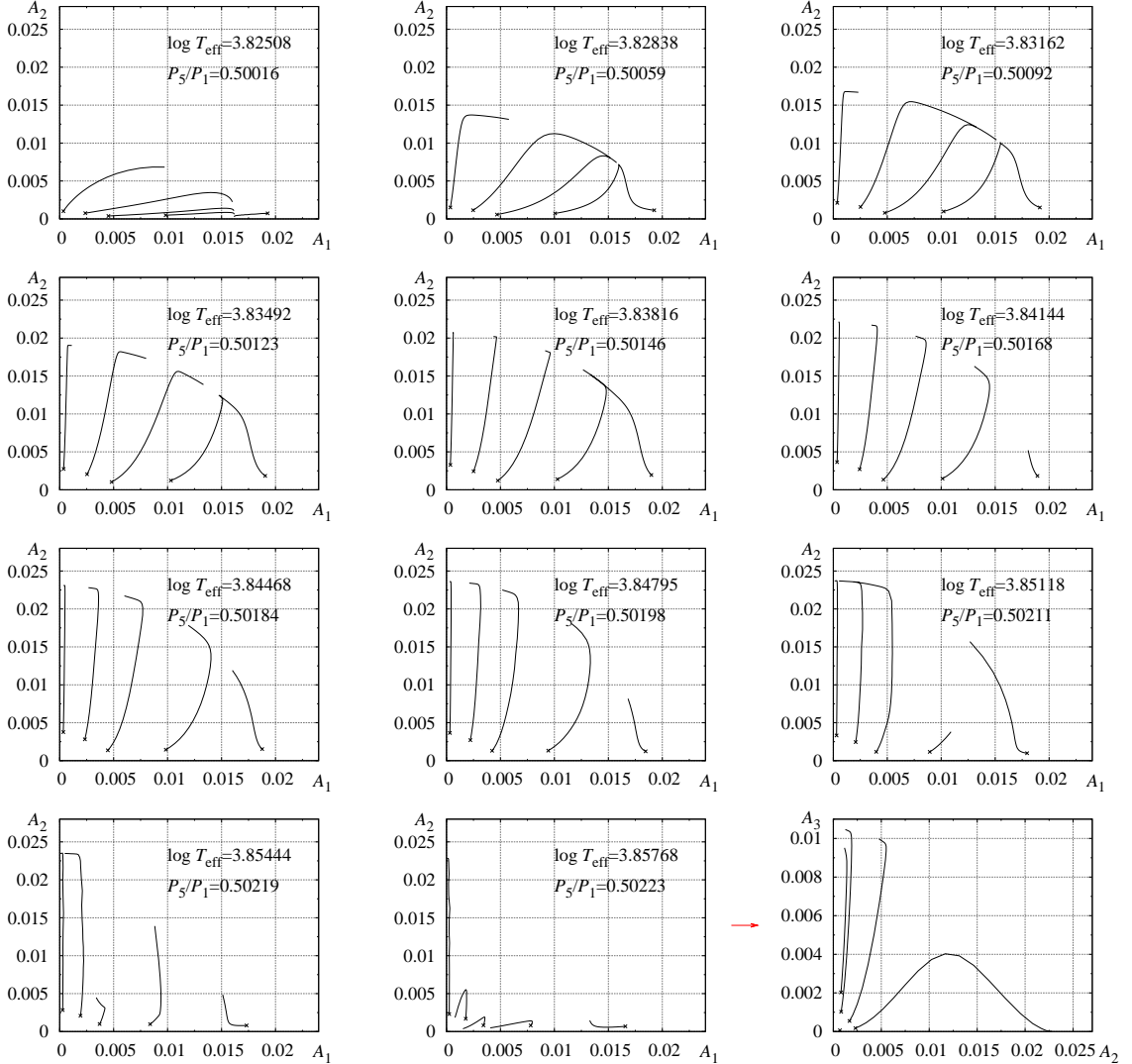

Figure 8.6: Results of direct nonlinear integrations for eleven consecutive models along evolutionary track of $2.5M_\odot$ ($Z = 0.006$). Hydrodynamical trajectories are plotted in $A_1 - A_2$ amplitude-amplitude plane. For the last model, trajectories are plotted also in $A_2 - A_3$ plane. Crosses mark the beginning of each trajectory. Effective temperatures of the models, as well as linear P_5/P_1 period ratios are given in each panel.

The most interesting modal selection scenario is visible within the instability strip along $2.5M_\odot$ evolutionary track (Figures 8.5 and 8.6). For the hottest model in this sequence, 2O/3O hysteresis is possible. Depending on the initial conditions, trajectories evolve either toward second overtone attractor or toward the third overtone attractor. For this particular model, trajectories are displayed in both $A_1 - A_2$

and $A_2 - A_3$ planes (last two panels in Figure 8.6). In five consecutive cooler models, only single-mode pulsation in the second overtone is possible. Then, a double-overtone domain emerges. Multimode attractor is clearly visible for models with $\log T_{\mathrm{eff}} = 3.83492$, 3.83162, and 3.82838 (Figure 8.6). The only model to the red of this domain pulsates in the first overtone. Double-overtone domain appears in between the first and second overtone pulsation domains. Although this is typical scenario for non-resonant mechanism, resonant one cannot be excluded *a priori*. Arrow in Figure 8.5 shows the location of the 2:1, $2\omega_1 = \omega_5$ resonance center. It is located quite close to the double-overtone domain. The resonant destabilization of the first overtone limit cycle, if located at a correct position along discussed path, can in principle lead to double-overtone domain, instead of either-or 1O/2O domain. It is worth to notice that the 2:1 resonances affect the pulsations in a rather wide range of period ratios, and that destabilization not necessarily occurs exactly at the resonance center (*see* Figure 7.2). Without more detailed analysis, strict statements about the nature of discovered doubly-periodic domain cannot be made.

Remaining five nonlinear model sequences of $Z = 0.006$ display qualitatively the same mode selection scenario, which however, is different from scenario described for $2.5\mathrm{M}_\odot$ sequence. Double-mode domain is not present. Instead, the either-or 1O/2O domain is located in between the single-mode first and second overtone pulsation domains (Figure 8.7). Discussed resonances, seem to have no visible effect on the modal selection along these sequences.

Five nonlinear model sequences were computed for higher metallicity, $Z = 0.008$. Three sequences correspond to first crossing evolutionary models of masses, $2.5\mathrm{M}_\odot$, $3.0\mathrm{M}_\odot$ and $3.5\mathrm{M}_\odot$. The remaining two sequences correspond to horizontal paths with artificially increased luminosity ($3.0\mathrm{M}_\odot$, $\Delta \log L = 0.4$ and $3.5\mathrm{M}_\odot$, $\Delta \log L = 0.4$). In the Petersen diagram, they cover the whole period range occupied by double-overtone Cepheids. Their location, as well as modal selection inferred from the hydrodynamical trajectories is shown in Figure 8.8. Individual hydrodynamical trajectories for models along $2.5\mathrm{M}_\odot$ sequence are displayed in Figure 8.9.

The overall modal selection is very similar as in case of lower metallicity models (compare Figures 8.8 and 8.5). Again, most interesting results are obtained for models of the shortest periods, with masses of $2.5\mathrm{M}_\odot$. For the two hottest models in this sequence, pulsation either in the third or in the second overtone is possible (hysteresis). Trajectories for these models are displayed in $A_2 - A_3$ plane at the bottom of Figure 8.9. For the four consecutive cooler models, single-mode pulsation in the second overtone is possible. Then, a multi-mode domain emerges. Simultaneous pulsation in the first and second overtones is possible for models with $\log T_{\mathrm{eff}} = 3.84029$, 3.83701, and 3.83377 (Figure 8.9). The center of the 2:1 resonance between first and fifth overtones, marked with arrow in Figure 8.8, falls exactly in the middle of discussed domain. This indicates that the resonance can be crucial in bringing up stable doubly-periodic behaviour. Models of longest periods along the discussed sequence pulsate in the first overtone.

For the remaining four model sequences with metallicity $Z = 0.008$ no traces of multimode behaviour are found. For models along evolutionary tracks ($3.0\mathrm{M}_\odot$ and $3.5\mathrm{M}_\odot$) either-or domain, in which pulsation in either second or first overtone is possible, separates the single-mode second overtone domain (shorter periods) and single-mode first overtone domain (longer periods). For models with luminosity
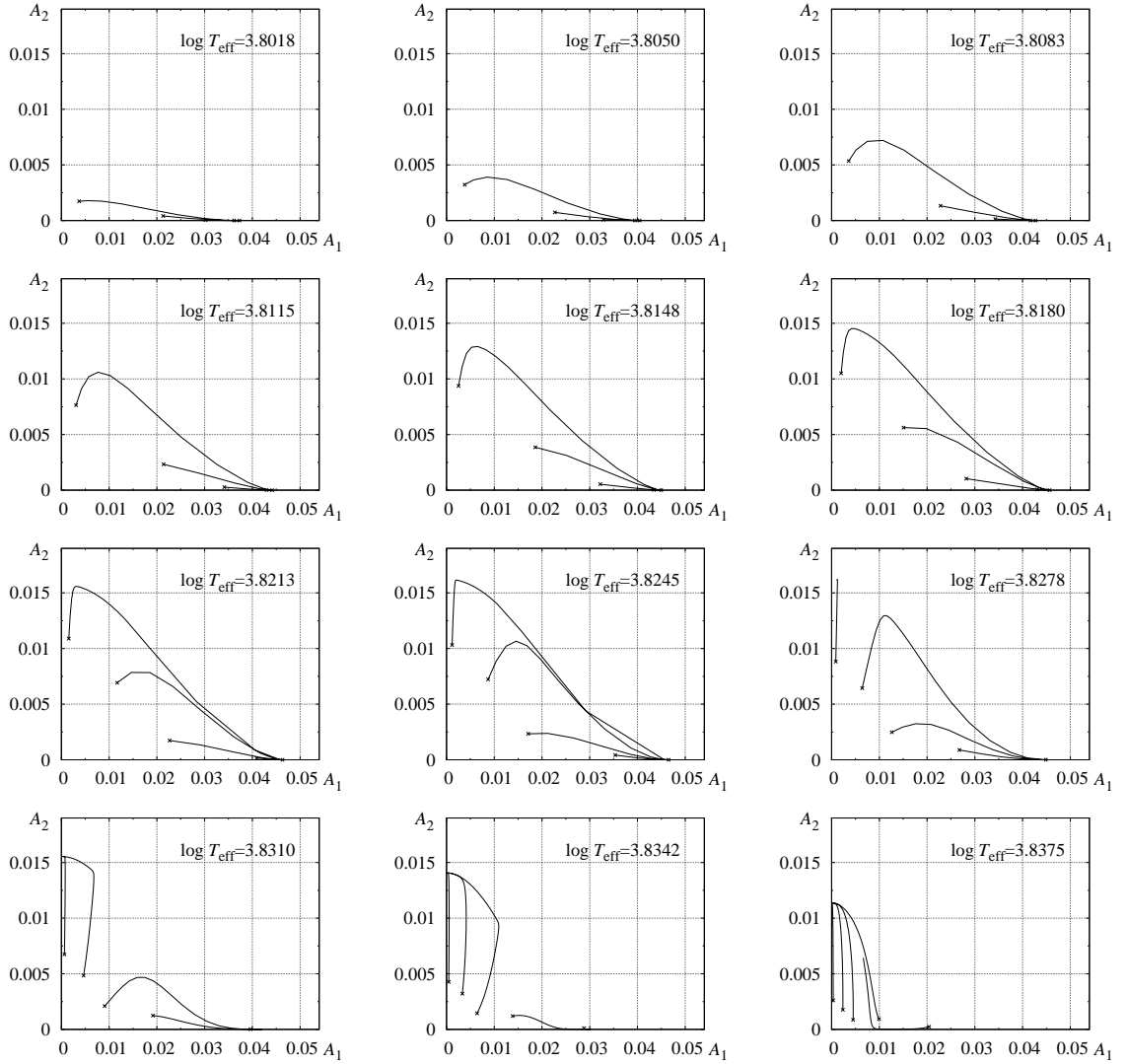
Figure 8.7: Results of direct nonlinear integrations for twelve consecutive models of $3.0 M_\odot$ and constant luminosity, increased by $\Delta \log L \approx 0.4$ relative to average luminosity along evolutionary track of the same mass. Metallicity of the models is $Z = 0.006$. Hydrodynamical trajectories are plotted in $A_1 - A_2$ amplitude-amplitude plane. Crosses mark the beginning of each trajectory. Effective temperatures of the models are given in each panel.

increase ($3.0 M_\odot$, $\Delta \log L = 0.4$ and $3.5 M_\odot$, $\Delta \log L = 0.4$) first overtone pulsation dominates. Only for $3.0 M_\odot$ sequence ($\Delta \log L = 0.4$) either-or domain exists at shortest periods, in which second overtone pulsation is also possible. Again, as in case of $Z = 0.006$ models, it seems that resonances do not affect the modal selection along model sequences of higher masses (longer periods).

Although some double-overtone models were found, overall results are not satisfactory. Double-overtone domain exists at shortest overtone periods, only. No double-overtone models are found at longer periods, particularly in a period range, $0.5\,\mathrm{d} < P_1 < 0.9\,\mathrm{d}$, at which double-overtone pulsation is the most common form of pulsation in the LMC. Surprisingly, in many models only pulsation in the second
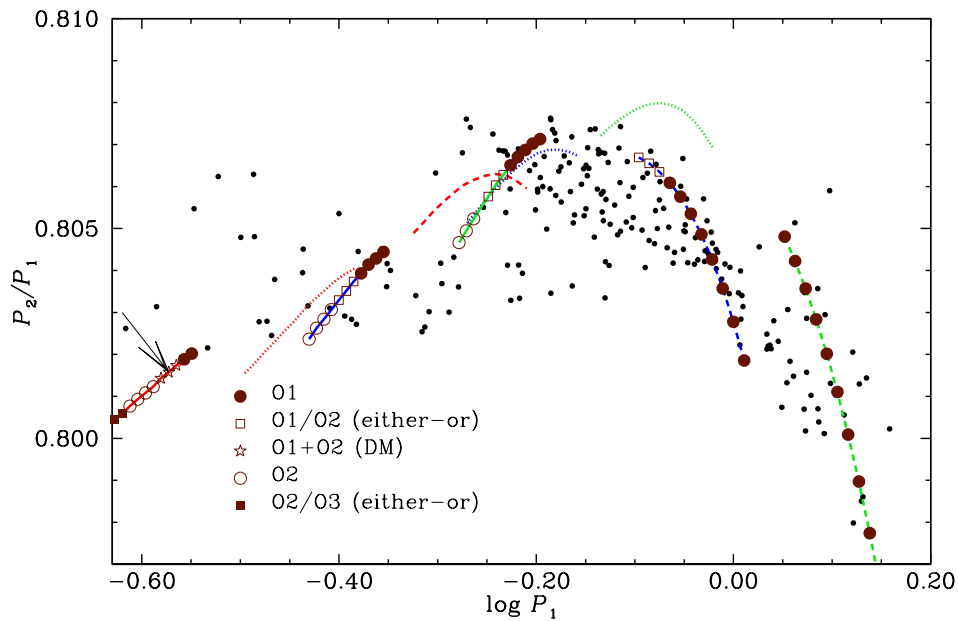
Figure 8.8: Petersen diagram showing the location and stability information for the computed nonlinear convective models. Lines showing the location of linear model sequences are the same as in Figure 8.4. Arrow marks the location of the $2\omega_1 = \omega_5$ resonance center along $2.5\mathrm{M}_\odot$ evolutionary path. All computations for metallicity parameter $Z = 0.008$.

overtone is possible. Observationally, this form of pulsation is very rare, as only 14 such objects are found in LMC (SOSZYŃSKI *et al.* 2008b). Therefore, also in case of 1O/2O double-mode Cepheids, convective hydrocode fails to reproduce the modal selection. This conclusion is not so strict as in case of F/1O Cepheids, as only one set of convective parameters was analysed. On the other hand, for hot overtone models, convection is not expected to play a crucial role, and results should not depend strongly on the values of convective parameters and/or effects included in the model. Certainly, more work is necessary to solve the puzzle of double-overtone pulsations.
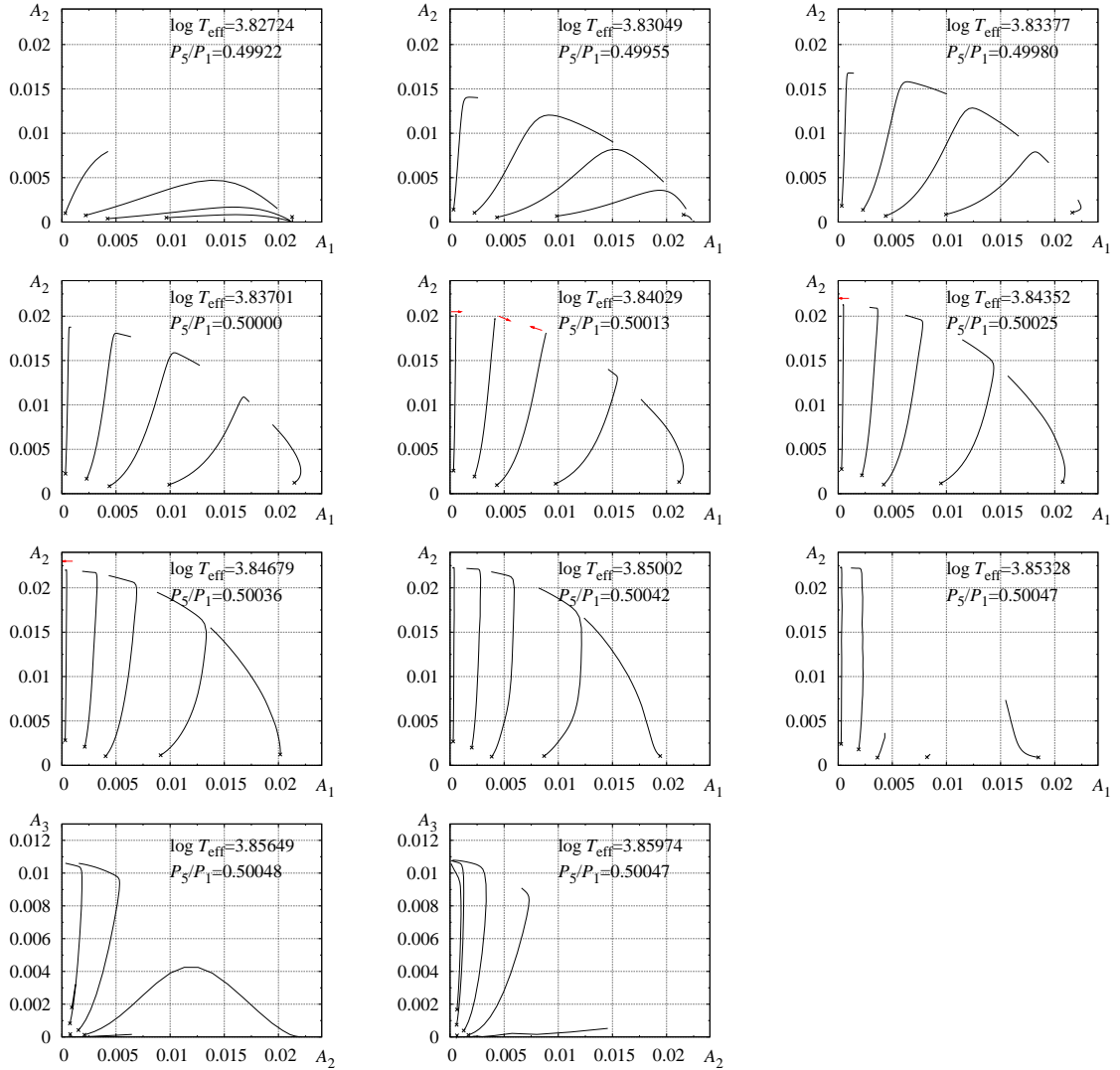
Figure 8.9: Results of direct nonlinear integrations for eleven consecutive models along evolutionary track of $2.5\mathrm{M}_\odot$ ($Z = 0.008$). Hydrodynamical trajectories are plotted in $A_1 - A_2$ amplitude-amplitude plane for the first nine models and in $A_2 - A_3$ plane for the last two models. Crosses mark the beginning of each trajectory. Red arrows at the end of some trajectories indicate the direction in which trajectory bend, which is sometimes not visible due to the scale adopted in the plots. Effective temperatures of the models, as well as linear P_5/P_1 period ratios are given in each panel.

Chapter 9

Summary and Conclusions

Through the last fifty years, numerical modeling of radial stellar pulsation allowed to understand many properties of the observed variables. Particularly, the great success was achieved in modeling of the single-mode pulsators. Already with radiative hydrocodes single-mode light and radial velocity curves were modeled quite successfully, allowing to understand the nature of *e.g.,* Hertzsprung bump progression observed in classical Cepheids (Chapter 1).

From the beginning of numerical computations, modeling of the double-mode pulsation was one of the major objectives. Two pulsation periods simultaneously observed, allow to put stringent constraints on stellar model. However, computation of stable double-mode pulsation appeared a difficult and challenging task. Despite extensive efforts, the problem remained unsolved for many years. This disturbing situation has changed with the inclusion of turbulent convection into the model equations. Robust double-mode behaviour, involving fundamental and first overtone modes, was computed for both RR Lyrae and Cepheid models (FEUCHTINGER 1998, KOLLÁTH *et al.* 1998; Chapter 2). The success was partial, however. Besides the simple claim that convection is necessary to obtain the double-mode behaviour and that its origin is non-resonant, our knowledge of underlying physical processes remained obscure. Particularly the specific effect of turbulent convection responsible for the occurrence of double-mode behaviour was not identified.

In this thesis, I describe the results of nonlinear modeling of Cepheid pulsation. The basic tools I used in this research, were convective pulsation hydrocodes; static model builder, linear nonadiabatic code, and nonlinear, direct time integration hydrocode. The first two codes were written by myself, while in the third case, I have modified the existing radiative hydrocode of STELLINGWERF (1975a). The codes are Lagrangian and treat the radiation in the diffusion approximation. For the convective energy transfer, I adopted the best currently available model suitable for nonlinear integrations – the KUHFUSS (1986) model. This is non-local time-dependent model, in which generation of turbulent energy is described through the one additional equation. Construction of static convective envelope is much more difficult than in the radiative case. Simple integration of model equations, allowing to construct the full static model in radiative case, now can be used to compute only initial model, which neglects the effects of turbulent pressure and overshooting. To include these effects, I implemented the relaxation scheme in which full model equations are solved iteratively. Similar scheme was implemented in the Florida-

Budapest codes (Yecko *et al.* 1998), but no details had been given. Linear nonadiabatic code was also written entirely by myself. To solve the linear eigenvalue problem, I adopted the method suggested by Glasner & Buchler (1993). Nonlinear direct time integration hydrocode was based on the radiative hydrocode of Stellingwerf (1975a), in which full nonlinear model equations are solved with the implicit Fraley (1968) method. Inclusion of turbulent convection into nonlinear scheme is a significant modification. Not only one additional equation for turbulent energy has to be implemented, but also remaining momentum and total energy equations must be supplemented with several convection-related terms. In order to preserve the total energy of the envelope during the model integrations, special averaging scheme has to be adopted. All codes require second derivatives of the thermodynamic quantities. To compute them, I implemented the analytical equation of state in the form of Stellingwerf (1982a).

The codes were tested by computing the sequences of single-mode Cepheid models, pulsating either in the fundamental or in the first overtone modes. I discussed extensively the structure and properties of some particular static and full amplitude models, to show how turbulent convection works in Cepheids. Computed radial velocity curves reproduce qualitatively the observed properties of these variables, particularly the progression of low order Fourier decomposition parameters with pulsation period (Chapter 4). Other test was the computation of stable double-mode F/1O behaviour. Search for such behaviour is not easy, as double-mode domain can be restricted to a narrow parameter range. It can also coexist with other stable single-mode solutions. Hence, some special techniques are necessary to establish the modal selection along model sequences. To this aim, I implemented the methods described by the Florida-Budapest group (*e.g.*, Kolláth *et al.* 2002), in which hydrodynamical computations are analysed with the help of the amplitude equation formalism. Unfortunately, no stable double-mode F/1O Cepheid model was found. This negative result motivated the research constituting the main part of this thesis.

Except single RR Lyrae model (Feuchtinger 1998), all other double-mode Cepheid and RR Lyrae models were computed with the use of the Florida-Budapest hydrocodes (*e.g.*, Kolláth *et al.* 1998, 2002, Szabó, Kolláth & Buchler 2004). These codes implement convection model very similar to that of Kuhfuß, however, with one important difference: negative buoyancy effects are neglected. Physical interpretation of this approximation, as well as its consequences for the computed models, were not studied by the Florida-Budapest group. These are severe, as I extensively analysed in Chapters 5 and 6 of this thesis. I implemented the Florida-Budapest approach (neglect of negative buoyancy) into the codes as an option. Then, a detailed comparison of models computed with negative buoyancy (default treatment) with those computed without negative buoyancy effects (Florida-Budapest), yielded the results and conclusions, I briefly summarize below.

i. Neglect of negative buoyancy effects leads to significant turbulent energies in convectively stable regions of the model. These energies are driven at the cost of pulsation energy through the eddy-viscous forces and are not damped effectively due to the lack of buoyant forces.

ii. The driving of turbulent energies by the eddy-viscous forces is associated with the eddy-viscous damping of the pulsations. Hence, amplitude of the single-mode models computed without negative buoyancy is smaller than the amplitude of the

models computed with negative buoyancy effects included.

iii. Amplitude of the fundamental mode is reduced much more than the amplitude of the first overtone. This is caused by the different spatial structure of the modes, particularly, by the different profiles of radial velocity within the model, powering the eddy-viscous damping.

iv. Reduction of amplitudes of models neglecting the negative buoyancy (Florida-Budapest), as compared to models including this effect (default in this thesis) is responsible for the double-mode behaviour found in the former models. Particularly, fundamental mode with its strongly reduced amplitude is no longer able to saturate the pulsation instability alone, allowing the growth of the first overtone. In terms of limit cycle stability, amplitude of the fundamental mode is reduced strongly enough to cause its destabilization in a parameter range in which first overtone is also unstable, thus, leading to stable double-mode pulsation.

v. As the neglect of negative buoyancy is physically not justified, double-mode F/1O Cepheid models computed with the Florida-Budapest hydrocode are incorrect.

vi. Despite extensive parameter study, no stable non-resonant double-mode pulsation was found with hydrocodes including negative buoyancy effects.

Non-resonant mechanism of exciting the double-mode pulsation is one of the two possibilities. The other is resonant excitation. In Chapter 7, I demonstrated the role of resonances in exciting the multi-periodic pulsation, based on radiative models of classical Cepheids and β Cephei stars. In the Cepheid models, the 2:1 resonance between the fundamental mode and the second overtone, $2\omega_0 = \omega_2$, was found to be responsible for the doubly-periodic F/1O Cepheid pulsation. This doubly-periodic behaviour manifests in prominent spiral attractors in amplitudes phase-space. It is the first case of such attractor found in hydrodynamical pulsation modeling. The three-mode resonance, $2\omega_1 = \omega_0 + \omega_2$, was found to be responsible for the F/1O doubly-periodic pulsation in β Cephei models. Interestingly, the resonant multimode domain is located on the same evolutionary track at which also non-resonant double-mode domain exists. Unfortunately, these δ Cephei and β Cephei models do not correspond to any real stars. The resonant doubly-periodic Cepheid models have much longer periods, than are observed. In real β Cephei stars, two radial modes *alone* are not observed. Non-radial pulsation dominates in these stars. Nevertheless, these models are of great value. As they are radiative, Floquet analysis of the stability of the single-mode limit cycles can be performed, allowing to understand how the resonant mechanism works.

In the period range occupied by F/1O double-mode Cepheids no low-order resonances among radial modes are found. However, I found several models in which higher-order three mode resonance, $2\omega_1 = \omega_0 + \omega_2$, can be conductive in bringing up stable doubly-periodic F/1O pulsation (Chapter 7). These are convective models, computed including negative buoyancy effects. Unfortunately, computed doubly-periodic behaviour is restricted to a narrow parameter range.

Analysis of the OGLE-III data from the Large Magellanic Cloud, lead to discovery of plenty of new double-overtone Cepheids, pulsating simultaneously in the first and second overtones. In some particular period range, $0.5\,\mathrm{d} < P_1 < 0.9\,\mathrm{d}$, this is the most common form of Cepheid pulsation in the LMC. These data motivated the search for stable double-mode 1O/2O Cepheid behaviour (Chapter 8). Linear analysis indicated that two types of resonances can be conductive in bringing up stable

double-mode pulsation in these stars. In objects with first overtone period shorter than ≈ 0.8 days, the 2:1 resonance between first and fifth overtones, $2\omega_1 = \omega_5$ can be operational. In intermediate period range, 0.45 days $< P_1 < 0.70$ days, high-order three-mode resonance involving consecutive three overtones, $2\omega_2 = \omega_1 + \omega_3$, is present. At longer periods, $P_1 > 0.80$ days, no resonances had been found and thus, a non-resonant mechanism must be operational. Conducted survey of nonlinear convective models revealed stable double-mode 1O/2O models, however, only at the shortest overtone periods, $P_1 < 0.30$ days. The 2:1 resonance, $2\omega_1 = \omega_5$, is most likely responsible for the double-mode behaviour observed in these models, however, more analysis is necessary to confirm this conclusion. In a period range occupied by majority of LMC double-overtone Cepheids no stable double-mode behaviour was found. Instead, either-or 1O/2O domain was found separating the single-mode first and second overtone domains.

The results presented in this thesis are rather disappointing. It was shown that double-mode F/1O Cepheid models published so far are incorrect, as they result from unphysical neglect of negative buoyancy effects. When these effects are included, attempts to model the double-mode phenomenon are mostly unsuccessful. Although some stable doubly-periodic models were found, involving both fundamental mode and first overtone and first and second overtones, in both cases they are restricted to very narrow period ranges. Resonant mechanism is the most likely cause of double-mode pulsation observed in these models. No double-mode models in which non-resonant mechanism would be operational were found. This is particularly disappointing, as linear analysis indicates that such mechanism should be responsible for most of the observed double-mode Cepheids. The problem of modeling the double-mode Cepheid pulsation remains open.

Double-mode Cepheids exist, and correct hydrocode should reproduce the observed double-mode behaviour. Presented results indicate that something is still missing in our hydrocodes. Most probably, the overall description of convection is too simplified. One-equation model, although suitable for nonlinear computations, may lack the important features of real three-dimensional turbulent convection, essential for the double-mode pulsation. Certainly, further work on modal selection requires new, more sophisticated treatment of convection.

Studying of double-mode phenomenon was the main subject of this thesis. However, it is also worth to mention some other results. Approximations adopted in different hydrocodes were analyzed in detail. This concerns not only the treatment of convectively stable layers, but also *e.g.*, the eddy-viscous terms (Chapter 5). Two forms of eddy-viscous terms are commonly adopted in pulsation hydrocodes. These are either eddy-viscous pressure or eddy-viscous momentum and energy transfer rates. It was found that the differences in models computed using these two approaches are quantitative only, models computed using eddy-viscous pressure being linearly less unstable and consequently having smaller amplitudes.

Fourier decomposition parameters for radial velocity curves of convective fundamental mode Cepheid models were computed and compared with observations. No such comparison was done earlier for convective models. Computed models agree quite satisfactorily with observations (Chapter 4). Significant discrepancy was noted only for amplitude ratio, R_{21}, for models with period shorter than 10 days. Increase of model R_{21} with pulsation period is not so steep as is observed. Similarly model-

ing of single-mode first overtone Cepheids is quite satisfactory. Here, a problem was noted for the Fourier phase, φ_{21}, at short overtone periods, where model values are slightly too high.

Still many interesting results concerning single-mode variables can be obtained with the described convective hydrocodes. Modeling of simultaneous pulsation in two or more modes, awaits a breakthrough.

Appendix A

Work integrals

In this Appendix, the derivation of work integrals, both nonlinear and linear, is presented. We consider the Kuhfuß convection model, described in Section 2.4. Model equations are summarized in Section 3.2. Focus is put on the eddy-viscous terms in the Kuhfuß form (*see* Section 5.1). Derivation of corresponding work integrals was first published by SMOLEC & MOSKALIK (2008a).

We follow the derivation method presented in the book of UNNO *et al.* (1989). Viscous momentum and energy transfer rates are written using Eqs. (3.7) and (3.8). Momentum and energy equations, (2.37) and (2.39), are,

$$\frac{\mathrm{d}\vec{u}}{\mathrm{d}t} = -\frac{1}{\rho}\nabla p_{\mathrm{tot}} - \nabla\Phi + 4\pi\frac{1}{r}\frac{\partial\mathcal{X}}{\partial M}\hat{e}_r, \tag{A.1}$$

$$\frac{\mathrm{d}(E + e_t)}{\mathrm{d}t} + p_{\mathrm{tot}}\frac{\mathrm{d}V}{\mathrm{d}t} = -\frac{1}{\rho}\nabla\vec{F} + 4\pi\mathcal{X}\frac{\partial(u_r/r)}{\partial M}, \tag{A.2}$$

Momentum equation was rewritten in the vector form. Above, $\hat{e}_r$ is unit vector in the radial direction, Φ is gravitational potential, $\nabla\Phi = GM_r/r^2$, u_r is radial (only) component of the velocity vector $\vec{u}$. Total pressure is denoted as, $p_{\mathrm{tot}} = p + p_t$, and $\vec{F}$ is the total flux, $\vec{F} = \vec{F}_{\mathrm{r}} + \vec{F}_{\mathrm{c}} + \vec{F}_{\mathrm{t}}$.

To obtain the equation of conservation of mechanical energy, momentum equation is multiplied by $\rho\vec{u}$,

$$\rho\frac{\mathrm{d}(\vec{u^2}/2)}{\mathrm{d}t} = -\vec{u}\nabla p_{\mathrm{tot}} - \rho\vec{u}\nabla\Phi + 4\pi\rho\frac{u_r}{r}\frac{\partial\mathcal{X}}{\partial M}. \tag{A.3}$$

Dividing above equation by ρ, and adding it to the energy equation we get,

$$\frac{\mathrm{d}(E + e_t + \vec{u^2}/2)}{\mathrm{d}t} = -\vec{u}\nabla\Phi - \frac{1}{\rho}\nabla(\vec{F} + p_{\mathrm{tot}}\vec{u}) + 4\pi\frac{\partial(\mathcal{X}u_r/r)}{\partial M}, \tag{A.4}$$

where we made use of continuity equation,

$$\rho\frac{\mathrm{d}V}{\mathrm{d}t} = \nabla\vec{u}. \tag{A.5}$$

Integrating over the mass of the envelope we get,

$$\frac{\mathrm{d}E_{\mathrm{tot}}}{\mathrm{d}t} = -\int_{M_{\mathrm{i}}}^{M}\frac{1}{\rho}\nabla(p_{\mathrm{tot}}\vec{u} + \vec{F})\,\mathrm{d}M + 4\pi\int_{M_{\mathrm{i}}}^{M}\frac{\partial}{\partial M}\left(\mathcal{X}\frac{u_r}{r}\right)\mathrm{d}M, \tag{A.6}$$

where E_{tot} is equal to the total energy of the envelope,

$$E_{\text{tot}} = \int_{M_i}^{M} (E + e_t + \vec{u}^2/2 + \Phi/2)\, \mathrm{d}M, \tag{A.7}$$

M_i is mass enclosed at the inner boundary of the envelope, and we made use of the following relation (*see* Eq. 25.5 of Unno *et al.* 1989),

$$\int_{M_i}^{M} \vec{u}\nabla\Phi = \frac{1}{2}\frac{\mathrm{d}}{\mathrm{d}t}\int_{M_i}^{M} \Phi\, \mathrm{d}M. \tag{A.8}$$

Note that the last integral in Eq. (A.6) vanish due to adopted boundary conditions; at the inner boundary $u_r = 0$ (Eq. 3.57) and at the outer boundary $\mathcal{X} = 0$ (Eq. 3.55). The remaining integral in Eq. (A.6) is rewritten in the following form

$$\frac{\mathrm{d}E_{\text{tot}}}{\mathrm{d}t} = -\int_{M_i}^{M} \frac{1}{\rho}\nabla(\vec{F})\, \mathrm{d}M - \int_{r=R} p_{\text{tot}}\vec{u}\, \mathrm{d}\vec{s}, \tag{A.9}$$

where R is radius of the star. The last surface integral vanish due to our outer boundary condition ($p_{\text{tot}} = 0$, Eq. 3.54). Using energy equation (A.2) again, we obtain

$$\frac{\mathrm{d}E_{\text{tot}}}{\mathrm{d}t} = \int_{M_i}^{M} \left[\frac{\mathrm{d}(E + e_t)}{\mathrm{d}t} + p_{\text{tot}}\frac{\mathrm{d}V}{\mathrm{d}t} - 4\pi\mathcal{X}\frac{\partial(u_r/r)}{\partial M}\right] \mathrm{d}M. \tag{A.10}$$

Nonlinear work integral is obtained through integrating over the whole pulsation cycle, which yields

$$W = \oint_0^{P} \mathrm{d}t \int_{M_i}^{M} \mathrm{d}M \left[p_{\text{tot}}\frac{\mathrm{d}V}{\mathrm{d}t} - 4\pi\mathcal{X}\frac{\partial(u_r/r)}{\partial M}\right] \tag{A.11}$$

$$W = \oint_0^{P} \mathrm{d}t \int_{M_i}^{M} \mathrm{d}M \left[p_{\text{tot}}\frac{\mathrm{d}V}{\mathrm{d}t} - E_q\right]. \tag{A.12}$$

First term in the above integral corresponds to ordinary pressure work, while the second term to eddy-viscous work.

Linear work integrals are obtained through considering above nonlinear work integrals in the linear approximation,

$$W = \oint_0^{P} \mathrm{d}t \int_{M_i}^{M} \mathrm{d}M \left[(\delta p_{\text{tot}})\frac{\mathrm{d}(\delta V)}{\mathrm{d}t} - 4\pi(\delta\mathcal{X})\frac{\partial(u_r/r)}{\partial M}\right]. \tag{A.13}$$

Using relation, $u_r = \mathrm{d}(\delta r)/\mathrm{d}t$, and assuming $\delta z = \Re(\delta z e^{i\omega t})$ for the perturbed quantities, after laborious but straightforward algebra we arrive at

$$W = -\pi \int_{M_i}^{M} \Im\left[(\delta p_{\text{tot}})^*(\delta V)\right] \mathrm{d}M + \pi \int_{M_i}^{M} \Im\left[(\delta\mathcal{X})^*\left(\frac{\delta V}{r^3} - \frac{3V}{r^3}\frac{\delta r}{r}\right)\right] \mathrm{d}M. \tag{A.14}$$

The first integral corresponds to ordinary pressure work integral, and the second term is eddy-viscous work integral, for the Kuhfuß form of eddy viscosity. In case of the Kolláth form, eddy viscosity has a form of ordinary pressure, and is simply included in p_{tot}.

Appendix B

Energy conservation

The form of the time averages that appear in finite difference nonlinear equations, is determined by the energy conservation considerations. Below, I present the derivation of appropriate averaging scheme for convective hydrocode. Derivation is a simple extension of the purely radiative case (FRALEY 1968), which will presented first.

B.1 Radiative case

We consider basic equations of radiation hydrodynamics, (1.3), (1.4) and (1.5). Their Lagrangian versions are following,

$$\frac{\mathrm{d}u}{\mathrm{d}t} = -4\pi r^2 \frac{\partial p}{\partial M} - \frac{GM_r}{r^2}, \tag{B.1a}$$

$$\frac{\mathrm{d}E}{\mathrm{d}t} = -p\frac{\mathrm{d}V}{\mathrm{d}t} - \frac{\partial L_\mathrm{r}}{\partial M}, \tag{B.1b}$$

$$\frac{\mathrm{d}r}{\mathrm{d}t} = u \tag{B.1c}$$

Finite difference form of the above equations is,

$$\frac{Du_i}{DT} = -4\pi\big\langle r_i^2\big\rangle\frac{\Delta\langle p_i\rangle}{DM2_i} - GM_i\Big\langle\frac{1}{r_i^2}\Big\rangle, \tag{B.2a}$$

$$\frac{DE_i}{DT} = -\big\langle p_i\big\rangle\frac{DV_i}{DT} - \frac{\Delta\big\langle L_{\mathrm{r},i}\big\rangle}{DM_i}, \tag{B.2b}$$

$$\frac{Dr_i}{DT} = \big\langle u_i\big\rangle. \tag{B.2c}$$

For the time averages we write,

$$\big\langle u_i\big\rangle = \zeta u_i^{(n+1)} + (1-\zeta)u_i^{(n)} \tag{B.3}$$

$$\big\langle p_i\big\rangle = \theta p_i^{(n+1)} + (1-\theta)p_i^{(n)} \tag{B.4}$$

$$\big\langle L_{\mathrm{r},i}\big\rangle = w_r L_{\mathrm{r},i}^{(n+1)} + (1-w_r)L_{\mathrm{r},i}^{(n)} \tag{B.5}$$

In the following we will use the below relation,

$$DV_i = \frac{4\pi}{3DM_i}\left(r_i^{3\ (n+1)} - r_{i-1}^{3\ (n+1)} - r_i^{3\ (n)} + r_{i-1}^{3\ (n)}\right)$$
$$= \frac{4\pi}{DM_i}DT\left(\langle u_i\rangle G_i - \langle u_{i-1}\rangle G_{i-1}\right) \tag{B.6}$$

where we made use of Eq. (B.2c), and denoted,

$$G_i = \frac{1}{3}\left(r_i^{2\ (n+1)} + r_i^{(n+1)}r_i^{(n)} + r_i^{2\ (n)}\right). \tag{B.7}$$

The total energy of the envelope is,

$$E_{\text{tot}} = \sum_{i=1}^{N}\left[DM_iE_i + 0.5DM2_iu_i^2 - \frac{GM_iDM2_i}{r_i}\right],$$

where the summation is extended over all model zones/interfaces. In order to preserve the total energy, its change during one time step, $\Delta E_{\text{tot}}/DT$, should equal to zero. We have,

$$\frac{\Delta E_{\text{tot}}}{DT} = \sum_{i=1}^{N}\left[DM_i\overbrace{\frac{DE_i}{DT}}^{\rightarrow(B.2b)} + 0.5\frac{DM2_i}{DT}\left(u_i^{2\ (n+1)} - u_i^{2\ (n)}\right) - \frac{GM_iDM2_i}{DT}\overbrace{\frac{r_i^{(n)} - r_i^{(n+1)}}{r_i^{(n)}r_i^{(n+1)}}}^{\rightarrow(B.2c)}\right]$$

$$= \sum_{i=1}^{N}\left[-DM_i\langle p_i\rangle\overbrace{\frac{DV_i}{DT}}^{\rightarrow(B.6)} + 0.5DM2_i\frac{Du_i}{DT}\left(u_i^{(n+1)} + u_i^{(n)}\right)\right.$$
$$\left. + GM_iDM2_i\frac{\langle u_i\rangle}{r_i^{(n)}r_i^{(n+1)}}\right]$$

$$= \sum_{i=1}^{N}\left[-4\pi\langle p_i\rangle\left(\langle u_i\rangle G_i - \langle u_{i-1}\rangle G_{i-1}\right)\right.$$
$$\left. + 0.5DM2_i\overbrace{\frac{Du_i}{DT}}^{\rightarrow(B.2a)}\left(2\langle u_i\rangle + \overbrace{u_i^{(n+1)} + u_i^{(n)} - 2\langle u_i\rangle}^{=\mathcal{A}=0\ \text{if}\ \zeta=1/2}\right) + GM_iDM2_i\frac{\langle u_i\rangle}{r_i^{(n)}r_i^{(n+1)}}\right]$$

$$= \sum_{i=1}^{N}\left[-4\pi\langle p_i\rangle\left(\langle u_i\rangle G_i - \langle u_{i-1}\rangle G_{i-1}\right)\right.$$
$$\left. + DM2_i\langle u_i\rangle\left(-4\pi\langle r_i^2\rangle\frac{\Delta\langle p_i\rangle}{DM2_i} - GM_i\langle\frac{1}{r_i^2}\rangle\right) + GM_iDM2_i\frac{\langle u_i\rangle}{r_i^{(n)}r_i^{(n+1)}}\right]$$

$$= \sum_{i=1}^{N}\left[-4\pi\langle p_i\rangle\left(\langle u_i\rangle G_i - \langle u_{i-1}\rangle G_{i-1}\right)\right.$$
$$\left. - 4\pi\langle u_i\rangle\langle r_i^2\rangle\Delta\langle p_i\rangle + GM_iDM2_i\langle u_i\rangle\left(\frac{1}{r_i^{(n)}r_i^{(n+1)}} - \langle\frac{1}{r_i^2}\rangle\right)\right].$$

The last term vanishes, if following time averaging is adopted,

$$\frac{1}{r_i^{(n)}r_i^{(n+1)}} = \left\langle\frac{1}{r_i^2}\right\rangle. \tag{B.8}$$

Note also, that the term denoted by $\mathcal{A}$ in above calculations, namely,

$$u_i^{(n+1)} + u_i^{(n)} - 2\langle u_i \rangle,$$

equals to zero if time centered definition for velocity averaging is adopted,

$$\zeta = \frac{1}{2}. \tag{B.9}$$

Expanding $\Delta \langle p_i \rangle$ into $\langle p_{i+1} \rangle - \langle p_i \rangle$ we get,

$$
\begin{aligned}
-\frac{\Delta E_{\text{tot}}}{4\pi DT} &= \sum_{i=1}^{N} \left[\langle p_i \rangle \left(\langle u_i \rangle G_i - \langle u_{i-1} \rangle G_{i-1} \right) + \langle u_i \rangle \langle r_i^2 \rangle \left(\langle p_{i+1} \rangle - \langle p_i \rangle \right) \right] \\
&= \sum_{i=1}^{N} \left[\langle p_{i+1} \rangle \langle u_i \rangle \langle r_i^2 \rangle - \langle p_i \rangle \langle u_{i-1} \rangle G_{i-1} + \langle p_i \rangle \langle u_i \rangle \left(G_i - \langle r_i^2 \rangle \right) \right].
\end{aligned}
$$

The last term in square braces vanishes, if following time averaging is adopted,

$$\langle r_i^2 \rangle = G_i. \tag{B.10}$$

The sum reduces to boundary terms,

$$\frac{\Delta E_{\text{tot}}}{4\pi DT} = \langle p_{N+1} \rangle \langle u_N \rangle G_N - \langle p_1 \rangle \langle u_0 \rangle G_0 = 0, \tag{B.11}$$

and vanish. Thus if $\zeta = 1/2$ and time averages (B.8) and (B.10) are adopted, total energy is preserved. Pressure has to be averaged in the same manner in both momentum and energy equations. The way we average the luminosity has no effect on the energy conservation.

B.2 Convective case

We consider equations (3.50) and (3.51). After following substitutions, $\tilde{p} = p + p_t$, $\tilde{E} = E + e_t$, $\tilde{L} = L_{\text{r}} + L_{\text{c}} + L_{\text{t}}$, their form is following,

$$\frac{Du_i}{DT} = -4\pi \langle r_i^2 \rangle \frac{\Delta \langle \tilde{p}_i \rangle}{DM2_i} - GM_i \left\langle \frac{1}{r_i^2} \right\rangle + \langle U_{q,i} \rangle, \tag{B.12}$$

$$\frac{D\tilde{E}_i}{DT} + \langle \tilde{p}_i \rangle \frac{DV_i}{DT} = -\frac{\Delta \langle \tilde{L}_i \rangle}{DM_i} + \langle E_{q,i} \rangle. \tag{B.13}$$

Now the total energy is,

$$E_{\text{tot}} = \sum_{i=1}^{N} \left[DM_i \tilde{E}_i + 0.5 DM2_i u_i^2 - \frac{GM_i DM2_i}{r_i} \right]. \tag{B.14}$$

Except the eddy-viscous terms, the form of the above equations is exactly the same as in radiative case (*cf.* Eqs. B.2a, B.2b). Hence, adopting exactly the same averagings

(Eqs. B.8, B.9 and B.10), the expression for total energy change during one time step reduces to,

$$\frac{\Delta E_{\text{tot}}}{DT} = \sum_{i=1}^{N} \left[DM_i \langle E_{q,i} \rangle + 0.5 DM2_i \langle U_{q,i} \rangle 2 \langle u_i \rangle \right] \tag{B.15}$$

For $\langle U_{q,i} \rangle$ and $\langle E_{q,i} \rangle$ we adopt following averagings, which guarantee energy conservation,

$$\langle U_{q,i} \rangle = \frac{4\pi}{\langle r_i \rangle} \frac{\langle \mathcal{X}_{i+1} \rangle - \langle \mathcal{X}_i \rangle}{DM2_i} \tag{B.16}$$

$$\langle E_{q,i} \rangle = 4\pi \langle \mathcal{X}_i \rangle \frac{\langle u_i \rangle / \langle r_i \rangle - \langle u_{i-1} \rangle / \langle r_{i-1} \rangle}{DM_i} \tag{B.17}$$

Indeed,

$$
\begin{aligned}
\frac{\Delta E_{\text{tot}}}{4\pi DT} &= \sum_{i=1}^{N} \left[\langle \mathcal{X}_i \rangle \left(\frac{\langle u_i \rangle}{\langle r_i \rangle} - \frac{\langle u_{i-1} \rangle}{\langle r_{i-1} \rangle} \right) + \frac{\langle u_i \rangle}{\langle r_i \rangle} \left(\langle \mathcal{X}_{i+1} \rangle - \langle \mathcal{X}_i \rangle \right) \right] \\
&= \sum_{i=1}^{N} \left[\langle \mathcal{X}_{i+1} \rangle \frac{\langle u_i \rangle}{\langle r_i \rangle} - \langle \mathcal{X}_i \rangle \frac{\langle u_{i-1} \rangle}{\langle r_{i-1} \rangle} \right] \\
&= \langle \mathcal{X}_{N+1} \rangle \frac{\langle u_N \rangle}{\langle r_N \rangle} - \langle \mathcal{X}_1 \rangle \frac{\langle u_0 \rangle}{\langle r_0 \rangle} \\
&= 0
\end{aligned}
\tag{B.18}
$$

as $u_0 = 0$ (bottom boundary condition, Eq. 3.57) and $\mathcal{X}_{N+1} = 0$ (upper boundary condition for turbulent energy, Eq. 3.55). The way in which $\langle \mathcal{X}_i \rangle$, $\langle u_i \rangle$, $\langle r_i \rangle$ are calculated, has no effect on energy conservation. One may set,

$$\langle \mathcal{X}_i \rangle = \theta_u \mathcal{X}_i^{(n+1)} + (1 - \theta_u) \mathcal{X}_i^{(n)}, \tag{B.19}$$

$$\langle r_i \rangle = \beta r_i^{(n+1)} + (1 - \beta) r_i^{(n)}. \tag{B.20}$$

For $\langle u_i \rangle$ and consequently for $\langle r_i \rangle$ it is natural to adopt the time-centered definition (Eq. B.9), just as in momentum equation.

Note also that in above considerations, the turbulent energy equation alone, was not used at all. Hence, the way in which the coupling term in this equation is averaged, has no effect on energy conservation.

The whole averaging scheme is much simpler if eddy-viscous pressure, p_ν (Eq. 2.75) is used instead of eddy-viscous terms. Then p_ν is treated as additional term in $\tilde{p}$ and model equations reduce to exactly the same form as in case of radiative computations. Hence, averaging scheme is the same as described in Section B.1.

Appendix C
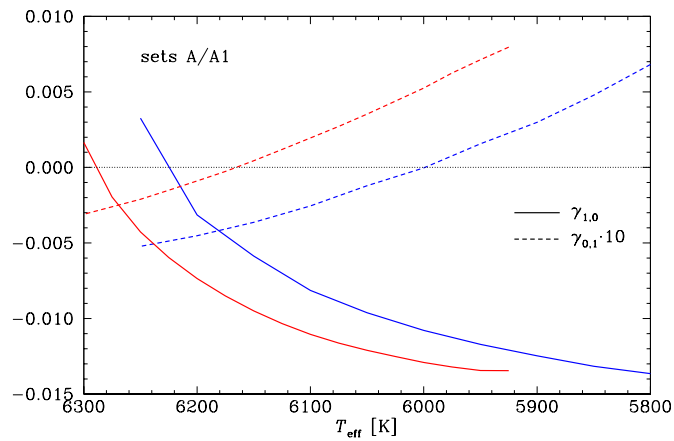
Stability coefficients for models of Section 6.3

Figure C.1: Comparison of stability coefficients of single-mode fixed points along sequence of Cepheid models adopting parameters of set A1 (Table 6.1; blue lines), with corresponding coefficients of basic set A.
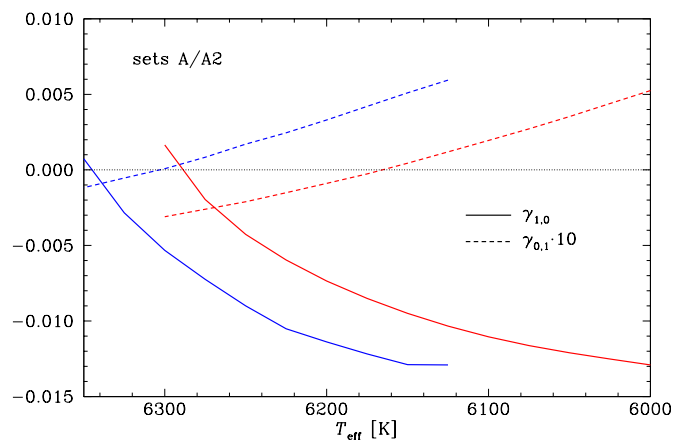
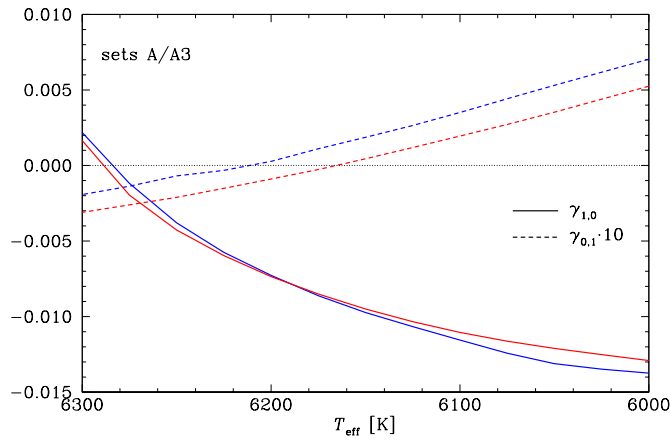

Figure C.2: The same as Figure C.1, but for set A2.

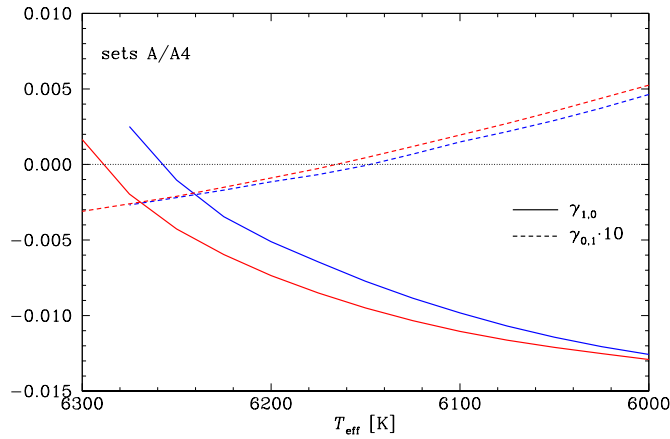Figure C.3: The same as Figure C.1, but for set A3.
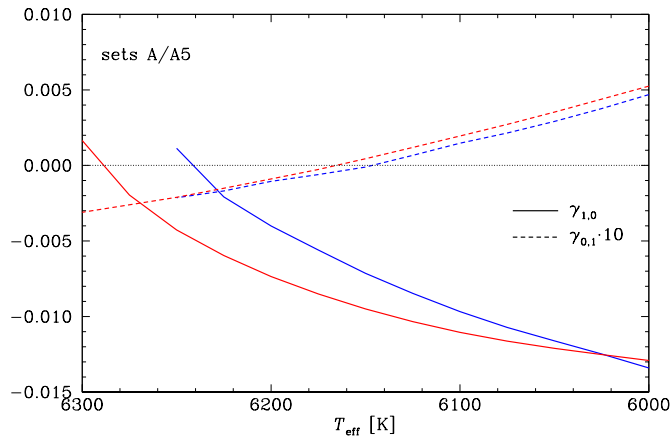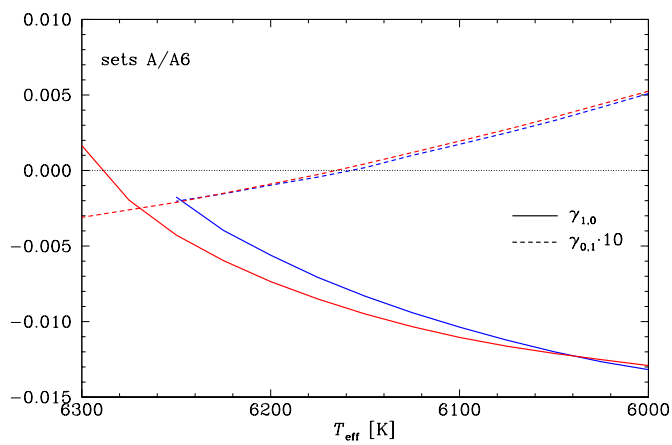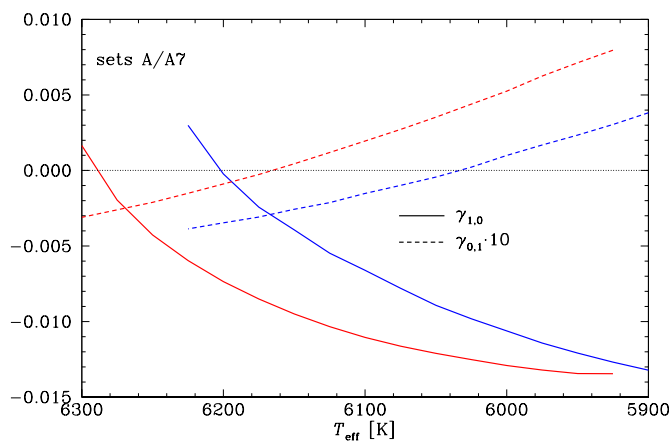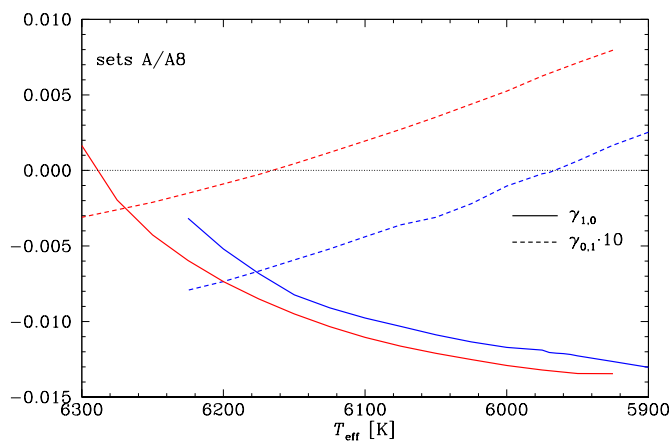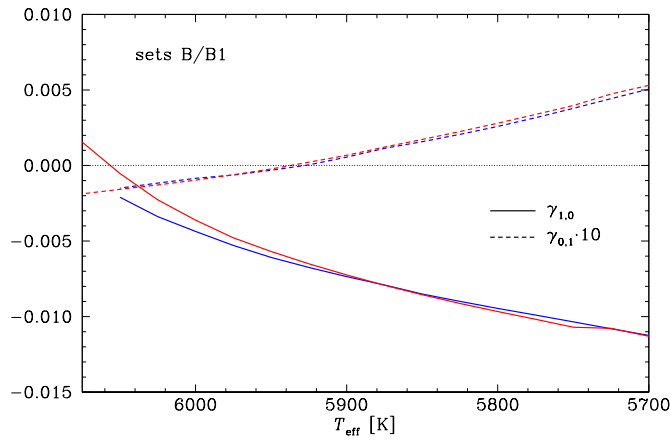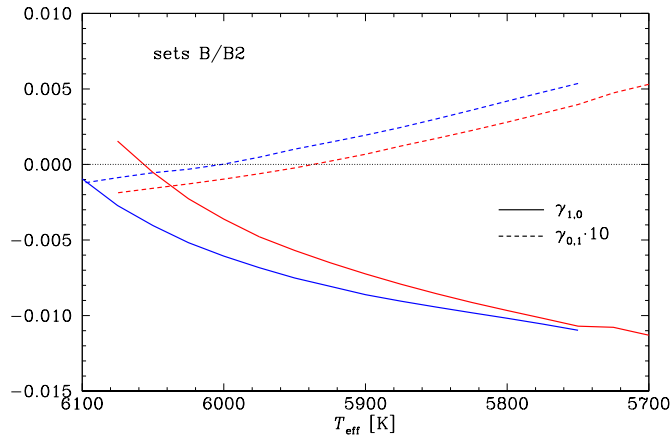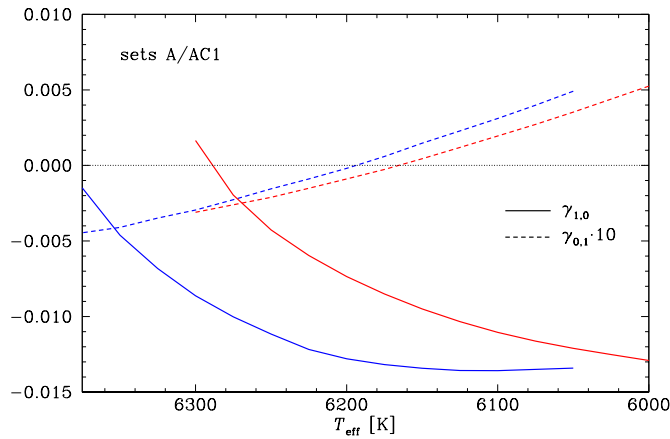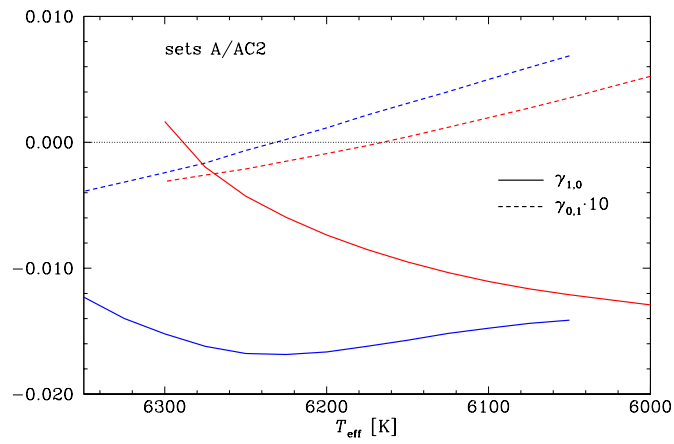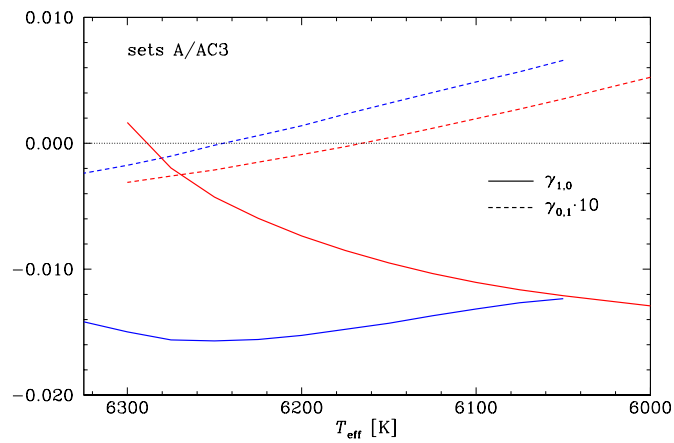

Figure C.4: The same as Figure C.1, but for set A4.

Figure C.5: The same as Figure C.1, but for set A5.

Figure C.6: The same as Figure C.1, but for set A6.

Figure C.7: The same as Figure C.1, but for set A7.

Figure C.8: The same as Figure C.1, but for set A8.

Figure C.9: The same as Figure C.1, but for set B1.

Figure C.10: The same as Figure C.1, but for set B2.

Figure C.11: The same as Figure C.1, but for set AC1.

Figure C.12: The same as Figure C.1, but for set AC2.

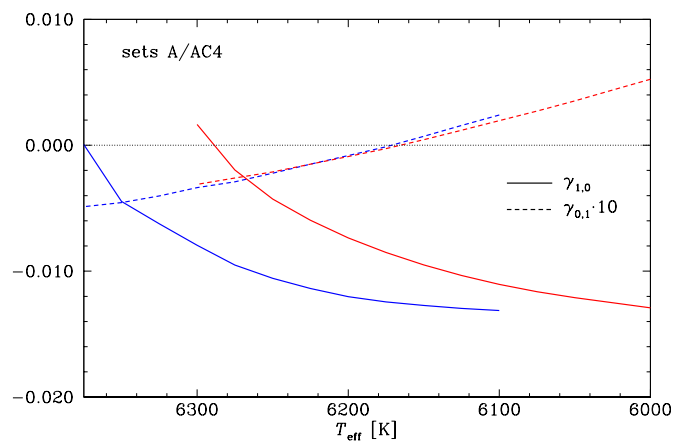Figure C.13: The same as Figure C.1, but for set AC3.

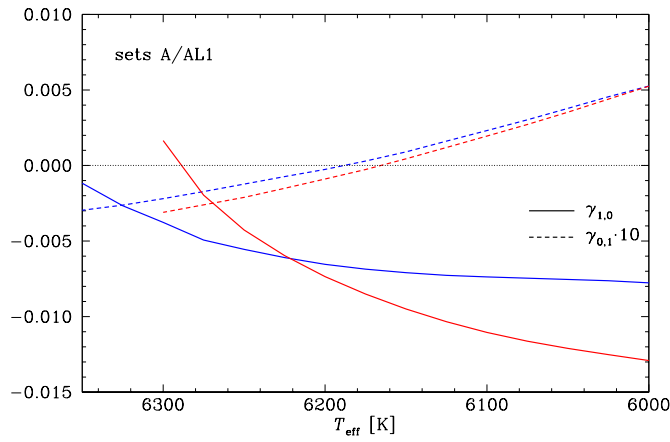

Figure C.14: The same as Figure C.1, but for set AC4.

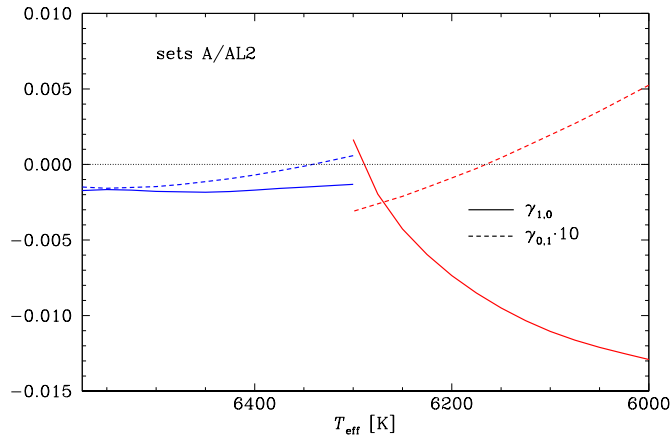Figure C.15: The same as Figure C.1, but for set AL1.

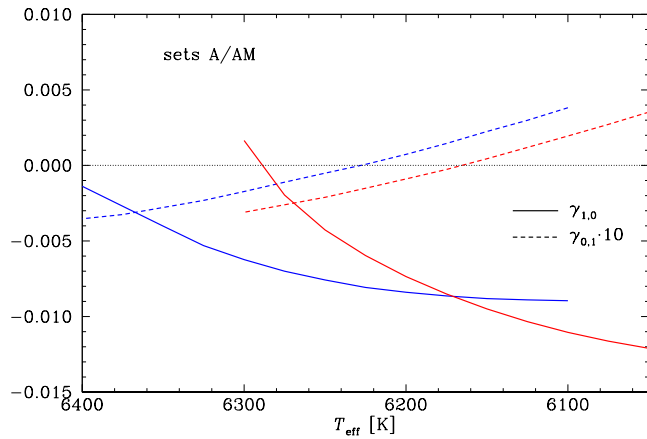Figure C.16: The same as Figure C.1, but for set AL2.

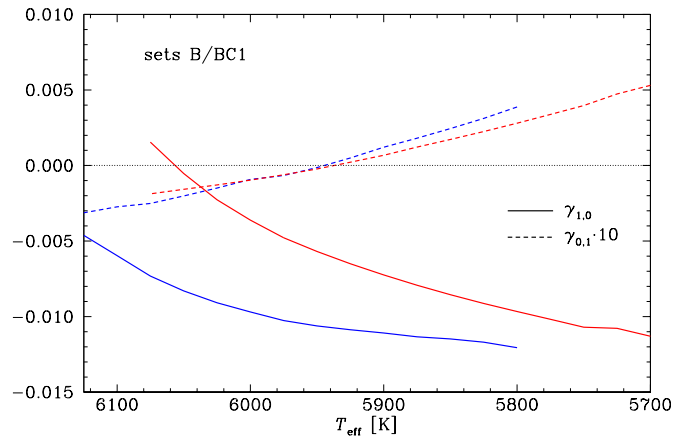Figure C.17: The same as Figure C.1, but for set AM.

Figure C.18: The same as Figure C.1, but for set BC1.
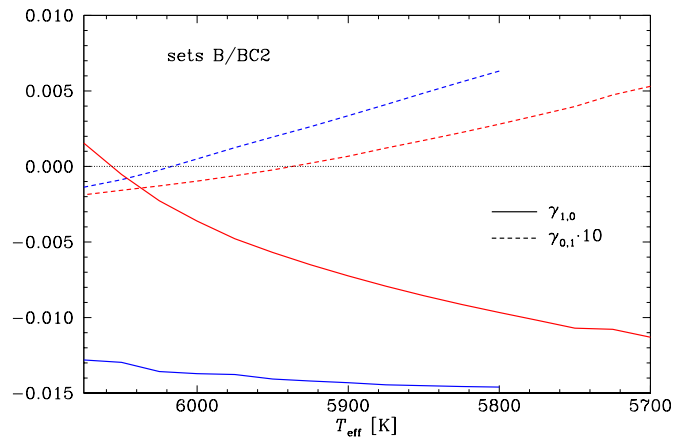

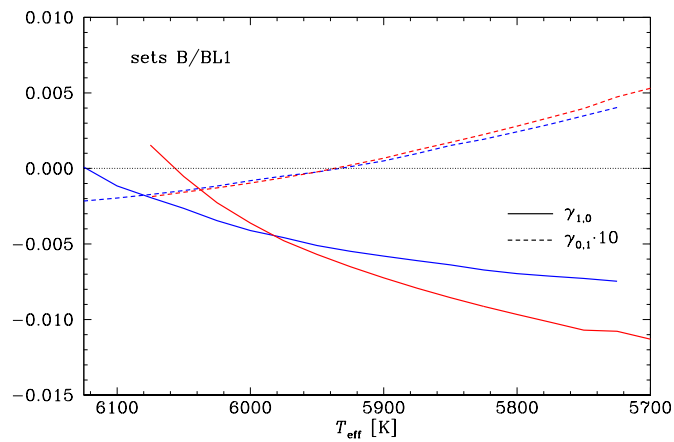Figure C.19: The same as Figure C.1, but for set BC2.

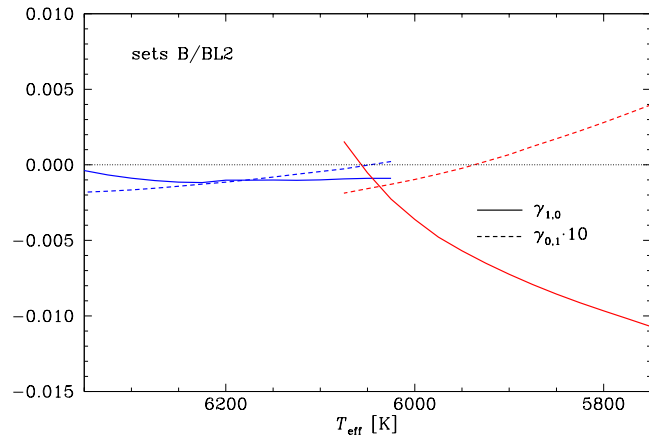Figure C.20: The same as Figure C.1, but for set BL1.

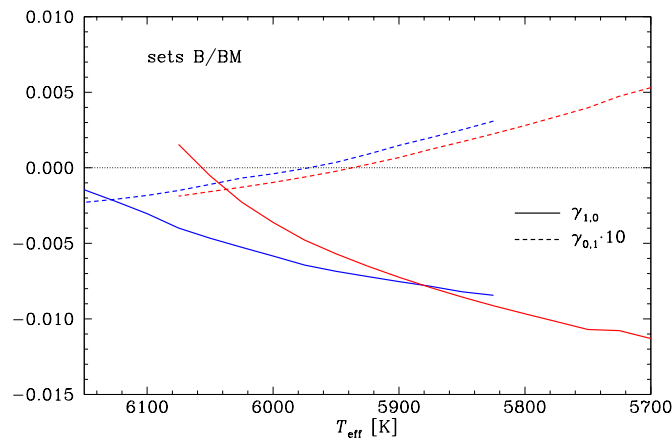Figure C.21: The same as Figure C.1, but for set BL2.

Figure C.22: The same as Figure C.1, but for set BM.

References

AIKAWA, T. & SIMON, N.R. (1983), *Astrophysical Journal*, **273**, 346; *Temperature-Grid Coordinates for Treating Pulsations in the Hydrogen Ionization Zone*

AIKAWA, T., ANTONELLO, E. & SIMON, N.R. (1987), *Astronomy & Astrophysics*, **181**, 25; *Hydrodynamic models for the short-period, classical Cepheid, SU Cas*

ALCOCK, C. *et al.* (1999), *Astrophysical Journal*, **511**, 185; *The MACHO Project LMC Variable Star Inventory. VI. The Second Overtone Mode of Cepheid Pulsation from First/Second Overtone Beat Cepheids*

ALEXANDER, D.R. & FERGUSON, J.W. (1994), *Astrophysical Journal*, **437**, 879; *Low-temperature Rosseland opacities*

ALIBERT, Y., BARAFFE, I., HAUSCHILDT, P. & ALLARD, F. (1999), *Astronomy & Astrophysics*, **344**, 551; *Perio-luminosity-color-radius relationships of Cepheids as a function of metallicity: evolutionary effects*

ANDERSON, E. *et al.* (1999), *LAPACK Users' Guide, Third Edition*, pub. Society for Industrial and Applied Mathematics, Philadelphia, PA, USA

ANDREASEN, G.K. (1988), *Astronomy & Astrophysics*, **201**, 72; *Stellar consequences of enhanced metal opacity. I. An attractive solution of the Cepheid period ratio discrepancies*

ANTONELLO, E. & PORETTI, E. (1986), *Astronomy & Astrophysics*, **169**, 149; *Structural properties of the light curves of s-Cepeids*

ANTONELLO, E. & MORELLI, P.L. (1996), *Astronomy & Astrophysics*, **314**, 541; *Search for resonance effects in long period Cepheids*

ANTONELLO, E., PORETTI, E. & REDUZZI, L. (1990), *Astronomy & Astrophysics*, **236**, 138; *The separation of s-Cepheids from classical Cepheids and a new definition of the class*

ANTONELLO, E. & AIKAWA, T. (1993), *Astronomy & Astrophysics*, **279**, 119; *Nonlinear models of first overtone mode Cepheids*

ANTONELLO, E. & AIKAWA, T. (1995), *Astronomy & Astrophysics*, **302**, 105; *A comparison between observations and nonlinear models of first overtone mode Cepheids*

ASPLUND, M., GREVESSE, N., SAUVAL, A.J., ALLENDE PRIETO, C. & KISELMAN, D. (2004), *Astronomy & Astrophysics*, **417**, 751; *Line formation in solar granulation. IV. [O I], O I and OH lines and the photospheric O abundance*

BAADE, W. (1926), *Astronomische Nachrichten*, **228**, 359; *Uber eine Möglichkeit, die Pulsationstheorie der δ Cephei-Veränderlichen zu prüfen*

BAKER, N.H. (1987), in "Physical Processes in Comets, Stars and Active Galaxies", p. 105; *Time Dependent Convection in Stars – a Review of the Theories*

BAKER, N.H. & GOUGH, D.O. (1979), *Astrophysical Journal*, **234**, 232; *Pulsations of Model RR Lyrae Stars*

BAKER, N.H. & KIPPENHAHN, R. (1962), *Zeitschrift für Astrophysik*, **54**, 114; *The Pulsations of Models of δ Cephei Stars*

BAKER, N.H. & KIPPENHAHN, R. (1965), *Astrophysical Journal*, **142**, 868; *The Pulsations of Models of δ Cephei Stars. II*

BAKER, N.H. & SENGBUSCH, VON K. (1969), *Mitt. Astr. Gesellschaft*, **27**, 162; *Nonlinear Periodic Pulsations of Stars*

BARANOWSKI, R., SMOLEC, R., DIMITROV, W. *et al.* (2009), *MNRAS*, **396**, 2194; *V440 Per: the longest period overtone Cepheid*

BEAULIEU, J.P. *et al.* (1995), *Astronomy & Astrophysics*, **303**, 137; *EROS variable stars: fundamental-mode and first-overtone Cepheids in the bar of the Large Magellanic Cloud*

BEAULIEU, J.P., BUCHLER, J.R., MARQUETTE, J.B., HARTMAN, J.D. & SCHWARZENBERG-CZERNY, A. (2006), *Astrophysical Journal*, **653**, 101; *Detection of Beat Cepheids in M33 and their Use as a Probe of the M33 Metallicity Distribution*

BONO, G. & STELLINGWERF, R.F. (1992), *Mem.S.A.It.*, **63**, 357; *RR Lyrae Convective Models*

BONO, G. & STELLINGWERF, R.F. (1993), in "New perspectives on stellar pulsation and pulsating variable stars", Eds. Nemec, J.M. & Matthews, J.M.; p. 275; *Double-mode RR Lyrae models*

BONO, G. & STELLINGWERF, R.F. (1994), *Astrophysical Journal Suppl. Ser.*, **93**, 233; *Pulsation and stability of RR Lyrae stars. I. Instability strip.*

BONO, G., MARCONI, M. & STELLINGWERF, R.F. (1999), *Astrophysical Journal Suppl. Ser.*, **122**, 167; *Classical Cepheid Pulsation Models. I. Physical Structure*

BONO, G., MARCONI, M. & STELLINGWERF, R.F. (2000), *Astronomy & Astrophysics*, **360**, 245; *Classical Cepheid Pulsation Models. VI. Hertzsprung progression*

BONO, G., CAPUTO, F., CASTELLANI, V. & MARCONI, M. (1997), *Astronomy & Astrophysics Suppl. Ser.*, **121**, 327; *Nonlinear investigation of the pulsational properties of RR Lyrae variables*

BÖHM-VITENSE, E. (1958), *Zs. f. Astrophys.*, **46**, 108; *Über die Wasserstoffkonvektionszone in Sternen verschiedener Effektivtemperaturen und Leuchtkrfte*

BUCHLER, J.R. (1990), in the proceedings of the NATO Advanced Research Workshop on The Numerical Modelling of Nonlinear Stellar Pulsations Problems and Prospects, Ed. Buchler, J.R.; p.1; *The Modelling of Nonlinear Stellar Pulsations*

BUCHLER, J.R. (1998), *ASP Conf. Ser.*, **135**, 220; *Nonlinear Pulsations*

BUCHLER, J.R. (2008), *Astrophysical Journal*, **680**, 1412; *Beat Cepheids as Probes of Stellar and Galactic Metallicity: The New AGS Abundances*

BUCHLER, J.R. & GOUPIL, M.-J. (1984), *Astrophysical Journal*, **279**, 394; *Amplitude Equations for Nonadiabatic Nonlinear Stellar Pulsators. I. The Formalism*

BUCHLER, J.R. & KOLLÁTH, Z. (2000), *NYAS*, **898**, 39; *Turbulent Convection in the Classical Variable Stars*

BUCHLER, J.R. & KOVÁCS, G. (1986a), *Astrophysical Journal*, **303**, 749; *The effects of a 2:1 resonance in nonlinear radial stellar pulsations*

BUCHLER, J.R. & KOVÁCS, G. (1986b), *Astrophysical Journal*, **308**, 661; *On the modal Selection of Radial Stellar Pulsators*

BUCHLER, J.R. & SZABÓ, R. (2007), *Astrophysical Journal*, **660**, 723; *Beat Cepheids as Probes of Stellar and Galactic Metallicity*

BUCHLER, J.R., KOLLÁTH, Z. & MAROM, A. (1997), *Astrophys. & Space Sci.*, **253**, 139; *An Adaptive Code for Radial Stellar Model Pulsations*

BUCHLER, J.R., MOSKALIK, P. & KOVÁCS, G. (1990), *Astrophysical Journal*, **351**, 617; *A Survey of Bump Cepheid Model Pulsations*

BUCHLER, J.R., KOLLÁTH, Z., BEAULIEU, J.P. & GOUPIL, M.-J. (1996), *Astrophysical Journal*, **462**, L83; *Do the Magellanic Cepheids Pose a New Puzzle?*

BUCHLER, J.R., YECKO, P., KOLLÁTH, Z. & GOUPIL, M.-J. (1999), *ASP Conf. Ser.*, **173**, 141; *Turbulent Convection in Pulsating Stars*

CANUTO, V.M. & DUBOVIKOV, M. (1998), *Astrophysical Journal*, **493**, 834; *Stellar Turbulent Convection. I. Theory*

CARSON, T.R. (1976), *Ann. Rev. Astron. Asrophys.*, **14**, 95; *Stellar opacity*

CARSON, T.R. & STOTHERS, R. (1976), *Astrophysical Journal*, **204**, 461; *Evolutionary Problems of Cepheids and Other Giants Investigated with New Radiative Opacities*

CARSON, T.R., HUEBNER, W.F., MAGEE, N.H., JR. & MERTS, A.L. (1984), *Astrophysical Journal*, **283**, 466; *Discrepancy in the CNO opacity bump resolved*

CASTOR, J.I. (1971), *Astrophysical Journal*, **166**, 109; *On the calculation of linear, nonadiabatic pulsations of stellar models*

CHARBONNEAU, P. (1995), *Astrophysical Journal Suppl. Ser.*, **101**, 309; *Genetic Algorithms in Astronomy and Astrophysics*

CHICONE, C. (1999), *Ordinary Differential Equations with Applications*, Springer-Verlag, New York

CHRISTY, R.F. (1964), *Reviews of Modern Physics*, **36**, 555; *The Calculation of Stellar Pulsation*

CHRISTY, R.F. (1966a), *Astrophysical Journal*, **144**, 108; *A Study of Pulsation in RR Lyrae Models*

CHRISTY, R.F. (1966b), *Astrophysical Journal*, **145**, 337; *A Model of W Wirginis with RV Tauri Characteristics*

CHRISTY, R.F. (1966c), *Astrophysical Journal*, **145**, 340; *Pulsation Models of Delta Cephei and Eta Aquilae*

CHRISTY, R.F. (1968), *Quarterly J. of the Roy. Ast. Soc.*, **9**, 13; *The Theory of Cepheid Variability*

COGAN, B.C. (1970), *Astrophysical Journal*, **162**, 139; *Pulsation Constants for Models of Cepheids*

COGAN, B.C. (1977), *Astrophysical Journal*, **211**, 890; *The Pulsation Periods of Stars with Convection Zones*

COX, A.N. (1980), *Ann. Rev. Astron. Asrophys.*, **18**, 15; *The Masses of Cepheids*

Cox, A.N. & Stewart, J.N. (1965), *Astrophysical Journal Suppl. Ser.*, **11**, 22; *Radiative and Conductive Opacities for Eleven Astrophysical Mixtures*

Cox, A.N. & Tabor, J.E. (1976), *Astrophysical Journal Suppl. Ser.*, **31**, 271; *Radiative opacity tables for 40 stellar mixtures*

Cox, A.N., Deupree, R.G., King, D.S. & Hodson, S.W. (1977), *Astrophysical Journal*, **214**, 127; *Revised Masses for the Double-Mode and Bump Cepheids*

Cox, A.N., Hodson, S.W. & King, D.S. (1978), *Astrophysical Journal*, **220**, 996; *Double-Mode Cepheid Period Ratios from Linear and Nonlinear Theory*

Cox, J.P. (1958), *Astrophysical Journal*, **127**, 194; *Non-Adiabatic Stellar Pulsation. I*

Cox, J.P. (1980), *Theory of Stellar Pulsation*, Princeton Univ. Press, Princeton

Cox, J.P. & Giuli, R.T. (1968), *Principles of Stellar Structure*, Gordon and Breach, Science Publishers, Inc., New York

Cox, J.P. & Whitney, C. (1958), *Astrophysical Journal*, **127**, 561; *Stellar Pulsation. IV. A Semitheoretical Period-Luminosity Relation For Classical Cepheids*

Cox, J.P., King, D.S. & Stellingwerf, R.F. (1972), *Astrophysical Journal*, **171**, 93; *Theoretical Pulsation Constants and Cepheid Masses*

Davis, C.G. & Davison, D.K. (1978), *Astrophysical Journal*, **221**, 929; *Theoretical Models of 10 Day Cepheids*

Deupree, R.G. (1977a), *Astrophysical Journal*, **211**, 509; *The theoretical red edge of the RR Lyrae gap. I - Dependence of convection on pulsation phase*

Deupree, R.G. (1977b), *Astrophysical Journal*, **214**, 502; *The theoretical red edge of the RR Lyrae gap. II - Dependence of the red edge on luminosity and composition, and observational consequences*

Dongarra, J. & Moler, C.B. (1983), *Technical Memorandum Argonne National Laboratory*, **12**; *EISPACK – A Package for Solving Matrix Eigenvalue Problems*

Dongarra, J., Bunch, J., Moler, C. & Stewart, P. (1979), *LINPACK User's Guide*, pub. Society for Industrial and Applied Mathematics, Philadelphia, PA, USA

Dorfi, E.A. & Feuchtinger, M.U. (1991), *Astronomy & Astrophysics*, **249**, 417; *Nonlinear stellar pulsations. I. Numerical methods, basic physics, initial models, and first results*

Dorfi, E.A. & Feuchtinger, M.U. (1995), *Computer Physics Communications*, **89**, 69; *Adaptive radiation hydrodynamics of pulsating stars*

Dziembowski, W.A. (1977), *Acta Astronomica*, **27**, 95; *Oscillations of giants and supergiants*

Dziembowski, W.A. (1982), *Acta Astronomica*, **32**, 147; *Nonlinear Mode Coupling in Oscillating Stars. I. Second Order Theory of the Coherent Mode Coupling*

Dziembowski, W.A. (1994), in the proceedings of the 162nd symposium of the International Astronomical Union, Eds. Balona, L.A., Henrichs, H.F. and Contel, J.M., p. 55; *The New Opacities and B-Star Pulsations*

Dziembowski, W.A. (2007), *Communications in Asteroseismology*, **150**, 175; *Oscillations in main sequence B-type stars - challenges to theory*

DZIEMBOWSKI, W.A. & KOVÁCS, G. (1984), *MNRAS*, **206**, 497; *On the role of resonances in double-mode pulsation*

DZIEMBOWSKI, W.A. & SMOLEC, R. (2009), *Acta Astronomica*, **59**, 19; *Double-Overtone Cepheids in the Large Magellanic Cloud*

EDDINGTON, A.S. (1918), *MNRAS*, **74**, 2; *On the Pulsations of a Gaseous Star and the Problem of the Cepheid Variables. Part I.*

EDDINGTON, A.S. (1919), *MNRAS*, **74**, 177; *The Pulsations of a Gaseous Star and the Problem of the Cepheid Variables. Part II.*

EDDINGTON, A.S. (1926), *Internal Constitution of the Stars*; *Cambridge University Press, Cambridge, England*

EDGAR, J.A. (1933), *MNRAS*, **93**, 422; *The Pulsation Theory of Cepheid Variables*

EPSTEIN, I. (1950), *Astrophysical Journal*, **112**, 6; *Pulsation Properties of Giant-Star Models*

FEUCHTINGER, M.U. (1998), *Astronomy & Astrophysics*, **337**, 29; *A nonlinear model for RR Lyrae double-mode pulsation*

FEUCHTINGER, M.U. (1999a), *Astronomy & Astrophysics Suppl. Ser.*, **136**, 217; *A nonlinear convective model for radial stellar pulsations. I. The physical description*

FEUCHTINGER, M.U. (1999b), *Astronomy & Astrophysics*, **351**, 103; *A nonlinear convective model of pulsating stars. II. RR Lyrae stars*

FEUCHTINGER, M.U., BUCHLER, J.R. & KOLLÁTH Z. (2000), *Astrophysical Journal*, **544**, 1056; *Hydrodynamical Survey of First-overtone Cepheids*

FRALEY, G.S. (1968), *Astrophys. & Space Sci.*, **2**, 96; *Supernovae explosions induced by pair-production instability*

FRICKE, K., STOBIE, R.S. & STRITTMATTER, P.A. (1971), *MNRAS*, **154**, 23; *Quantitative Results of Stellar Evolution and Pulsation Theories*

GABOR, D. (1946), *J. Inst. Electr. Eng.*, **93**, 429; *Theory of Communication*

GAUTSCHY, A. (2003), ETH, Eidgenössische Technische Hochschule Zürich, ETH Bibliothek; http://e-collection.ethbib.ethz.ch/view/eth:28283; *The history of radial stellar pulsation theory. A short look at the long road to understand what was seen*

GEHMEYR, M. (1992a), *Astrophysical Journal*, **399**, 265; *On Nonlinear Radial Oscillations in Convective RR Lyrae Stars. I. The Mathematical Description*

GEHMEYR, M. (1992b), *Astrophysical Journal*, **399**, 272; *On Nonlinear Radial Oscillations in Convective RR Lyrae Stars. II. Comparison of a Radiative and a Convective Model*

GEHMEYR, M. (1993), *Astrophysical Journal*, **412**, 341; *On Nonlinear Radial Oscillations in Convective RR Lyrae Stars. III. A Full-Amplitude Investigation of the Red Edge*

GEHMEYR, M. & WINKLER, K.-H.A. (1992a), *Astronomy & Astrophysics*, **253**, 92; *On a new, one-dimensional, time-dependent model for turbulence and convection. I. A basic discussion of the mathematical model*

GEHMEYR, M. & WINKLER, K.-H.A. (1992b), *Astronomy & Astrophysics*, **253**, 101; *On a new, one-dimensional, time-dependent model for turbulence and convection. II. An elementary comparison of the old and the new model*

GIRARDI, L., BRESSAN, A., BERTELLI, G. & CHIOSI, C. (2000), *Astronomy & Astrophysics Suppl. Ser.*, **141**, 371; *Evolutionary tracks and isochrones for low- and intermediate-mass stars: from 0.15 to 7 M$_\odot$, and from Z=0.0004 to 0.03*

GLASNER, A. & BUCHLER, J.R. (1993), *Astronomy & Astrophysics*, **277**, 69; *On the spectrum of the linear nonadiabatic radial stellar modes*

GONCZI, G. & OSAKI, Y. (1980), *Astronomy & Astrophysics*, **84**, 304; *On Local Theories of Time-dependent Convection in the Stellar Pulsation Problem*

GOODRICKE, J.B. (1783), *Phil. Trans. of the Roy. Soc. of London*, **73**, 474; *A series of observations on, and a discovery of, the period of the variation of the light of the bright star in the Head of Medusa, called Algol*

GOODRICKE, J.B. (1786), *Phil. Trans. of the Roy. Soc. of London*, **76**, 48; *A Series of Observations on, and a Discovery of, the Period of the Variation of the Light of the Star Marked δ by Bayer, Near the Head of Cepheus. In a Letter from John Goodricke, Esq. to Nevil Maskelyne, D. D. F. R. S. and Astronomer Royal*

GOUGH, D.O. (1965), *Geophys. Fluid Dyn. II*, p. 49

GOUGH, D.O. (1968), *J. Atm. Sci.*, **26**, 448; *The Anelastic Approximation for Thermal Convection*

GOUGH, D.O. (1977), *Astrophysical Journal*, **214**, 196; *Mixing-Length Theory for Pulsating Stars*

GREVESSE, N. & NOELS, A. (1993), in Origin and Evolution of the Elements, Eds. Pratzo, N., Vangioni-Flam, E. and Casse, M., Cambridge Univ. Press., p. 15; *Cosmic abundances of the elements*

HANSEN, C.J., KAWALER, S.D. & TRIMBLE, V. (2004), *Stellar Interiors: Physical Principles, Structure, and Evolution*, Springer-Verlag New York, Inc.

HEN, L. & SCHWARZSCHILD, M. (1949), *MNRAS*, **109**, 631; *Red-Giant Modelswith Chemical Inhomogeneities*

HERTZSPRUNG, E. (1905), *Zeitschrift für Wissenschaftliche Photographie*, **3**, 429; *Zur Strahlung der Sterne*

HERTZSPRUNG, E. (1907), *Zeitschrift für Wissenschaftliche Photographie*, **5**, 86; *Zur Bestimmung der photographischen Sterngrössen*

HERTZSPRUNG, E. (1914), *Astronomische Nachrichten*, **196**, 201; *Über die räumilche Verteilung der Veränderlichen vom δ Cephei-Typus*

HERTZSPRUNG, E. (1926), *Bull. Astr. Inst. Netherlands*, **3**, 115; *On the relation between period and form of the lightcurve of variable stars of the δ Cephei type*

HODSON, S.W. & COX, A.N. (1976), in: "Proc. Los Alamos Solar and Stellar Pulsation Conf.", Eds. Cox, A.N. & Deupree, R.G.; p. 202

HODSON, S.W. & COX, A.N. (1980), in: "Nonradial and Nonlinear Stellar Pulsation", Eds. Hill, H.A. & Dziembowski, W.A., p. 34; *Nonlinear Calculations for Bump Cepheids*

HOSKIN, M. (1979), *Journal for the History of Astronomy*, **10**, 23; *Goodricke, Pigott and the quest for variable stars*

HOYLE, F. & LYTTLETON, R. (1943), *MNRAS*, **103**, 21; *The Theory of Cepheid Variables and Novae*

HURWITZ, A. (1964), in Selected Papers on Mathematical Trends in Control Theory, Ed. Ballman, R.T. *et al.* ; New York: Dover; *On the Conditions under which an Equation has only Roots with Negative Real Parts*

IBEN, I. (1967), *Ann. Rev. Astron. Asrophys.*, **5**, 571; *Stellar Evolution Within and off the Main Sequence*

IGLESIAS, C.A. & ROGERS, F.J. (1991), *Astrophysical Journal*, **371**, L73; *Opacity Tables for Cepheid Variables*

IGLESIAS, C.A. & ROGERS, F.J. (1996), *Astrophysical Journal*, **464**, 943; *Updated Opal Opacities*

IGLESIAS, C.A., ROGERS, F.J. & WILSON, B.G. (1990), *Astrophysical Journal*, **322**, L45; *Opacities for Classical Cepheid Models*

JEANS, J.H. (1925), *MNRAS*, **85**, 797; *On Cepheid and Long-period Variation and the Formation of Binary Stars by Fission*

KIENZLE, F., MOSKALIK, P., BERSIER, D. & PONT, F. (1999), *Astronomy & Astrophysics*, **341**, 818; *Structural properties of s-Cepheid velocity curves. Constraining the location of the $\omega_4 = 2\omega_1$ resonance*

KING, D.S., COX, J.P., EILERS, D.D. & DAVEY, W.R. (1973), *Astrophysical Journal*, **182**, 859; *Nonlinear Cepheid Pulsation Calculations and Comparison with Linear Theory*

KOLLÁTH, Z. & BUCHLER, J.R. (2001), *ASSL*, **257**, 29; *Double-Mode Stellar Pulsations*

KOLLÁTH, Z., BEAULIEU, J.P., BUCHLER, J.R. & YECKO, P. (1998), *Astrophysical Journal*, **502**, 55; *Nonlinear Beat Cepheids Models*

KOLLÁTH, Z., BUCHLER, J.R., SZABÓ, R. & CSUBRY, Z. (2002), *Astronomy & Astrophysics*, **385**, 932; *Nonlinear beat Cepheid and RR Lyrae models*

KOVÁCS, G. & BUCHLER, J.R. (1988), *Astrophysical Journal*, **324**, 1026; *A Survey of RR Lyrae Models and Search for Steady Multimode Pulsations*

KOVÁCS, G. & BUCHLER, J.R. (1989), *Astrophysical Journal*, **346**, 898; *The Cepheid Bump Progression and Amplitude Equations*

KOVÁCS, G. & BUCHLER, J.R. (1993), *Astrophysical Journal*, **404**, 765; *Double-mode pulsation in radiative RR Lyrae models*

KOVÁCS, G. & KANBUR, S.M. (1998), *MNRAS*, **295**, 834; *Modelling RR Lyrae pulsation: mission (im)possible?*

KOVÁCS, G., BUCHLER, J.R. & DAVIS, C.G. (1987), *Astrophysical Journal*, **319**, 247; *Application of time-dependent Fourier analysis to nonlinear pulsational stellar models*

KUHFUSS, R. (1986), *Astronomy & Astrophysics*, **160**, 116; *A model for time-dependent turbulent convection*

KUHFUSS, R. (1987), "Ein Modell fur zeitabhangige Konvektion in Sternen", PhD-Thesis, Munchen

KURUCZ, R.L. (2004), http://kurucz.harvard.edu/

LEAVITT, H.S. (1908), *Harvard Obs. Ann.*, **60**, 87; *1777 Variables in the Magellanic Clouds*

MAGEE, N.H., JR., MERTS, A.L. & HUEBNER, W.F. (1984), *Astrophysical Journal*, **283**, 264; *Is the metal contribution to the astrophysical opacity incorrect?*

MANTEGAZZA, L. & PORETTI, E. (1992), *Astronomy & Astrophysics*, **261**, 137; *The Fourier decomposition as a mode discriminator - New first overtone pulsators among Cepheids with P less than 5.5 d*

MARQUETTE, J.B. *et al.* (2009), *Astronomy & Astrophysics*, **495**, 249; *The beat Cepheids in the Magellanic Clouds: an analysis from the EROS-2 database*

MOFFETT, T.J. & BARNES, T.G., III (1985), *Astrophysical Journal Suppl. Ser.*, **58**, 843; *Observational studies of Cepheids. III - Catalog of light curve parameters*

MOSKALIK, P. & BUCHLER, J.R. (1989), *Astrophysical Journal*, **341**, 997; *The effects of 3:1 resonances in stellar pulsations*

MOSKALIK, P. & DZIEMBOWSKI, W.A. (2005), *Astronomy & Astrophysics*, **434**, 1077; *Seismology of triple-mode classical Cepheids of the Large Magellanic Cloud*

MOSKALIK, P. & KOŁACZKOWSKI, Z. (2008), *Communications in Asteroseismology*, **157**, 343; *Nonradial modes in classical cepheids*

MOSKALIK, P. & KOŁACZKOWSKI, Z. (2009), *MNRAS*, **394**, 1649; *Frequency analysis of Cepheids in the Large Magellanic Cloud: new types of classical Cepheid pulsators*

MOSKALIK, P., BUCHLER, J.R. & MAROM, A. (1992), *Astrophysical Journal*, **385**, 685; *Toward a Resolution of the Bump and Beat Cepheid Mass Discrepancies*

MOSKALIK, P., KOŁACZKOWSKI, Z. & MIZERSKI, T. (2004), *ASP Conf. Ser.*, **310**, 498; *Nonradial pulsations in classical Cepheids of the Magellanic Clouds*

OLIVIER, E.A. & WOOD, P.R. (2005), *MNRAS*, **362**, 1396; *Non-linear pulsation models of red giants*

PAMYATNYKH, A.A. (1999), *Acta Astronomica*, **49**, 119; *Pulsational Instability Domains in the Upper Main Sequence*

PETERSEN, J.O. (1973), *Astronomy & Astrophysics*, **27**, 89; *Masses of Double Mode Cepheid Variables Determined by Analysis of Period Ratios*

PETERSEN, J.O. & JORGENSEN, H.O. (1972), *Astronomy & Astrophysics*, **17**, 367; *Pulsation of Models in the Lower Part in the Cepheid Instability Strip and properties of AI Velorum and δ Scuti Variables*

PICKERING, E.C. (1912), *Harvard Circ.*, **173**; *Periods of 25 Variable Stars in The Small Magellanic Cloud*

PIETRINFERNI, A., CASSISI, S., SALARIS, M. & CASTELLI, F. (2004), *Astrophysical Journal*, **612**, 168; *A Large Stellar Evolution Database for Population Synthesis Studies. I. Scaled Solar Models and Isochrones*

PIGOTT, E. (1785), *Phil. Trans. of the Roy. Soc. of London*, **75**, 127; *Observations of a New Variable Star. In a Letter from Edward Pigott, Esq. to Sir H. C. Englefield, Bart. F. R. S. and A. S.*

PIGULSKI, A. (2007), *Communications in Asteroseismology*, **150**, 159; *The present day of asteroseismology of β Cephei stars: observations*

POJMAŃSKI, G. (1997), *Acta Astronomica*, **47**, 467; *The All Sky Automated Survey*

PORETTI, E. (1994), *Astronomy & Astrophysics*, **285**, 524; *The Fourier decomposition of new light curves of Cepheids with $P < 7d$*

PRANDTL, L. (1952), *Essentials of Fluid Dynamics*, Blakie, London

RICHARDSON, R.S. & SCHWARZSCHILD, M. (1948), *Astrophysical Journal*, **108**, 373; *A Stellar Model for Red Giants of High Central Temperature*

RICHTMYER, R.D. (1957), *Difference Methods for Initial Value Problems*, Interscience, New York

RITTER, A. (1879), *Wiedemanns Annalen*, **VIII**, 173

RODGERS, A.W. (1970), *MNRAS*, **151**, 133; *The Masses of Pulsating Stars*

ROGERS, F.J. (2000), *Physics of Plasmas*, **7**, 51; *Ionization equilibrium and equation of state in strongly coupled plasmas*

RUSSELL, H.N. (1913), *Observer*, **36**, 324; *"Giant" and "Dwarf" Stars*

RUSSELL, H.N. (1914), *Popular Astronomy*, **22**, 275; *Relations Between the Spectra and Other Characteristics of the Stars*

RUSSELL, H.N. (1927), *Astrophysical Journal*, **66**, 122; *On the Relations Between Period, Luminosity, and Spectrum among Cepheids*

SANDAGE, A., TAMMANN, G.A. & REINDL, B. (2004), *Astronomy & Astrophysics*, **424**, 43; *New period-luminosity and period-color relations of classical Cepheids. II. Cepheids in LMC*

SCHAEFER, B.E. (2008), *Astron. Journal*, **135**, 112; *A Problem with the Clustering of Recent Measures of the Distance to the Large Magellanic Cloud*

SCHALLER, G., SCHAERER, D., MEYNET, G. & MAEDER, A. (1992), *Astronomy & Astrophysics Suppl. Ser.*, **96**, 269; *New grids of stellar models from 0.8 to 120 solar masses at Z = 0.020 and Z = 0.001*

SHAPLEY, H. (1914), *Astrophysical Journal*, **40**, 448; *On the Nature and Cause of Cepheid Variation*

SCHWARZSCHILD, M. (1900), *Publ. d.v. Kuffer'schen Sternwart*, **50**, 100

SIMON, N.R. (1972), *Astronomy & Astrophysics*, **21**, 45; *Iterative Nonlinear Pulsations in Massive Stars. I. The Iterative Approach*

SIMON, N.R. (1979), *Astronomy & Astrophysics*, **75**, 140; *Double Mode Pulsation as a Resonance Phenomenon*

SIMON, N.R. (1982), *Astrophysical Journal*, **260**, L87; *A Plea for Reexamining Heavy Element Opacities in Stars*

SIMON, N.R. & SCHMIDT, E.G. (1976), *Astrophysical Journal*, **205**, 162; *Evidence Favoring Nonevolutionary Cepheid Masses*

SIMON, N.R. & LEE, A.S. (1981), *Astrophysical Journal*, **248**, 291; *The Structural Properties of Cepheid Light Curves*

SIMON, N.R. & DAVIS, C.G. (1983), *Astrophysical Journal*, **266**, 787; *The Light and Velocity Curves of Classical Cepheids: Theory Versus Observation*

SIMON, N.R. & KANBUR, S.M. (1995), *Astrophysical Journal*, **451**, 703; *Long-Period Cepheids: Models and Observations*

SIMON, N.R., COX, A.N. & HODSON, S.W (1980), *Astrophysical Journal*, **237**, 550; *Modal Selection in Pulsating Stars*

SMOLEC, R. (2008), *Communications in Asteroseismology*, **157**, 149; *The role of negative buoyancy in convective Cepheid models. Double-mode pulsations revisited*

SMOLEC, R. (2009), *EAS Publications Series*, **38**, 175; *Double-Mode Radiative β Cephei and δ Cephei Models*

SMOLEC, R. & MOSKALIK, P. (2007), *MNRAS*, **377**, 645; *Amplitude Saturation in β Cephei Models*

SMOLEC, R. & MOSKALIK, P. (2008a), *Acta Astronomica*, **58**, 193; *Convective Hydrocodes for Radial Stellar Pulsation. Physical and Numerical Formulation*

SMOLEC, R. & MOSKALIK, P. (2008b), *Acta Astronomica*, **58**, 233; *Double-Mode Convective Cepheid Models – Revisited*

SONNEBORN, G., KUZMA, T.J. & COLLINS, G.W. (1979), *Astrophysical Journal*, **232**, 807; *The Effects of Enhanced Helium Abundance on the Visible Spectra of Luminous F and G Stars*

SOSZYŃSKI, I. *et al.* (2008a), *Acta Astronomica*, **58**, 153; *The Optical Gravitational Lensing Experiment. Triple-Mode and 1O/3O Double-Mode Cepheids in the Large Magellanic Cloud*

SOSZYŃSKI, I. *et al.* (2008b), *Acta Astronomica*, **58**, 163; *The Optical Gravitational Lensing Experiment. The OGLE-III Catalog of Variable Stars. I. Classical Cepheids in the Large Magellanic Cloud*

STELLINGWERF, R.F. (1974), *Astrophysical Journal*, **192**, 139; *The Calculation of Periodic Pulsations of Stellar Models*

STELLINGWERF, R.F. (1975a), *Astrophysical Journal*, **195**, 441; *Modal Stability of RR Lyrae Stars*

STELLINGWERF, R.F. (1975b), *Astrophysical Journal*, **199**, 705; *Nonlinear Effects in Double-Mode Cepheids*

STELLINGWERF, R.F. (1976), *Astrophysical Journal*, **206**, 543; *The Role of Turbulent Pressure in Mixing-Length Convection*

STELLINGWERF, R.F. (1978), *Astron. Journal*, **83**, 1184; *Helium ionization driving in Beta Cephei stars*

STELLINGWERF, R.F. (1982a), *Astrophysical Journal*, **262**, 330; *Convection in Pulsating Stars. I. Nonlinear Hydrodynamics*

STELLINGWERF, R.F. (1982b), *Astrophysical Journal*, **262**, 339; *Convection in Pulsating Stars. II. Convection and Stability*

STELLINGWERF, R.F. (1984a), *Astrophysical Journal*, **277**, 322; *Convection in Pulsating Stars. III. The RR Lyrae Instability Strip*

STELLINGWERF, R.F. (1984b), *Astrophysical Journal*, **277**, 327; *Convection in Pulsating Stars. IV. Nonlinear Effects*

STELLINGWERF, R.F. (1984c), *Astrophysical Journal*, **284**, 712; *Convection in Pulsating Stars. V. Limit Cycle Characteristics*

STOBIE, R.S. (1969a), *MNRAS*, **144**, 461; *Cepheid Pulsation – I. Numerical Technique and Test Calculations*

STOBIE, R.S. (1969b), *MNRAS*, **144**, 485; *Cepheid Pulsation – II. Models Fitted to Evolutionary Tracks*

STOBIE, R.S. (1969c), *MNRAS*, **144**, 511; *Cepheid Pulsation – III. Models Fitted to a New Mass-Luminosity Relation*

STOTHERS, R. (1979), *Astrophysical Journal*, **234**, 257; *Magnetic Cepheids*

STOTHERS, R. (1982), *Astrophysical Journal*, **255**, 227; *Nonlinear Models of Classical Cepheids Endowed with Tangled Magnetic Fields*

STÖKL, A. (2008), *Astronomy & Astrophysics*, **490**, 1181; *A two-column formalism for time-dependent modelling of stellar convection. I. Description of the method*

SWARZTRAUBER, P.N. (1984), *Parallel Computing*, **1**, 45; *Fast Fourier Transforms Algorithms for Vector Computers*

SZABÓ, R., BUCHLER, J.R. & BARTEE, J. (2007), *Astrophysical Journal*, **667**, 1150; *The Cepheid Phase Lag Revisited*

SZABÓ, R., KOLLÁTH, Z. & BUCHLER, J.R. (2004), *Astronomy & Astrophysics*, **425**, 627; *Automated nonlinear stellar pulsation calculations: Applications to RR Lyrae stars. The slope of the fundamental blue edge and the first RRd model survey*

TAKEUTI, M. & AIKAWA, T. (1981), *Science Rap. Tôhoku Univ.*, Eighth Series, Vol. 2, p. 106; *Resonance phenomenon in classical cepheids*

UDALSKI, A. *et al.* (1999), *Acta Astronomica*, **49**, 223; *The Optical Gravitational Lensing Experiment. Cepheids in the Magellanic Clouds. IV. Catalog of Cepheids from the Large Magellanic Cloud*

UNNO, W. (1967), *PASJ*, **19**, 140; *The Stellar Radial Pulsation Coupled with the Convection*

UNNO, W., OSAKI, Y., ANDO, H., SAIO, H. & SHIBAHASHI, H. (1989), *Nonradial Oscillations of Stars*, University of Tokyo Press

VEMURY, S.K. & STOTHERS, R. (1978), *Astrophysical Journal*, **225**, 939; *Bump Cepheids: The Mass Anomaly as an Opacity Effect*

VITENSE, E. (1953), *Zs. f. Astrophys.*, **32**, 135; *Die Wasserstoffkonvektionszone der Sonne*

WHITNEY, C. (1956), *Astron. Journal*, **61**, 192; *The velocity humps of classical Cepheids*

WUCHTERL, G., FEUCHTINGER, M.U. (1998), *Astronomy & Astrophysics*, **340**, 419; *A simple convection model for selfgravitating fluid dynamics. Time-dependent convective energy transfer in protostars and nonlinear stellar pulsations*

YECKO, P., KOLLÁTH, Z. & BUCHLER, J.R. (1998), *Astronomy & Astrophysics*, **336**, 553; *Turbulent convective cepheid models: linear properties*

ZHEVAKIN, S.A. (1953), *Astron. Zhurnal*, **30**, 161

ZHEVAKIN, S.A. (1963), *Ann. Rev. Astr. & Astrophys.*, **1**, 367; *Physical Basis of the Pulsation Theory of Variable Stars*